Colloidal semiconductor nanocrystals for optoelectronic applications : photodetectors and light emitting diodes

Junling Qu

THÉSE DE DOCTORAT DE SORBONNE UNIVERSITÉ

Spécialité: Physique et chimie des Matériaux

École doctorale 397

Réalisée à l'Institut des NanoSciences de Paris (INSP)

Présentée par Junling QU

Pour obtenir le grade de docteur de SORBONNE UNIVERSITÉ

Sujet de la thèse

Colloidal semiconductor nanocrystals for optoelectronic applications: photodetectors and light emitting diodes

Soutenue le 29 avril 2021

Devant le jury composé de

Dr. Dmitry Aldakov	CEA Grenoble	Rapporteur
Dr. Lionel Hirsch	Université de Bordeaux	Rapporteur
Prof. Bruno Masenelli	INSA Lyon	Examinateur
Prof. Davy Gérard	UTT Troyes	Examinateur
Prof. Corinne Chanéac	Sorbonne université	Examinatrice
Dr. Emmanuel Lhuillier	INSP	Directeur de thése

Table of contents

Notations and abbreviations

Physical constants

Symbol	value	description
e	1.609×10^{-19} C	Electron charge
c	299792458 m/s	Speed of light
h	6.62×10^{-34} Js	Plank constant
$\hbar$	1.05×10^{-34} Js	Reduced plank constant
m_0	9.11×10^{-31} kg	Free electron mass
ϵ_0	8.85×10^{-12} kg^{-1}m^{-3}s^{4}A^2	Vacuum permittivity

Abbreviations

Abbreviation	Description
NC(s)	Nanocrystal(s)
QD, CQD	Quantum dot, colloidal quantum dot
QW, CQW	Quantum well, colloidal quantum well
DOS	Density of states
NPL	Nanoplatelet
FET	Field effect transistor
XPS, UPS	X-ray photoemission spectroscopy
XRD	X-ray diffraction
EDX	Energy-dispersive X-ray spectroscopy
RBS	Rutherford Backscattering Spectrometry
SEC	spectroelectrochemistry
TEM	Transmission electron microscopy
FTIR	Fourier-transform infrared spectroscopy
CB, VB	Conduction band, valance band
LOMO	Lowest occupied molecular orbital
HOMO	Highest occupied molecular orbital
UV	Ultraviolet
IR, NIR	Infrared, near infrared
SWIR	Short-wave infrared
MWIR	Mid-wave infrared
LWIR	Long-wave infrared

Notations and abbreviations

Abbreviation	Description
QCL	Quantum cascade laser
c-ALD	Colloidal-atomic layer deposition
Ag2Se, t-Ag$_2$Se	Silver selenide, tetragonal silver selenide
ITO	Indium tin oxide
AZO	Aluminum doped zinc oxide
LSPR	Localized surface plasmonic resonance
LED	Light emitting diodes
QD-LED	Quantum dot light emitting diode
OLED	Organic light emitting diode
LCD	Liquid crystal display
QD-LCD	quantum dot enhanced LCD
TCO	Transparent conductive oxides
CTL	Charge transport layer
ETL	Electron transport layer
HTL	Hole transport layer
Au	gold
Ag	Silver
EQE	External quantum efficiency
IQE	Internal quantum efficiency
PL	Photoluminescence
PLQY	Photoluminescence quantum yield
EL	Electroluminescence
Li-Fi	Light Fidelity
PEDOT:PSS	poly(3,4-ethylenedioxythiophene) polystyrene sulfonate
Poly-TPD	Poly(N,N'-bis-4-butylphenyl-N,N'-bisphenyl)benzidine
PVK	Poly(9-vinyl) carbazole
EDT	Ethanedithiol
MPA	3-Mercaptopropionic acid

Notations

Notation	Description
T	Temperature
$h\nu$	Photon energy
m_e^*	Effective mass of electrons
m_h^*	Effective mass of holes
m_{eh}^*	Reduced mass of electron/hole pair
ϵ_r	Dielectric constant of the semiconductor
ϵ_∞	High frequency dielectric constant
a_0	Excitonic Bohr radius
k	Wave vector
$\phi_{n,L}$	n^{th} root of the spherical Bessel function of the Lth order
E_g	Band gap energy
E_C	Confinement energy
E_F	Fermi level
W_F	Work function
$1\,S_e$	The first energy level of the conduction band
$1\,S_h$	The first energy level of the valence band
$1\,P_e$	The second energy level of the conduction band
α	Absorption coefficient
σ	Absorption cross-section
I_{light}	Light current
I_{dark}	Dark current
P_{inc}	Incident photon energy
V_{GS}	Gate bias in a field effect transistor
V_{DS}	Drain-source bias in a field effect transistor

Acknowledgements

At the end of this PhD journey, I am so glad that I have survived while enjoyed it. I owe this unexpectedly rich experience to all the wonderful people I have met during the last several years, and here I would like to express my sincere gratitude to them.

First, I would like to thank the members of the jury: Corinne Chanéac, Dmitry Aldakov, Lionel Hirsch, Bruno Masenelli, and Davy Gérard, for reviewing my manuscript and proposing provoking discussions during the defense.

My special thanks go to my supervisor Emmanuel Lhuillier. It is fun to think about the process we became supervisor and student. I was then an aimless master student who was trying to find a host group in Paris for CSC application, not knowing what to expect. It almost shocked me when I got a reply in half an hour asking for further details. I guess we were like a blind box for each other in the beginning, but I believe it have worked out great. During the last three years and half, I have continuously been impressed by your passion for science, your sharp sense for the reaerch field, and your magic skills to make the team running, even at the worst situations. As a student, I have benefited a lot from your previsional yet explicit organizations throughout the course of the PhD. Above all, thank you for offering me the opportunity to work in the amazing OCN team, where I have never stopped absorbing knowledge and growing in so many aspects.

I then wish to thank my colleagues from the OCN team of INSP. Specially, I want to express my gratitude to Nicolas Goubet for introducing me to nanocrystal synthesis, on which I had zero experience and knowledge before. But more importantly, you gave me the wise advices such as "you have to find a way to work" and "try to collect some data everyday", which really helped me to go through the PhD years. Clément, it was so lucky of me to have your warm help when I joined the team. You have taught me so many stuffs and I am still using the little "livachian" tools you introduced me. Please stop breaking yourself, and I expect that we will meet again! Bertille has always been a wonderful teacher to me. I could always get clear explanations for whatever I did not understand, without feeling stupid of myself. How lucky your students are! Charlie has always amazed me with resourcefulness and open creative mind. Thank you for being so helpful for keeping the equipment working. I indeed agree that, Charlie should not be the first solution to all the problems:) Audrey, to me you are like a super girl full of energy. Cannot thank you more for being so kind and caring to me. You will do a great job on whatever you will take, with your passion, determination, and brilliance. Prachi, I have really appreciated the quality time we spent together in and out of the lab. I will remember the walks in the rains and snows (coincidence?), the festival of light, and your super tasty home cooking. I wish all the best for you in life and career. I also wish to thank Amardeep and Julien, the former postdocs of the team, for their help in experiments and fun conversations. Adrien and Tung, keep good work and wait for the day of opening. Erwan and Corentin, you are super great students, and it is such a pleasant experience to work with you! I kind of think that I have learned more from you than what I had taught you. Mariarosa, I hope you have enjoyed here.

I also wish to thank the colleagues from the LPEM lab of ESPCI. I am very grateful for Sandrine Ithurria for being so nice, warm, cheerful, and always ready to help. I am also extremely lucky to have met Xiangzhen Xu in the beginning of the PhD, for exhaustive explanations on TEM, and additionally, relaxing chats on familiar topics, which is definitely precious when I am 8000 km away from home. For a similar reason, I want to thank Ye Jiang for company and introducing me the Chinese friends and restaurants around the lab when I just arrived. I also appreciate the friendly help and interesting communications with Marion Dufour, Eva Izquierdo, and Mannon Debayle, as well as the "new" PhD students, Nicolas Moghaddam and Sobha Jana, with whom I had great time during the Germany summer school in 2019.

Acknowledgements

General introduction

Semiconductors lie in the center of electronics and optoelectronics that have founded the information age we are living in. The growing demands for smarter devices in all walks of life, including information, communication, sensing, entertainment, therapy, and energy harvesting, has spurred the revolution of semiconductors toward by-design tailored chemical-physical properties and compatibility with new manufacturing technologies targeting low-cost, large-area, flexible and wearable devices.

Quantum engineering, which tailors the electronic properties of semiconductors for specific applications, is proposed back in the 60s of the last century. Thanks to the development of molecular beam epitaxial (MBE) technique that allows atom-by-atom deposition of semiconductors, 2D quantum wells was first obtained, followed by the discovery of epitaxially grown 1D quantum rods and 0D quantum dots (QDs). The first QDs obtained were small islands of InAs on the GaAs substrates induced by a large lattice mismatch.[1] The semiconductors with one or more dimensions in the nanoscale exhibit size-dependent electronic and optoelectronic properties due to quantum confinement. On-demand properties as they can provide, the epitaxial growth is limited to niche applications such as defense and research, due to their high cost (comes with high-vacuum equipment), selective range of suitable materials and substrates, and compatibility with only the rigid and planar devices.

The emergence of colloidal nanocrystals has opened new opportunities for quantum engineering at low cost and with solution-processibility. In 1993, Bawendi's group synthesized the first monodispersed II-VI semiconductor QDs using wet-chemistry[2]. Since then, in a short time, the community has been developed the synthesis to grow nanocrystals with fine control over size, shape,[3,4] composition, and even heterostructures[5] analogy to traditional semiconductors. These chemically synthesized nanocrystals are featured with an inorganic semiconductor core (2 to 20 nm) capped by organic molecule ligands (typically alkane chain with 12-18 carbons). The inorganic core, as a single-crystal fragment of corresponding bulk materials, can provide size-tunable properties, whereas the organic ligands allow for their dispersion in solvents, hence compatibility to solution-processed deposition technologies for rigid or flexible substrates. Combining the advantages of inorganic and organic materials, colloidal nanocrystals is regarded as the most interesting building block for the next generation of optoelectronics such as light emission, sensing, and harvesting.

After more than two decades of development, colloidal nanocrystals achieved their first commercialization when Sony released their BRAVIA QDTV in 2013 using the QDs from QD Vision, Inc., after which Samsung followed suit. Although it is only a manifestation of the high color purity and photostability of QDs, it has encouraged their integration into practical consumer devices. There are two domains of optoelectronic applications where the colloidal nanocrystals are particularly interesting.

One is for **infrared photodetection**. In the wavelength above 1 μm, Si-based photodetectors which combines good performance and extremly low price, is not operative, neither the organic electronics, the low-cost alternative to Si electronics. At present, the infrared photodetection is dominated by epitaxially grown quantum wells[6] and type II superlattice[7] or narrow band gap semiconductors such as InSb and mercury cadmium telluride (MCT).[8] The cost rupture required for civilian-oriented quantum photodetectors, is most likely from colloidal nanocrystals derived from narrow-bandgap semiconductors and semimetals. PbS nanocrystals, for example, are already commercially available for SWIR cameras.[9] The photodetectors for longer wavelength in the infrared (above 3 μm) is being addressed by mercury chalcogenides featuring the widest optical absorptions from visible to THz. However, the heavy metals such as lead and mercury

have raised a toxicological concern to the mass market[10], and the searching and evaluation of heavy-metal-free nanocrystals is extremely essential.

Another important playground for colloidal nanocrystals is **light emitting diodes**. The narrow emission linewidth of nanocrystals makes them promising candidates for large gamut displays. With the development of core/shell heterostructure nanocrystals with near-unity PLQY and enhanced stability, the QD-based LEDs of three primary colors, have achieved the EQE close to the theoretical upper limit (>20%), and high brightness on par with commercially available organic LEDs.

In this context, my PhD conducted at INSP under the supervision of Dr. Emmanuel Lhuillier, is focused on the colloidal nanocrystal-based infrared photodetectors and light emitting diodes. During my PhD, benefiting from this topic at the interface of chemistry and physics, I have developed knowledge and skills of the synthesis of various nanocrystals, clean room fabrication, and the optical and electrical characterization of the fabricated devices.

Organization of the manuscript:

Part I is a general introduction to colloidal nanocrystals. It starts with the size and dimension dependence of optoelectronic properties of nanocrystals. Then, it advances to the synthetic approach of colloidal nanocrystals and their development towards different shape and heterostructures. Then, I will switch to the electronic perspective and focus on the transport and doping of the nanocrystal arrays, which are essential for their device integration. I will introduce the techniques to determine the doping and the electronic spectrum of the nanocrystal arrays.

Part II and Part III will be dedicated to nanocrystal-based photodetectors and light emitting diodes, respectively.

Part II will begin with an introduction to the infrared photodetection, after which the results of two heavy-metal-free nanocrystals for infrared detection will be presented. The first material is self-doped **silver selenide (Ag$_2$Se)** nanocrystals with size-tunable mid-infrared absorption thanks to **intraband transition**. The second material is **tin doped indium oxide (ITO)** nanocrystals with widely tunable infrared absorption raised by **plasmonic resonance**, whose energy is defined remotely by the tin dopants in the nanocrystals. For both heavy-metal-free material systems, I start by synthesizing the materials. Then, I probe their electronic properties including the doping and band alignment in the form of a nanocrystal array. Last, I put the nanocrystals into a photoconductive device and evaluate their capacity of infrared detection.

Part III of this thesis will begin with an introduction to the application of nanocrystals as light emitters, with an emphasis on the light emitting diodes. In the following I will first present the core/shell **nanoplatelets (NPLs)** as emitting layer for visible LEDs. The synthesis of NPLs, the design and fabrication of the LED device will be introduced, and the characterization of the LED performance will be presented. Specially, by applying a low temperature strategy at the whole device level, we investigate the origin of efficiency roll-off, which is a common problem faced by all LEDs. Last, we build the first all-nanocrystal-based Li-Fi like communication setup with home-made LED and PbS photodetector. Then I will focus on the use of **HgTe nanocrystal emitter** for LEDs emitting in the short-wave **infrared**. I will introduce the design of the all-nanocrystal LED structure, the synthesis and characterization of the constituting nanocrystal layers, and the fabrication and characterization of the LED devices. Two types of HgTe nanocrystals from different synthetic routes are tested in this device stack. The bright home-made HgTe LED is demonstrated to be capable of active imaging as light source.

Publications and conferences

Pbulications

2021

1. Y. Prado, **J. Qu**, C. Gréboval, C. Dabard, P. Rastogi, A. Chu, A. Khalili, X. Z. Xu, C. Delerue, S. Ithurria, and E. Lhuillier, Seeded Growth of HgTe Nanocrystals for Shape Control and Their Use in Narrow Infrared Electroluminescence, Chem. Mater. 33, 2054 (2021).

2. C. Gréboval, A. Chu, D. V. Magalhaes, J. Ramade, **J. Qu**, P. Rastogi, A. Khalili, S.-S. Chee, H. Aubin, G. Vincent, S. Bals, C. Delerue, and E. Lhuillier, Ferroelectric Gating of Narrow Band-Gap Nanocrystal Arrays with Enhanced Light–Matter Coupling, ACS Photonics 8, 259 (2021).

3. P. Rastogi, A. Chu, T. H. Dang, Y. Prado, C. Gréboval, **J. Qu**, C. Dabard, A. Khalili, E. Dandeu, B. Fix, X. Z. Xu, S. Ithurria, G. Vincent, B. Gallas, and E. Lhuillier, Complex Optical Index of HgTe Nanocrystal Infrared Thin Films and Its Use for Short Wave Infrared Photodiode Design, Advanced Optical Materials 2002066 (2021).

2020

4. **J. Qu**, P. Rastogi, C. Gréboval, C. Livache, M. Dufour, A. Chu, S.-S. Chee, J. Ramade, X. Z. Xu, S. Ithurria, and E. Lhuillier, *Nanoplatelet-Based Light-Emitting Diode and Its Use in All-Nanocrystal LiFi-like Communication*, ACS Appl. Mater. Interfaces 12, 22058 (2020).

5. **J. Qu**, P. Rastogi, C. Gréboval, D. Lagarde, A. Chu, C. Dabard, A. Khalili, H. Cruguel, C. Robert, X. Z. Xu, S. Ithurria, M. G. Silly, S. Ferré, X. Marie, and E. Lhuillier, *Electroluminescence from HgTe Nanocrystals and Its Use for Active Imaging*, Nano Lett. 20, 6185 (2020).

6. C. Gréboval, P. Rastogi, **J. Qu**, A. Chu, J. Ramade, A. Khalili, C. Dabard, T. H. Dang, H. Cruguel, A. Ouerghi, N. Witkowski, M. G. Silly, and E. Lhuillier, *Time-Resolved Photoemission to Unveil Electronic Coupling between Absorbing and Transport Layers in a Quantum Dot-Based Solar Cell*, J. Phys. Chem. C 124, 23400 (2020).

7. N. Moghaddam, C. Gréboval, **J. Qu**, A. Chu, P. Rastogi, C. Livache, A. Khalili, X. Z. Xu, B. Baptiste, S. Klotz, G. Fishman, F. Capitani, S. Ithurria, S. Sauvage, and E. Lhuillier, *The Strong Confinement Regime in HgTe Two-Dimensional Nanoplatelets*, J. Phys. Chem. C 124, 23460 (2020).

8. J. Ramade, **J. Qu**, A. Chu, C. Gréboval, C. Livache, N. Goubet, B. Martinez, G. Vincent, and E. Lhuillier, *Potential of Colloidal Quantum Dot Based Solar Cells for Near-Infrared Active Detection*, ACS Photonics 7, 272 (2020).

9. P. Rastogi, A. Chu, C. Gréboval, **J. Qu**, U. N. Noumbé, S.-S. Chee, M. Goyal, A. Khalili, X. Z. Xu, H. Cruguel, S. Ithurria, B. Gallas, J.-F. Dayen, L. Dudy, M. G. Silly, G. Patriarche, A. Degiron, G. Vincent, and E. Lhuillier, *Pushing Absorption of Perovskite Nanocrystals into the Infrared*, Nano Lett. 20, 3999 (2020).

10. D. Amelot, P. Rastogi, B. Martinez, C. Gréboval, C. Livache, F. A. Bresciani, **J. Qu**, A. Chu, M. Goyal, S.-S. Chee, N. Casaretto, X. Z. Xu, C. Méthivier, H. Cruguel, A. Ouerghi, A.

Nag, M. G. Silly, N. Witkowski, and E. Lhuillier, *Revealing the Band Structure of FAPI Quantum Dot Film and Its Interfaces with Electron and Hole Transport Layer Using Time Resolved Photoemission*, J. Phys. Chem. C 124, 3873 (2020).

11. N. Goubet, M. Thomas, C. Gréboval, A. Chu, **J. Qu**, P. Rastogi, S.-S. Chee, M. Goyal, Y. Zhang, X. Z. Xu, G. Cabailh, S. Ithurria, and E. Lhuillier, *Near- to Long-Wave-Infrared Mercury Chalcogenide Nanocrystals from Liquid Mercury*, J. Phys. Chem. C 124, 8423 (2020).

2019

12. **J. Qu**, C. Livache, B. Martinez, C. Gréboval, A. Chu, E. Meriggio, J. Ramade, H. Cruguel, X. Z. Xu, A. Proust, F. Volatron, G. Cabailh, N. Goubet, and E. Lhuillier, *Transport in ITO Nanocrystals with Short- to Long-Wave Infrared Absorption for Heavy-Metal-Free Infrared Photodetection*, ACS Appl. Nano Mater. 2, 1621 (2019).

13. M. Dufour, **J. Qu**, C. Greboval, C. Méthivier, E. Lhuillier, and S. Ithurria, *Halide Ligands To Release Strain in Cadmium Chalcogenide Nanoplatelets and Achieve High Brightness*, ACS Nano 13, 5326 (2019).

14. C. Livache, B. Martinez, N. Goubet, C. Gréboval, **J. Qu**, A. Chu, S. Royer, S. Ithurria, M. G. Silly, B. Dubertret, and E. Lhuillier, *A Colloidal Quantum Dot Infrared Photodetector and Its Use for Intraband Detection*, Nature Communications 10, 2125 (2019).

15. C. Livache, N. Goubet, C. Gréboval, B. Martinez, J. Ramade, **J. Qu**, A. Triboulin, H. Cruguel, B. Baptiste, S. Klotz, G. Fishman, S. Sauvage, F. Capitani, and E. Lhuillier, *Effect of Pressure on Interband and Intraband Transition of Mercury Chalcogenide Quantum Dots*, J. Phys. Chem. C 123, 13122 (2019).

16. B. Martinez, R. Plamont, C. Gréboval, P. Rastogi, Y. Prado, **J. Qu**, A. Chu, C. Livache, X. Z. Xu, H. Cruguel, S. Ithurria, M. G. Silly, N. Goubet, and E. Lhuillier, *Azobenzenes as Light-Activable Carrier Density Switches in Nanocrystals*, J. Phys. Chem. C 123, 27257 (2019).

17. B. Martinez, J. Ramade, C. Livache, N. Goubet, A. Chu, C. Gréboval, **J. Qu**, W. L. Watkins, L. Becerra, E. Dandeu, J. L. Fave, C. Méthivier, E. Lacaze, and E. Lhuillier, *HgTe Nanocrystal Inks for Extended Short-Wave Infrared Detection*, Advanced Optical Materials 7, 1900348 (2019).

18. C. Gréboval, U. Noumbe, N. Goubet, C. Livache, J. Ramade, **J. Qu**, A. Chu, B. Martinez, Y. Prado, S. Ithurria, A. Ouerghi, H. Aubin, J.-F. Dayen, and E. Lhuillier, *Field-Effect Transistor and Phototransistor of Narrow-Band-Gap Nanocrystal Arrays Using Ionic Glasses*, Nano Lett. 19, 3981 (2019).

19. C. Gréboval, E. Izquierdo, C. Livache, B. Martinez, M. Dufour, N. Goubet, N. Moghaddam, **J. Qu**, A. Chu, J. Ramade, H. Aubin, H. Cruguel, M. Silly, E. Lhuillier, and S. Ithurria, *Impact of Dimensionality and Confinement on the Electronic Properties of Mercury Chalcogenide Nanocrystals*, Nanoscale 11, 3905 (2019).

20. Chu, C. Gréboval, N. Goubet, B. Martinez, C. Livache, **J. Qu**, P. Rastogi, F. A. Bresciani, Y. Prado, S. Suffit, S. Ithurria, G. Vincent, and E. Lhuillier, *Near Unity Absorption in*

Nanocrystal Based Short Wave Infrared Photodetectors Using Guided Mode Resonators, ACS Photonics 6, 2553 (2019).

21. Chu, C. Gréboval, N. Goubet, B. Martinez, C. Livache, **J. Qu**, P. Rastogi, F. A. Bresciani, Y. Prado, S. Suffit, S. Ithurria, G. Vincent, and E. Lhuillier, *Near Unity Absorption in Nanocrystal Based Short Wave Infrared Photodetectors Using Guided Mode Resonators*, ACS Photonics 6, 2553 (2019).

2018

22. **J. Qu**, N. Goubet, C. Livache, B. Martinez, D. Amelot, C. Gréboval, A. Chu, J. Ramade, H. Cruguel, S. Ithurria, M. G. Silly, and E. Lhuillier, *Intraband Mid-Infrared Transitions in Ag2Se Nanocrystals: Potential and Limitations for Hg-Free Low-Cost Photodetection*, The Journal of Physical Chemistry C 122, 18161 (2018).

23. C. Livache, N. Goubet, B. Martinez, A. Jagtap, **J. Qu**, S. Ithurria, M. G. Silly, B. Dubertret, and E. Lhuillier, *Band Edge Dynamics and Multiexciton Generation in Narrow Band Gap HgTe Nanocrystals*, ACS Appl. Mater. Interfaces 10, 11880 (2018).

24. A. Jagtap, N. Goubet, C. Livache, A. Chu, B. Martinez, C. Gréboval, **J. Qu**, E. Dandeu, L. Becerra, N. Witkowski, S. Ithurria, F. Mathevet, M. G. Silly, B. Dubertret, and E. Lhuillier, *Short Wave Infrared Devices Based on HgTe Nanocrystals with Air Stable Performances*, J. Phys. Chem. C 122, 14979 (2018).

25. A. Jagtap, C. Livache, B. Martinez, **J. Qu**, A. Chu, C. Gréboval, N. Goubet, and E. Lhuillier, *Emergence of Intraband Transitions in Colloidal Nanocrystals*, Opt. Mater. Express, 8, 1174 (2018).

Conferences
1. Conference: Nanax 9, 16-20 September, 2019, Hamburg, Germany (Poster)
2. Summer school: Exciting nanostructures, 21-26 July, 2019, Bad Honnef, Germany (Poster)
3. Summer school: Physical and chemical principles in materials science, 09-15 July, 2018, Nanjing University, Nanjing, China (Poster)

Part I Introduction to colloidal nanocrystals

I.1 Colloidal semiconductor nanocrystals

I.1.1 Quantum confinement effect

In a semiconductor, when an electron in the valance band (VB) is excited by a photon with an energy higher than that of the bandgap, the electron can be promoted to the conduction band (CB), leaving a hole in the VB. The formed electron/hole pair, bonded with electrostatic interaction, is called an exciton. The average distance of the electron/hole pair is defined as excitonic Bohr radius, which is given as:

$$a_0 = \frac{4\pi\epsilon_0\epsilon_r\hbar^2}{m_0 m_{eh}^* e^2} \tag{I-1}$$

Where ϵ_0 is the permittivity of the free space, ϵ_r is the dielectric constant of the semiconductor, $\hbar$ is the reduced Plank constant, m_0 is the rest mass of an electron, e is the charge of an electron, and m_{eh}^* is the reduced mass of electron/hole pair, which is calculated as:

$$\frac{1}{m_{eh}^*} = \frac{1}{m_e^*} + \frac{1}{m_h^*} \tag{I-2}$$

With m_e^* and m_h^* the effective mass of electrons and holes, respectively. For example, the Bohr radius is around 6 nm for CdSe, 21 nm for PbS and 40 nm for HgTe.

For strongly confined nanocrystals (quantum dots when they are sphere) whose size is close to or smaller than a_0, a photo-induced exciton can be treated as a particle in a box, where the nanocrystal composition defines the effective mass and shape and size define the dimension of the box, leading to a discrete atom-like energy spectrum. The most common way to describe these discrete states is to use the effective mass approximation.[11] In this model, the wavefunction in the confinement direction of the nanocrystal is approximated as a product of Bloch wavefunction and an envelope wavefunction. The Bloch wavefunction describes the carrier motion in the potential of the crystal lattice, whereas the envelope wavefunction is to describe the motion of carriers in the confinement potential.

By solving the Schrodinger equation of a band in a quantum dot with a radius of R (R≤ a_0), the envelope wavefunction can be obtained, with spherical Bessel function (j_L) as one of the factors. And the energies are given by:

$$E_{n,L} = \frac{\hbar^2 \phi_{n,L}^2}{2m^* R^2} \tag{I-3}$$

With n the principal quantum number, m^* the effective mass of electrons or holes, and $\phi_{n,L}$ the nth root of the spherical Bessel function of the Lth order. Thus, the discrete energy levels can be derived from the parent bulk semiconductor (see the E-k dispersion of the bulk in Figure I.1) but with discrete wavevectors (k) in the momentum space. The allowed value of k is determined by:

$$k = \frac{\phi_{n,L}}{R} \tag{I-4}$$

The quantized energy level of a quantum dot can thus be ordered in energy according to the value of $\phi_{n,L}$, which is π for 1S (n=1, L=0), 4.49 for 1P (n=1, L=1), 5.76 for 1D (n=1, L=2), etc., see Figure I.1 a to the right. The corresponding ground state energy is given as:

$$E_{1,0} = \frac{\hbar^2 \pi^2}{2m^* R^2} \tag{I-5}$$

Which suggests that the first conduction (1S$_e$) and valence(1S$_h$) band states shifts to larger values with decreasing QD size, giving rise to the size-dependent banggap of nanocrystals:

$$E_g = E_{g,bulk} + \frac{\hbar^2 \pi^2}{2m_e^* R^2} + \frac{\hbar^2 \pi^2}{2m_h^* R^2} - \frac{1.8\,e^2}{\varepsilon_\infty R} \tag{I-6}$$

Where ε_∞ is the high frequency dielectric constant of the semiconductor. If we define the bandgap widening resulting quantum confinement as confinement energy E_C:

$$E_C = \frac{\hbar^2 \pi^2}{2m_e^* R^2} + \frac{\hbar^2 \pi^2}{2m_h^* R^2} = \frac{\hbar^2 \pi^2}{2m_{eh}^* R^2} \tag{I-7}$$

Then the bandgap can be interpreted as the parent bulk bandgap increased by the confinement energy (Ec) and decreased by coulombic interaction of the electrons and holes.
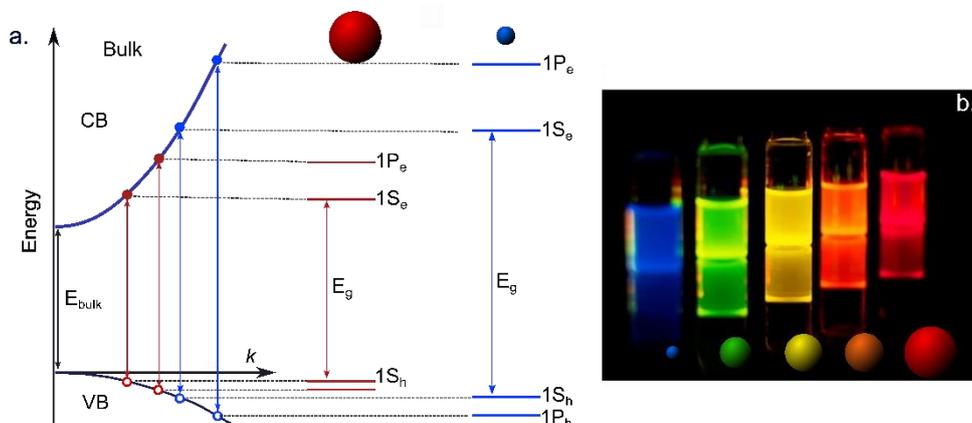
Figure I.1 (a) E-k dispersion relation of a bulk semiconductor (solid parabolic curves to the left) and energy levels of a spherical quantum dot of the same materials but of different sizes. (b) A picture of CdSe quantum dots in solution, with a size ranging from 6 nm to 2 nm, providing photoluminescence from red to blue due to quantum confinement.[12]

Figure I.1 b shows a picture of CdSe quantum dots with a size from 2 nm to 6 nm, presenting photoluminescence from blue to red, covering the whole visible range. The size-tunable emissive properties have been the most targeted function for QDs, especially for displays in the visible.

From the band gap of nanocrystals given in equation (I-7), the size-tunability of a material is determined by the effective mass of electrons and holes, or the curvature of the E-k dispersion curve. The longest wavelength (the smallest bandgap) of QD is limited by the bandgap of the bulk material, whereas the shortest wavelength (the largest band gap) is limited by the smallest size of QD we can obtain. To achieve optical features of longer wavelength such as infrared range, materials with a small bulk bandgap are required. PbS with a bulk bandgap of 0.4 eV (≈ 3 μm) has been widely explored in QD form for infrared photodetection and for harvesting the infrared part of solar spectrum, exploiting their tunable bandgap. Another category of material that naturally works for infrared applications is mercury chalcogenides (HgX), especially HgTe and HgSe, whose bulk bandgap is zero due to their semimetal nature. The bandgap of the quantum dots derives from HgTe and HgSe is solely controlled by the quantum confinement, which in theory can provide band gaps as small as possible.

Dimensionality and quantum confinement

In addition to the size, the shapes and the dimensionality of nanocrystals can also strongly influence the electronic spectrum of charge carriers as well as the optical properties of the nanocrystals. As can be seen from Figure I.2, unlike bulk semiconductors, where the density of the states (DOS) increases continuously with energy due to continuous bands, the 2D quantum well (QW) confines the motions of electrons in the thickness direction, whereas the in-plane motion of the carriers is still continuous, resulting in a staggered density of states. Quantum engineering in nanoscale was firstly realized in the epitaxially grown 2D quantum well system with electronic properties tailored to user's specifications. Soon after, the 1D quantum wire and 0 D quantum dot was also obtained by epitaxial techniques. They confines the motion of carriers in more dimensions, bringing in further interesting optoelectronic features.

Dimension	Bulk (3D)	Well (2D)	Wire (1D)	Dot (0D)
Shape				
Density of states	ρ_{DOS} $\propto E^{1/2}$	ρ_{DOS} $\propto E^0 = cst$	ρ_{DOS} $\propto E^{-1/2}$	ρ_{DOS} $\delta(E)$
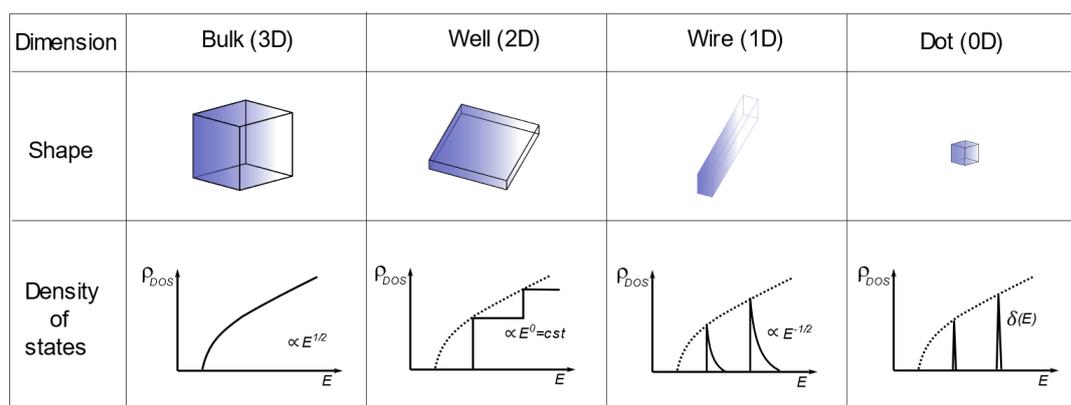
Figure I.2 The density of states of semiconductor form 3 D to 0 D dimensions. The energy density of states strongly dependent on the number of confined directions: the density of electron and hole states changes from monotonically increasing with energy in a 3 D bulk material, to the step-like quasicontinuum in 2 D quantum well, a saw-like quasicontinuum in quasi-one-dimensional nanorods and to discrete levels for zero-dimensional quantum dots.

I.1.2   Hot injection synthesis of colloidal nanocrystals

Chemically synthesized colloidal nanocrystals have become an exciting class of materials with precise control over a wide range of size, shape, and composition. The solution-processability of colloidal nanocrystals generates tremendous technological opportunities as they can be deposited with simple methods such as spin-coating, spray-coating and dip-coating, or patterning techniques including inkjet printing and nanoimprint lithography. As a result, nanocrystals are ideal building blocks for future low-cost electronics,[13] optoelectronics,[14] and photonics.[15]

Synthesis of colloidal nanocrystals with controlled size distribution is the first step for the utilization of their size dependent properties. The milestone for the synthesis of high quality colloidal nanocrystals was achieved in the early 1990s by the group of Brus[16] and Bawendi[2]. Using a "hot injection" method, they introduced organometallic precursors into high boiling point coordinating solvents. It was the first time when II-VI CdE (E = S, Se or Te) QDs were obtained with nearly monodisperse size and shape, and resultant sharp optical (absorption and emission) features at room temperature. This finding has set the basis for the rational synthetic schemes of colloidal nanocrystals over the past four decades.

 In a typical hot injection synthesis, there are mainly three steps, see Figure I.3:

(1) **Degassing.** The cation (or anion) precursor, ligands, and high boiling point coordinating solvent are mixed in a three-neck flask connected to Schlenk line. The mixture is kept under vacuum at an elevated temperature to remove the oxygen, water, and impurities.

(2) **Hot injection.** After degassing, the atmosphere is switched to an inert gas (Ar or N_2) to further increase the temperature. When the temperature is stabilized at the reaction temperature, the anion (or cation) precursor is rapidly injected into the reaction bath. The nucleation is initiated upon rapid injection due to the saturation, and soon terminated due to the temperature drop after the addition of room temperature precursor. The temporal separation between nucleation and growth is thus achieved and ensures the monodisperse size and shape of the nanocrystals.

According to the target material system and size, as well as the reactivity of the precursor, the reaction temperature varies. For example, the synthesis of cadmium chalcogenides requires relatively high reaction temperature of around 250 °C, whereas for the synthesis of mercury chalcogenides, the temperature is usually below 100 °C. The size of the nanocrystal can also be tuned by the duration of reaction.

It is also worth noting that, in general, the cation precursor is injected prior to the anion precursor, whereas in some cases the sequence is reversed. For instance, during the synthesis of silver chalcogenides, the silver precursor is injected into a flask containing chalcogenides precursor. Because, in the absence of any chalcogenide, silver nanocrystals will be formed.[17]

(3) **Quenching of the reaction.** To stop the growth of the nanocrystals, excessive of ligands are generally injected into the system to avoid the precursors from accessing to the nanocrystals, and the flask is cooled by air flux or by a water or ice bath.
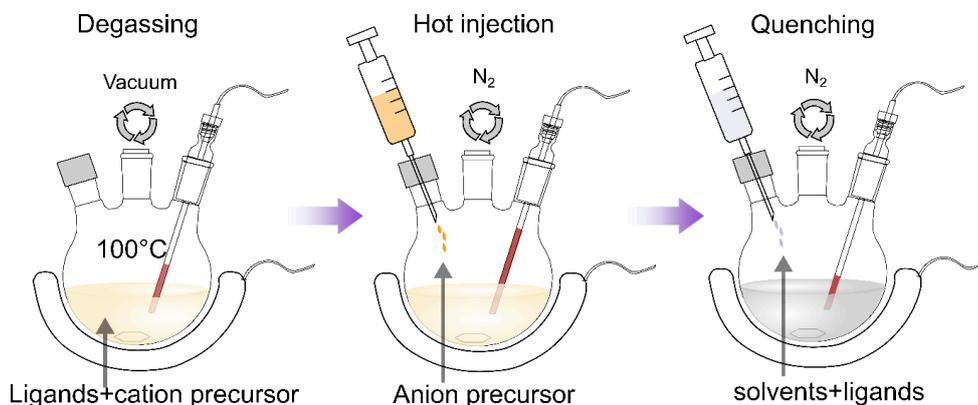
Figure I.3 Typical hot injection synthesis of colloidal nanocrystals including degassing of solvents and precursors, hot injection in an inert atmosphere and the quenching of reaction.

Purification of nanocrystals

To extract the nanocrystals from the reaction products, a purification process is conducted. Typically, a polar solvent such as ethanol, methanol, or acetone, is added to the reaction mixture. The change of the polarity of the solvent leads to the flocculation of the nanocrystals, leaving the excess ligands and unreacted precursors in the solvent, enabling the precipitation of nanocrystals by centrifugation. The precipitated nanocrystals are then dispersed in non-polar solvents such as hexane, toluene, or chloroform. The purification is conducted at least twice before storing the clean nanocrystals in a nonpolar solvent.
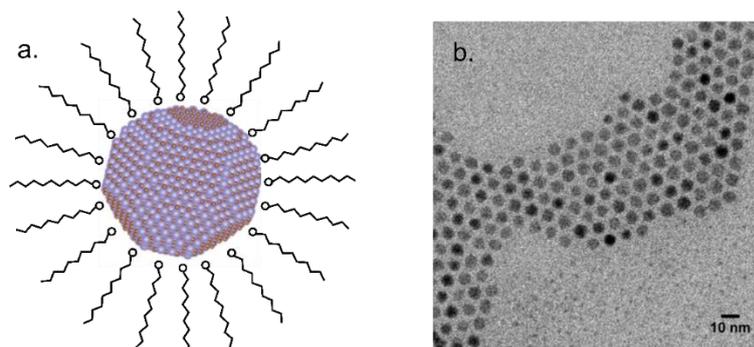
Figure I.4 (a) Illustration of a single CQD comprising an inorganic semiconductor core capped by an organic ligand made of long hydrocarbon molecule with a functional end anorchid to the surface of the core. (b) TEM image of CdSe/CdS quantum dots with high monodispersity.

I.1.3   Ligands of nanocrystals

A typical CQD consists of an inorganic nanocrystal core capped by long-alkyl-chain ligands, see Figure I.4 a. Figure I.4 b shows a TEM image of CdSe/CdS CQDs with a diameter of around 9 nm, revealing a high degree of monodispersity, which is mandatory to resolve the discrete energy levels of a CQD assembly and resultant optical properties.

Although the nanocrystalline core drives the target optoelectronic properties of the CQDs, their surface ligands are paid substantial attention owing to the large surface /volume ratio of nanomaterials. The commonly used ligands for colloidal nanocrystals are hydrocarbon molecules with anchoring end groups. The chain of the molecules is usually long with 12 to 18 carbons, and the end functional groups are usually thiols, amines, carboxylic acid, and phosphines. There are multiple roles played by the ligands throughout the synthesis, processing, and application:

(1) The nonpolar nature of the long alkane ligands ensures the colloidal stability of the nanocrystals in a nonpolar solvent, which is critical for solution-processable fabrication.

(2) During the growth, the ligands rapidly adsorb and desorb from the surface of the growing nanocrystals, which regulate the addition and the removal of the atoms to the crystalline surface, slowing down the growth rate and in turn circumventing the aggregation and enabling fine control over the growth.[3]

Furthermore, some capping ligands can selectively bond to certain facets of the nanocrystals and in turn terminate the growth of the facet[18]. It is widely used for the synthesis of anisotropic shapes such as nanorods[3] and nanoplatelets[4].

(3) The capping ligand can passivate the electronic trap states induced by the dangling bonds on the QD surface, preserving the photoluminescence and exciton lifetime.

(4) The length of the ligands determines the interparticle spacing in a nanocrystal solid. The native long-chain ligand massively hindering their electrical coupling. Ligand exchange toward shorter species is needed for application-targeted high-mobility NC films.

I.1.4   Heterostructure of nanocrystals

Along with the study of the single-component nanocrystals, the synthesis of heterostructure nanocrystals, achieved by epitaxially growing an inorganic shell onto the core nanocrystal, has been developed.[5,19] This is first motivated by the potential that the heterostructures, beyond single-component counterparts, can bring novel electrical and optical properties and carrier

behaviors. From the application point of view, the inorganic shell can better passivate the unsaturated bonds of the core nanocrystal surface than the ligands, enhancing the photoluminescence; it can also work as a physical barrier, making the optical-active core less sensitive to the environmental changes and surface chemistry. This robustness brought by shelling is critical for their integration to a device, where the materials will be inevitably exposed to harsh conditions such as strong electric field, significant heat, strong photo-irradiation and the solvents.[20] All the above conditions can be challenging for single-component nanocrystals to maintain their optical properties, especially emission properties.

The carrier localization and the optoelectronic properties depend heavily on the relative position of the conduction and valence band of the core/shell nanocrystal components. Thus the core/shell nanocrystals can be categorized into type I and type II band configurations according to their band offset.[11]

As in a typical type I CdSe/ZnS QD, the band edge of the CdSe core is fully included in that of the ZnS shell, confining the electrons and holes in the core (Figure I.5 a), thus facilitating the radiative recombination of the excitons. Indeed, after Hines and Guyot-Sionnest published reports of ZnS-capped CdSe QDs showing luminescence up to 50% PLQY,[5] considerable efforts were devoted to optimizing QD structures to achieve intense and narrow emissions [21-23], which has paved the way for the synthesis of nanocrystals with near-unity efficiency and size-tunable emission for display. It is worth noting that the lattice mismatch of the heterostructure materials should be treated carefully to avoid the interfacial defects. The common solution to release the strain and to maintain high PLQY of the heterostructure is to alloy the shell or to build a chemical gradient of core/shell materials.[24]

In a typical type II band alignment (Figure I.5 c), the offset of conduction bands and valence bands are of the same sign. CdTe/CdSe core/shell nanocrystals,[25] for example, its electrons are localized in the shell materials with a lower conduction band while the hole wave function is restrained in the CdTe core. This spatial separation of electron and hole wave function reduces the recombination rates of the excitons, thereby prolonging the PL decay time. This type II heterostructure also allows access to optical transition energies that are not restricted to band-gap energies and can emit at lower energies than the band gaps of comprising materials.[25]

In between the carrier-localized type I and carrier-separated type II, there is a situation defined as quasi type II, where one carrier is confined in one material whereas the other can move across the entire heterostructure. This requires the conduction band or the valence band of the constituent materials close in energy. The most popular manifestation of quasi type II band alignment is CdSe/CdS nanocrystals,[26] in which the holes are localized in the CdSe core and the electrons delocalizing in the two materials. This band alignment can provide high photoluminescence quantum yield as type I heterostructure for light emission. One of the interesting characterizations of this materials is that the emission red shifts with the increase of shell thickness, demonstrating the delocalization of the electrons.

Regarding the different carrier localization and the consequent interesting optical properties brought by different band alignment of the heterostructures, it is critical to engineer the core/shell materials for the design of optoelectronic devices. For example, the type I core/shell heterostructure is beneficial for high PLQY and stability required by light emission applications, whereas the type II structure can facilitate the charge carrier separation, which is preferable for photovoltaic devices and photodiodes.
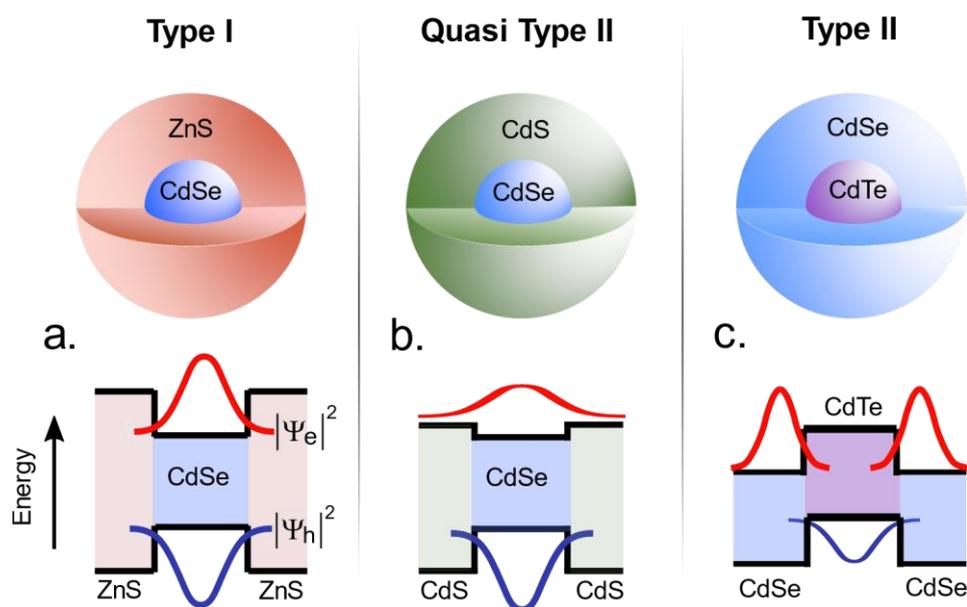
Figure I.5 Schematic diagram of CdSe/ZnS (a), CdSe/CdS (b), and CdTe/CdSe (c) nanocrystals with type I, quasi type II, and type II band alignment, respectively. The localization of excited carriers wavefunctions are indicated.

I.1.5   Shape control of Nanocrystals

Ever since the establishment of hot injection synthesis of near-spherical CQDs, the synthesis of anisotropic nanocrystals with various shapes and dimensionality has been followed. In 2000, Peng et al. reported the first anisotropic "quantum rods" and demonstrated their directional emission.[3] It was until 2008 that the zinc blende CdSe nanoplatelets (NPLs), with one dimension much smaller than the other two, was discovered, which presents extremely narrow thickness-dependent emission.[27]

In this part, I will focus on colloidal nanoplates, also called colloidal quantum well (CQW), as they have the electronic properties of the 2D quantum well grown by molecular beam epitaxy. Colloidal NPLs with their unique growth mechanism, allows a large lateral extension, while the confinement direction is flat with atomic precision, see the scheme of a CdSe NPL with 3 monolayers of Se atoms and 4 monolayers of Cd covering the surface in Figure I.6 a, and a TEM of CdSe NPL in Figure I.6 b. As a result, the excitons in the NPLs can move freely in the 2D plane but are strongly confined in the thickness direction (1-2 nm). For sphere QDs, their size is more or less continuous, which inevitably induces inhomogeneous broadening of the optical features, whereas the atomically flat NPL presents extremely narrow linewidth of absorption and emission (below 10 nm) due to high monodispersity. It has been reported that the linewidth of NPLs in the solution is the same as that of the single NPL, demonstrating that there is no inhomogeneous broadening of the NPL batch.[28]

So far, among all known nanomaterials, NPLs provide the highest color purity owing to the thickness control down to the atomic level, making them the most promising nanocrystal for high-quality light emitting applications. Moreover, the 2D structure with an in-plane 2D optical dipole can result in polarized emission, which can be harnessed to improve the extraction efficiency in a planar LED device .[29,30]

Although the single content nanoplatelets has already been interesting for light emission device, there are several drawbacks: (1) NPLs with only integral monolayers of atoms can be obtained, limiting their size-tunability in the confinement direction and consequently their emission wavelengths. (2) Like all the single component colloidal nanocrystals, the dangling bonds on the surface of NPLs generate trap states and damages their PLQY. Also, they are sensitive to the change in the environment medium and photo-oxidation and show poor optoelectronic stability, hindering their integration to operational devices.

To overcome the above-mentioned limitation, the core/shell heterostructures of NPLs have also been developed.[31] Figure I.6 c and d respectively show the cartoon and the TEM image of a core/shell CdSe/CdS NPLs. It can be clearly observed that both CdSe core and ZnS shell can be grown with atom-resolved thickness, and there is a flat interface between the core and the shell, as indicated by the image contrast due to their different atomic density. In the early stage, the core/shell structure is obtained via colloidal atomic layer deposition (c-ALD) [32]. In a typical c-ALD process, the cationic and anionic precursors are successively added into the reaction system. Each reaction step is self-limited by the surface binding sites, which allows the removal of excess precursors after each reaction, preventing their reaction with the following regent. In this manner, CdS shell with a thickness of up to 7 monolayers is grown on the CdSe NPLs core, emitting at 665 nm with a narrow linewidth of 20 nm.

The c-ALD approach, conducted at room temperature, can only provide core/shell NPLs with moderate PLQY (typically below 50%) and stability. The exploration of high-PLQY core/shell NPLs for high-performance light emitting devices has been continued and a breakthrough was reported in 2016[33] by adopting hot injection to the shell growth. CdSe/ZnS NPLs with reproducible near-unity PLQY were reported by Demir's group in 2019.[34] Soon after, the same group demonstrated a NPL-based LED with the record-high external quantum efficiency of 19.2% [35], close to what has been achieved by the QDs, although the stability of the LED device needs to be further improved.
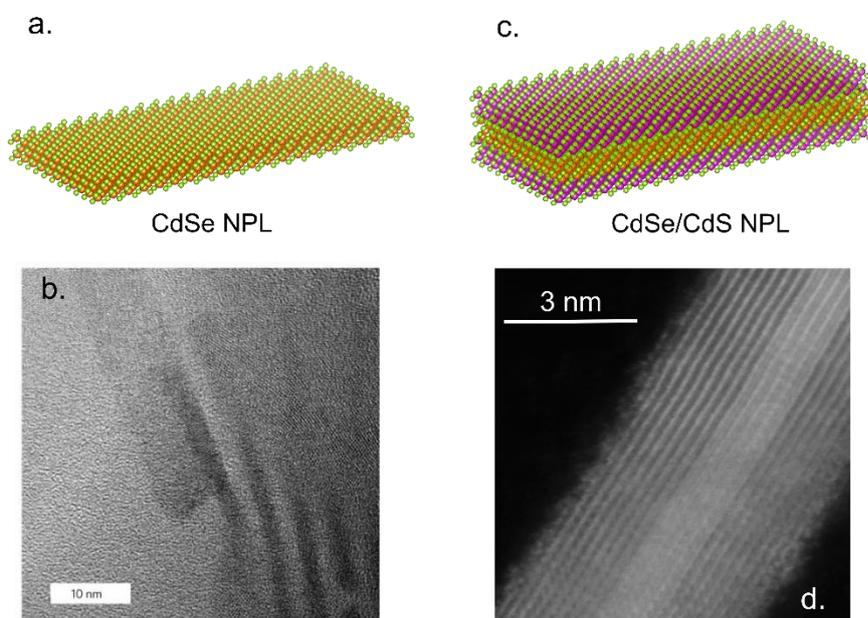

Figure I.6 Scheme of a core-only CdSe NPL (a) and a corresponding TEM (b), adapted from the reference[4]. Scheme of a CdSe/CdS core/shell NPL (c) and a corresponding TEM image of CdSe/CdS core/shell NPL demonstrating atomic resolution (d), TEM adapted from the reference. [36]

I.2 The transport and doping of colloidal nanocrystal arrays

In the preceding part, I have been focusing on the synthesis, composition, heterostructures and shape control of colloidal nanocrystals. In this part, I will emphasize the electronic properties of colloidal nanocrystals, including transport properties, doping and their energy levels in the absolute energy scale, which are critical for the design of a complex device and for the understanding of their performance.

I.2.1 The hopping transport in nanocrystal solids and ligand exchange

The emergence of high-mobility nanocrystal solids[37] up to 400 $cm^2\,V^{-1}\,s^{-1}$ has open up interesting opportunities for high-performance electronic and optoelectronic devices, such as field effect transistors (FET)[38–40], photodetectors[41–43], solar cells[44], and light emitting diodes (LEDs)[45,46].

At room temperature and under an electric field, the transport of a charge carrier in a nanocrystal solid occurred through hopping from one nanocrystal to its nearest neighbor, as shown in Figure I.7 a. The mobility of the carriers in a nanocrystal array is determined by the electronic coupling strength between nanocrystals, and more directly speaking, by the hopping rate. During a hopping event, the carrier needs to overcome the tunnel barrier. As illustrated in Figure I.7 b and Figure I.7 c, the height of the tunnel barrier is controlled by the nature of the barrier material (typical value for organic ligands is probed to be 2 eV),[40] while the tunnel width (d) is the inter-dot spacing (i.e., the length of ligands). In a nanocrystal solid with native ligands , the tunnel width is around 1.5 nm the typical length of alkyl chains (Figure I.7 b), which makes the nanocrystal film insulating with mobility of around 10^{-8} $cm^2\,V^{-1}\,s^{-1}$. [40]

To boost the conductance of the nanocrystal arrays while preserving the quantum confinement, ligand exchange of native long ligands toward shorter organic molecules or small inorganic ions[47] by either solid-state method[40] or solution phase transfer[47] has been well established. It is reported that, in the absence of other changes, the mobility is supposed to increase exponentially with decreasing ligand length.[40] To change the original long ligands with their short counterparts, the most common strategy is solid-state ligand exchange. For example, by immersing a nanocrystal films capped with long ligands into a solution of ethanethiol (EDT) in ethanol. The EDT of higher concentration will occupy the surface and replace the origin ligands. After ligand exchange towards EDT, the tunneling barrier width can be decreased to 0.3 nm (Figure I.7 c), and the mobility of the carriers improved by about 6 orders of magnitudes.[40] The loss of ligand volume during this solid-state ligand exchange leads to voids in the thin film, which can be filled by multilayer deposition and exchange. It is worth noting that, for the target of light emission, the ligand species as well as the solvents for ligand exchange need to be carefully chosen to preserve the PL efficiency while enhancing the mobility.

The replacement of original ligands with compact inorganic ions such as S^{2-} ions[48] and halides[44], can simultaneously reduce the tunnel barrier and height, leading to the stronger electronic coupling of the nanocrystals. Interestingly, small ions such as OH^- and Cl^-, helps to match the density of ligands to the number of surface atoms, in turn benefits the electronic passivation of surface dangling bonds[49]. For the ligand exchange toward small molecules or ions, phase-transfer ligand exchange is usually adopted. Typically, a polar solvent with the small ligands is mixed with the original nanocrystal solution. After sonication or vigorous agitation, the small molecular ligands are attached to the nanocrystal surface and bring the nanocrystal in the polar phase, whereas the original long-chain ligands are stripped from the nanocrystal and remain in the original nonpolar phase. In this phase-transfer manner, we can obtain an "ink" of nanocrystals with short ligands, which enables the deposition of thick films with good quality in one step, instead of the conventional layer-by-layer solid-state ligand exchange.
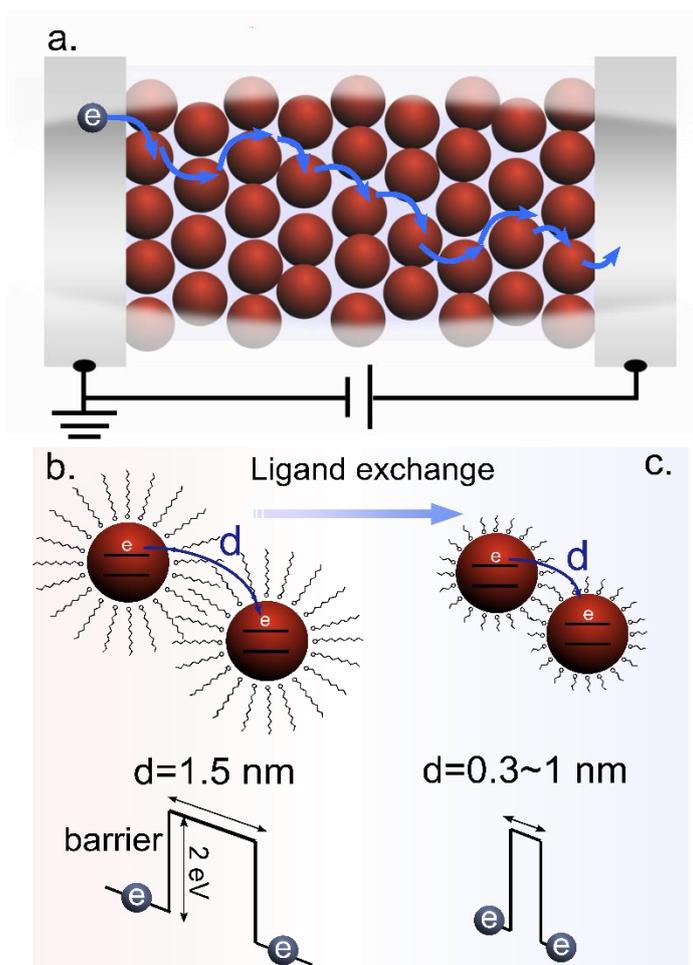
Figure I.7 (a) Illustration of hopping of an electron in a nanocrystals solid form one electrode to the other. (b) Cartoons of the electron hopping in a nanocrystal array with native long ligands. In this case, the hopping of an electron from one nanocrystal to another needs to overcome both a high tunneling barrier and a wide tunneling width defined by the inter-dot spacing. (c) Cartoons of an electron hopping occurred in a nanocrystal array after ligand exchange, in which the shorter ligands reduce inter-dot spacing and in turn the barrier width.

Along with the development of nanocrystal based optoelectronic devices, more complex ligand exchange strategies have been adopted. For example, the use of hybrid organic-inorganic (ammonium acetate-metal halide) inks of PbS nanocrystals has provided a nanocrystal solid with both high carrier mobility and good surface passivation, leading to high power efficiency of PbS nanocrystals-based solar cells[50]. In a recent report, a HgSe film with a hybrid ligand of amine/halogen and thiols using solution phase transfer demonstrates mobility of 1 cm² V⁻¹ s⁻¹, two orders of magnitude higher than that of the film obtained with traditional solid-state ligand exchange using EDT solution.[51]

I.2.2 Field effect transistor

For the design of semiconductor optoelectronic devices, the insight of the electronic properties of the materials including doping, carrier mobility and energy levels are required. Since the Hall effect, which is commonly used in solid state physics, is not easy to conduct in a nanocrystal solid due to its low carrier mobility,[52] field effect transistor (FET) has become the most straightforward way to identify their majority carrier and carrier mobility. Although FET itself

has been one of the target applications for the next generation of low-cost nanocrystals-based electronics, here the goal of the FET configuration is not application-oriented but rather probing the transport characteristics of the nanocrystal solids and providing insights on the nature of majority carrier, and the mobility of the carriers in a nanocrystal solid.

The most common FET configuration is shown in Figure I.8 a. In this structure, a pre-patterned metal electrode is used as drain and source, a heavily doped Si is used as the bottom gate, which is insulated from the FET channel with a thin layer of SiO_2 (typically 300 nm). The channel is made of a ligand-exchanged nanocrystal film. The gating effect is illustrated in Figure I.8 b: under a certain drain-source bias, when we apply a positive gate bias (V_{GS}>0), the positive charges will accumulate at the side of SiO_2 near the nanocrystal channel, while the negative charges accumulate near the gate. To screen the positive charges near the nanocrystal film, there are electrons injected into the channel. With the same principle, if we apply a negative bias (V_{GS}<0), holes will be injected into the nanocrystal channel.

If the majority carriers of the nanocrystal array are electrons (i.e., the nanocrystal is n-doped), the increase of gate bias in the positive range (the injection of electrons) will open the channel for the current to flow. In contrast, if the nanocrystal film has holes as its majority carriers (i.e., p-doped), the conductivity of the channel will be enhanced with more negative gate bias (the injection of holes). Under the third circumstance, the conductivity of electron and hole of the same nanocrystal film can be enhanced by the injection of electrons and holes. This kind of transport is defined as ambipolar transport.

The ability of a FET system to tune the channel carriers is determined by the capacity of the gate insulator. In this conventional dielectric back gate configuration (Figure I.8a), the capacitance (C) of the dielectric can be calculated from the formula below,

$$C = \frac{\varepsilon_0 \varepsilon_r S}{d} \qquad \text{(I-8)}$$

where ε_0 is the permittivity of free space, ε_r is the dielectric constant of the gate insulator, S is the surface area of the channel and d is the thickness of the dielectric layer.

The formula clearly indicates that a high capacitance can be obtained by using high dielectric materials and (or) decreasing the thickness of the dielectric layer. The capacitance of SiO_2 with a thickness of 300 nm is around 10 nF/cm², leading to a weak modulation of the charge density in the channel material. Further decreasing the thickness of SiO_2 is not a practical way to increase the capacitance, as the thin dielectric layer is prone to breakdown, especially in the dielectric FET system where high bias (several tens of volt) is required to induce gate effect.

Despite the the low capacity for the charge barrier injection, this FET configuration is (1) very easy to obtain, (2) compatible with fast sweep of gate bias and (3) allows for the measurement across a wide temperature range from 4 K to 300 K. A possible way to increase the capacitance can be changing the low dielectric constant SiO_2 (ε_r=3.9) to high dielectric materials (high-k dielectrics), such as Al_2O_3 (ε_r=7.5) and HfO_2 (ε_r=25).[53]

Another FET configuration routinely used in our team is an electrolyte top-gated FET. As schemed in Figure I.8 c, the same pre-patterned metal electrode is used, and the nanocrystal channel is made in the same manner as the dielectric FET configuration (Figure I.8 c). Here an electrolyte on the top of the nanocrystal channel is used for gating. The electrolyte is obtained by dissolving $LiClO_4$ in a polymer matrix of PEG. Again, when we apply a positive gate bias (V_{GS}>0), the ClO_4^- anions accumulate near the gate, whereas the mobile Li^+ will migrate across the PEG matrix and diffuse deep into the nanocrystal film.
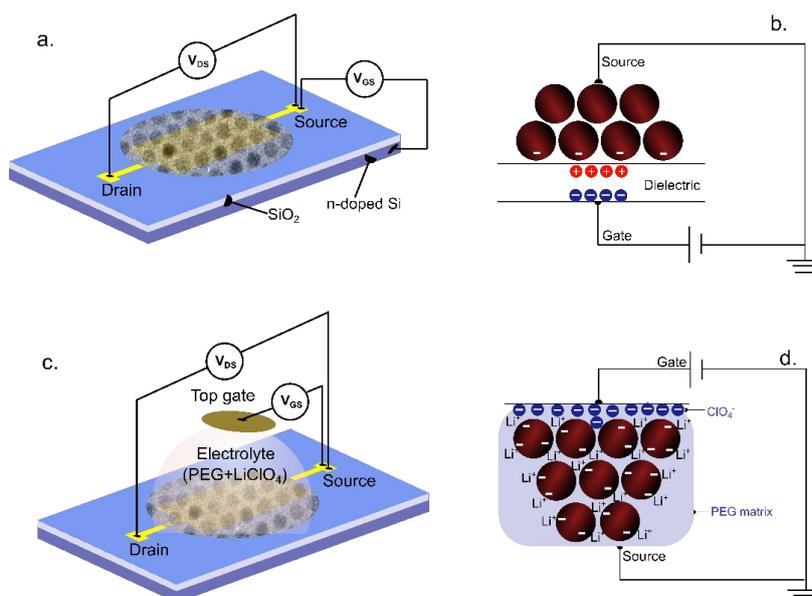
Figure I.8 (a) Scheme of a conventional back gate FET with SiO_2 as dielectric and a heavily doped Si as gate electrode. (b) The gate effect induced in a nanocrystal film when V_{GS} above 0 V. (c) Scheme of an electrolyte top gate FET. (d) Gate effect induced in an electrolyte gated FET when V_{GS} above 0 V.

This electrolyte gate can powerfully tune the carrier density of the channel under low gate bias. This is owing to its capacitance in the range of $\mu F/cm^2$, two orders of magnitude higher than that of the SiO_2. This high capacitance makes it easier to gate higly doped nanocrystals. In addition, the ions from electrolytes can percolate deep into the nanocrystal films, enabling the gate of thick films.

However, there are several drawbacks of this FET configuration: (1) It only operates near room temperature (300 K) and fails to work below 280 K[54] due to the freezing of the ions. (2) Because the injection of carriers involves the diffusion of Li^+ ions in the matrix, a very slow sweep rate is required. (3) the electrochemical stability of the electrolyte limits the gate bias below 3 V. (4) It is difficult to evaluate the mobility from the transfer curve, since the precise capacitance is hard to obtain.

Nevertheless, the electrolyte is very useful to probe the nature of majority carriers, especially for heavily doped nanocrystals.

I.2.3   X-ray photoemission to build energy diagrams of nanocrystal arrays

Although FET is a useful tool to understand the doping and the mobility of the nanocrystal films, it cannot locate the absolute energy levels, such as the Fermi level, the conduction and the valence band. Knowing the relative energy levels is the prerequisite to determine contact nature (Ohmic or Schottky) of the electrode/nanocrystal and nanocrystal/nanocrystal interface, the band bending and in turn the injection of the carriers inside the device. More and more evidence has shown that the energy diagram of a nanocrystal is not only determined by the size but also hugely modified by the surface chemistry.[55,56] This makes it critical to master the information of the energy diagram of all the constituting materials of a photovoltaic device[57] or light emitting diodes[11], to guide the design and the understanding of the device operation.

X-ray photoemission spectroscopy (XPS) is a powerful tool to probe the energy levels, determine the doping type, and reconstruct the energy spectrum of a nanocrystal film. Figure I.9 shows

the scheme of a XPS setup. Various light sources such as X-ray sources (Kα of Mg or Al), synchrotron sources and UV light (for UPS) can be used to excite the electrons from different energy levels by the photoelectric effect. Upon the X-ray incidence, the photo-generated electrons can get rid of the binding energy (BE) and escape from the sample with a kinetic energy (KE). An analyzer is used to sort the electrons according to their energy, while a detector is used to count the number of electrons of each kinetic energy. The kinetic energy of a photoelectron can be related to the binding energy according to energy conservation law: BE=hν-KE, with hν the energy of the incident photon.

For the reconstruction of the energy level spectrum of nanocrystals, XPS can provide the information of the Fermi level (E_f) and relative energy of E_f and the valence band. The lowest KE of the XPS spectrum is from the electrons with just enough kinetic energy to escape from fermi level to the vacuum, that is to say, their kinetic energy is supposed to be 0 at the vacuum level. Since E_f of the detector is the same as that of the sample, the lowest kinetic energy detected is the work function value (W_F) of the materials.

The lowest BE edge cutoff of XPS spectrum corresponds to the energy difference between the valence band maximum (VBM) and the Fermi level, as depicted in Figure I.9 b. Hence, we can further identify the position of the VBM using the W_F value obtained from low kinetic energy cutoff. The conduction band can thus be determined by adding the bandgap (E_g) of the materials to the VBM. The bandgap of the materials is approximate by the optical spectrum.
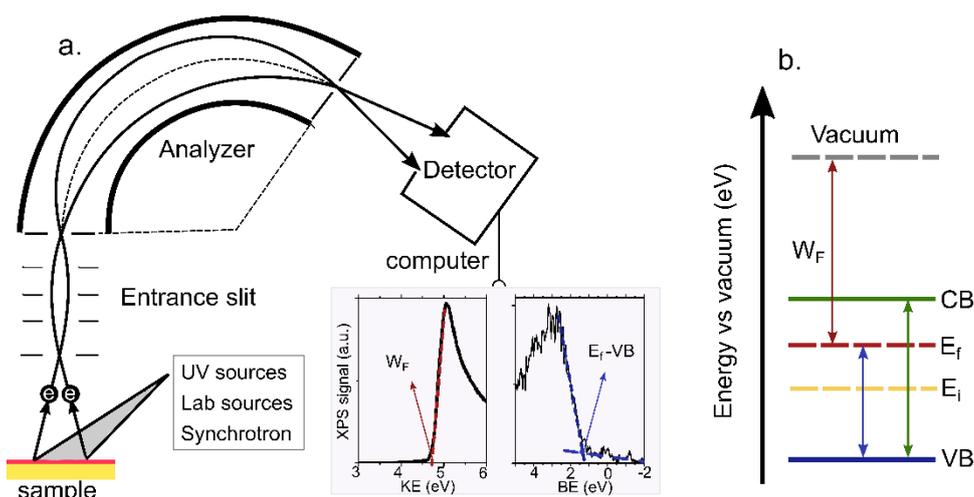
Figure I.9 (a) A typical x-ray photoemission spectroscopy setup. The incident X-ray or ultraviolet light source can promote the electrons in the sample and the kinetic energy of the photoelectrons can be detected.

Following the method above, we can determine the energetic levels of the materials, as illustrated in Figure I.9 b. The doping of the nanocrystal film can be clearly identified by the position of the Fermi level with respect to the middle of the bandgap (E_i): when E_f is above the E_i, the materials is n-doped, when the E_f is below the E_i, the material is p-doped and when E_f is overlap with E_i, it is intrinsic. Furthermore, when the E_f located above the conduction band (1Se), the material is regarded as degenerately n doped.

During my PhD, I combine the FET and XPS techniques to understand the doping and electronic structures of the nanocrystal films that I will integrate into photodetection or light emitting device.

Part II Heavy-metal-free nanocrystals for mid-infrared photodetection

Related publiactions:

1. **J. Qu**, N. Goubet, C. Livache, B. Martinez, D. Amelot, C. Gréboval, A. Chu, J. Ramade, H. Cruguel, S. Ithurria, M. G. Silly, and E. Lhuillier, *Intraband Mid-Infrared Transitions in Ag2Se Nanocrystals: Potential and Limitations for Hg-Free Low-Cost Photodetection*, The Journal of Physical Chemistry C 122, 18161 (2018).

2. **J. Qu**, C. Livache, B. Martinez, C. Gréboval, A. Chu, E. Meriggio, J. Ramade, H. Cruguel, X. Z. Xu, A. Proust, F. Volatron, G. Cabailh, N. Goubet, and E. Lhuillier, *Transport in ITO Nanocrystals with Short- to Long-Wave Infrared Absorption for Heavy-Metal-Free Infrared Photodetection,* ACS Appl. Nano Mater. 2, 1621 (2019).

II.1   Introduction to nanocrystal-based infrared photodetection

In the visible range, the photodetection is dominated by Si-based electronics, which well combines high performance with low cost. While infrared photodetector with high performance still relies on expensive techniques such as molecular beam epitaxy (MBE) grown quantum wells, type II superlattice and alloying of single crystals, which limits the infrared photodetection to the domain of defense, astronomy, and scientific research.

However, the emerging civilian applications, such as thermal imaging, night driving assistance and industrial inspections, require infrared photodetectors with reasonably fast response and an affordable price. Bolometer, as a type of cheap infrared thermal detector sensitive to the incident energy flux, is however inherently slower than quantum photodetectors that react to the photon flux. Organic electronics, the low-cost alternative to Si-based optoelectronics, is not functioning in the infrared. In this context, the colloidal nanocrystals have been the most promising candidate to bring down the cost of high-performance quantum photodetectors.

II.1.1   Infrared photodetection

There are various ways to categorize the infrared wavelengths, and one of the most used division in the photodetection community is based on the atmospheric transmission windows. Beyond silicon-achievable wavelengths (≈ 1 µm), there are mainly three regions that are transparent to the atmosphere, see Figure II.1 a, which are especially interesting for long-range infrared photodetection.
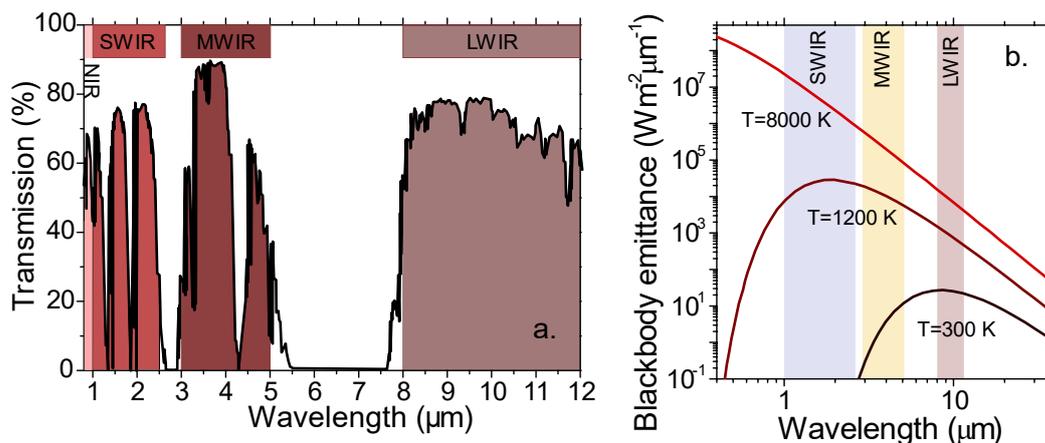
Figure II.1 (a) Spectral dependence of atmospheric transmission and (b) Spectral emittance for a blackbody at various temperatures.

The wavelength from 1 µm to 2.5 µm is classified as short-wave infrared (SWIR). Imaging in this range is usually through active imaging, where a SWIR photodetector collected the infrared photons reflected from the surface of an object/scene. Active imaging, not influenced by ambient conditions, is widely used for long-range surveillance and industrial sorting. SWIR also covers the telecommunication wavelengths (1250 nm to 1600 nm) where the optical loss is minimum when the SWIR photons travel through the optical fiber. There are also biological windows (1000 -1350 nm and 1550 -1870 nm) in the SWIR, and the photons in the windows can penetrate deep into the bio tissues, enabling high resolution bioimaging.

The range of 3-5 µm is defined as mid-wave infrared (MWIR). This range is especially interesting since it is above 3 µm that the blackbody emittance of a room temperature object (T=300 K) prevails the reflectance of warmer light sources (i.e., the sun), see Figure II.1 b the blackbody

emittance spectra of objects at different temperatures. Consequently, MWIR can be used for thermal imaging where the contrast is generated from the temperature difference from different parts of the scene.

Long-wave infrared (LWIR) falls in the range of 8-12 μm of the electromagnetic spectrum. From the blackbody emittance spectrum (Figure II.1 b), we can see that the blackbody emittance of a room temperature object maximizes at around 10 μm, making it the most preferable wavelength for thermal imaging.

II.1.2 Photoconductors and photodiodes

For nanocrystal-based photodetectors, there are mainly two types of device geometries: the planar photoconductor and the vertical photodiode. As illustrated in Figure II.2 a, a photoconductor consists of a prepatterned electrode (typically interdigitated) which forms an ohmic contact with the nanocrystal arrays. This configuration is the simplest in terms of fabrication, because the photoconductance in this case is not sensitive to the film quality, allowing for various deposition methods, such as spin coating, spray coating and even drop casting.

In an operational photoconductor under illumination, the absorption of the incident photons generates electron-hole pairs in the nanocrystal film (see Figure II.2 a) and in turn increase the conductivity of the device, as demonstrated from a typical I-V curve in the dark and under illumination (Figure II.2 b). The modulation of the current upon illumination is the detection signal (i.e., photocurrent). Therefore, to obtain high performance from a photoconductive device, it is critical to have a low dark current, which is challenging for infrared nanocrystals that either have narrow bandgap susceptible to thermal excitations or are heavily doped. This issue can be partly solved by adding a gate to the photoconductor to form a phototransistor,[54,58] in which the doping of the nanocrystals can be tuned to decrease the dark current so as to achieve the maximum detection performance.

A more complex structure for nanocrystals-based photodetectors is photovoltaic (or photodiode) geometry, as schemed in Figure II.2 c. Photodiodes have the similar working principle to nanocrystal based solar cells. In both devices, by forming a p-n junction or a Schottky junction inside the device, a built-in potential is introduced, making it possible to efficiently extract and collect the photo-generated carrier, even under zero bias. The zero-bias operation, with low dark current and high photo-to-dark current is attractive to photodetection with a high signal-to-noise ratio.

As illustrated in Figure II.2 c, a typical photovoltaic device contains a back electrode made of transparent conductive oxides (TCO) through which the incident light can go all the way to absorbing materials. and a metal electrode on the top of the device. Electron transport layers (ETL, usually n-type ZnO or TiO_2 layers) and p-type hole transport layers (HTL) are inserted between the active layer and the cathode and anode, respectively. The materials for each layer are rationally chosen in terms of doping and energy levels to facilitate the carrier separation and collection. Figure II.2 d shows typical IV curves of a photodiode in dark conditions and under illumination. In the dark, and the device showed a rectification behavior, demonstrating the diode structure. Under illumination, a strong enhancement of the current can be observed, especially in the reversed bias regime. The operation bias of the photodiodes is 0 V, where highest photocurrent/dark current can be obtained.

Although the photodiode has offered attractive performance, this geometry is, however, sensitive to the film quality of all the layers. Pinholes in the layers can be detrimental for the device performance and even short the device.
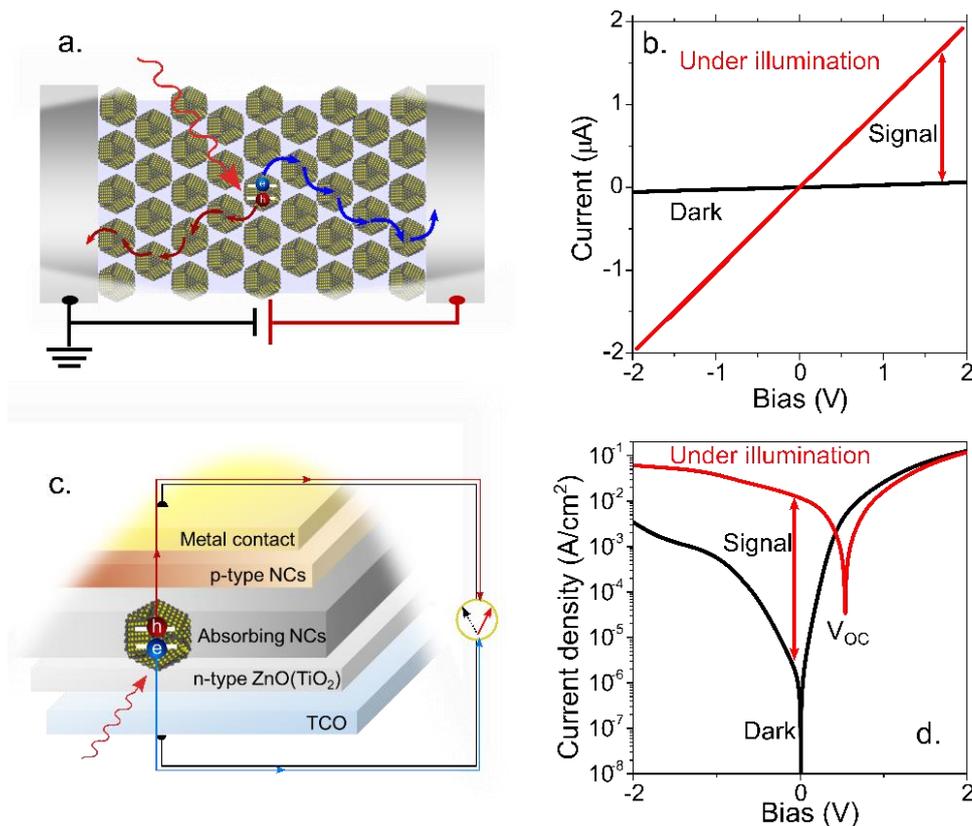
Figure II.2 (a) A scheme of a planar photoconductive device. (b) A typical IV curve of the photoconductive device in the dark and under illumination. (c) A scheme of a vertical photodiode comprising of a stack of TCO/ETL/absorbing layer/HTL/metal top contact. (d) IV characteristics of a photodiode.

II.1.3 Figures of merit for infrared photodetection

To compare the performance of various photodetectors, here I will introduce several figures of merits that are commonly used..

Responsivity (R), estimated as the ratio of current modulation to the incident optical power (P_{inc}), is a straightforward measure of the ability of the device to convert light power to electrical signals. It is essential to quote the wavelength and the modulation frequency for a fair comparison.

$$R = \frac{I_{photo} - I_{dark}}{P_{inc}} \tag{II-1}$$

External quantum efficiency (EQE) is defined as the ratio of the photogenerated electrons to the number of **incident** photons.

Internal quantum efficiency (IQE) is defined as the ratio of the generated electrons with respect to the **absorbed** photons.

Response time and **speed** both characterize how fast the photodetector can react to the incident light signal. A response time much faster than 10 ms, which is typical for a thermal detector, is expected from the photodetectors. Speed characterizes the modulation frequency

above which the photo response drops. The bandwidth is typically defined as 3 dB drop, which corresponds to the frequency at which the photoresponse is dropped to half of the maximum.

Detectivity (D*) is the most important figure of merit for photodetectors, which measures the signal-to-noise ratio. In other words, this value evaluates the ability of a photodetector to discriminate the useful signals from noise signals. Detectivity is usually expressed in the unit of cm Hz$^{1/2}$W^{-1} (or Jones). To precisely determine the value of detectivity, it is important to figure out the type of noise that prevails.

Noise: For conventional quantum detectors, there are generally two origins of noise, both of which can be analytically calculated. The thermal noise, also referred to as Johnson or Nyquist noise, is due to the scattering of carriers by thermal motions. Another type of noise is generation-recombination noise, which is due to the fluctuation of carriers through generation-recombination process. As these mechanisms are distinct from each other, they may be treated as independent non-correlated sources of noise. However, in the case of nanocrystal-based photodetector, the dominating noise is 1/f noise induced by the disorder of the conductive matrix[59]. As a result, the noise of the nanocrystal photodetector needs to be measured experimentally.

II.1.4 Infrared-active nanocrystals

Figure II.3 presents an overview of nanocrystals and their corresponding working wavelengths. In the visible, the target application of nanocrystals is light emission, especially for high quality display. The spectrum of Cd-based nanocrystals has covered the whole visible range, while the InP, as a less toxic alternative, is also under development. Perovskite nanocrystals emerging during the last few years, has been able to offer emission up to near infrared[60].

The infrared optical properties, which involve low energy transitions below 1 eV, are generally limited to narrow-bandgap materials, such as lead chalcogenides (PbX),[61] mercury chalcogenides (HgX)[62–65] and III-V InAs[66] and InSb.[67] Particularly, over the last 2 decades of development, the HgX has been able to exhibit optical features ranging from visible to THz[62,63,65,68,69]. In the meantime, the exploration of heavy-metal-free infrared-active nanocrystals such as Ag$_2$Se and metal oxides is progressing, and part of my thesis is dedicated to evaluating the potential of these heavy-metal-free nanocrystals for infrared photodetection.
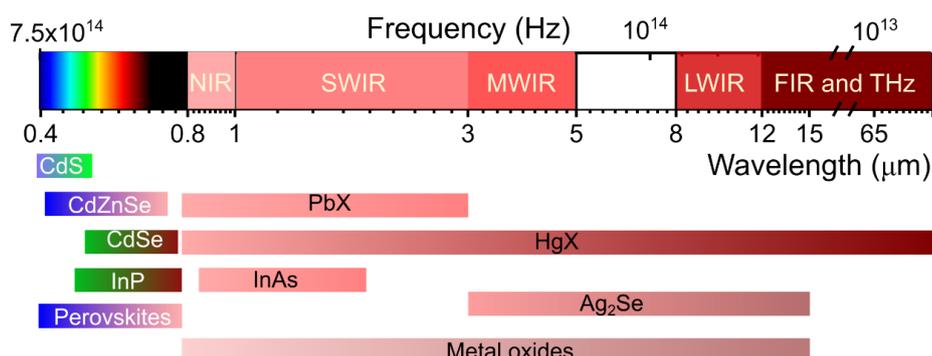
Figure II.3 The nanocrystals working for various ranges of electromagnetic radiations. In the visible, the Cd based nanocrystals dominate, while the infrared optical properties are provided by lead chalcogenides and especially mercury chalcogenides which provide the highest turnability covering the whole infrared range. Heavy-metal-free nanocrystals for infrared applications such as Ag$_2$Se and metal oxides are also presented.

Here, we take the example of HgX nanocrystals, the most versatile system for infrared photodetection, to elucidate the origins of their infrared transitions. As presented in Figure II.4,

the infrared transitions of HgX nanocrystals can originate from different mechanisms according to the target wavelengths: the interband transition of undoped HgTe nanocrystals mainly covers the SWIR range (1-2.6 μm) and MWIR range (3-5 μm), the intraband transitions of doped HgSe and HgTe nanocrystals covers the MWIR and LWIR (8-12 μm) range, and the plasmonic absorption of heavily doped HgTe and HgSe nanocrystals can enter the THz range.
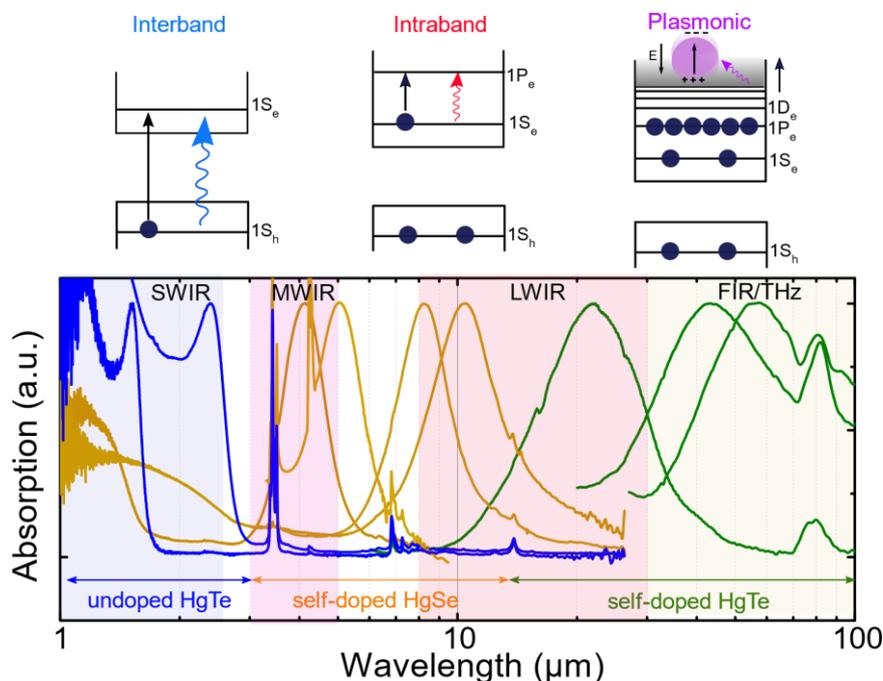
Figure II.4 Absorption spectra for mercury chalcogenide (HgSe and HgTe) nanocrystals with various sizes. Above the absorption window are brief energy diagrams indicating the interband transition of undoped HgTe nanocrystals, the intraband transition of self-doped HgSe and the plasmonic absorption of heavily doped HgTe and HgSe nanocrystals. This graph is adapted from reference [70]

II.1.5 The state-of-the-art of nanocrystal-based photodetectors

After decades of exploration on the synthetic chemistry of the nanocrystals and the optimization of device design, the nanocrystal-based photodetectors have gained a considerably high maturity in different regions in the infrared.

In the SWIR, photodetectors based on epitaxially-grown single-crystal InGaAs have been dominating. To move the SWIR imaging from a specialized niche into broader commercial markets, PbS nanocrystals have been developed as active material since 2005[71]. Up to now, there are PbS CQD based SWIR cameras commercially available in the market, which provides higher resolution than the InGaAs cameras at lower cost per megapixels[9]. Mercury chalcogenides have also been explored in SWIR[72,73], and their integration to focal plane array (FPA) imaging has been demonstrated[73,74].

The traditional materials for MWIR rely on epitaxial InSb, alloyed Mercury Cadmium Telluride (MCT) and GaAs quantum wells separated by AlGaAs barriers. Due to the high interest of this range for thermal imaging, a cost breakdown highly desired and the promise offered by nanocrystals is even more attractive. Although PbS serves well in the SWIR, the bulk bandgap of around 0.4 V of PbS limits its spectral tunability toward wavelengths longer than 3 μm

considering the confinement energy. As a result, mercury chalcogenides (HgX) with zero bulk bandgap are the most investigated materials for MWIR photodetection.[69,75,76]

LWIR, as introduced before, is the most preferential wavelength range for thermal imaging at room temperature objects. The current driving technology for LWIR is bolometric detectors which is however relatively slow (>10 ms). As can be expected, to use the intraband transition of nanocrystals requires large particle size, which usually comes with poor colloidal stability. Instead, the LWIR transitions are more promising to come from the intraband or plasmonic transitions of heavily doped nanocrystals.

II.1.6 Challenges of nanocrystal based infrared photodetectors

Like solar cells, the photodetectors suffer from a trade-off between the absorption and diffusion length of the carriers, which limits the carrier extraction efficiency. Generally, the absorption depth of infrared nanocrystal arrays is in the magnitude of several μm, while the carrier diffusion length is limited below 100 nm due to low mobility of nanocrystal arrays. To overcome this, light-matter coupling in a thin film can be enhanced by introducing patterns such as plasmonic disks,[77] guide mode resonators[78] into the system to achieve higher absorption.

Another issue that should be kept in mind is the toxicity of heavy metal containing nanocrystals, which can be a major flaw for the mass market. Since the narrow bandgap materials comes with high Z atoms, which restrain the candidate to the category of doped semiconductors. In this sense, self-doped Ag_2Se nanocrystals with size tunable mind infrared intraband transitions and metal oxides which provide tunable infrared plasmonic resonance by extrinsic doping attract our interest.

In the first part of the thesis, I will explore the potential of Ag_2Se nanocrystals and Tin doped Indium Oxide (ITO) nanocrystals for infrared photodetection.

II.2   Ag₂Se nanocrystals for mid-infrared photodetection

Colloidal nanocrystal-based infrared photodetector is a promising low-cost alternative to the currently dominating epitaxial semiconductor technologies. However, since mid-infrared detection requires small energy transitions (250~400 meV), most of the efforts has been focused on the heavy metal based nanocrystals with a dense band, such as Pb[79] and Hg[69,75] containing compounds. Among them, mercury chalcogenides (HgTe[43,80], HgSe[76] and HgS[81]) have achieved the highest maturity in addressing mid-infrared photodetection using their interband or intraband transition. Their toxicity, as a major conern for mass market, motivates the investigation of the nontoxic infrared-active alternatives.[10]

Ag₂Se nanocrystals appear as an ideal nontoxic candidate for infrared sensing owing to their narrow bulk bandgap of 0.15 eV[82] and a size tunable mid-infrared feature[17], which is very similar to that of HgSe nanocrystals (see Figure II.5 a). Long after the first synthesis of doped Ag₂Se nanocrystals by Sahu *et al* [17,83], the interest for this material has been driven by thermoelectric applications[84,85] or *in vivo* imaging using their near infrared photoluminescence[86–90]. Until 2017, the mid-infrared phtotoconduction of Ag₂Se nanocrystals remained unaddressed. The topic became hot after 2017, and we are among the first groups to study their mid-infrared photoconduction and to evaluate their potential for mid-infrared photodetection[91–93]. Very recently, the first vertically stacked mid-infrared photodetector using the intraband transition of Ag₂Se nanocrystal was reported.[94] By introducing a barrier layer of PbS nanocrystals between two Ag₂Se nanocrystal layers, the vertical device shows a 70 times higher responsivity than the planary photoconductors.[94]

In this part, I will discuss several open questions of Ag₂Se nanocrystals before integrating them into mid-infrared photodetection. The first question is the nature of their infrared absorption features, which stayed unclear several years after their discovery. Very recently, Park *et al*[93] demonstrate that the mid-infrared transition is an intraband transition instead of plasmonic resonance using spectroelectrochemistry[93]. Next, taking advantage of the similar surface chemistry of Ag₂Se to mercury chalcogenides, on which the group has gained a comprehensive understanding[56,65,95,96], we expand the investigation of Ag₂Se nanocrystals by unveiling its band diagram with XPS, probing the transport nature of Ag₂Se film in an field effect transistor configuration and testing their performance for infrared photodetection in a photoconductive configuration.

During this project, I did the synthesis, material characterization, device fabrication and characterization as well as data processing. I also received help from my colleagues. The nanocrystals synthesis and characterization are accomplished under the supervision of Dr. Nicolas Goubet, the former postdoc of the team. The photoemission spectroscopy is a team work at Tempo beamline of synchrotron SOLEIL with the assistance of Dr. Mathieu Silly, the beamline scientist. Transmission electronic microscopy is conducted under the supervision of Xiang Zhen Xu, the ESPCI engineer. The photoresponse measurements of the Ag₂Se based photodetector is done with the help of Clément Livache, the former PhD colleague of the team.

II.2.1   Tunable mid-infrared intraband transitions of Ag₂Se

II.2.1.1   Colloidal synthesis of Ag₂Se nanocrystals

The synthesis of Ag₂Se nanocrystals is based on the one-pot hot-injection method proposed by Sahu *et. al* [17,83], but with minor modifications. Briefly, AgCl and Se powers are separately dissolved in trioctylphosphine (TOP) to obtain TOP: AgCl and TOP: Se at the molar concentration of 1 M. A mixture of TOPO and OLA is degassed at 120 °C in vacuum and switched to Ar atmosphere after 1 h. Then, 6 mL of TOP: Se is injected into the mixture and the temperature is increased to 140-250 °C. Next, 4 mL of TOP: AgCl is quickly injected to the

solution and the reaction is allowed for 1-20 min. Both the reaction temperature and duration can be tuned to obtain nanocrystal with different size. The reaction is quenched by injecting 0.5 mL of DDT, which is found to have improved the colloidal stability of the nanocrystals. The reactor is then cooled down with air flux and 5 mL butanol is injected at 60 °C to avoid the solidification of the reaction products. The nanocrystals are precipitated with ethanol and redispersed in chloroform twice. Finally, Ag_2Se nanocrystals in chloroform are filtered with a 0.22 μm filter to get rid of unstable phases. The obtained Ag_2Se nanocrystals can stay colloidally and spectrally stable for more than one year.
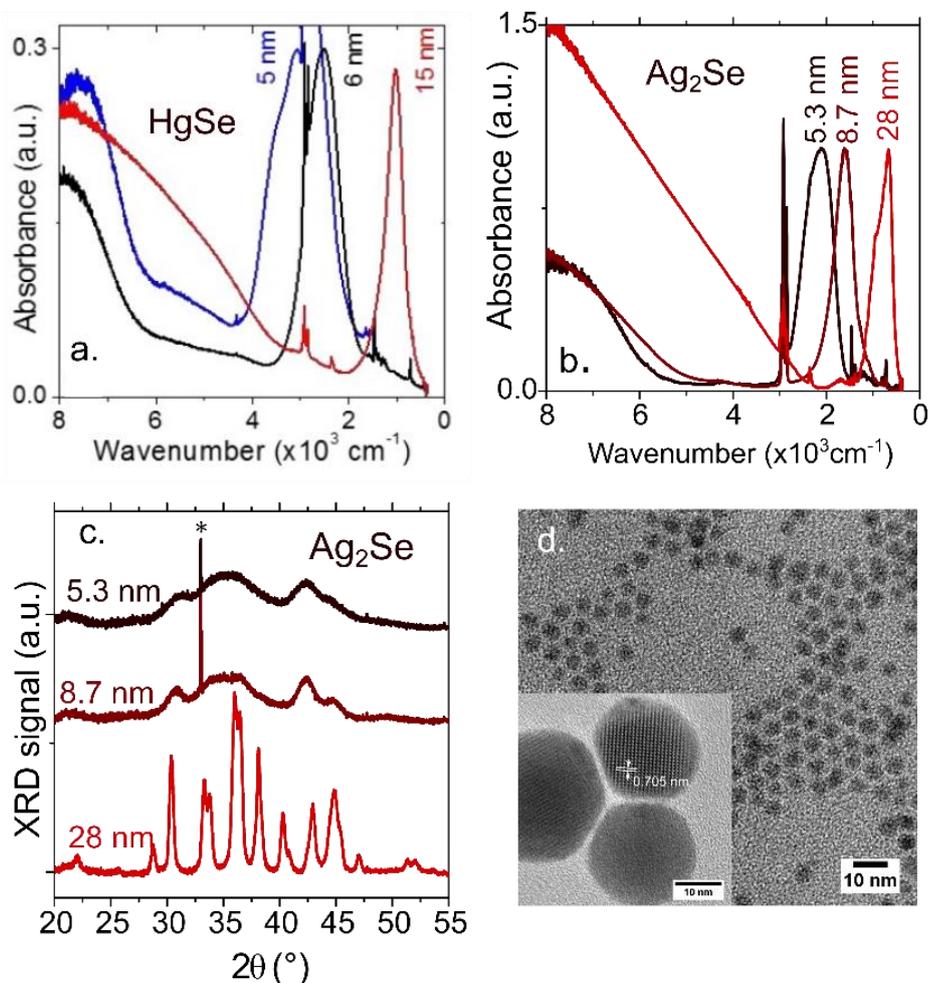
Figure II.5 (a) FTIR spectra of HgSe nanocrystals with diameters of 5 nm, 6 nm and 15 nm, and the corresponding intraband absorption peak are at 3000, 2500 and 1000 cm⁻¹, respectively. The graph is adapted from reference [97] (b) FTIR and (c) the X-ray diffraction patterns of Ag_2Se nanocrystals of three different sizes ranging from 5 nm to 28 nm. * in the XRD pattern indicates the diffraction peak from Si substrate. (d) TEM image of Ag_2Se with a size of 5.3 nm. Inset: TEM image of Ag_2Se with a size of 28 nm showing tetragonal crystal structure.

The synthesis of Ag_2Se nanocrystals is unconventional compared to most of the colloidal nanocrystal synthesis, in which the cation precursors are introduced before anion precursors. Here, the cation precursor (TOP: Se) is injected earlier than TOP: AgCl to avoid the reduction of TOP: AgCl and the formation of Ag nanoparticles.

With the reaction temperature-duration of 140 °C-1 min, 180 °C-20 min and 250 °C-20 min, spherical Ag_2Se nanocrystals with an average size of 5.3 nm, 8.7 nm, and 28 nm are synthesized,

respectively. As presented in Figure II.5 b, the infrared absorption spectra of all three are featured with interband transitions at short wavelength and a strong absorbing peak in the longer wavelength. Tuning the size of the nanoparticles from 5.3 nm (see the TEM image in Figure II.5 d) to 28 nm (inset of Figure II.5 d) allows to tune the energy of the infrared feature from 2100 cm^{-1} (260 meV or 4.8 μm) to 650 cm^{-1} (80 meV or 15.4 μm). X-ray diffraction patterns (see Figure II.5 c) of the nanocrystals present a Scherrer broadening with size. The 28 nm Ag$_2$Se nanocrystals possessing the highest crystallinity can be assigned to a tetragonal crystal structure[98], which is a metastable phase of Ag$_2$Se nanocrystals. The tetragonal crystal structure of 28 nm Ag$_2$Se is further confirmed by high-resolution TEM (inset of Figure II.5 d), in which the interplanar spacing of around 0.705 nm can be assigned to (100) and (010) facets of tetragonal Ag$_2$Se crystal, as has been proposed by Norris' group (a=b=0.706, c=0.498 nm)[17].

II.2.1.2   The determination of the intraband nature of mid infrared transition

The nature of the mid-infrared transition of Ag$_2$Se nanocrystals had remained vague for long after their discovery. In 2011, Heiss' group demonstrated the quantum confinement effect of Ag$_2$Se nanocrystals absorbing and emitting in the near infrared range[99]. While for the mid-infrared absorption feature of Ag$_2$Se nanocrystals, Sahu et.al. first ruled out the possibility that the absorption is a plasmonic resonance through the stoichiometry analysis of the compound[83]. Furthermore, they attributed mid-infrared features to the quantum confinement effect by fitting the size dependence of the bandgap, however, based on the assumption that the absorption came from band edge transition[17].
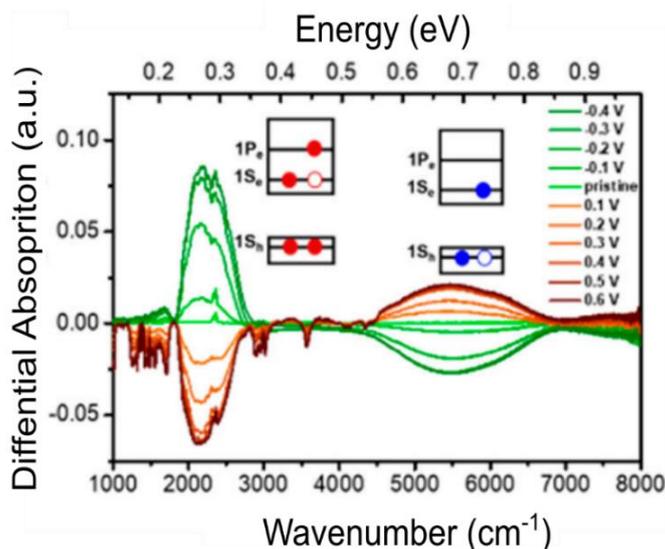
Figure II.6 Differential absorption spectra of Ag$_2$Se nanocrystals with different electrochemical potentials: the green curve indicates the oxidation of the system while the red curve the reduction of the system. Reproduced with permission from form reference[93]. Copyright (2018) American Chemical Society.

Until recently, based on the similarity between Ag$_2$Se and HgS nanocrystals, Park *et al*[93] provide more convincing evidence for the intraband nature of the mid-infrared absorption using spectroelectrochemistry (SEC) and photoluminescence measurements. With this SEC technique, one can monitor the spectral change of the material under different electrochemical potentials. The differential absorption spectra of Ag$_2$Se nanocrystals under different potentials, as reproduced in Figure II.6, showed that under an electrochemical potential corresponding to the reduction of the system (*i.e.* the injection of electrons), the mid-infrared transition of Ag$_2$Se nanocrystal is increased while the near-infrared transition is bleached; the reversed

phenomenon is observed when applying the potential corresponding to the oxidation of the system. The spectra variation with the injection of electron or holes can be reconciled by the explanation that the near- and mid-infrared transition share the same $1S_e$ and can be ascribed as bandgap ($1S_h$-$1S_e$) and intraband ($1S_e$-$1P_e$) transition, respectively, as schemed in the inset of Figure II.6. The mid-infrared photoluminescence found in Ag_2Se nanocrystals again convincingly rules out the possibility that the mid-infrared feature being plasmonic resonance[93].

II.2.1.3 Reconstruction of electronic structure of 5 nm Ag₂Se nanocrystals

To integrate Ag_2Se nanocrystals into optoelectrical devices with an optimized ohmic contact, it is critical to be aware of their electronic structure in absolute energy scale. To build their electronic structure diagram, we conduct X-ray photoemission (XPS) at the TEMPO beamline of Synchrotron SOLEIL. For the XPS measurements and the following investigation, I focus on the 5 nm nanocrystals since its intraband transition (4.8 µm) is the most interesting for the target photodetection range of 3-5 µm (MWIR), which is atmospheric transparent and enables long-distance detection. And it fit well with our 4.4 µm quantum cascade laser (QCL), which will be used later to resonantly excite this mid-infrared transition.

For XPS measurements, the Ag_2Se nanocrystal solution is drop-casted on an Si/SiO_2 wafer coated with 80 nm gold. To avoid the charging of the sample, the pristine long ligands of the nanocrystals are exchanged toward short ones. More detailly, during ligand exchange, the drop casted Ag_2Se film is first dipped in a solution of Ethanedithiol (EDT, 1% wt) in ethanol for 90 s and then rinsed with ethanol for 30 s to remove the residual ligands on the film. The ligand exchange process is repeated at least one more time to fill the cracks induced by the previous ligand exchange step, which enhances the conductivity and at the same time avoids the exposure of Au substrate.
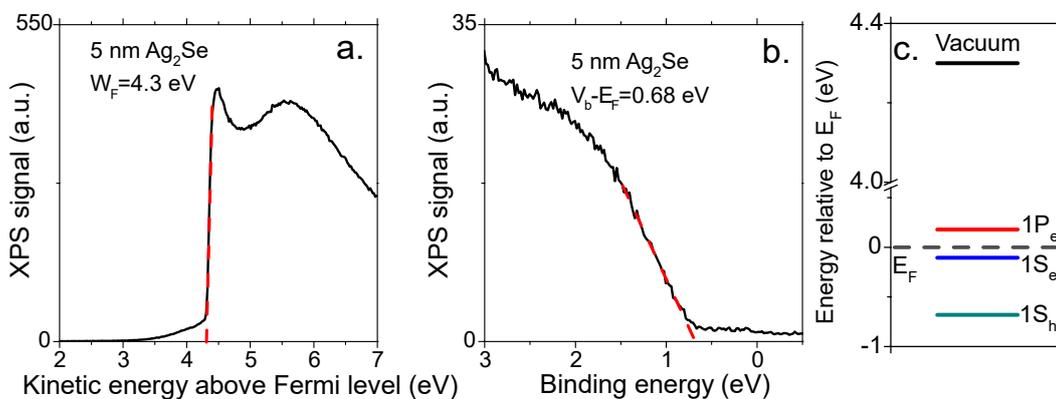
Figure II.7 (a) Photoemission signals of secondary electron cut-off for a film made of 5 nm Ag_2Se nanocrystals. The determined work function is 4.3 eV. (b) Photoemission signals associated with the valence band for a film made of 5 nm Ag_2Se nanocrystals. The Fermi level is 0.68 eV above the valence band. (c) A proposed electronic spectrum in the absolute energy scale for 5 nm Ag_2Se nanocrystals, with a Fermi level in the conduction band.

As shown in Figure II.7 a, a zoom in the cut-off of the secondary electrons reveals a work function of 4.3 eV. The low binding energy part of the spectrum (Figure II.7 b) is used to locate the valence band with respect to the Fermi level, from which we can deduce that the valence band is 0.68 eV below the Fermi level. From the results of SEC measurement provided by Park *et al.*, the bandgap for this size of Ag_2Se is estimated to be about 0.6 eV[93], which locates $1S_e$ state below the Fermi level, suggesting a degenerate n-type doping of the 5 nm Ag_2Se nanocrystal. With the intraband transition energy extracted from FTIR spectrum, we can deduce that the $1P_e$ state is 260 meV above $1S_e$ state. Combining all the information above, a reconstructed

electronic spectrum is proposed in Figure II.7 c. The obtained energy spectrum is also close to that of the HgSe nanocrystals with a similar size.[56]

II.2.2 The origin of doping for Ag₂Se nanocrystals

With photoemission, we managed to demonstrate the degenerate n doping of the 5 nm Ag₂Se nanocrystals. From the spectroelectrochemistry measurement, Park *et. al.* claimed that there are 1-2 electrons in the conduction band per Ag₂Se nanocrystal[93]. However, the origin of doping for Ag₂Se nanocrystals remains a question. To address this, we start with the stoichiometry study.

II.2.2.1 The Stoichiometry of Ag₂Se nanocrystals

Research on the stoichiometry of Ag₂Se nanocrystals however give controversial results. Sahu *et. al* [17,83] reported a Ag/Se ratio close to but lower than 2 with electron-probe microanalysis (EMPA); the Energy Dispersive X-ray spectroscopy (EDX) results of aqueous synthesized[89] and the 1-octanethiol-medicated[88] Ag₂Se nanocrystals all showed a slightly Ag deficiency. However, Park *et al*,[93] from a similar synthesis, have reported an Ag excess in these particles using EDX. The actual stoichiometry of their compound is reported to be Ag₂.₃Se.

From our side, we first conducted the EDX analysis. The sample is deposited onto a Si wafer before being introduced into a FEI Magellan scanning electron microscope coupled with an Oxford EDX probe. The results from the EDX spectrum shown in Figure II.8 a reveal that a ratio of Ag/Se=2.6 for Ag₂Se nanocrystals.

Rutherford Backscattering Spectrometry (RBS) has been used as a complementary analysis to the EDX. During the RBS experiment, the SAFIR source at INSP is used with He⁺ ions accelerated under 1.8 MV bias. The beam size is 1.5 mm² and the collection angle is 165°. The He⁺ beam current is operated at 50 nA. The energy calibration is done using a Bi-implanted Si wafer with a 6×10^{15} cm⁻² dose. From the backscattered yield, the Ag/Se ratio is determined by $R = \frac{A_{Ag}}{A_{Se}} \left(\frac{Z_{Se}}{Z_{Ag}} \right)^2$ in which A_{Ag} the area of the peak resulting from backscattering at Ag atoms, A_{Se} the area of the Se peak, and Z_{Ag} and Z_{Se} the atomic number of Ag and Se, respectively. The analysis leads to a value of Ag/Se atom ratio of 2.57, as presented in Figure II.8 b

Figure II.8 (a) EDX signal of a film made of 5 nm Ag₂Se nanocrystals, revealing a ratio of Ag/Se=2.61. (b) RBS signal is associated with a film made of 5 nm Ag₂Se nanocrystals, leading to Ag/Se= 2.57.
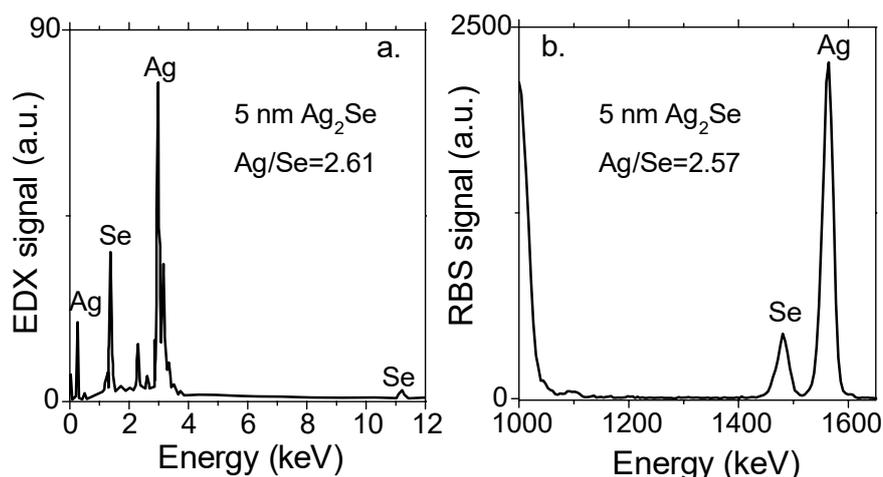
For our material, both EDX and RBS show consistent results of a silver excess and a real stoichiometry of Ag₂.₆Se, in consistency with the Ag excess reported by Park *et al*[93]. The metal

excess in Ag_2Se nanocrystals resembles II-VI semiconductor nanocrystals, whose metal-rich surface can lead to a n-type character.

II.2.2.2 With or without Ag^0 in the nanocrystal?

For other metal-rich n-type semiconductors, for example HgSe, the excess cation is in the form of metal cations (Hg^{2+}). While in the case of Ag_2Se nanocrystals, the observation of Ag^0 with TEM (Figure II.9 a) indicates that the form of Ag needs to be further revealed.

First, we observe some Janus-like nanocrystals with some darker spots on the TEM image, see Figure II.9 a. A careful analysis of the fast Fourier transform (FFT) based on area 1 (see inset of Figure II.9 a to the down left) and area 2 (see inset of Figure II.9 a to the up right) reveals that the main part of the particle is made of tetragonal Ag_2Se, while the dark spot is made of pure metallic silver. In addition, from the TEM image shown in Figure II.9 b, we notice that there are defects of twins with a 5-symmetry feature inside a nanocrystal, as indicated by the arrows. Its corresponding FFT image is given in Figure II.9 c, and the 5-fold symmetry of the twins, which is characteristic of noble metal nanoparticles (Ag nanocrystal in this case) with face-centered cubic (FCC) lattice, are confirmed and indexed. These results suggest that metal Ag nanocrystals are in co-existence with Ag_2Se nanocrystals.

The observation of Ag^0 thus leads to another hypothesis of doping origin: the transfer of electrons from the metallic Ag^0 phase to its neighbor narrow-band-gap semiconductor t-Ag_2Se phase. Indeed, Ag^0 is commonly used as a cathode (electron injector) thanks to its low work function (4.1-4.2 eV) for light emitting diodes [100].
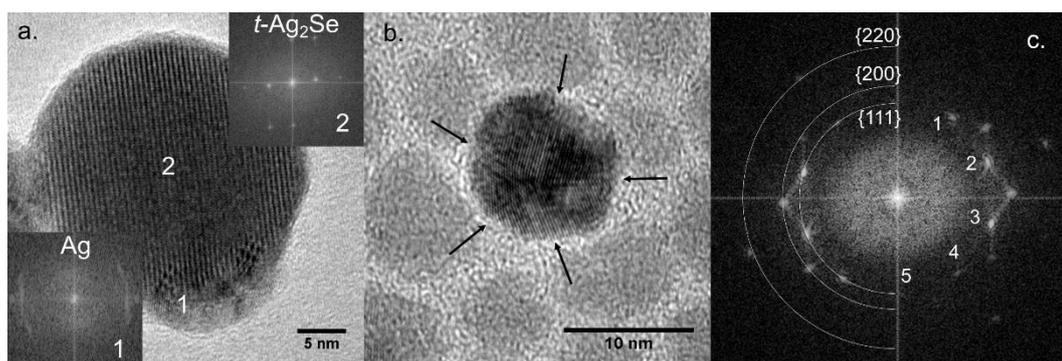
Figure II.9 The identification of Ag^0 from the TEM of Ag_2Se nanocrystals. (a) The TEM image of the 28 nm nanocrystals. FFT of the area 1 (inset to the down left) and the area 2 (inset to the up right) revealing a crystal structure of Ag metal and tetragonal Ag_2Se. (b) TEM image of Ag_2Se nanocrystal in which five arrows indicates five twins. (c) The corresponding FFT of (b), indexed with FCC crystal structure of silver.

To further verify this hypothesis, we conduct X-ray photoemission (XPS), which is the most suitable tool to discriminate two oxidation states of a chemical species. The overview XPS signal (see Figure II.10 a) reveals the presence of gold (Au) from the substrate and oxygen due to air exposure of the sample, while other peaks (Ag, Se from the nanocrystal core and S, C from the ligands) come from the sample itself. The signal from the Ag 3d peak is shown in Figure II.10 b, and without ambiguity can be fitted by a single Voigt contribution. The binding energy of the Ag $3d_{5/2}$ state is measured to be 368.06 eV, with a spin-orbit coupling of 6 eV and a full width at half maximum (FWHM) of 0.65 eV. This value of the binding energy is 200 meV below the typical value reported for Ag^0. Moreover, there is no loss feature observed in the spectrum, which could have been a signature of metallic silver. Thus, we can confidently state that XPS only reveals Ag^+ from the film made of Ag_2Se nanocrystals. On the other hand, the appearance of Ag^0 in the TEM image can be attributed to the interaction between electron beam of TEM and Ag^+, which is in accordance with the claim of Norris' group that the Ag_2Se and Ag_2Te

nanocrystals could not stay stable under the electron gun of TEM for a long time.[17] Electron-beam induced instability can also be encountered by perovskites, in which Pb^{2+} tend to be reduced to Pb^0 during TEM imaging.[101]

Herein, we can conclude that n-type doping in Ag_2Se is from a cation excess in the surface, like most of the II-VI nanocrystals. For the sake of completeness, we also have analyzed the signal relative to the Se 3d state, see Figure II.10 c. In this case, two components are observed, corresponding to the Se on the surface and deep within the nanocrystal. The more electron-rich peak is centered at a binding energy of 53.7 eV while the second peak presents a binding energy of 54.3 eV. Both contributions are fitted with a FWHM of 0.71 eV and spin-orbit coupling of 0.86 eV.
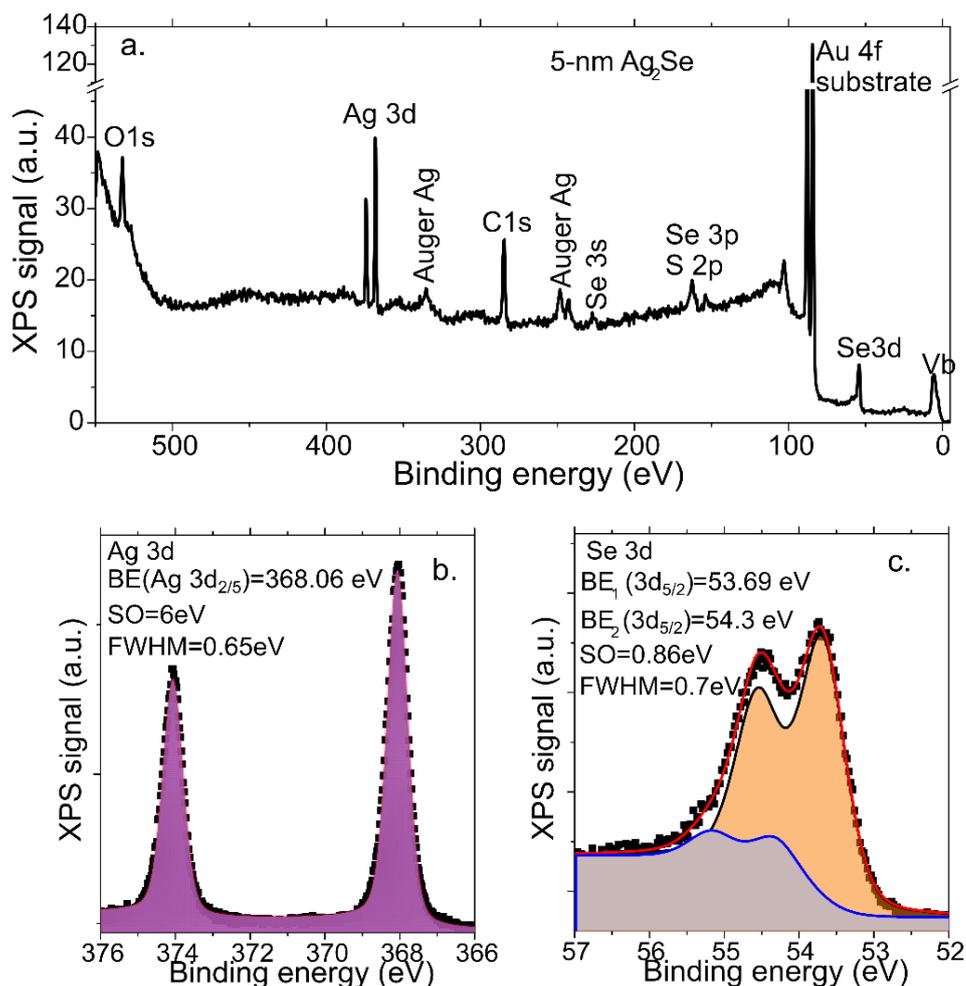
Figure II.10 (a) The XPS overview of a film made from 5 nm Ag_2Se nanocrystals. (b) Ag 3d core level of a film made from 5 nm Ag_2Se nanocrystals. (c) Se 3d core level of a film made from 5 nm Ag_2Se nanocrystals.

II.2.3 Transport properties of Ag_2Se nanocrystal arrays in dark conditions

So far, we have determined the electronic structure of the Ag_2Se nanocrystals. The next step is to integrate the nanocrystals into the solid conductive arrays to build a photoconductive device. Their transport characteristics in the dark conditions, including their transfer curve in a field

effect transistor (FET) configuration will be investigated. The temperature dependence of the conductance for Ag_2Se nanocrystal arrays will also be probed.

II.2.3.1 Transfer property of Ag₂Se nanocrystals

To integrate Ag_2Se nanocrystal into photoconductive devices, ligand exchange toward shorter molecules is required to boost the inter dot coupling and thus the conductivity of the nanocrystal array. Several layers of Ag_2Se nanocrystals are deposited onto interdigitated Au electrodes with 20 μm channels. After each deposition, a solid-state ligand exchange is conducted by dipping the device into a diluted ethanethiol (EDT) solution in ethanol (typically 1% in volume) and rinced with clean ethanol. The devices are ready for transport measurements when a resistance between 100 and 500 kΩ is achieved.

From the infrared spectra of Ag_2Se nanocrystal film before and after ligand exchange with EDT, as presented in Figure II.11 a, we can see that the ligand exchange procedure well preserves the intraband feature of Ag_2Se nanocrystal arrays, but the relative intensity of intraband transition to interband transition is decreased, indicating a decreased doping level. This change of doping and optical spectrum upon ligand exchange has also been observed from HgSe films.[95] As schemed in Figure II.11 b, the energy bands of the pristine Ag_2Se nanocrystals are assumed to be flat with a Fermi level above the conduction band, in which case the interband transition is weak or bleached, while the intraband transition is strong due to a large population of the conduction band electrons. However, when the nanocrystals are capped with EDT, surface dipoles pointing their negative charge toward the nanocrystal surface are formed, resulting in the positive charges shifting toward the surface and thus a band bending. In the latter case, the population of the conduction band is decreased, which enables the debleaching of interband transition and in turn, a higher inter/intraband transition ratio than that of the film without ligand exchange is obsreved. We also observed a small red-shift of the intraband transition after EDT ligand exchange, which is due to partial wave-function delocalization and improved inter dot coupling, common for II-VI semiconductor nanocrystals upon ligand exchange.
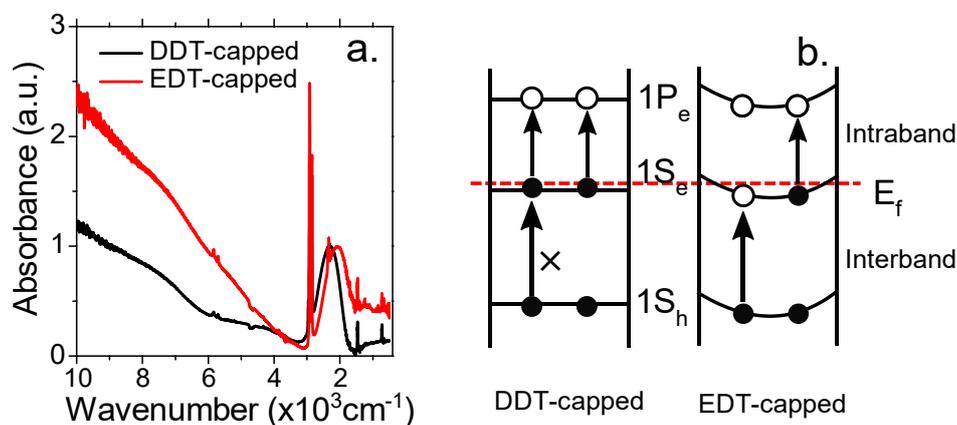
Figure II.11 (a) FTIR spectra of 5 nm Ag_2Se capped with DDT and EDT ligands. (b) A scheme describing the band bending and doping conditions of the Ag_2Se nanocrystals capped with DDT and EDT.

Then the 5 nm Ag_2Se nanocrystal arrays are integrated into an electrolyte gated FET. A scheme of the FET is shown in Figure II.12 a, in which a conventional photoconductive device is used with an electrolyte gate on the top of the Ag_2Se film. The electrolyte gate made of $LiClO_4$ embedded in a polyethylene glycol (PEG) matrix has a large capacitance, making it convenient to probe the gate effect of heavily doped nanocrystals. Also, the Li^+ ions can percolate into nanocrystal arrays, which enables the gating of thick films. The transfer curve of Ag_2Se

nanocrystal arrays shown in Figure II.12 b reveals a clear n-type behavior with an increase of conductance upon electron injection (i.e. under positive gate bias), which is fully consistent with the electronic spectrum proposed in Figure II.7 c. The transistor shows a low on-off ratio of ≈50, which is typical for degenerately doped semiconductors.
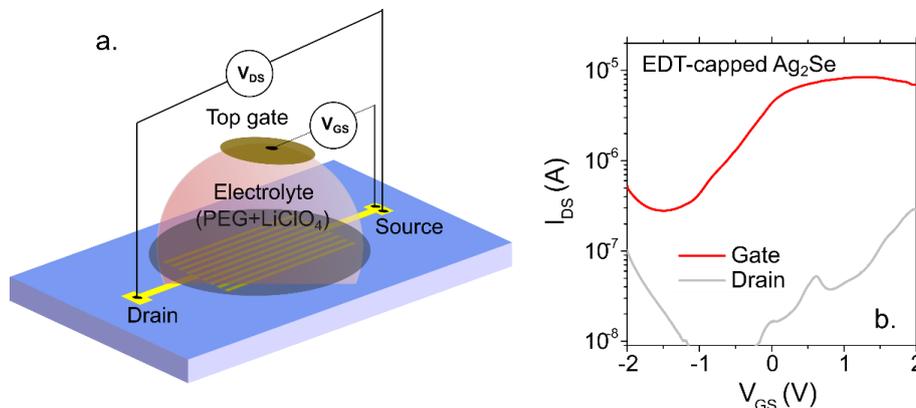
Figure II.12 (a) Scheme of electrolyte gated FET. (b) The transfer curve of EDT-capped Ag_2Se nanocrystals, with a constant drain-source voltage of 20 mV.

II.2.3.2   Temperature dependence of dark transport

Low temperature transport has been a powerful tool to reveal thermal properties and transport mechanisms of semiconductor nanocrystals. Practically, for infrared photodetection, cooling is widely used to avoid thermally activated carriers and thus decreasing the dark current which generates noise.

First, the device made of EDT-capped Ag_2Se nanocrystals is cooled down under a constant bias of 0.2 V to probe the temperature dependence of its conductivity. As shown in Figure II.13 a, the current decreases monotonically with temperature during cooling. Specially, the current in high temperature range (300-200 K) can be fitted with Arrhenius law, yielding an activation energy of 164 meV, which can be ascribed to the thermal activation of electrons from Fermi level to the $1P_e$ state (180 meV), the first empty state available for transport.

Then, the I-V characteristics of the device based on Ag_2Se nanocrystals are collected at different temperatures. At room temperature (300K), a butterfly shape I-V feature is observed, as presented in Figure II.13 b. In this I-V curve, there is a liner (ohmic) regime under the bias below 200 mV, while beyond that, the conductance starts to strongly deviate from the linear region and the current even decrease with increased bias. Nevertheless, at a temperature below 175 K, the I-V of the device recovers its ohmic behavior, and there is even no hysteresis, see Figure II.13 c. This change of I-V from butterfly shape to Ohmic characteristic is confirmed later by Hafiz *et al.* [92] when they study the same photoconductive device sensitized by Ag_2Se nanocrystals. This nonlinear electrochemical signature of I-V curve can be explained by Ag^+/Ag transformation with injection of electrons or holes at relatively high temperatures. This electrochemical instability of the Ag_2Se nanocrystals is a severe limitation for high quality photodetectors, which requires low dark current which is linear and predictable with bias.
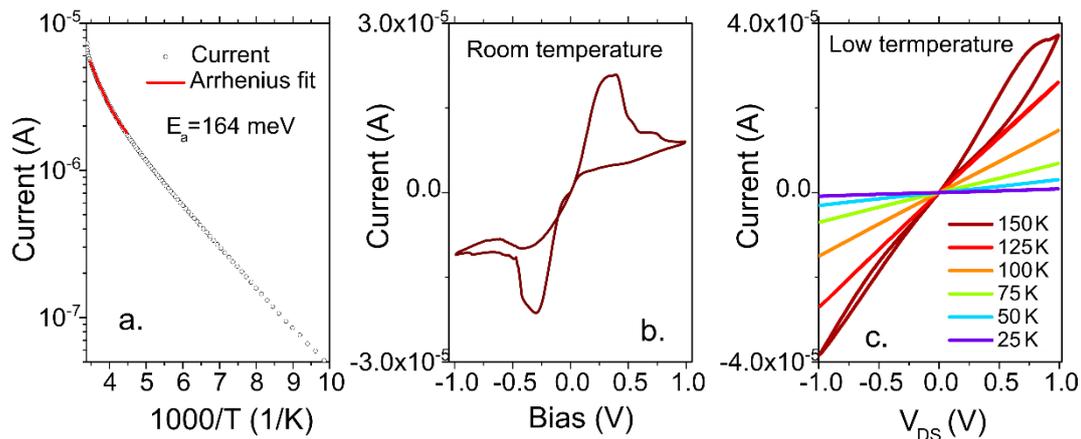
Figure II.13 (a) Variation of dark current with temperature of a device based on EDT-capped Ag$_2$Se. (b) I-V curve of Ag$_2$Se nanocrystal-based device at room temperature showing large hysteresis and nonlinear feature. (c) I-V curve at low temperatures below 175 K, showing an ohmic feature and no hysteresis.

II.2.4 Photoconductance of Ag$_2$Se nanocrystal arrays

In this part, I test the potential of Ag$_2$Se nanocrystals for infrared. As indicated in Figure II.14, we specifically use two light sources to excite the Ag$_2$Se nanocrystals according to their absorption spectrum: a laser diode with a wavelength of 1.55 µm is used to pump the interband transition, while a quantum cascade laser (QCL) of 4.4 µm is used to resonantly excite the intraband transition. In both cases, photoconductive behavior is observed.
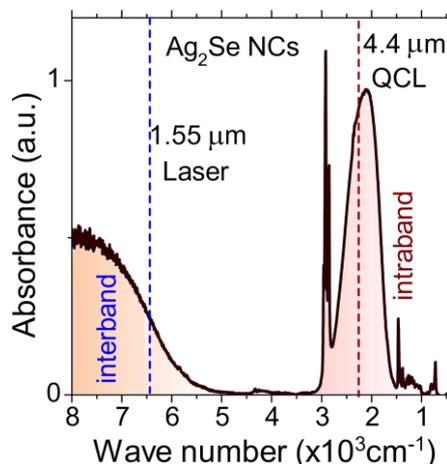
Figure II.14 FTIR of 5 nm Ag$_2$Se nanocrystals, with its interband and intraband transitions excited by 1.55 µm laser diode (indicated by blue dash line) and 4.4 µm quantum cascade laser (indicated by red dash line), respectively.

II.2.4.1 Interband photoconduction of Ag$_2$Se nanocrystal arrays

When excited at the band edge with 1.55 µm laser diode at the ohmic region (i.e. below 0.2 V, see the blue region of Figure II.15 a) , the Ag$_2$Se nanocrystal based device displays a clear and fast photo response. Figure II.15 b shows the current modulation under a 10 Hz laser pulse. The near-infrared photo response is investigated under different frequency and turns out to be reasonably fast, with a 3 dB cut-off frequency (the frequency at which the signal drop to half of the maximum) around 20 kHz, see Figure II.15 c, which is compatible with the frame rate for

infrared imaging. Figure II.15 d show the frequency and bias dependence of the device photocurrent, from which we can see that its frequency dependence is not significant under various bias, indicating a fast photoresponse, whereas the bias dependence of photocurrent follows the butterfly trend, that is, the photocurrent increase with bias in the ohmic regime while under higher bias regime, the photocurrent starts to decrease, which is far from reliable photodetection.
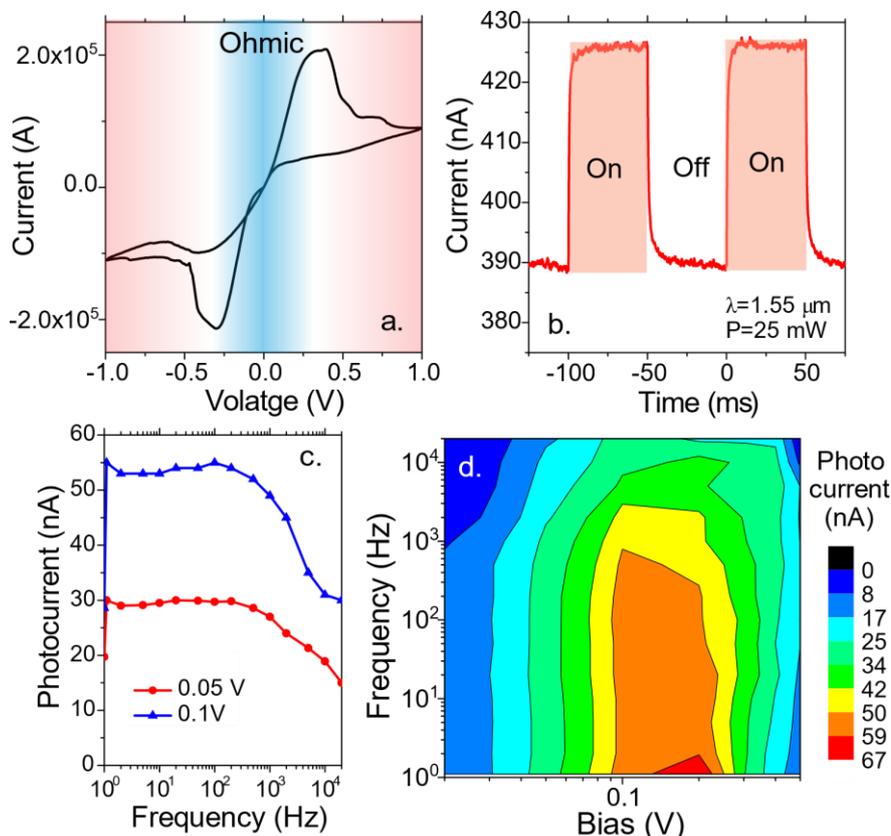
Figure II.15 Photoresponse and photocurrent of 5 nm Ag_2Se nanocrystal based device under the excitation of interband with 1.5 μm laser at room conditions. (a) The I-V curve of the photoconductive device, which can be divide into ohmic region at low bias (blue region) and nonlinear region at high bias (red region). (b) The temporal trace of current when the laser is chopped at a frequency of 10 Hz (c) Bode diagram of the device working under the bias of 0.05 V (red) and 0.1 V (blue). (d) Photocurrent as a function of frequency of the laser pulse and the working bias.

II.2.4.2   Intraband photoconduction of Ag_2Se nanocrystal arrays

We then test the potential of Ag2Se nanocrystals for intraband mid-infrared photodetection, which is the actual goal of this study. Using a photoconductive device based on EDT-capped 5 nm Ag_2Se nanocrystal array, we resonantly excite the intraband transition of Ag_2Se nanocrystals with a 4.4 μm quantum cascade laser coupled with a cryostat, see the scheme of the setup in Figure II.16 a. The laser can be chopped mechanically with a chopper or electrically with a wavefunction generator. An amplifier is used to amplify the photocurrent signal and can filter the DC dark current. It turns out that low temperature (< 200 K) is required to obtain a clear photocurrent for Ag_2Se based photoconductive device. Figure II.16 b exhibits the I-V curves of the device both in the dark and under 10 mW illumination at 25 K, and an increase of conductivity can be observed under illumination. Figure II.16 c shows the current of the device as a function of time, and from the modulation of current upon 10 mW illumination, a

responsivity of 8 µA.W^{-1} can be extracted, which is 3 orders of magnitude lower than the best reported responsivity for HgSe nanocrystals[76,96]. On the other hand, like HgSe, the intraband photo response is extremely slow with both rise and fall time of several seconds, see Figure II.16 c. From the frequency dependence of photocurrent shown in Figure II.16 d, we can see that the photocurrent drops fast with laser frequency, again demonstrating a slow photo response. This weak and slow photoresponse strongly contrasts with performance in HgTe nanocrystal where time response as short as 20 ns has been reported at the same wavelength.[102]
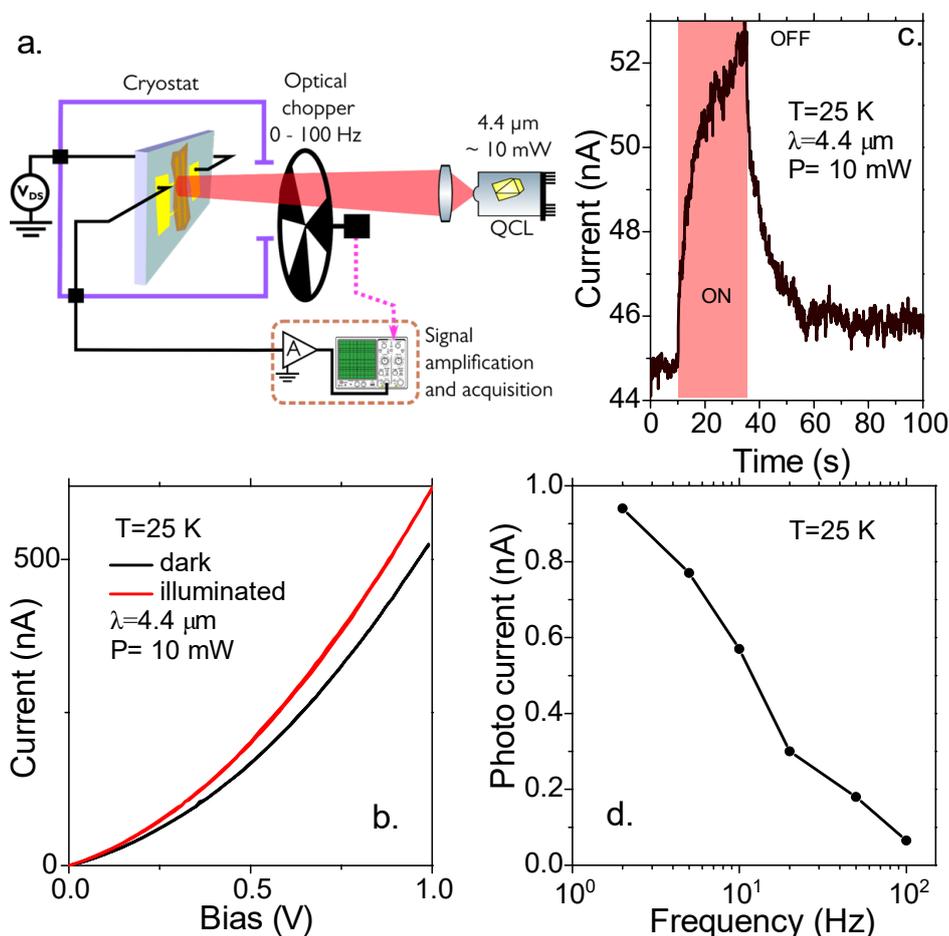
Figure II.16 (a) Scheme of the experiment setup reprinted from reference[102] . A 4.4 µm QCL is aligned to illuminate the photoconductive device enclosed in a cryostat. (b) I-V curves of Ag$_2$Se nanocrystal-based device in the dark and under illumination. (c) Current as a function of time while QCL is turned on and off. (d) Photocurrent as a function of chopping frequency.

II.2.5   Conclusions and perspectives

In search of non-toxic alternatives to mercury chalcogenides to address mid-infrared, we first target at tetragonal Ag$_2$Se nanocrystals which presents size tunable interband transition in the mid-infrared. With the experience on mercury chalcogenides of the group, especially HgSe nanocrystals with similar spectral properties and surface chemistry with Ag$_2$Se nanocrystals, I explored this relatively new material and answered several open questions relating to its use for mid-infrared detection.

First, by XPS, the reconstructed band structure with respect to vacuum level is proposed for 5 nm Ag$_2$Se nanocrystals, which will give insights for the design of device with preferential ohmic

contact. Additionally, we find that the Fermi level lies in the conduction band, which indicates a degenerate n-type doping of this material.

Then, a cation excess stoichiometry of $Ag_{2.6}Se$ is consistently demonstrated by EDX and RBS analysis. By carefully analyzing the core-level X-ray photoemission of Ag 3d, we demonstrate that the excess silver is only under Ag^+ form and there is no Ag^0 in the nanocrystal film, indicating that the n-doping of Ag_2Se nanocrystals originates from the material non-stoichiometry, like HgSe and other II-VI nanocrystals.

Next, I fabricate the photoconductive device based on Ag_2Se nanocrystal arrays. A standard ligand exchange with EDT is used to obtain photoconductive films. However, a very limited range of bias stability (200 mV) at room conditions is observed while the ohmic behavior recovered at low temperatures below 175K. It is likely due to the oxidation and reduction of the Ag^+ at room temperature.

Last, I have probed the potential of Ag_2Se nanocrystals as infrared active materials. Under the excitation of interband in the near infrared, the device shows fast photoresponse, while under mid-IR excitation resonant with the intraband absorption, the photoconduction is found to be very weak and slow compared with performances reported for Hg-containing nanocrystals.

Soon after we published the results above, Hafiz *et al* revisit the Ag_2Se nanocrystals for mid-infrared photoconductance [92]. With the same device structure and surface chemistry (ligand exchange with EDT) as ours, they obtained a higher responsivity of 350 µA/W at the similar wavelength. The improvement is likely from the fact that they use thicker films, which can enhance the light absorption and photocurrent yet at the price of higher noise. Also, their bias are driven at 4 V, while in our case the bias is 0.2 V.

To push Ag_2Se nanocrystals toward mid-infrared photodetection using its intraband transition, the first issue needs to be addressed is their electrochemistry instability, possibly by the addition of a shell, which is challenging with a metastable tetragonal lattice. It is worth noting that, tetragonal as a metastable phase of Ag_2Se nanocrystals can transfer to orthorhombic phase at fairly low temperature of 60 to 67 °C irreversiblly[18], and proper ways are thus required to handle this material.

Another major limitation is the high dark current comes with degenerate doping, which is the common difficulty faced by the intraband/intersubband photodetectors. To overcome this, one way is to carefully control the dopants to obtain the ideally doped situation, that is to have a filled $1S_e$ and an empty $1P_e$ level, which may come from higher-level control of synthesis or surface chemistry.[75] Another more promising approach is to uncouple the absorption and transport of the nanocrystals, which has been proved successful in the case of doped HgSe[76,96] and PbS nanocrystals[103]. One way is to use a hybrid array in which the infrared absorption is provided by doped HgSe[76] (or PbS), while the transport is driven by a wider-band-gap semiconductor nanocrystals, HgTe (or perovskite), which can be used to reduce dark current. Another strategy proposed in this context for HgSe nanocrystal is to grow a shell of HgTe[96], a decrease of dark current, an increase of activation energy and a faster photo response are observed.

II.3   Degenerately doped ITO nanocrystals for mid-infrared detection

In the screening of heavy-metal-free nanocrystals for low-cost mid-infrared photodetection, we are limited to doped semiconductors with low-energy transitions. In the previous chapter, we have explored the potential of self-doped Ag_2Se nanocrystals with tunable intraband transition in the mid-infrared. However, its performance for photodetection remains far weaker than its Hg-containing counterparts and its electrochemical instability raise challenges for further improvement. The category of degenerately doped nanocrystals (i.e. metal oxides[104], metal chalcogenides[105] and doped Si nanocrystals[106]), which provide strong localized surface plasmon resonance (LSPR) absorption from near infrared to THz[107], has thus attracted our interest.

Infrared active LSPR semiconductors, especially metal oxides with aliovalent impurity doping, has achieved high synthesis maturity and spectra ranging from near infrared to long-wave infrared via remote doping. Due to their high LSPR spectral tunability and large absorption cross-section, Sn, Ce and Ti doped In_2O_3 [104,108–111], Al doped ZnO (AZO)[112] and Nb doped TiO_2[113], has been investigated for IR electrochromic smart windows[114,115], photothermal imaging and therapy[116–119] and enhanced spectroscopy[120]. However, their potential for mid-infrared photodetection stayed unexplored, in spite of their large light absorption cross-section and textbook straightforward doping mechanism, in contrast to the doping of III-V and II-VI nanocrystals whose doping are usually induced by surface effects and difficult to control. Herein, we use well-established Sn doped In_2O_3 (ITO) nanocrystals as a platform to reveal their capacity for mid-infrared photodetection.

In the context of photodetection, the photocurrent is proportional to two key parameters which are material absorption and photocarrier lifetime. For interband and intraband transitions, the absorption cross-section per nanoparticle is weak, typically in the 10^{-15} cm^2 range[121], implying that for an intraband transition from a lightly doped semiconductor (1 carrier per dot), only one electron is active every 10^3-10^4 atoms. On the other extreme, metals with 1 active carrier per atom can reach high absorption cross-section (10^{-12} cm^2)[122]. In a degenerately doped semiconductor, the situation is intermediate: a higher doping magnitude results in a larger absorption cross-section, yet a shorter carrier lifetime compared with those of marginally doped semiconductors. As a result, the photocurrent of LSPR excitation remains unclear. Another critical parameter for photodetection is the dark current, which comes inevitably with doping. In this regard, we need to quantize how the increased absorption of LSPR competes with the shorter carrier lifetime and higher dark current, to reveal the exact potential of LSPR nanocrystals for infrared photoconduction.

This part will start with an introduction of Drude-Lorentz model, which is commonly used to describe LSPR. Then the synthesis of ITO nanocrystals with different doping levels and resultant optical properties will be presented. Next, the transport properties of ITO nanocrystal arrays will be investigated both in the dark and under illumination according to the different part of their spectra. We find that the infrared absorption peak of doped ITO can be well described by Drude model, while that of In_2O_3 nanocrystals strongly deviates from it and appears more like an intraband transition, in contrast to the common view that the infrared peak of In_2O_3 nanocrystals has been an oxygen vacancy induced LSPR.[120] Also, we obtain the infrared photoresponse of ITO nanocrystals-based photoconductive device and we finally assign the response as a result of bolometric effect, instead of photocurrent.

II.3.1   LSPR in conducting nanostructures

II.3.1.1   LSPR described with Mie theory and Drude-Lorentz model

LSPR occurs in conductive nanostructures when the collective oscillations of their free charge carriers resonate with incident electromagnetic radiations. The frequency of LSPR is determined

by the complex dielectric function of the material $\epsilon_p(\omega)$, see (II-1), the size and shape of the nanoparticle and the dielectric constant of the environment ϵ_M.[105] Using Mie theory which is established to solve the optical properties of sphere-shaped nanoparticles under the quasi static approximation (applicable when the particle size is much smaller than the wavelength of light), the absorption and scattering of a nanoparticle can be analytically solved as shown in (II-2) and (II-3).[120]

$$\epsilon_p(\omega) = \epsilon_1(\omega) + i\epsilon_2(\omega) \tag{II-1}$$

$$C_{abs}(\omega) = 4\pi R^2 \left[k(\epsilon_M)^{\frac{1}{2}}R\right] Im\left\{\frac{\epsilon_p(\omega) - \epsilon_M}{\epsilon_p(\omega) + 2\epsilon_M}\right\} \tag{II-2}$$

$$C_{sca}(\omega) = 4\pi R^2 \left[k(\epsilon_M)^{1/2}R\right]^4 \left|\frac{\epsilon_p(\omega) - \epsilon_M}{\epsilon_p(\omega) + 2\epsilon_M}\right|^2 \tag{II-3}$$

From (II-2), we can deduce that when the real part of the dielectric function $\epsilon_1(\omega) = -2\epsilon_M$, the absorption is maximized, which is the physic basis of LSPR. The corresponding frequency is thus the LSPR frequency of the material.

For conducting materials, their optical properties are dominated by the collective resonance within the conduction or valence band where electrons or holes act as free carrier gas. As a result, their dielectric function is often expressed with Drude-Lorentz model. The real part and the imaginary part of the dielectric function can thus be given as (II-4) and (II-5):

$$\epsilon_1(\omega) = \epsilon_\infty - \frac{\omega_p^2}{\omega^2 + \gamma^2} \tag{II-4}$$

$$\epsilon_2(\omega) = \frac{\omega_p^2 \gamma}{\omega(\omega^2 + \gamma^2)} \tag{II-5}$$

In which ϵ_∞ is the high frequency dielectric constant of the material, γ is the damping constant representing the scattering of the carriers, and ω_p is the bulk plasma oscillation frequency associated with free carrier gas, as given in (II-6):

$$\omega_p = \sqrt{\frac{ne^2}{\varepsilon_0 m_e}} \tag{II-6}$$

Here, n, e, ϵ_0 and m_e represents the carrier density, the electron charge, the dielectric constant of the material and the effective carrier mass of the material, respectively.

Thus, using the Mie theory in combination with Drude-Lorentz model, the free carrier density can be related to LSPR frequency through the bulk plasma frequency, and thus we can deduce that:

$$\omega_{LSPR} = \sqrt{\frac{ne^2}{\varepsilon_0 m_e(\varepsilon_\infty + 2\varepsilon_M)} - \gamma^2} \tag{II-7}$$

Although simplistic, this model has been proved effective when predicting and modeling the behavior of both metal and semiconductor LSPR.

II.3.1.2 Absorption energy as a function of doping magnitude

The doping magnitude of the nanocrystals is directly related to the nature and energy of infrared absorption. As summarized in Figure II.17, in highly doped materials (typically with a carrier density above 10^{19} cm^{-3}) such as metals and degenerately doped semiconductors, collective LSPR dominates the absorption, while in the marginally doped nanocrystals (carrier density below 10^{19} cm^{-3}), the infrared absorption is obtained by intraband transition. However, the LSPR of metal nanocrystals are limited to the visible and near infrared owing to their high electron density (10^{22}-10^{23} cm^{-3})[120] determined by their metallic nature. On the other hand, for the marginally doped nanocrystals such as Ag$_2$Se[123], HgSe[56] and HgTe[65] nanocrystals, their doping is induced by the surface effects and hard to control. Degenerately doped nanocrystals is advantageous in the sense that by tuning the doping, the carrier density can be tuned over orders of magnitude (10^{18} -10^{21} cm^{-3})[120], leading to LSPR absorptions from near infrared to THz and motivate more application potentials.
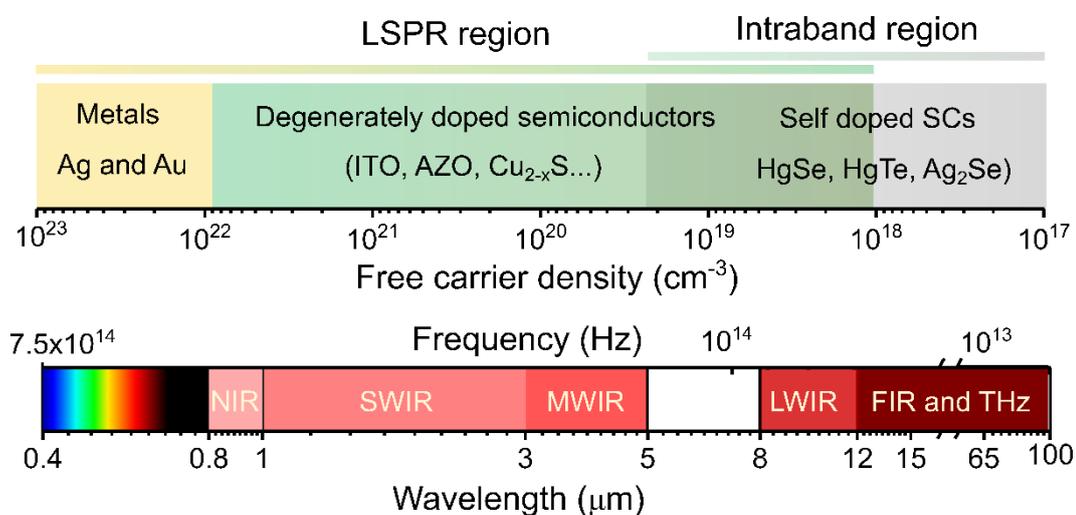
Figure II.17 The relation between the absorption spectra and the doping magnitude. The lower panel shows a spectrum from visible to THz, and the upper panel indicates the corresponding carrier density required for such absorptions, either in the form of LSPR when the materials are highly doped or in the form of intraband transition when the material is in a confined regime with margin doping.

II.3.2 Synthesis and optical properties of ITO nanocrystals

The synthesis route of metal oxides is typically based on the alcoholysis of the metal carboxylates precursors which generate metal hydroxide and eventually condense to form the metal oxide at high temperature accompanied by loss of water[120]. A successful incorporation of aliovalent dopants relies on a balanced reactivity between the host and dopant metal precursors. The ITO nanocrystals have achieved the best doping control among the doped metal oxides class, not only owing to the good compatibility between In and Sn metal carboxylates but also benefiting from the continuous injection of the precursors.[104]

II.3.2.1 Synthesis and characterization of ITO nanocrystals

In this study, the ITO nanocrystals are synthesized with a two-step slow-injection method established by Jansons et al.[104] with minor modifications. Typically, in a three-neck flask, 5 mmol of metal acetates comprising of indium acetate and tin (IV) acetate with a desired ratio, is mixed in 10 mL of oleic acid. The mixture is heated at 150 °C under Ar until all the powders are fully dissolved. The obtained metal oleate solution (0.5 M) is light yellow in color. In another flask, 13 mL of oleyl alcohol is heated to 305 °C under Ar. Then 1 mL of the as-prepared metal oleate

solution is injected to the oleyl alcohol bath at a rate of 0.2 mL/min using a syringe-pump. After the injection, the reaction is heated at the same temperature under Ar for 20 min before being cooled down. The nanocrystals are precipitated with ethanol and redispersed in chloroform for 3 times and finally dispersed in chloroform for storage. The nominal doping of Sn in nanocrystal is determined by the Sn/(In+Sn) ratio in the mixed oleate precursor. A scheme of the colloidally synthesized ITO nanoparticle is shown in Figure II.18 a, which indicates that some In^{3+} sites are replaced by Sn^{4+}.

In this manner, I synthesized a series of ITO nanocrystals with nominal doping from 0% (In_2O_3) to 15% of Sn. As shown in Figure II.18 b, the solution of the nanocrystals switches from colorless for undoped In_2O_3 to blue for 10 % Sn doped nanocrystals. The nanocrystals are of similar size (≈12 nm) with a truncated cube shape for all doping levels, as revealed by TEM image in Figure II.18 c. The X-ray diffraction pattens in Figure II.18 d demonstrates that all the nanocrystals are of bixbyite crystal structure of In_2O_3.
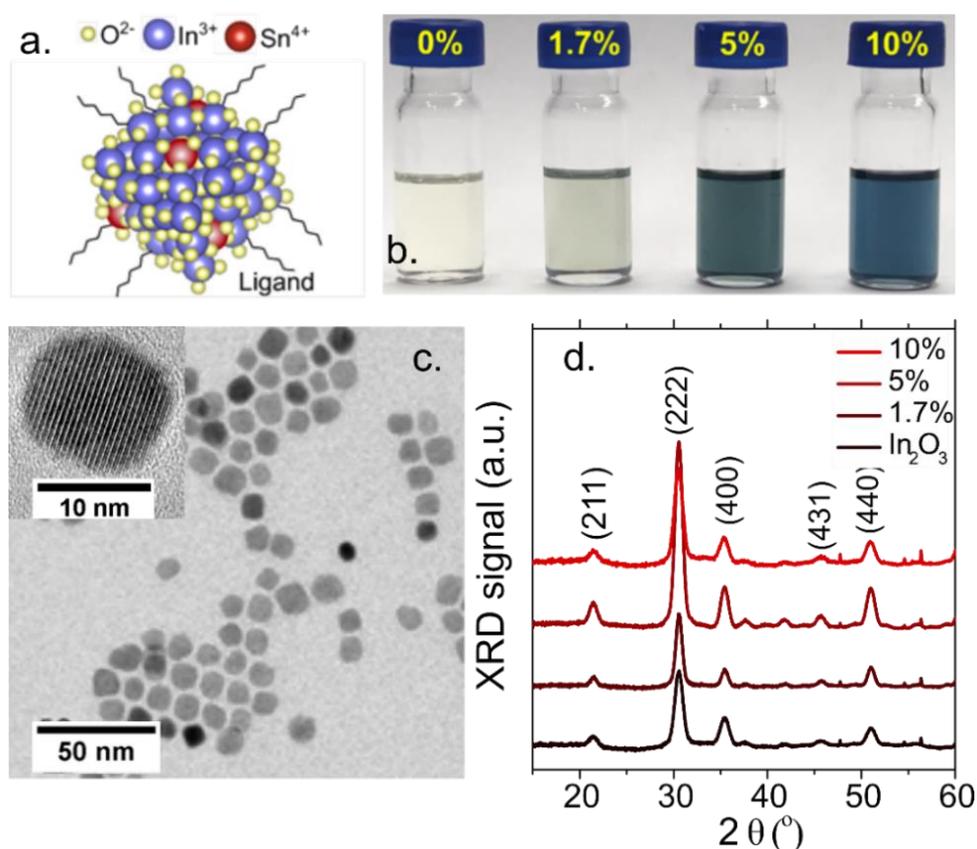
Figure II.18 (a) Scheme of a colloidal ITO nanocrystal with an ITO core surrounded by organic ligands. (b) Image of ITO nanocrystals dispersed in $CHCl_3$ with various levels of Sn content. (c) TEM image of the 1.7% Sn ITO nanocrystals. In the inset is a corresponding high-resolution TEM image. (d) XRD patterns of the synthesized ITO nanocrystals of different doping levels showing an identical bixbyite structure.

II.3.2.2 Optical properties of ITO nanocrystals

From the full-range absorption spectra presented in Figure II.19 a, we can see that all the ITO nanocrystals show a band edge absorption in the UV range and an absorption peak in the infrared, and both of the transitions blueshift with the increase of Sn content. The increase of optical band gap with more Sn dopants is a Burstein-Moss shift[124,125], due to the filling of conduction states and the bleaching of bandgap absorption. The infrared peaks span from 9.3 μm (≈148 meV) for the In_2O_3 nanocrystals, commonly believed to be LSPR raised by excessed

electrons resulted from oxygen vacancies,[126] to 2 µm (≈614 meV) for the 10% Sn doped ITO nanocrystals, see Figure II.19 a. However, when the Sn content is above 10%, the infrared transition barely blueshifts but strongly broadens, possibly due to the increased electron-electron scattering[127], ionized impurities scattering, strain induced scattering[120] and reduced size control. Such broadening can be balanced by the introduction of Cr as co-dopant agent[128]. To the interest of mid-infrared photodetection, I will focus on undoped (In_2O_3), 1.7% Sn and 10% Sn doped ITO nanocrystals which locate in the long-wave infrared (LWIR, 8–12 µm), mid-wave infrared (MWIR, 3–5 µm) and shortwave infrared (SWIR, 1–2.5 µm), respectively.
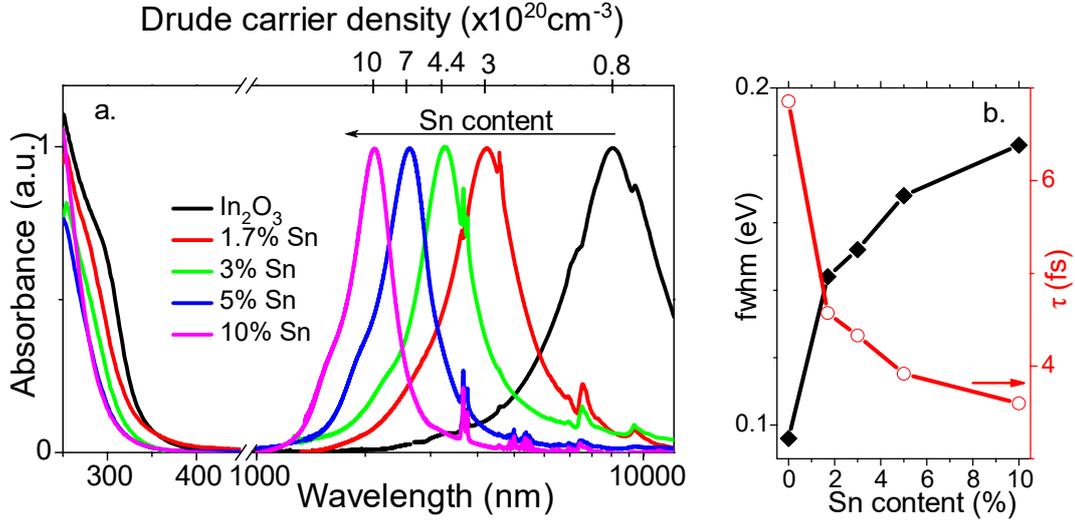
Figure II.19 (a) Infrared and UV-visible spectra of ITO nanocrystals with various levels of Sn doping. The estimated carrier density based on Drude model is indicated on the top. (b) Full width at half maximum (fwhm) of the infrared absorption peak and the estimated average electron scattering time τ ($\hbar/fwhm$) as a function of the Sn content.

Assuming all the infrared peak of the nanocrystals with different Sn doping as LSPR, their free electron density can thus be extracted with the Drude-Lorentz model, as introduced in (II-8):

$$n = \frac{\varepsilon_0 m_e (\varepsilon_\infty + 2\varepsilon_M)(\omega_{LSPR}^2 + \gamma^2)}{e^2}$$

(II-8)

Here in the case of ITO nanocrystals, $m_e = 0.4\, m_0$ is taken as the effective mass of free electrons with m_0 the electron rest mass, $\varepsilon_\infty = 4$ is taken as the high frequency dielectric constant, $\varepsilon_M \approx 2$ is taken as the dielectric constant of the environment in a form of film, and the plasmon damping constant γ are taken from the fwhm of the plasmonic peak.

Using the Drude model, we thus determine the carrier density of the nanocrystals to be in the 10^{20}-10^{21} cm^{-3} range, as indicated in Figure II.19 a, which corresponds to 80 free charges per In_2O_3 nanocrystal, 250 free charges per 1.7% Sn ITO nanocrystal, and almost ≈1000 free charges in the case of the 10% doped ITO nanocrystals, as shown in Figure II.20 b.

Another information that can be extracted from the infrared LSPR absorption is the average electron scattering time τ, which can be estimated by $\gamma = \hbar/\tau$, with $\hbar$ the reduced Planck constant. The value of τ has been estimated to be ≈ 5±1 fs for all the doped ITO nanocrystals, see Figure II.19 b. The parameter of τ is important to estimate the photogenerated change of carrier density, as we will discuss later.

II.3.2.3 Determination of the absorption cross-section of ITO nanocrystals

The large cross-section of LSPR materials has attracted interest for applications such as photothermal therapy[129] and perfect IR absorbers[130]. However, there is no value of the

absorption cross section for ITO nanocrystals reported before. Since photo absorption is an important factor for photodetection, we for the first time obtained the absorption cross-section by measuring the absorption coefficient of ITO nanocrystal arrays. Knowing the value of absorption, A, the corresponding film thickness t, and the volume fraction f (0.64 for a randomly close-packed film), the absorption coefficient α can be calculated with (II-9):

$$\alpha = \frac{A \ln 10}{t \cdot f} \tag{II-9}$$
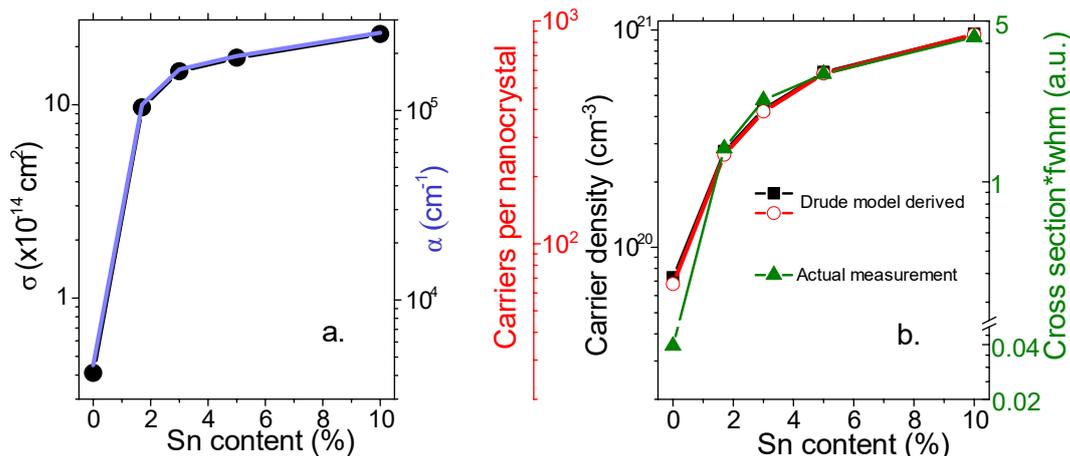
Figure II.20 (a) The measured absorption coefficient α and the corresponding absorption cross section σ as a function of Sn content.(b)The estimated carrier density and the number of carriers per nanocrystal from Dude model, in comparison with the production of and LSPR fwhm and absorption cross section, as a function of Sn content.

The cross-section per nanocrystal can thus be obtained by multiplying the absorption coefficient by the nanoparticle volume, assuming that all the nanocrystals are spheres with a diameter of 12 nm. As presented in Figure II.20 a, doped nanocrystals show a cross-section, at the infrared peak energy, in the range of $1\text{-}3\times10^{-13}$ cm^2, which corresponds to an absorption coefficient from 1×10^5 to 3×10^5 cm^{-1}. While the cross-section increases quasi linearly with Sn content for doped nanocrystals, the undoped In$_2$O$_3$ nanocrystals present a weaker absorption by almost 2 orders of magnitude, with a cross-section of 4×10^{-15} cm^2 (see Figure II.20 a), closer to that of interband and intraband transitions than LSPR[121].

Table II-1 Energy of the infrared absorption peak, estimated number of charges in each nanocrystal based on Drude model and the absorption cross-section associated with the infrared transition for three differntly doped nanocrystals.

Sn content (%)	Infrared peak energy (meV)	Estimated carriers per nanocrystals with Drude model	Infrared absorption cross section ($\times10^{-15}$ cm^2) from measurement
0	148 (8.3 μm)	80	4
1.7	315 (3.95 μm)	250	90
10	614 (2 μm)	900	220

In particular, we notice that the product of the cross section and the infrared peak linewidth, which indicates the actual free carrier density, follows the trend of estimated carrier density in the case of the doped ITO nanocrystals, but the value for undoped In_2O_3 nanocrystal is at least one order of magnitude lower than the Drude estimation, see Figure II.20 b. In other words, the Drude model overestimate the carrier density in the case of In_2O_3 nanocrystals.

To summarize, by measuring the absorption cross-section of ITO nanocrystals with different Sn content, we deduced that the carrier density of doped nanocrystals can be well described by Drude model, while the carrier density is largely overestimated in the case of undoped In_2O_3 nanocrystals. The absorption cross-section of In_2O_3 nanocrystals being in the range of 10^{-15} cm² indicates that its infrared absorption is likely an intraband transition instead of LSPR, and this speculation will be further supported by the transport measurements in the following study.

II.3.3   Transport properties of ITO nanocrystals

The transport properties of ITO nanocrystals are probed in a photoconductive device. The ITO nanocrystals are coated on an Au electrode with a channel width of 100 μm. To ensure a strong interparticle coupling in the film, a ligand exchange step is required. However, the hard-base nature of In^{3+} leads to a poor affinity for thiols and amines, which have been extensively used for Cd, Hg and Pb based nanocrystals. Here we choose a hard acid, according to Pearson's hard soft acid base (HSAB) theory, such as acetic acid to replace the initial oleic acid ligands of the ITO nanocrystals[131].

II.3.3.1   FET characteristics of ITO nanocrystals

The transport properties of ITO nanocrystal arrays are probed with FET configuration. As schemed in the inset of Figure II.21 a, the FET configuration is based on a photoconductive device with an electrolyte gating. The electrolyte, made by dissolving $LiClO_4$ in a polyethylene glycol matrix, ensures a large gate capacitance, which is critical to modulate the current density of heavily doped materials. In addition, the electrolyte can diffuse though the thickness direction of nanocrystals, which allow for the gating of thick films.
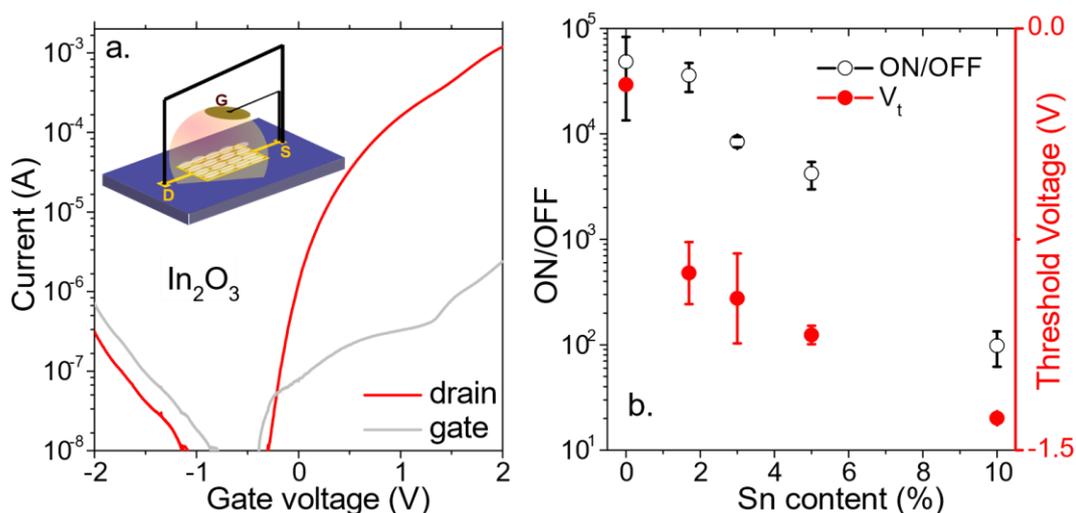
Figure II.21 (a) Transfer curve (drain and gate current as a function of the applied gate voltage) for a transistor whose channel is made of In_2O_3 nanocrystals. In the inset is a scheme of an electrolyte gated transistor. (b) ON/OFF ratio and threshold voltage as a function of Sn content for transistors made of ITO nanocrystals.

From the FET measurement, see Figure II.21 a the transfer curve of In_2O_3 thin film as an example, there is only n-type conduction observed with a rise of conductance upon the injection electrons

(under positive gate bias), while there is no sign of hole conductance. The ITO nanocrystals presents a similar n-type only conductance, which is consistent with previous reported Hall effect[132] and thermoelectric measurements[133]. However, there is a clear decrease of current modulation (ON/OFF ratio) and a shift of threshold voltage (V_t) toward negative bias with the increase of doping, as shown in Figure II.21 b., both of which can be explained by a deeper Fermi level within the conducion band induced by a higher level of doping.

II.3.3.2 Low temperature transport of ITO nanocrystals

To understand the hopping of carriers in ITO nanocrystal films, the current as a function of temperature under a constant bias is measured. Around room temperature, the transport of the ITO nanocrystal arrays is thermally activated. By fitting the I-T curve near room temperature with Arrhenius function, the activation energy can be extracted. In the case of In_2O_3, an activation energy of almost 100 meV is obtained, while for doped ITO samples the value is 30±5 meV, independent of the doping level, see the inset Figure II.22.

The clear difference of thermal activation energy between In_2O_3 nanocrystals and doped ITO nanocrystals could be raised by different hopping mechanisms. Hopping transport[134–136] is characterized by different behaviors of semiconductors and metals. In semiconductor materials at a low temperature, the channel of variable-range hopping (VRH) prevails[137,138] and the hopping is described using Mott model, which indicates that the transfer of carriers from one particle to another is limited by the availability of the empty arrival state. Thus, the activation energy reflects the density of states of the nanocrystals[56,139]. If the states are sparse, fairly large value of activation energy can be obtained, as is the case for undoped In_2O_3 nanocrystals. On the other hand, for the transport in metal and strongly doped nanocrystals, the density of states is no longer a limit and only the coulombic charging energy (E_C) has to be overcome.[140] The latter can be evaluated by $E_C = \frac{e^2}{2C}$, with C the self-capacitance of the nanocrystal and e the electron charge. Here, C can be estimated from $C = 2\pi\varepsilon_0\varepsilon_r d$, with ε_0 the vacuum permittivity, ε_r the material dielectric constant (4 for ITO nanocrystals) and d the nanoparticle diameter (12 nm), leading to a E_C of 29 meV for ITO nanocrystals, which perfectly coincide the value of measured activation energy. As a result, the characteristic energy of the hopping transport in the array of degenerately doped semiconductors is the same as for metallic nanoparticles.[140]
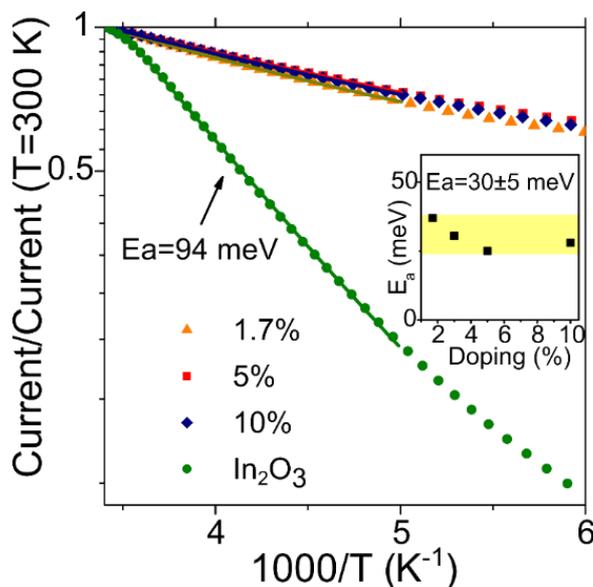
Figure II.22. Current as a function of temperature for ITO nanocrystal arrays with various Sn contents. The inset provides the activation energy for doped ITO nanocrystals extracted from Arrhenius fit of the high temperature part of the I-T curve.

From the transport point of view, In_2O_3 nanocrystals show distinct properties from doped ITO nanocrystals such as higher ON/OFF ratio, less negative threshold voltage and higher thermal acvitation energy, all of which are likely induced by a much lower doping magnitude and sparser density of states of In_2O_3 than ITO nanocrystals. The observations above, in combination with a two magnitude lower absorption cross section of In_2O_3 nanocrystals than that of ITO nanocrystals, again indicate that the infrared absorption feature of In_2O_3 nanocrystals is rather a result of intraband transition than LSPR.

II.3.4 Photoconductance in ITO nanocrystal films

While dark conduction in ITO nanocrystal film has already been intensively explored,[134,141,142] their photoconductive properties remain unrevealed. Herein, we choose three kinds of thin films made of nondoped In_2O_3 nanocrystals and ITO nanocrystals with 1.7% Sn and 10% Sn, presenting an infrared absorption peak in the range of LWIR (8-12 μm), MWIR (3-5 μm) and SWIR (1-3 μm), respectively. Four light sources are used to excite the different part of their spectra. As indicated in Figure II.23, a UV lamp is used to excite the band edges of the three samples, a 1.55 μm laser diode and a 4.4 μm QCL are used to excite the infrared LSPR of ITO nanocrystals with 10% Sn and 1.7% of Sn, respectively, and a black body at 980 °C is used as a broadband light source to excite the intraband transition of In_2O_3 nanocrystals.
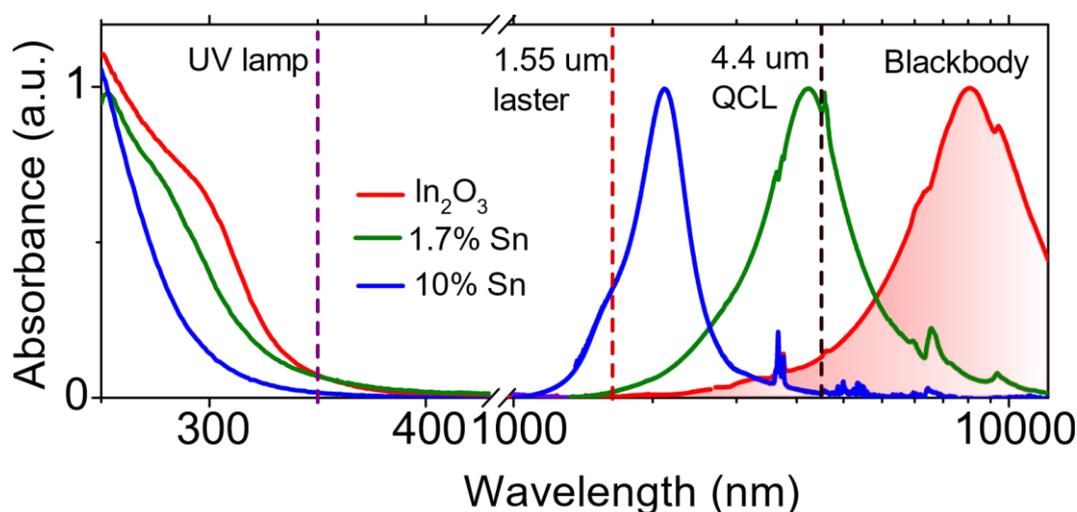
Figure II.23 The UV-Vis and FTIR spectra of ITO nanocrystals with different Sn content. A UV lamp (purple dash line) is used to excite the band edges of the three different nanocrystal arrays, a 1.55 μm laser diode (red dash line) and a 4.4 μm QCL (black dash line)are used to excite the LSPR of ITO nanocrystals with 10% Sn and 1.7% Sn, respectively, and a black body at 980 °C (red area under the infrared peak of In_2O_3 nanocrystals) is used as a broad band light source to excite the intraband transition of In_2O_3 nanocrystals.

II.3.4.1 Proposition of band structures for ITO nanocrystals

With a tauc-plot of UV-Vis spectra, the optical bandgap (the energy between the valence band the top of the conduction band) of ITO nanocrystals can be determined[131]. As shown in Figure II.24 a, with the increase of Sn content, the optical bandgap, as indicated by the intersection of dotted line with X axis, has increased from 3.75 eV for In_2O_3 nanocrystals to 4.3 eV for 10% Sn doped ITO nanocrystals, which is typically a Burstein-Moss shift induced by the bleached exciton with doping. Thus in Figure II.24 b we can propose a band diagram of three ITO nanocrystals, showing that the In_2O_3 nanocrystals has an intraband transition with an energy of

148 meV, while the doped ITO nanocrystals have a densely populated conduction band. Along with a widening effect of optically observed bandgap with the increase of doping, the real band gap is expected to narrow with a upward shift of valence band and downward shift of conduction band as a result of electron-electron and electron-impurity scattering[126,141], and these shifts are presented qualitatively in the band diagram. Figure II.24 b again indicates the four light sources used to excite the transitions of the ITO nanocrystals: UV is used to excite the band edges of the nanocrystals, while blackbody working at 982°C with a broad band infrared emission, 4.4 μm quantum cascade laser and 1.5 μm laser diodes are used to excite the infrared transition of In_2O_3, 1.7% Sn and 10 % Sn doped ITO nanocrystals, respectively.
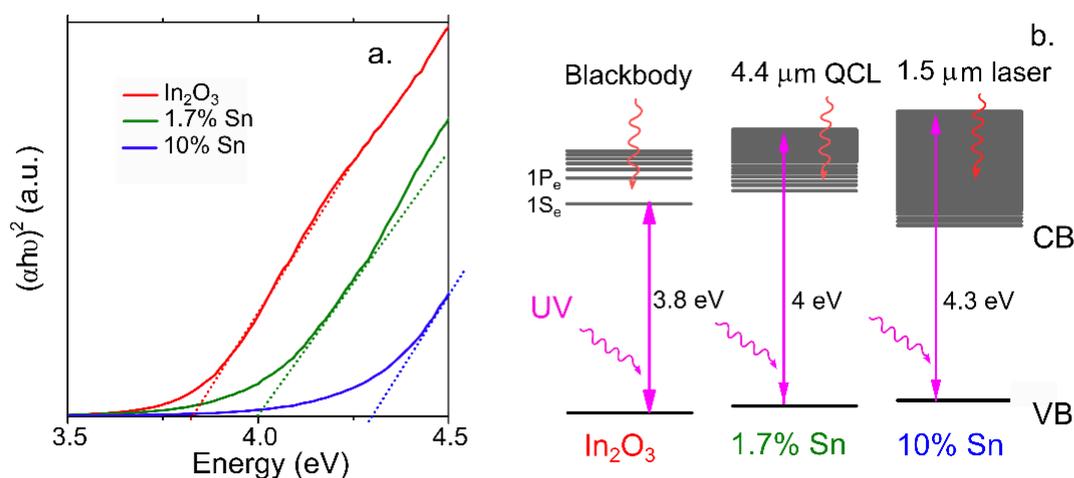
Figure II.24 (a) Tauc-plot of UV-Vis spectra of ITO nanocrystals, with the intersection of the liner region with x-axis as the optical bandgap. (b) Band diagram of undoped In_2O_3, 1.7% Sn and 10 % Sn doped ITO nanocrystals. UV is used to excite the band edges of the nanocrystals, while blackbody, 4.4 μm quantum cascade laser and 1.5 μm laser diodes are used to excite the infrared transition of In_2O_3, LSPR transition of 1.7% Sn and 10 % Sn doped ITO nanocrystals.

II.3.4.2   Photoconductance of ITO nanocrystals under UV

Under UV excitation, a large current modulation is observed, especially for In_2O_3 nanocrystals, which presents an increase of conductance by four orders of magnitude under UV illumination, see Figure II.25 a. A striking feature relative to the excitation of the band edge is the slow response of the photocurrent, see Figure II.25 b. The decay time can be 1h, which signifies that the deep traps are involved in the photoconductive process. Similar memory effect has been observed for ZnO nanoparticles[143,144] which has been used as a strategy to activate the conduction of electron transport layer[145] in a solar cell device. The magnitude of the photo/dark current tends to decrease while the Sn content is increased. The undoped nanocrystals present an almost 3 orders of magnitudes larger modulation than that of all the doped ITO nanocrystals (see Figure II.25 c). The huge difference of light modulation can be ascribed to a much lower dark current in In_2O_3 nanocrystal arrays, which is consistent with the previous result that In_2O_3 nanocrystals showed a carrier density more than 1 magnitude lower than the doped ones. As a result, the low dark current of In_2O_3 nanocrystal film again support the claim that there are no LSPR occurred in the In_2O_3 nanocrystals but intraband transition.

As proposed in the case of self-doped HgS quantum dots[146] and doped ZnO nanocrystals[147], there is an evolution from single-electron intraband transition mode to a collective surface plasmon mode with the increase of doping. In the case of ITO, the threshold of these two regimes corresponds to a carrier density below 100 electrons /particle ($\approx 10^{20}$cm^{-3}).
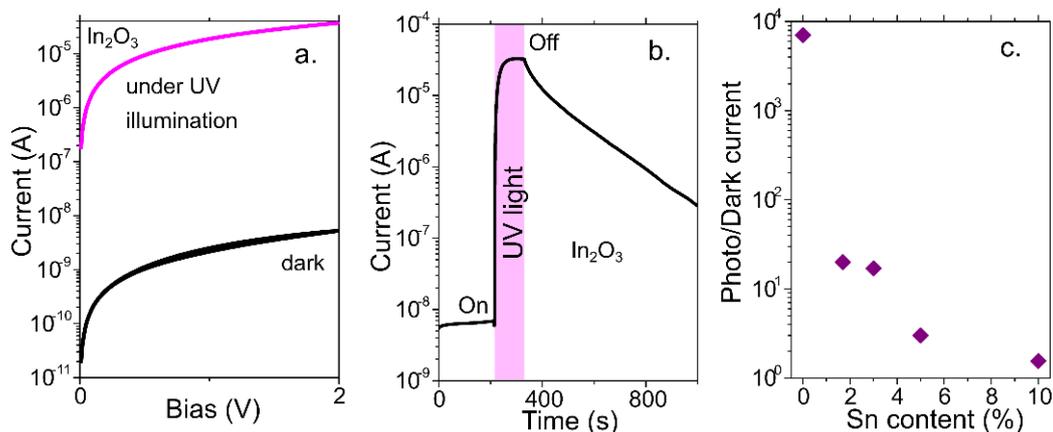
Figure II.25 (a) I-V curve of In_2O_3 nanoparticles under dark condition and under UV illumination. (b) Current as a function of time while a thin film In_2O_3 nanoparticle is exposed to a pulse of UV light. (c) Current modulation (ratio of the photocurrent over the dark current) as function of the Sn content of an ITO thin film exposed to a short illumination of UV light.

II.3.4.3 Photoconductance of ITO nanocrystals under infrared

To probe the potential of ITO nanocrystals for infrared detection, which is the ultimate goal of this study, we use three different ITO nanocrystals to target mid-infrared detection according to three atmospheric transparent windows, with In_2O_3 nanocrystals for LWIR using black body (980 °C) as broad band infrared source, 1.7% Sn ITO nanocrystals for MWIR using 4.4 μm QCL and 10% Sn ITO for SWIR using 1.55 μm laser diode, as already introduced in Figure II.23 and Figure II.24 b.

To suppress the thermally activated carriers and in turn the dark current, the samples are cooled down, see Figure II.26 a, d and g. Under infrared illumination, a responsivity of 40 μA/W is achieved by the film of In_2O_3 nanocrystals in the LWIR range (see Figure II.26 b), 4 μA/W by the 1.7% Sn ITO nanocrystals in the MWIR range at 4.4 μm (see Figure II.26 e) and 14 μA/W by the 10 % Sn ITO nanocrystals at SWIR at 1.55 μm (see Figure II.26 h).

The performances are relatively weak compared with that of HgTe nanocrystals with interband transition, in which case responsivity in the 1 A/W has been achieved in the MWIR[148], with more complex and favorable structures. In a photodiode structure, HgSe nanocrystals has been demonstrated a responsivity of 5 mA/W using intraband transition in the MWIR[76]. On the other hand, for other Hg-free material such as Ag_2Se nanocrystal, which present intraband absorption around 4.5 μm, the performance is still limited, with the highest responsivity reported at 350 μA/W.[92] The active materials, working wavelength, device structures as well as the responsivity of the state-of-the-art MWIR nanocrystals photodetectors are compared in Table II-2.
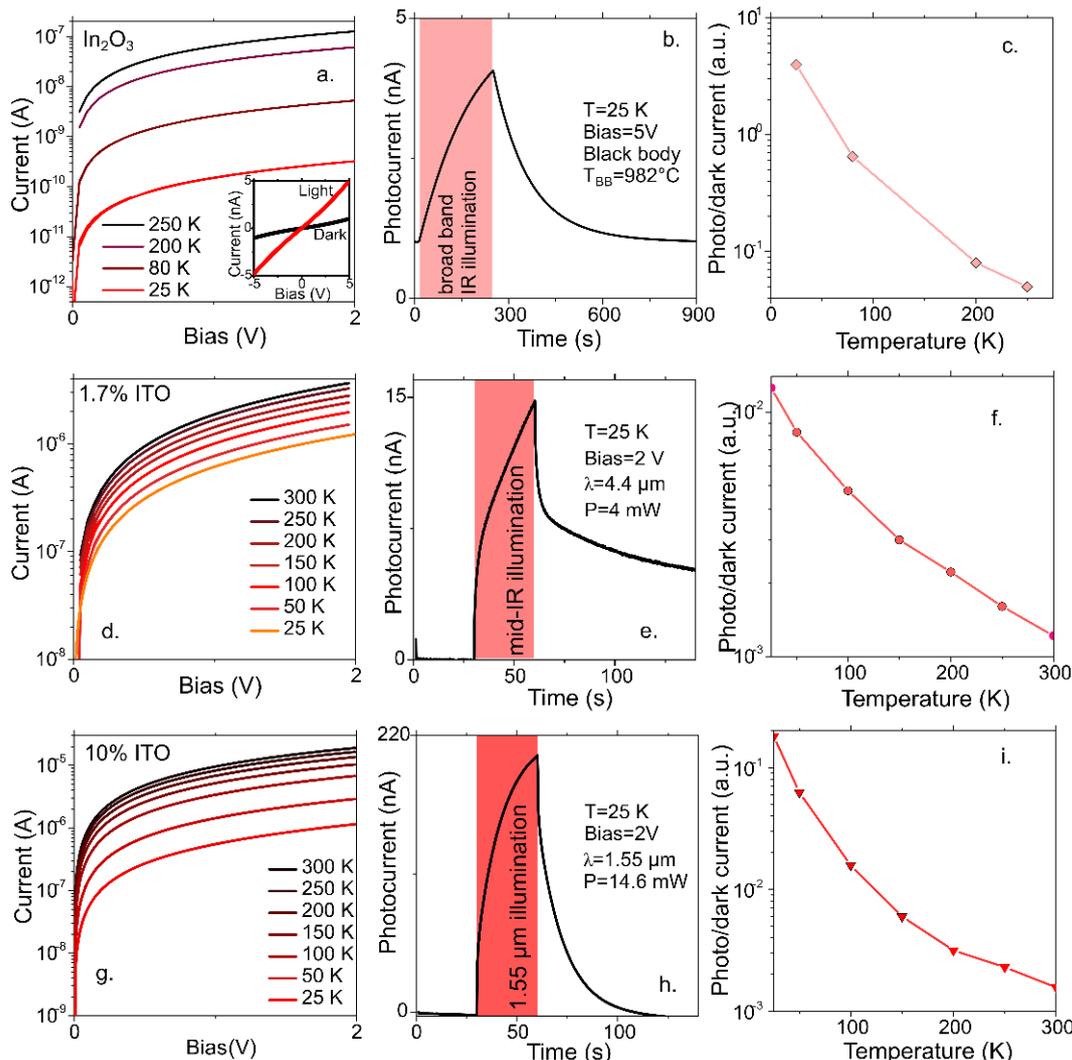
Figure II.26 I-V curves of a thin film of (a) In_2O_3, (d) 1.7% Sn ITO and (g) 10% Sn ITO nanocrystals at various temperatures ranging from room temperature to 25 K. The inset in (a) is the I-V curves at 25 K under dark condition and under illumination by a blackbody source (T=982°C). Current as a function of time of a thin film of (b) In_2O_3, (e) 1.7% Sn ITO and (h) 10% Sn ITO nanocrystals which exposed to a pulse illumination by (b) a blackbody source, (e) a quantum cascade laser operating at 4.4 µm and (h) a 1.55µm laser diode. Ratio of the photocurrent over the dark current as a function of the temperature for a thin film of (c) In_2O_3 nanocrystals exposed to the excitation from a blackbody source, (f) 1.7% Sn ITO nanocrystals exposed to the excitation from a 4.4 µm QCL and (i) 10 % Sn ITO nanocrystals exposed to the excitation from a 1.55 µm laser diode.

Regarding the time response, the In_2O_3 nanocrystals is dramatically slow with turn-on and turn-off time close to 10 min (see Figure II.26 b). All doped nanoparticles have a similar time response, with a turn-on time above 10 s and a turn-off time of ≈1 min (see Figure II.26 e and h). Even if their dynamics are shorter than the photoconductive dynamics at the band edge, they remain extremely slow compared with other infrared active colloidal materials in the same range of wavelengths. For example, with HgTe quantum dots, time response shorter than the µs are commonly reported.[149,150] This long-time response suggests that the current modulation results from a bolometric effect, instead of a change of carrier density.

Table II-2 State-of-the-art nanocrystal based MWIR photodetectors

Active material	Wavelength (µm)	Device structure	Responsivity (mA/W)
HgTe[151]	3.5	HgTe/As$_2$S$_3$ phototransistor	100
HgTe[148]	4~5	ITO/HgTe QD/Ag$_2$Te/Au	1000
HgSe[152]	4.4	Al/p-HgTe/HgSe+HgTe/Au	5
Ag$_2$Se[92]	4.5	Photoconductive	0.35
Ag$_2$Se	4.5	Ag/Ag2Se/PbS/Ag2Se/ Ag	13.3
1.7% Sn ITO[123]	4	Photoconductive	0.004

This conclusion of bolometric photoresponse of ITO nanocrystal arrays can also be further rationalized. Knowing the values of the cross-section (σ) and photocarrier lifetime (τ), we can estimate the photogenerated change of carrier density under illumination to be[153] $\Delta n = e\sigma\tau\Phi/E_{ph}$ with e the proton charge, Φ the power flux per unit area and E_{ph} the photon energy. In the case of the 1.7% Sn ITO nanocrystals ($\sigma \approx 10^{-13} cm^2$; $\tau \approx 5 fs$) and with the illumination condition used in Figure II.26 e ($E_{ph} = 0.28\ eV$), the light induced change of carrier density is $\approx 5 \times 10^{-9}$ electron/particle, which greatly contrasts the steady doping of 200 electron /particle. Since the photocurrent and dark current is respectively proportional to the photogenerated carrier and steady doping, the photo/dark current is thus expected to be very low. Experimentally, the light to dark modulation is nevertheless higher (in the 10^{-3} to 10 range) than this ratio, see Figure II.26 c, f and i, which confirms that the bolometric origin is prevailing.

Regarding the operating temperature of such films, the photocurrent remains a marginal modulation compared with the dark current, see Figure II.26 c, f and i. Only the undoped In$_2$O$_3$ nanocrystals achieve BLIP (background limited performances, defined here as the temperature when dark current becomes smaller than the photocurrent) operation at T<50 K, see Figure II.26 c. This is a result of the large doping, which is required to achieve plasmonic absorption but comes at the price of a large dark current.

II.3.5   Conclusions and perspectives

In this chapter, to take advantage of their easy doping mechanism and strong absorption, we use ITO nanocrystals as a platform to probe the potential of LSPR for infrared photoreaction.

We first synthesized a series of ITO nanocrystals with continuously tunable infrared absorption from LWIR to SWIR with a Sn content from 0% to 10%. During the quantification of their absorption cross-section, we find that the absorption cross-section is in the range of 10^{-13} cm^2 for the doped ITO nanocrystals, while the value for In$_2$O$_3$ nanocrystals is more than 1 magnitude lower, i.e., in the range of 10^{-15} cm^2, suggesting that the LWIR absorption of In$_2$O$_3$ nanocrystals is rather a single electron transition than a collective plasmonic resonance induced by doubly ionized oxygen vacancy. This claim is further evidenced by transport measurements, with In$_2$O$_3$ nanocrystals showing higher thermal activation energy (100 meV), higher on/off ratio and lower dark current than those of the ITO nanocrystal films.

This intraband transition of In$_2$O$_3$ nanocrystals is transformed into a plasmonic feature as Sn doping is introduced. There are several significant consequences to this observation beyond the obvious facts that undoped In$_2$O$_3$ nanoparticles have lower conductivity and weaker absorption.

Because the transition in In_2O_3 is determined by the semiconductor density of states, the energy of this transition will be only marginally tunable through doping. Reducing the doping and even the residual material non-stoichiometry will not allow for the redshift of the transition toward wavelengths longer than 9 µm. This may be a limitation for detection application in the low energy part of the 8-12 µm atmospheric transparency window. Secondly, if the tunability of intraband transition of In_2O_3 nanocrystals needs to be investigated, alternative paths such as change of confinement or material alloying need to be considered.

We probe the photoconductance of the ITO nanocrystals by exciting them at different part of the band diagram. A UV source is used to excite the interband of the ITO nanocrystal arrays, a 1.55 µm laser diode and a 4.4 µm QCL are used to excite the LSPR of ITO nanocrystals with 10% Sn and 1.7% Sn, respectively, and a black body at 980 °C is used as a broadband light source to excite the intraband transition of In_2O_3 nanocrystals. Under UV illumination, In_2O_3 nanocrystals showed 3 orders of magnitude higher current modulation than the ITO nanocrystals because of lower dark current. For the photo response under infrared illumination of different wavelengths, the responsivity is in the µA/W magnitude, which is extremely low compared to the responsivity of 1A/W for a HgTe nanocrystal-based device in the MWIR. On the other hand, the photoresponse is extremely low, with a rise time of several seconds and a fall time of 1 min, strongly suggesting that the photo response is a result of bolometric effect.

The bolometric photoresponse is supported by the negligibly low photo-excited carrier density with respect to the steady state doping of the ITO nanocrystals, which suggests that the benefit of a stronger absorption brought by the LSPR is strongly balanced by the short lifetime of the photocarrier. Thus, to take full benefit of the large plasmonic absorption, a fast extraction of the hot electrons will have to be implemented. A possible strategy to reach this goal will be to reduce the device size down to the nanometer scale, which will be valuable to apply large electric field and reduce the carrier transit time.

Part III Nanocrystal-based LEDs and their applications

Related publiactions:

1. **J. Qu**, P. Rastogi, C. Gréboval, C. Livache, M. Dufour, A. Chu, S.-S. Chee, J. Ramade, X. Z. Xu, S. Ithurria, and E. Lhuillier, *Nanoplatelet-Based Light-Emitting Diode and Its Use in All-Nanocrystal LiFi-like Communication*, ACS Appl. Mater. Interfaces 12, 22058 (2020).

2. **J. Qu**, P. Rastogi, C. Gréboval, D. Lagarde, A. Chu, C. Dabard, A. Khalili, H. Cruguel, C. Robert, X. Z. Xu, S. Ithurria, M. G. Silly, S. Ferré, X. Marie, and E. Lhuillier, *Electroluminescence from HgTe Nanocrystals and Its Use for Active Imaging*, Nano Lett. 20, 6185 (2020).

3. M. Dufour, **J. Qu**, C. Greboval, C. Méthivier, E. Lhuillier, and S. Ithurria, *Halide Ligands To Release Strain in Cadmium Chalcogenide Nanoplatelets and Achieve High Brightness*, ACS Nano 13, 5326 (2019).

4. Y. Prado, **J. Qu**, C. Gréboval, C. Dabard, P. Rastogi, A. Chu, A. Khalili, X. Z. Xu, C. Delerue, S. Ithurria, and E. Lhuillier, Seeded Growth of HgTe Nanocrystals for Shape Control and Their Use in Narrow Infrared Electroluminescence, Chem. Mater. 33, 2054 (2021).

III.1 Introduction to nanocrystal light emitters

The QD enhanced LCD (QD-LCD) TV produced by Samsung since 2014 has been the first mass market success of colloidal nanocrystals since its discovery more than two decades ago. The mature synthesis of nanocrystals with near-unity photoluminescence quantum yield (PLQY), superior photostability and highest color purity and tunability has made them the natural candidate emitters for the new generation of display. Meanwhile, in the infrared where easy-accessible, spectrally tunable, and multi-substrate-compatible light emission materials are lacking, the nanocrystal emitters also hold a promise.

In this introduction part, I will first introduce two main technologies for nanocrystals for display: as downconverter or as emitting layer in a light emitting diode (LED). Then I will advance to the use of nanocrystals for infrared light emitting diodes.

III.1.1 Colloidal nanocrystals for display with large gamut

Color gamut is defined as the range of colors that a particular device can produce or record. In the CIE (Commission Internationale de l'Éclairage)1931 color space (Figure III.1b), the triangle defined by the three primary colors that a display can provide is called its gamut, and all the colors inside the triangle can be produced by changing the relative intensity of the three primary colors. An ideal display is expected to deliver a picture with the same color as can be perceived by the human eye. In other words, the larger the color gamut, the more vivid the display.
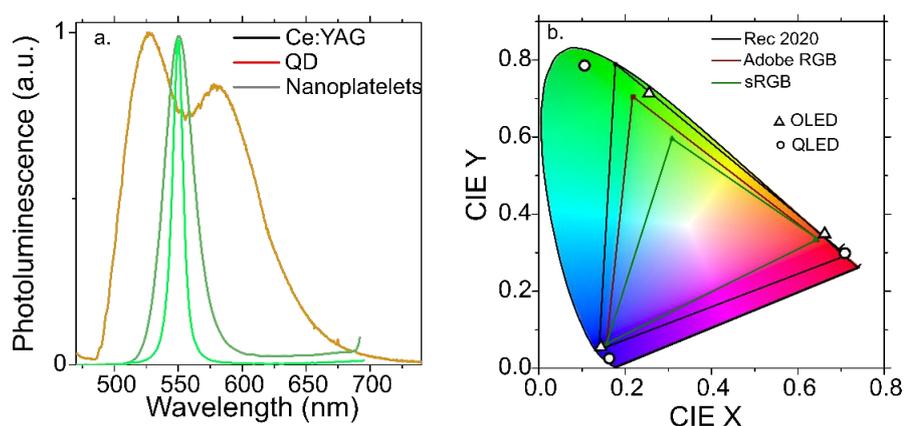
Figure III.1 PL spectra of traditional phosphor (Ce:YAG), QDs and NPLs, with nanocrystals showing much narrower linewidth. (b) CIE 1930 chromatograph of different display gamut and the gamut that can be achieved by organic LEDs and quantum dot LEDs.

With the advances of the display industry, there have been several standard gamuts for display, see Figure III.1b with different triangles representing different color gamuts. sRGB gamut is designed for cathode-ray tube (CRT) display, which has been replaced by liquid crystal display (LCD). Adobe RGB is mainly developed for standard printing. The most recent and challenging wide-color-gamut standard is Rec.2020 set for ultra-high-definition televisions (UHD TV), which requires extremely high color purity of the emitters with a linewidth below 10 nm, excluding the traditional phosphors from the competition. As shown in Figure III.1a, the emission spectra of traditional yellow phosphor (cerium-doped yttrium aluminum garnet, Ce: YAG) is much broader than the green quantum dots and green NPLs, indicating a much lower color purity. NPLs and QDs show near color-saturated emission, especially NPLs without an inhomogeneous broadening of linewidth, which is among very few candidates promising to be the building block to meet the latest standards. Figure III.1 b also labels the color gamut that

can be achieved by organic LED (OLED) and QD based LED (QD-LED), with QD-LED closer to the gamut of Rec 2020.

III.1.2 Nanocrystals as down converters for QD-LCD display

The present-day dominating display technique is still liquid crystal display (LCD). The traditional liquid crystal display (LCD) technology uses a backlight which transmits through a device stack containing polarizers, liquid crystals, and color filters. The backlight is usually a cold white light source made of the light from blue LED and a yellow phosphor (Ce:YAG), see its emission spectrum in Figure III.1 a. The latter is the most efficient and economical combination so far, but the pale white light from blue and yellow hues cannot express the natural colors of objects faithfully in general circumstances, and the low saturation of the phosphor made it mandatory to use color filters, which cause large energy losses and heating of the LCD stack.

Recently, as a step forward high color purity display, highly luminescent red and green QDs have been used to replace the traditional phosphors within a LCD architecture, see Figure III.2, while other layers of LCD remain the same as before. In this QD enhanced LCD display, the back blue LED is used as not only a highly saturated blue light source, but also to excite the green and red emissions from the QDs. The process of down-converting is schemed in the right of Figure III.2. The pure colors produced by QDs render a larger color gamut display with increased brightness than traditional phosphors. Also, as downconverters, the remarkable stability of nanocrystals has been demonstrated at working conditions, i.e., a high temperature above 100 °C and a high excitation flux of 1-5 W cm^{-2},[20] which is superior to that of organic chromophores.
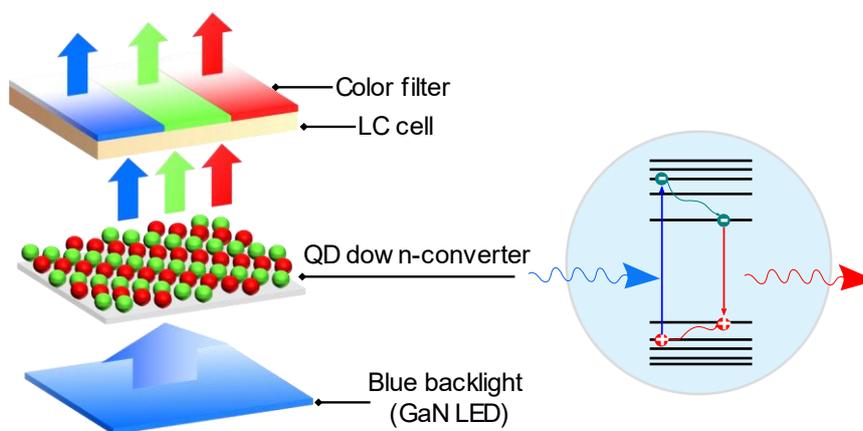
Figure III.2 Scheme of a QD-LCD with green and red nanocrystals as down converters. The back blue GaN is used as a blue light source and at the same time to excite the green and red emissions from quantum dots. The white light produced is then transmitted by the liquid crystal cells and then matched to the transmission bands of the color filters.

III.1.3 QLED for future display

The application of QD emitters for light-emitting diodes (LEDs) was first proposed by the group of Alivisatos[154] in 1994, and was demonstrated capable of electrically driven full-color QD-LED displays[155] by Kim et. al. in 2011. Until recently, the improved material chemistry of both emitting nanocrystals and charge transport materials, together with the advanced engineering of the LED structures, has brought the efficiency and the lifetime of the nanocrystal-based LEDs to a high

level. Especially, the development of solution-processed charge transport layers has enabled the all-solution fabrication of QLEDs, which leads to continuous and pinhole-free films.

The second part of my thesis is dedicated to the development of nanocrystal-based LEDs, in the visible and infrared. In the following part of the introduction, I will focus on the structure of nanocrystal-based LEDs, their advantage over LCDs and OLEDs when used for display and their limitations to address.

III.1.3.1 The structure of QD-LED

Figure III.3 a illustrates a typical QD-LED stack, in which the red QD emitting layer is sandwiched by charge transport layers (CTLs) which deliver electrons and holes injected from cathode and anode, respectively, to the emitting layer. A photon is produced when one electrically produced electron-hole pair radiatively recombine at the band edge of the QDs, and this process of light emission is called electroluminescence. The emission of the QD-LEDs is directly driven by the current flow through each pixel, which is controlled by a thin film transistor (TFT) back panel.
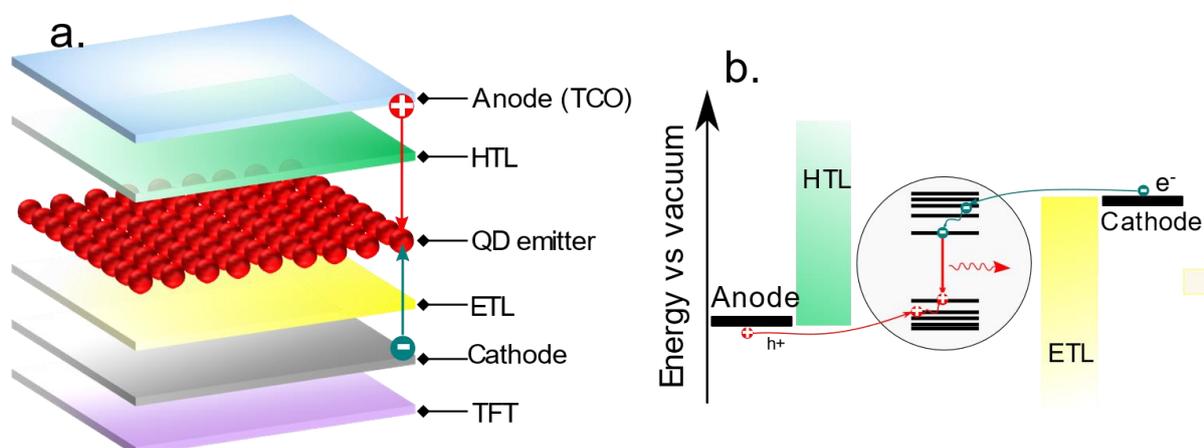
Figure III.3 (a) Scheme of a nanocrystal-based light emitting diode. The electrons and holes injected respectively from cathode and anode, are mediated by electron transport layers (ETL) and hole transport layers (HTL), and radiatively recombine with each other to give out electroluminescence with an energy of the nanocrystal band gap. For display, the subpixels are driven separately by a thin film transistor (TFT) and the photons emitted from each subpixel are directly driven by the electrons injected. (b) A preferential energy diagram of a nanocrystal-based light emitting diode.

To improve the efficiency, that is to produce more photons under a given electrical supply, the energy levels of all the device layers should be rationally engineered. Figure III.3b shows an idealized band alignment of a LED device, in which the energy levels of the charge transport layers not only facilitate the injection of one carrier, but at the same time, serving to block the opposite carrier to boost the recombination and avoid the leaking. The balance of the charge carrier injection to the QD emitting layer is another important issue for the efficiency and lifetime of the device, which will be discussed in detail later in this part.

QLED in comparison with QD-LCD

Compared to QD-LCDs, the electrically driven self-emissive QD-LEDs share more advantages with the state-of-the-art OLEDs:

(1) The LED structure is much lighter than that of LCDs including QD-LCDs. The LEDs are free from bulky liquid crystal cell and color filters, making them easy to process and compatible with bendable substrates and promising for ultrathin profile lightweight and large area devices.

(2) In an electrically driven LED, the backlight for optically driven LCD is no more necessary, which not only decreases the power consumption but makes possible a real dark state of the sub-pixels and consequently a higher contrast. In addition, the involvement of color filters in the subpixels of LCD also wastes at least 2/3 of the incoming photons[156], while LEDs has no such concern.

(3) In the LED, there is no backlight and liquid crystals involved in the color-switching process. Instead, the color of a subpixel is tuned by the magnitude of current flow driven by the TFT back panels, making the time response of QD-LED display much faster than that of LCDs. The state-of-the-art LCD is capable of a refresh rate of 60 to 480 Hz, while an electrically driven LED, such as OLED, can theoretically enable a refresh rate of up to 100 kHz. The response time becomes critical when there is a large number of pixels in a display.

(4) Since there is no polarizer, which comes with the liquid crystal cell, in a QD-LED configuration, there will be no viewing angle problems, considering the Lambertian profiles of QD emission.

QLEDs in comparison with OLEDs

The QLEDs share the similar structure with the better-developed OLED technology. Although the OLED has been available in the display market (Samsung, LG, TCL..), there is still motivation for the development of QD-LED, mainly from the emission quality point of view:

(1) The finely tuned color-saturated emission from nanocrystals cannot be matched by organic dyes. Due to the strong electron-phonon coupling in organic semiconductors, their electroluminescence spectra usually comprise multiple emission peaks[11]. As a result, the typical full width at half-maximum (fwhm) of the organic phosphors is around 40-60 nm[156]. In contrast, the PL fwhm of quantum dots in typically below 30 nm , and fwhm below 10 nm can be easily obtained from core-only NPLs. The high color purity of inorganic nanocrystals circumvents the use of color filters that is needed for OLED, thus saving the power. The QD-LED can have sub-bandgap turn on voltage, which is beneficial for low power consumption.

(2) The development of core/shell heterostructures in which the excited states are localized in the core materials and protected by the inorganic shell presents outstanding photochemical and photothermal stability, which cannot be matched with organic molecules. The better photostability leads to a less serious efficiency droop of QLEDs, making them promising for high brightness display.

III.1.3.2 The figure of merits for nanocrystals based LEDs

There are multiple figure of merits in the light emitting diodes and here I will introduce several major ones that is used in the community and in this thesis.

External quantum efficiency (EQE) is defined as the number of photons leaving the LED device divided by the electrically injected electron-hole pairs. The injected electrons can be directly calculated from the driving current, while the calculation of photon flux leaving the device is related to the geometry of the setup.

Luminance (in cd/m²) or radiance (in W/Sr m²) is used to evaluate the brightness of the LED device. **Luminance** is related to human eye sensitivity in the visible. **Radiance** is defined as the power of outcoupled photons per solid angle per area, which will be used for infrared LEDs.

Turn-on voltage is the voltage when the brightness of the LED achieved a certain value.

Half lifetime (T_{50}) is the duration when the LED drops to half of its initial luminance. Usually a halftime with an initial luminance of 100 cd/m² (typical brightness of a mobile phone screen) is compared to evaluate the stability of the device.

III.1.3.3 The state-of-the-art for QD-LED and the main issues

Since their inception in 1994,[154] QD-LED has reached a peak external quantum efficiency (EQE) of above 20% for red[100], green[157] and blue[158], respectively, which is close to the theoretical limits considering light outcoupling efficiency of planar devices (≈20%). In a typical planar LED structure, 70% to 80% of the light generated by the emitters is lost inside the device, mainly in the waveguide mode, as a result that the refractive index of the device is larger than that of air.[159]. Table III-1 lists the performance metrics of the best heterostructure QLEDs of the three primary colors, including external quantum efficiency (EQE), luminance (in cd/m²) and the half lifetime at 100 cd/m², which corresponds to the brightness required for the mobile phone display. The maximum luminance reported for QD-LEDs is par with the commercially available OLEDs[160], which is encouraging for the QD-LED used as the future of display.

Table III-1 QD-based LED of the best performance

Color	Emitting materials (QDs)	EQE (%)	Luminance (cd/m²)	T_{50}@100 cd/m² (h)
Red[100]	CdSe/CdS	20.5%	42,000	100,000
Green[157]	ZnCdSe/ZnSe/ZnSeS/ZnS	23.9%	100,000	1, 655, 000
Blue[158]	ZnTeSe/ZnSe/ZnS	20.2%	88,900	15,850

The droop of QD-LEDs

The common problem faced by most types of LEDs is that, at high current densities, these devices suffer from decreasing efficiency. This behavior is termed efficiency droop or efficiency roll-off. To understand the origin of the roll-off is essential for the development of high-brightness LEDs. There has been a debate on this origin. One of the viewpoints is that the roll-off comes from Auger nonradiative recombination at high current densities,[24,161] while another standpoint is that the roll-off is due to an electric-field-induced quenching of PL efficiency.[162] Over the years of research, the former has been prevalent, especially after the report of a droop-free LED by suppressing the Auger recombination.[11,24,161]

The nonradiative Auger recombination is an interaction between an exciton and another charge carrier (electron or hole) in the emitting nanocrystals. In this process, the recombination energy of an exciton is not used to generate photons but to excite another charge carrier. When a LED is driven at high charge flow, the imbalance of the charge injection to the emitting layer is more significant. The charging of nanocrystals leads to the domination of Auger nonradiative recombination consequently efficiency droop, since the Auger rate is one magnitude faster than that of radiative recombination.[163] The LEDs with efficiency droop will have to require higher current density for high brightness, which will cause irrecoverable damages to the device due to Joule heating. The design of LED with balanced charge injection is thereby critical especially to high brightness operations.

To prevent the build-up of one charge type in the emissive layer, there are two aspects to tune the charge balance of the LED. The first is to engineer the energy profiles of the constituting materials so that one of the charge carriers will face no more barriers than the opposite kind of carrier. Another critical parameter that needs to be considered is the carrier mobility of the constituting layers. Up to now, the most successful LED structures are all based on organic-

inorganic hybrid charge transport layers. ZnO nanocrystals since its first integration in 2008, has been the most widely used electron transport layer due to their solution-processability, proper conduction band (-3.8 eV) for the electron injection and a high electron mobility (1.8×10^{-3} cm²V⁻¹s⁻¹) for transport. Besides, the deep valence band (-7.8 eV) of ZnO nanocrystals can well block the hole from leaking. The most used hole transport layers, due to the paucity choice of inorganic material with proper band alignment, is however dominated by organic materials, which usually comes in stacks to smooth the energy barriers for hole transport. For the all-solution fabrication of QD-LEDs, the soluble molecules are often used, although comes with a low hole mobility, for example, poly-TPD[23,164] and PVK[165] has hole mobilities of 1×10^{-4} and 2.5×10^{-6} cm²V⁻¹s⁻¹, respectively. The evaporated organic molecules such as CBP[166] (1×10^{-3} cm²V⁻¹s⁻¹) provides higher hole mobility, yet not solution-processible.

Table III-2 HOMO (VB), LOMO (CB), and the carrier mobility of materials widely used as CTLs

CTL	Materials	HOMO (VB) (eV)	LOMO (CB) (eV)	Mobility (cm²V⁻¹s⁻¹)	Typical solvent
HTL	PEDOT:PSS[167]		5.2	0.77	Water
	poly-TPD[164]	5.2	2.3	1×10^{-4}	Chlorobenzene
	PVK[165]	5.8	2.2	2.5×10^{-6}	m-xylene
	CPB[166]	6.3	3.2	1×10^{-3}	/
	TFB[168]	5.3	2.3	2×10^{-3}	/
	NiOx NCs[23,169]	5.49	1.85	3.75×10^{-3}	Water
ETL	ZnO NCs[100]	7.5	3.8	1.8×10^{-3}	Ethanol
	TiO2 NCs[170]	7.8	4.1	$\approx10^{-4}$	Ethanol

Continuous efforts have been taken to improve the performance of hybrid QD-LED with organic HTLs and inorganic ETLs over the recent 10 years. In general, this kind of device is electron-rich because of the better conductivity of electrons over holes. One breakthrough is achieved by Peng's group in 2014 when they reported the best-performing solution-processed red QD-LED based on a stack of ITO/PEDOT:PSS/Poly:TPD/PVK/QDs/PMMA/ZnO/Ag.[100] The LED exhibits color-saturated deep-red emission, sub bandgap turn-on at 1.7 V, high external quantum efficiencies of up to 20.5% and low efficiency roll-off a long operational lifetime of more than 100,000 hours at 100 cd m². This device was conceptually new in that a PMMA layer was inserted between the emitting layer and ZnO ETL to block the excess electrons, hence equilibrating the charge injection. Another versatile way to boost charge balance and suppress Auger is to engineer the band profile of the emitters. By growing QDs feature with a compositionally graded interlayer and a final barrier layer, nonradiative Auger is suppressed, which leads to a droop-free QD-LED.[161] It has also been demonstrated that by adjusting the chain length of the capping ligands, the charge injection balance in a LED device can be optimized and lead to high efficiency and brightness.[171]

III.1.4 Nanocrystal-based LEDs beyond QD and visible

III.1.4.1 NPL-based LEDs

To cover 99% of the Rec.2020 color gamut, the emission linewidth of the three primary colors is required to be below 10 nm.[20] Although there are reports on QDs with single-dot linewidth below 10 nm by specifically engineering the strain between the core and shell materials[172], the inevitable inhomogeneous broadening will decrease the color purity of QD arrays.

To address the demand for thin linewidth, the colloidal nanoplatelets free of inhomogeneous broadening have emerged as an important candidate. Strikingly, soon after the development of high-temperature shell growth of CdSe based core/shell heterostructures,[34] the EQE of NPL-LED was brought from below 1% in 2014[173], to the record high value of 19.2% reported by Demir's group in 2020.[35] Although the EQE of the latter device is close to its theoretic upper limit, the operational lifetime is extremely short (T_{50}=10h at 100cd/m²)[35], far from industrial requirements.

The insufficiency reports on NPL-LEDs and their prospects for large-gamut display has motivated the third part of my thesis. Alloyed CdSe/CdZnS core/shell NPLs is used as emitting layer in the LED stack of ITO/PEDOT: PSS/Poly:TPD/PVK/NPLs/ZnO/Ag. By engineering the bandgap of the NPLs, I obtain a device with the lowest turn-on voltage (1.6 V) among all the nanocrystal-based LED, the longest lifetime (11,000 h at ≈ 100 cd/m²) for the NPL-LEDs. The modest EQE of 5.2% is limited by the PLQY of the emitter, not the structure. Specially, we revisit the origin of droop by probing the low temperature behaviour of the LED, which is barely explored before. By analyzing the temperature dependence of current-voltage-luminance and emission spectra, we found that when the temperature decreases, the peak EQE is increased and the EQE droop is postponed to higher current density. We ascribe this delay of droop with cooling to an more balanced charge transport in the charge transport layers. Last, we demonstrate the potential of all-nanocrystal LiFi-like communication using a homemade LED as lighting source and PbS nanocrystal based solar cell as a broadband photodetector.

III.1.4.2 Infrared LEDs

The experience in nanocrystal-based optoelectronic device including LEDs, photodiodes and solar cells has also motivate the development of LEDs in the infrared, which is demanding for telecom, active imaging, gas sensing, etc. Although the epitaxially grown III-V materials work well for telecom, they suffer from poor spectral tunability and substrate compatibility. Hence nanocrystals with the highest wavelength tunability in the infrared and solution-processibility has attracted tremendous interest. HgTe nanocrystals with the most versatile spectral tunability from visible to the THz has been intensively studied for infrared photodetection and have delivered outstanding performance[42,43,63,72,148], especially in the mid infrared wavelength above 3 µm. Paradoxically, their infrared emission has barely been investigated,[174,175] even though a high PLQY[62] up to 75% from a seed of HgTe emits at SWIR range. The most investigated materials for infrared LED is PbS nanocrystals,[176–178] from which a EQE of 8% and a radiance of 30 WSr⁻¹m⁻² are obtained. However, the wavelength of PbS is limited below 3 µm. The high degeneracy of PbS[18] makes it difficult for the population inversion required for stimulated emission.

This part of my thesis also demonstrates the SWIR electronluminescence of HgTe nanocrystals with a vertical stack inspired by solar cells: ITO/ZnO/HgTe-ZnO/PbS/gold, in which the emitting layer consists of a heterojunction formed by the p-type HgTe and n-type ZnO. The LED devices base on 4 nm HgTe present sub-bandgap turn on voltage of 0.6 V (bandgap ≈ 1 V) and a high brightness even at a modest EQE of 0.7% thanks to the high droop current. In a LED device made with 2.5 nm HgTe seeds, high brightness up to 19 W. Sr⁻¹.m⁻² is achieved, and long operational lifetime is demonstrated: no decay observed during 200 h of continuous operation at a radiance range of 2-5 W. Sr⁻¹.m⁻² and 80 h with a high radiance above 13 W. Sr⁻¹.m⁻².

III.2 Nanoplatelet-based LEDs for all-nanocrystal LiFi-like communication

Nanocrystal-based LED has continued to evolve since their inception in 1994.[154] Peak external quantum efficiency (EQE) of ≈20% for nanocrystal-based LEDs of three primary colors, which corresponds to an internal quantum efficiency (IQE) of 100%, has all been achieved. The maximum luminance reported for nanocrystal-based LEDs are comparable with those of commercially available OLEDs.[160], whilethe external quantum efficiency droop at high current flow and device stability (i.e., operational lifetime) still challenges the industrial integration of nanocrystal-based LEDs.

To address these questions, although there is space for the structure improvement, the choice of materials remains the center of the question. Colloidal CdSe-based 2D nanoplatelets (NPLs)[179] appear as an interesting candidate for light emitting, because apart from the advantages of CdSe nanocrystals such as tunable emission by quantum confinement[180–183] and doping[184–187], maturity in synthesis, solution processability and photochemical stability, their anisotropic geometry brings more interesting properties for LED applications: (i) As 2D nanocrystals, their excitons are only confined in the thickness direction. Their specific growth mechanism leads to no roughness along the thickness, and consequently the PL linewidth is not as limited by inhomogeneous broadening as for spherical nanoparticles[28]. (ii), NPLs show polarized emission induced by in-plane oriented electronic dipole[188], which is expected to enhance the outcoupling by a factor of 2 when the NPLs planes are well aligned to face the substrates[189,190]. (iii) Because the charge carriers are delocalized in the plane of NPLs, the Auger recombination is expected to be less probable with such extended volume,[191] thus promising to overcome the efficiency droop which mainly comes from nonradiative Auger recombination.

Since their discovery in 2008[27], zinc blende CdSe NPLs have been explored for optoelectronic devices such as transistors,[192] light detectors[153] and low threshold lasers.[193–196] While the narrow PL achieved by NPLs has motivated the design of LED from core-only objects,[182,197] the integration of NPLs into LED has strongly benefit from the development of core/crown[198] and core/shell structures. For long, only low temperature methods,[199] such as colloidal atomic layer deposition (c-ALD),[32] has been employed to grow core/shell NPLs. This approach enhances the PL quantum efficiency (PLQY) by passivating the surface dangling bonds and preserves the narrow linewidth of the NPLs, but the PLQY remains below 50% with a large batch-to-batch fluctuation. In spite of these limitations, first core/shell NPL-based LEDs[200,201] have been reported by Chen et al.[173] and improved later by Giovanella *et al.*[202] More recently, high temperature growth of shells on NPL cores while preserving their 2D shape have been developed,[34,203–208] leading to high PLQY (>90%) especially in the red. The improvement in the PLQY of NPL emitter has significantly enhanced the EL efficiency[35,208], thus pushing the NPL-based LEDs to a new level of performance, with the highest reported external quantum efficiency (EQE) up to 19.2%[35], corresponding to a near-unity internal quantum efficiency (IQE). The performance of the state-of-the-art NPL-based LEDs are listed in Table III-3, in which the material aspects including the NPL structure, their PL wavelength and PL quantum yield (PLQY) can be found; device performance wise, figure of merits including EQE, maximum luminance (L_{max}), turn-on voltage (V_{on}) at which the luminance reaches 0.01 cd/m², and the half lifetime with an initial luminance (L_0) of 100 cd/m² (time after which the power drops by half) are compared.

Nanocrystal-based visible LEDs in this stage mainly relies on organic hole transport layers (HTLs) and inorganic electron transport layers (ETLs) such as ZnO and TiO₂. Even in the most successful LED structures, HTLs are identified as limiting blocks because of (i) limited stability of the organic molecules and, more importantly, (ii) the lower carrier mobility and less favorable energy barrier for hole injection and transport compared with those of ETLs for electron injection. The unbalanced charge injection at high current flow leads to an negatively charged

emitting layer[209], which is more susceptible to the Auger nonradiative recombination[11] and results in lower EL efficiency.

Table III-3 Performance of the state-of-the-art NPL-based LEDs

Ref	Materials (NPL)	Wavelength (nm)	PLQY (%)	FWHM (nm)	EQE (%)	L_{max} (cd/m²)	V_{on} (V)	$t_{1/2}$ at 100 cd/m² (h)
35	CdSe/Cd$_{0.15}$Zn$_{0.85}$S	648	86		5.7	16010	2.4	
	CdSe/Cd$_{0.25}$Zn$_{0.75}$S	650	≈100	26	19.3	23490	2.4	12.8
	CdSe/ZnS	618	85		4.7	18730	2.8	
208	CdSe/CdS/CdZnS	634-648	75-89	21	9.9	46000	2.3	560
	CdSe/CdS	650	48	21	1.8	10650	2.3	
202	CdSe/CdZnS	658	40±5		8.4	1540	4.05	
198	CdSe/CdSeTe Core/crown	599	85	>40	3.6	34520	1.9	
210	CdSe/CdS	556	60	14	5	33000	2.25	
173	CdSe/CdZnS	646	30	26	0.6	4499	4.7	
197	CdSe/CdSSe	520	35	12.5		100	2.1	
Our work	CdSe/CdZnS	620	35	28	5.2	35100	1.6	11 000

In the followingof this section for visible LEDs, the first goal is to build an CdSe/CdZnS NPL based LED with a balanced charge carrier injection. Instead of starting a new structure from the scratch, I take a validated LED structure that works well for CdSe based nanocrystals[100] and focus ontailoring energy level of emitting CdSe/CdZnS NPLs to optimize the charge carrier injection. The energy levels is tuned by varying the alloy content of CdS in the shell of CdSe/CdZnS NPLs. The scheme of the LED structure is presented in Figure III.4, with a stack of glass/ITO/HTLs (PEDOT:PSS/PolyTPD/PVK)/ CdSe/CdZnS core/shell NPLs/ZnO/Ag, in which PEDOT:PSS, Poly-TPD and PVK are respectively poly(3,4-ethylenedioxythiophene) polystyrene sulfonate, Poly(N,N'-bis-4-butylphenyl-N,N'-bisphenyl)benzidine and Poly(9-vinyl) carbazole. In this stack, the PEDOT:PSS with a highest occupied moclecular orbital (HOMO) energy level close to the ITO work funciton, is used as a hole injector. The bilayered poly-TPD/PVK hole transport layer (HTL) takes advantage of relatively high hole mobility of polyTPD to achieve low turn-on voltage, and the deep HOMO energy level of PVK to smooth the energy barriers for efficient hole injection to the emitting NPL layer.[100] Colloidal ZnO nanocrystals are used as electron-transport interlayers (ETLs) due to their of high electron mobility, proper energy levels for electron injection and hole blocking.
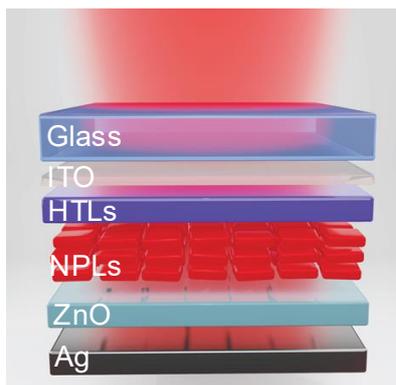
Figure III.4 Schematic diagram of a LED made of glass/ITO/HTLs (PEDOT:PSS/PolyTPD/PVK)/ CdSe/CdZnS core/shell NPLs/ZnO/Ag, with ITO and Ag as anode and cathode, respectively.[100]

Based on the LED with the best performance, we for the first time provide insights on the thermal influences on the efficiency droop in the device scale. By characterizaing the LED performance at low temperature, we find that the efficiency droop occurs at higher current and bias at lower temperature. By ruling out emitter material factors in our case, we believe that the efficiency droop strongly relies on charge transport layers of the device, which suggests new pathways to mitigate the efficiency droop.

Finally, the high maturity of nanocrystal-based LEDs and photodetectors motivates us to integrate the two into a all-nanocrystal complex system. To achieve this goal, we develop LEDs with large pixel (56 mm²) which give out more photons, and then we coupled it to a PbS nanocrystal-based solar cell used as a broadband detector. We demonstrate an all-nanocrystals-based the LiFi-like communication setup, in which the LED is not only a light source but also carries information invisible to the eyes but can be detected by a photodetector.

This work involves the collaboration inside and outside the team. The X-ray photoemission is again a teamwork with the assistance of Mathieu Silly at Tempo beamline of synchrotron SOLEIL. The LiFi communication setup is installed with the help of Clément Livache and Charlie Gréboval, colleague PhD students of the team. The solar cell used for broadband detector is fabricated by Prachi Rostagi, postdoc of the team. The TEM images are received from Xiang Zhen Xu the engineer of ESPCI.

III.2.1 Synthesis and characterization of CdSe/CdZnS NPLs

ZnS has been widely grown as an inorganic shell for CdSe nanocrystals to passivate their surface trap states by forming a type-I band alignment, in which electrons and holes are confined in the CdSe core instead of trapped in the surface states. Alloying of ZnS with a small amount of CdS, which exhibits a smaller lattice mismatch with CdSe core (4%), has proved effective to release the strain and hence reduce the defects. On the other hand, the amount of CdS alloyed with ZnS plays an significant role in the extent of carrier delocalization and allow for a continuous tuning the band structure of the core/shell CdSe/CdZnS NPLs.[205]

To obtain NPLs with the most suitable band alignment with the LED structure in Figure III.4, we choose to tune the confinement energy of the emitting material by continuously changing the Cd content of the alloyed shell, rather than changing the core thickness of the single-object NPLs, which leads to discrete values for band edge energy.

III.2.1.1 The synthesis of CdSe/CdZnS NPLs

CdSe/CdZnS NPLs with varying Cd contents (0%, 5% and 10%) in the shell are synthesized with well-established protocols[27,33]. It is a two-step synthesis, in which the pre-synthesized CdSe NPL cores are injected as the seed for shell growth. The latter is conducted at high temperature with continuous pump injection of metal ($Cd_xZn_{1-x}OA_2$) and sulfur precursor (1-Octanethiol) at the same time, as presented in Figure III.5. The synthesis of CdSe NPls and CdSe/CdZnS core/shell NPLs, including their precursor preparation and nanocrystal growth, are described in the following.

CdSe NPL core $Cd_xZn_{1-x}OA_2$+1-Octanethiol   CdSe/CdZnS core/shell

300 °C
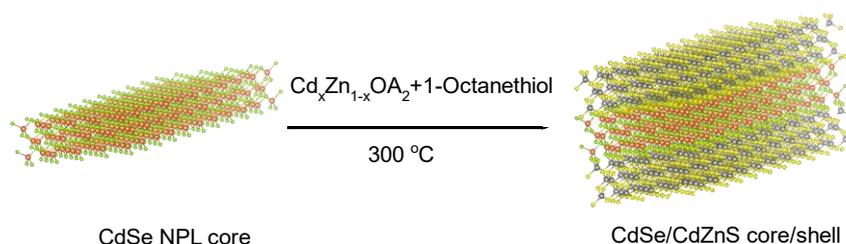
Figure III.5 Scheme of the high temperature growth of CdZnS shell from a CdSe NPL core.

CdSe core NPLs synthesis

- Precursor preparation

Cadmium myristate $Cd(Myr)_2$: In a 50 mL three neck flask, 2.56 g of CdO and 11 g of myristic acid are mixed and degassed at 90 °C for an hour. Then, under Ar flux, the temperature is set to be 200 °C. When the solution turns colorless (in approximately 40 minutes), the reaction is stopped, and the temperature is decreased. At 60 °C, 30 mL of methanol is added to the mixture. The cadmium myristate is washed 4 times with methanol and dried overnight at 50 °C under vacuum.

- Nanocrystal growth and precipitation

A mixture of 340 mg of $Cd(Myr)_2$ (0.6 mmol), 24 mg of Se powder (0.3 mmol) and 30 mL of ODE are degassed in a three neck flask for 30 min under vacuum. Then, under Ar flux, the temperature is set to 240 °C and as it reached 180 °C, 80 mg (0.3 mmol) of $Cd(OAc)_2 \cdot 2H_2O$ solid is rapidly added to the flask. 12 min after the addition of $Cd(OAc)_2$, the reaction is quenched by injecting 2 mL of OA. Then the mixture is cooled down to room temperature. Hexane and ethanol are added to the reaction mixture before it is precipitated by centrifugation. A second cleaning is conducted with hexane/ethanol and the final CdSe core NPLs are redispersed in 12 mL of ODE.

Shelling of CdSe/$Cd_xZn_{1-x}S$ core/shell NPLs

- Precursor preparation

Zinc oleate in ODE (0.1 M): In a 250 mL flask, 50 mmol of ZnO (4.074 g) and 100 mL of oleic acid are introduced. The mixture is heated to 180 °C and kept at that temperature until there is a clear solution. The reaction is cooled down immediately to 120 °C and degassed at this temperature to remove the water. Then the heating mantle is removed, and the mixture are allowed to cool down naturally. To get 0.1 M zinc oleate, 16 mL of ODE is added to 4 mL of 0.5 M zinc oleate. The precursor is heated prior to use.

Cadmium oleate in ODE (0.1M): CdO (6.42 g, 50 mmol) is added to 100 mL of oleic acid in a 250 mL three-neck flask and heated at 160 °C. When the mixture becomes colorless, the flask is cooled down to 70 °C and degassed under vacuum for 1 h. Then 400 mL of ODE are added to obtain the final concentration. The solution is transferred into a bottle and stored for several months. The precursor is heated prior to use.

Cd_xZn_{1-x} oleate (0.1 M) is obtained by mixing cadmium oleate (0.1 M) and zinc oleate (0.1 M) described above according to the desired ratio.

- Nanocrystal growth and precipitation

The recipe is taken from literature with modifications.[33]15 mL of trioctylamine (TOA) is added to a 100 mL three-neck flask and degassed at 100 °C for 30 min. Then the atmosphere is switched to Ar and the temperature is set as 300 °C. Meanwhile, 7 mL of 0.12 M n-octanethiol and 7 mL of 0.1 M of Cd_xZn_{1-x} oleate (x=0, 0.05 or 0.1) are put into two syringes. When the temperature is stabilized at 300 °C, the syringe pumps are started and pumped at a constant rate of 4.7 mL/h. After several drops of injection, 3 mL of NPL core dispersed in ODE are swiftly injected to the flask. After the precursor injection, the mixture is baked for another 90 min at 300 °C after all the injection are finished. The flask is then cooled down with air flux and at the temperature of 100 °C, 2 mL of OA is injected. 15 mL of hexane and 10 mL of ethanol are added to precipitate the NPLs by centrifugation. After a second purification with ethanol and hexane, the NPLs are finally dispersed in 5 mL of toluene.

III.2.1.2 Optical properties and morphologies of varying CdSe/CdZnS NPLs

Using the protocols described above, CdSe/ZnS, $CdSe/Cd_{0.05}Zn_{0.95}S$, and $CdSe/Cd_{0.1}Zn_{0.9}S$ are obtained. All the NPLs are of a parallelipedic shape with a lateral extension of about 10×40 nm², as shown in Figure III.6 d, e and f, respectively. As can be seen from the absorption and emission spectra presented in Figure III.6 a, b and c, with the increase of Cd content in the shell, the photoluninescence of of the core/shell NPLs red shift from 604 nm for CdSe/ZnS NPLs, 620 nm for $CdSe/Cd_{0.05}Zn_{0.95}S$ and to 638 nm for $CdSe/Cd_{0.1}Zn_{0.9}S$. The red shift comes from the favored electron delocalization over the whole structure with the incorporation of CdS.
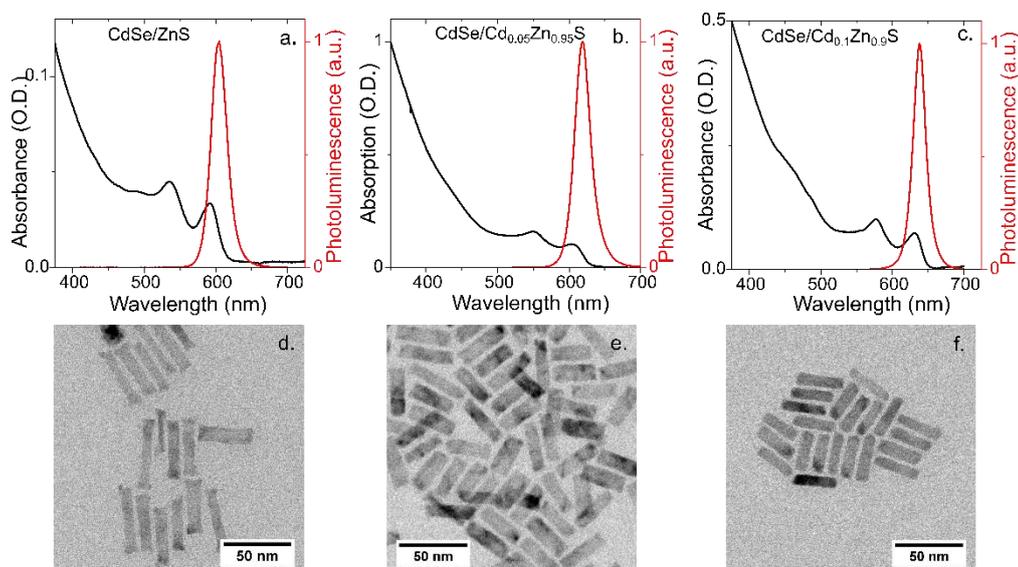

Figure III.6 Absorption and photoluminescence spectra and TEM images of CdSe/ZnS (a) and (d), $CdSe/Cd_{0.05}Zn_{0.95}S$ (b) and (e), and $CdSe/Cd_{0.1}Zn_{0.9}S$ (c) and (f) core/shell NPLs.

III.2.2 Fabrication and characterization of NPL based LED

The fabrication of NPL-based LED involves the patterning of the ITO electrode with UV lithography, the spin coating of organic HTLs, nanocrystal emitters and ETLs, and the thermal evaporation of the top Ag electrode followed by the encapsulation of the device, which is critical to avoid the oxidation of top electrodes and the deterioration of organic layers under moisture.

III.2.2.1 Patterning of Indium Tin Oxide (ITO) substrates

ITO substrates (10 Ω/sq) are cut into 15 mm × 15 mm pieces and cleaned by sonication in an acetone bath for 5 min. After sonication, the substrates are rinsed with acetone and isopropanol before dried completely with N_2 flow. The substrates are further cleaned with O_2 plasma for 5 min to remove organic residuals on the surface. After cleaning, TI-Prime and AZ5214E photoresist are sequentially spin-coated on the surface of ITO at a rate of 4000 rpm for 30 s and baked at 110 °C for 120 s and 90 s, respectively. Next, a mask aligner is used to expose the substrates to UV light for 20 s through a lithography mask (1 mm width). Photoresist is then developed using AZ 726 developer for 20 s before rinsed with deionized water and dried with N_2 flux. After another 5 minute plasma cleaning, the substrates are etched in a 25% HCl (in water) bath for 10 min at 40 °C before they were dipped immediately in deionized water. Finally, the lift-off is conducted in an acetone bath.

A scheme of the patterned ITO substrates is shown in Figure III.7 a, with the green part as ITO thin film while the other part bare glass. The large top contact of the substate is designed to contact the thermal evaporated metal electrodes while the eight separated legs are designed for eight LED pixels which will be introduced in the following. A microscopy image in Figure III.7 b in which the ITO pattern is in yellow.
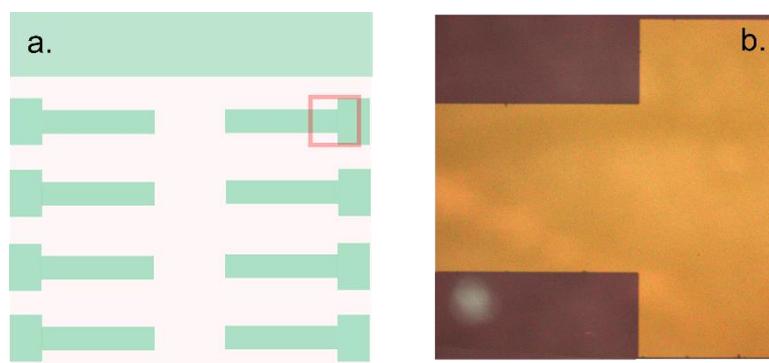
Figure III.7 (a) A scheme of a patterned ITO on a glass substrate. There are one top contact and eight legs. (b) a microscopy of the square area indicated in (a).

III.2.2.2 LED device fabrication

To start, the patterned ITO substrates are cleaned with acetone and isopropanol first and put under plasma for 10 min. PEDOT: PSS solution (filtered with 0.45 µm filter) is spin-coated on a patterned ITO glass electrode at 4000 rpm for 60 s and annealed at 140 °C for 10 min in air. Inside a Nitrogen-filled glovebox, Poly-TPD (8 mg/mL in chlorobenzene), PVK (1.5 mg/mL in m-xylene), NPLs and ZnO nanoparticles are successively spin-coated at 2000 rpm for 45 s on the PEDOT: PSS-coated substrate. After the deposition of Poly-TPD, the sample is annealed at 110 °C for 20 min, and for PVK the annealing is at 170 °C for 30 min. Next, 80 nm of Ag is deposited on top of the ZnO layer by thermal evaporation. The thickness of NPL and ZnO layer are 18 nm and 80 nm, respectively. To complete the fabrication, the devices are encapsulated inside the glove box with a piece of glass using ultraviolet-curable resin. The size of the pixel is 1 mm² which is defined by the overlap of ITO and Ag electrodes, as indicated as a red square

spot in the scheme in Figure III.8 a. The 4 working pixels driven at forward bias is shown in Figure III.8 b.
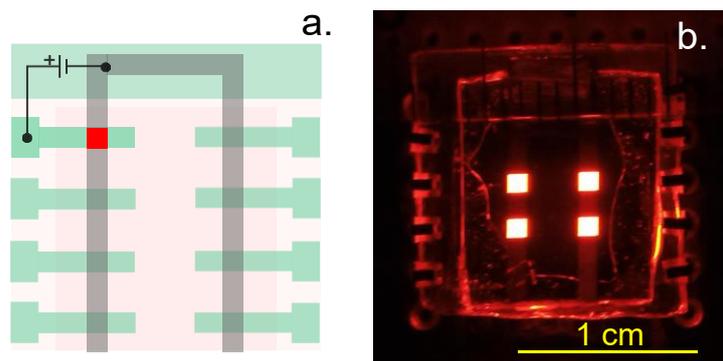
Figure III.8 (a)Scheme of the LED device where the red square represents a working pixel when applied with a forward bias. The gray "U" shape pattern represents the Ag electrode deposited under a shadow mask. (b) A working LED based on CdSe/Cd$_{0.05}$Zn$_{0.95}$S core/shell NPLs with 4 pixels (1 mm²) driven under the forward bias.

III.2.3 Characterization of the LED devices based on different CdSe/CdZnS NPLs

In this part, the emission properties including the color purity and the emission pattern are determined first. The current-voltage-luminance characteristics are collected and from which the figure of merits including EQE, turn-on voltage, luminance and lifetime can be determined.

III.2.3.1 Color of the emissions from CdSe/CdZnS NPLs with different shell

The EL spectra of the LEDs based on CdSe/CdZnS NPLs with varying Cd contents in the shell (0%, 5% and 10%) are obtained in ambient conditions. The normalized spectra show an EL emission at 609 nm, 622 nm and 639 nm respectively with the increase of Cd content, see Figure III.9 a. The linewidth of the EL ranges from 23 nm to 29 nm, narrow enough to enable pure red colors located on the edge of the chromaticity diagram, with CIE (Commission internationale de l'éclairage) coordinates of (0.632, 0.367), (0.69, 0.31) and (0.7, 0.3) for the EL of LED based on CdSe/ZnS, CdSe/Cd$_{0.05}$Zn$_{0.95}$S and CdSe/Cd$_{0.1}$Zn$_{0.9}$S NPLs, respectively.(see Figure III.9 b). Figure III.9 c presents a typical bias dependence of EL for CdSe/Cd$_{0.05}$Zn$_{0.95}$S NPLs-based LED. With the increase of bias, the EL intensity increases rapidly while the peak position barely shifts.
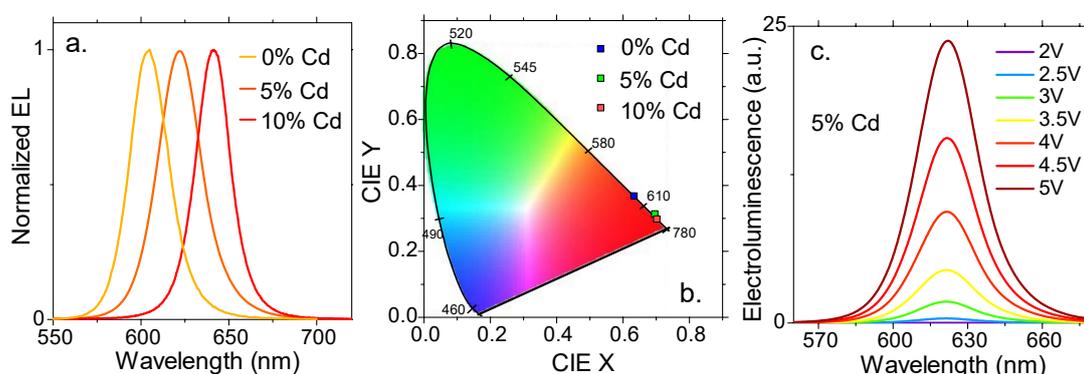
Figure III.9 (a) Normalized EL spectra of the LED with an emitting layer of CdSe/ZnS, CdSe/Cd$_{0.05}$Zn$_{0.95}$S and CdSe/Cd$_{0.1}$Zn$_{0.9}$S core/shell NPLs at room temperature.(b) Chromaticity diagram and the colors associated with the EL spectra of the LED based on CdSe/ZnS (blue), CdSe/Cd$_{0.05}$Zn$_{0.95}$S (green) and CdSe/Cd$_{0.1}$Zn$_{0.9}$S (red) core/shell NPLs. (c) EL spectra of LED based on CdSe/Cd$_{0.05}$Zn$_{0.95}$S NPLs under different bias.

III.2.3.2 Emission profile of NPLs based LEDs

For the characterization of a LED, the emission pattern is critical to determine the fraction of photons that can be detected among the outcoupled photons. For QD-LEDs, the emission pattern is conventionally assumed to be Lambertian, which characterizes an isotropic emitter.

With the polarized emission of single NPL nanocrystal in mind,[204] we held the hope to obtain an polarized EL from our LED based on NPL emitting layer, which can be promising to improve the outcoupling efficiency. To verify the exact emission pattern of the NPL based LED, the angular dependence of EL spectra is investigated using the setup shown in Figure III.10 a. In this setup, a detector is placed at the same height as the working pixel but at a distance. The detector is then rotated around the pixel site from -90° to 90° relative to the normal of the LED plane, and EL spectra are collected at several different angles. Figure III.10 b plots the normalized angular dependence of the EL intensity, which closely follows Lambert's cosine law. The Lambertian emission profile of our NPL LED can be explained by the fact that the NPLs are prone to be vertically aligned with respect to the substrate during spin coating, while the directional emission of NPL is more prominent when the plane is parallel to the substrate.[211]
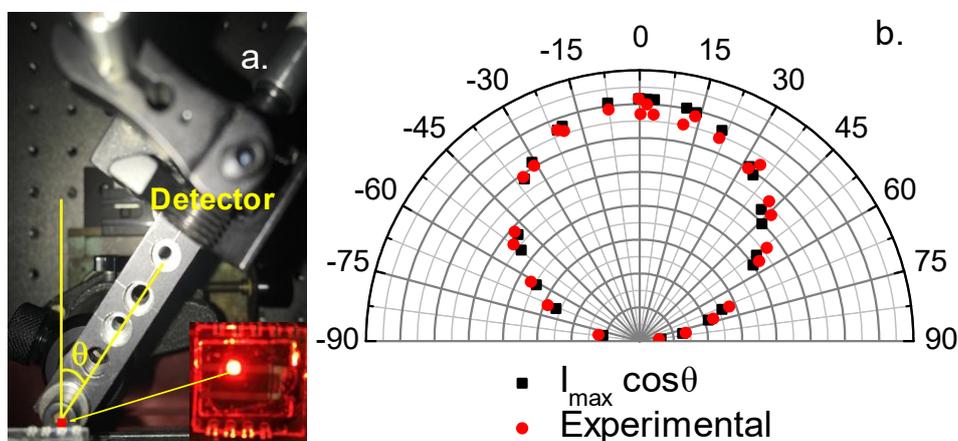
Figure III.10 (a) Scheme of the setup used to measure the angular dependence of EL, in which the angle θ is the angle between the detector and the normal of LED plane. In the inset is the working pixel. (b) Comparison between the experimental EL intensity and a cosine dependence of EL intensity for the light emitted by the NPL based LED.

III.2.3.3 The determination of EQE and Luminance of LED device

EQE determination

The external quantum efficiency (EQE) is defined as the number of photons leaving the LED device divided by the electrically injected electron-hole pairs. The later can be directly calculated from the driving current, while the calculation of photon flux leaving the device from the forward direction is related to the geometry of the setup. In our case, current-voltage-luminance characteristics are collected with a Keithley K2634B source meter unit and a PM100A power meter coupled with the S120 C Si detector from Thorlabs. Based on this setup, we can determine the EQE of LED device according to a proposed method[212], as described in the following:

Considering the Lambertian emission of the pixel, the flux leaving the device in the forward direction F_{ext} can be described as:

$$F_{ext} = \int_0^{\pi/2} 2\pi L_0 \cos\theta \sin\theta \, d\theta = \pi L_0 \tag{III-1}$$

with L_0 the flux per solid angle of light leaving the device in the forward direction.

Since the solid angle from the photodetector to the light source Ω is:

$$\Omega = \frac{S_1}{l^2} \tag{III-2}$$

with S_1 the area of the detector and l the distance between the light source and the detector.

Thus, L_0 and F_{ext} can be deduced as:

$$L_0 = \frac{P_{det}}{\Omega} = \frac{P_{det} l^2}{s_1} \tag{III-3}$$

$$F_{ext} = \frac{\pi P_{det} l^2}{s_1} \tag{III-4}$$

Consequently, the number of photons emitted per second to the forward direction can be calculated by:

$$N_P = \frac{F_{ext}}{h\nu} = \frac{\pi P_{det} l^2 \lambda}{s_1 hc}, \tag{III-5}$$

with λ the wavelength of electroluminescence, h the Plank's constant, and c the speed of light.

On the other hand, the number of electrons injected per second N_e can be obtained by

$$N_e = \frac{I}{e}, \tag{III-6}$$

with I the current flow of the device.

Finally, the EQE can be calculated by:

$$EQE = \frac{N_p}{N_e} = \frac{\pi P_{det} l^2 \lambda e}{s_1 hcI} \tag{III-7}$$

Knowing that the working diameter of detector area is 9.5 mm and assuming the distance between detector and device to be 6.5 mm in our case, the geometry-related value of $\frac{l^2}{s_1} \approx 0.6$ in our setup.

Luminance of the LED

Luminance (in cd/m2 or lm/sr m²) describes the **luminous flux** (in lm) emitted from a unit area to a particular direction. By definition, a monochromatic source emitting 1 W at 555 nm (where the human eye has its maximum sensitivity) has a luminous flux of 683 lm. Thus, the luminous flux of a monochromatic source with a wavelength of λ and a power of F_{ext} (W) is $683 * V(\lambda) * F_{ext}$, with $V(\lambda)$ the function of photonic eye sensitivity. The luminance of an LED can then be calculated as[18]:

$$L = \frac{683.V(\lambda).F_{ext}}{\pi.S_2} = \frac{683.V(\lambda)\pi P_{det} l^2.}{\pi.S_2 S_1} \tag{III-8}$$

III.2.3.4 I-V-Luminance characteristics of LED device based on CdSe/CdZnS NPLs

Using the method introduced in the previous part, three groups of LEDs with the same structure but different CdSe/CdZnS emitting layer (0%, 5% and 10% of CdS in the shell) are tested and compared. Their current density and luminance as a function of bias, and their EQE and luminance as a function of current density are plotted in Figure III.11 .The main figure of merits of them are extracted and compared in Table III-4.
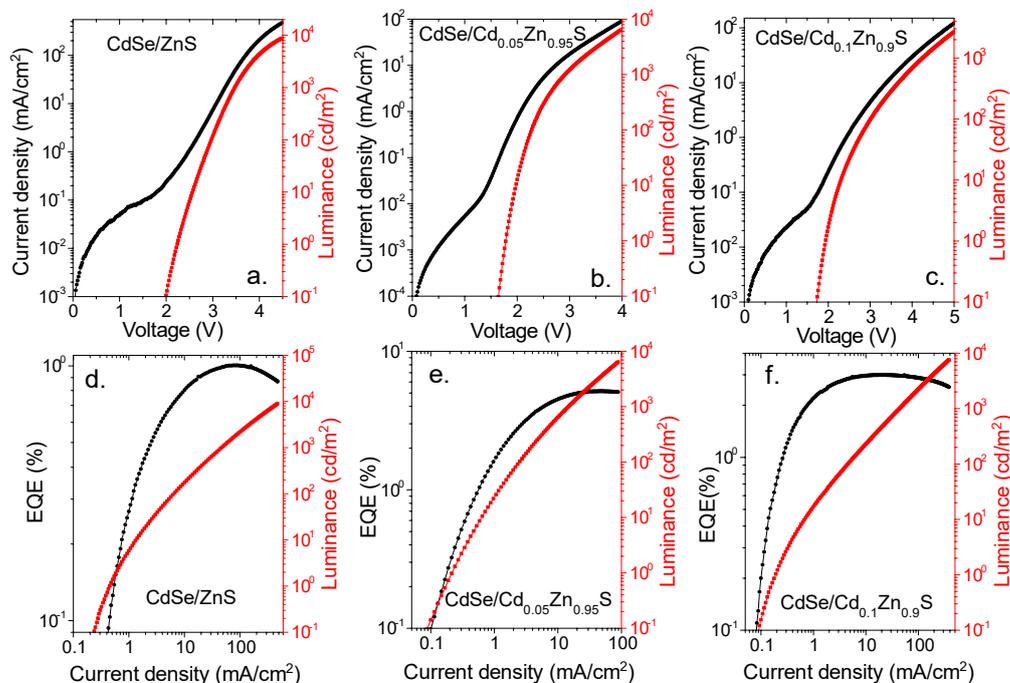
Figure III.11 (a), (b) and (c) show current density and luminance as a function of the applied bias for LEDs based on CdSe/ZnS, CdSe/Cd$_{0.05}$Zn$_{0.95}$S and CdSe/Cd$_{0.1}$Zn$_{0.9}$S core/shell NPLs, respectively. (d), (e), and (f) show external quantum efficiency (EQE) and luminance as a function of driving current for LEDs based on CdSe/ZnS, CdSe/Cd$_{0.05}$Zn$_{0.95}$S and CdSe/Cd$_{0.1}$Zn$_{0.9}$S core/shell NPLs, respectively.

From the current-voltage-luminance characteristics (Figure III.11 a, b and c), we can find that all the LEDs exhibit a clear rectifying IV characteristic and each of the devices shows sub-bandgap turn-on voltage, demonstrating that this LED structure works well for the CdSe-based nanocrystals. It is worth noting that the CdSe/Cd$_{0.05}$Zn$_{0.95}$S NPLs based LED presents the lowest turn-on voltage (1.63 V) ever reported among all the nanocrystal based LED[213]. However, there is a clear difference in the maximum EQE of the three, in which the CdSe/Cd$_{0.05}$Zn$_{0.95}$S group exhibits the highest value of 5.15% even at a modest PL efficiency of around 35%, while the other two groups showed much lower EQE values, only 1% for the LED device based on unalloyed CdSe/ZnS NPLs and 3% for the device made of CdSe/Cd$_{0.1}$Zn$_{0.9}$S NPLs, see Figure III.11 d, e and f and Table III-4. This highest EQE and lowest turn-on voltage of CdSe/Cd$_{0.05}$Zn$_{0.95}$S based LED suggest that there is a more balanced charge injection. This claim will be further supported by the XPS results in the following.

It is worth pointing that Kelestemur *et al*[208] recently reported a similar LED based on high-temperature grown CdSe/CdS and CdSe/CdS/CdZnS core/shell NPLs. In their diode, PEDOT:PSS and PVK are used as HTLs (see Table III-3), without the PolyTPD layer. In terms of performance, the EQE of their LED device based on CdSe/CdS NPLs is lower than our CdSe/CdZnS NPL based LED, while the one using CdSe/CdS/CdZnS NPLs reaches a higher EQE value of 10% , which is nearly 2 times higher than our CdSe/CdZnS NPL LED (5.15%). However, this higher EQE does not come from the device structure, but from a higher PLQY of the

CdSe/CdS/CdZnS NPLs (90%) than that of the CdSe/CdZnS NPLs (35%). The higher turn-on voltage (2.3 V) of the CdSe/CdS/CdZnS NPLs-LED indicates a less optimized charge injection.

Table III-4 Comparison of PL energy, maximum EQE and the turn-on voltage of LEDs based on three different NPLs

NPLs	PL peak	EQE max	Turn-on voltage
CdSe/ZnS	605 nm (2.06 eV)	1.02%	2 V
$Cd_{0.05}ZnS_{0.95}$	620 nm (2 eV)	5.15%	1.63 V
$Cd_{0.1}ZnS_{0.9}$	638 nm (1.94 eV)	3%	1.7 V

III.2.3.5 Band alignment of LED based on CdSe/$Cd_{0.05}Zn_{0.95}$S NPLs

The energy levels of CdSe/$Cd_{0.05}Zn_{0.95}$S with respect to the vacuum level are probed with X-ray photoemission (XPS) at synchrotron SOLEIL. From the secondary electron cut-off, we determined the work function of the material and locate the Fermi level 4.4 ±0.1 eV below the vacuum level (see Figure III.12 a); from the lowest binding energy of the photoelectrons, we can locate the valence band of the CdSe/$Cd_{0.05}Zn_{0.95}$S NPLs 1.3±0.1 eV below the Fermi level (see Figure III.12 b). Taking the band gap as 2 eV from the PL centered at 620 nm, the Fermi level is thus locate in the upper part of the band gap, indicating a n-type nature of CdSe/$Cd_{0.05}Zn_{0.95}$S NPLs. We thus can propose an effective electronic spectrum for the CdSe/$Cd_{0.05}Zn_{0.95}$S NPLs in the absolute energy scale, as given in Figure III.12 c. A band alignment of the LED structure with CdSe/$Cd_{0.05}Zn_{0.95}$S NPLs is thus proposed in Figure III.12 d.
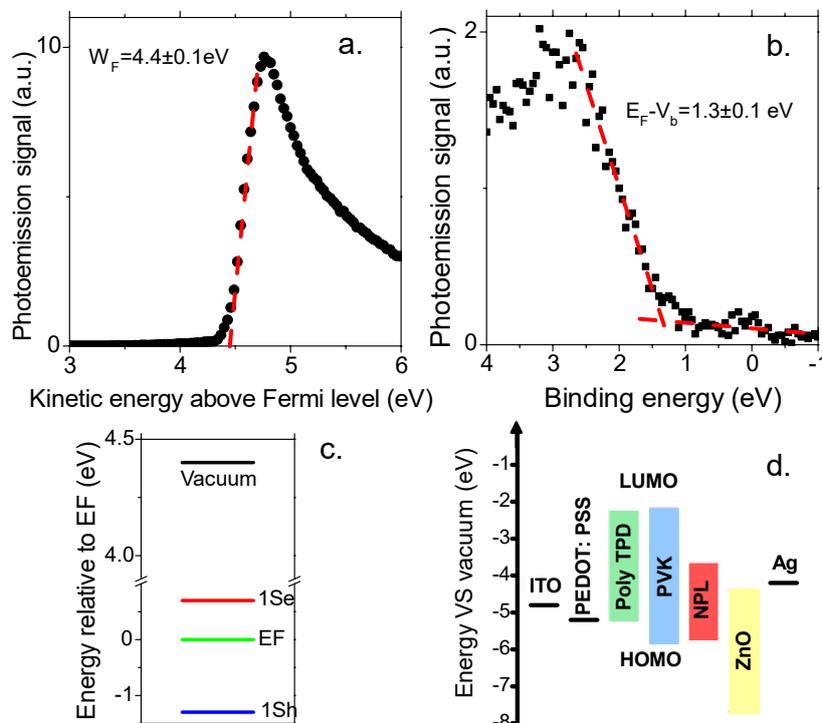
Figure III.12 (a) Photoemission spectrum relative to the secondary electron cut-off for the core/shell CdSe/$Cd_{0.05}Zn_{0.95}$S NPLs. (b) Photoemission spectrum relative to the valence band for the core/shell CdSe/$Cd_{0.05}Zn_{0.95}$S NPLs. (c) Electronic spectrum the CdSe/$Cd_{0.05}Zn_{0.95}$S NPLs. (d) Band alignement for the LED structure based on CdSe/$Cd_{0.05}Zn_{0.95}$S NPLs. The energies for the different layer except the NPL are taken from ref. [100,173]

III.2.3.6 The stability of CdSe/Cd$_{0.05}$Zn$_{0.95}$S NPLs based LED

Device operating lifetime

The lifetime of nanocrystal based LED is one of the key limitations for further inudstrial applications. For example, display applications requies a typical luminance[18] of 100 cd/m² and a operating time of at least several thousands of hours,[156] while the industrial lighting requires a luminance of several thousands of cd/m² and a operating times up 1000 h to compete with traditional incandescent lamps.[214] The device lifetime is conventionally evaluated by measuring the luminance over a period of time under constant current density. The lifetime is defined by half lifetime (T_{50}), which is the duration when the LED drops to half of its initial luminance.

For our optimized LED based on CdSe/Cd$_{0.05}$Zn$_{0.95}$S NPLs, the luminance evolution with initial luminance of 73 cd/m² and 1000 cd/m² are measured under constant current density. As shown in Figure III.13, at a initial luminance of 73 cd/m² (driven at 1.4 mA/cm²), the half lifetime extrapolated from the log-scale plot is 11000 h, with the black scatters the experimental data while the grey solid line the extrapolation. On the other hand, the half lifetime with a intitial luminance of 1000 cd/m² (driven at 12 mA/cm²) is measured to be 100 h. Assuming that the $L^{1.5}T_{50}$ is a constant[100], with L the initial luminance and 1.5 the accelaeration factor, we can determine the half lifetime under 100 cd/m² luminance to be 3160 h, which is the longest reported for NPLs based LED. Although a LED device with similar high temperature NPLs as emitting layers exhibiting the record-high efficiency of 19.2% has been reported[35], its half lifetime at 100 cd/m² is less than 13 h, which is far from the industrial requirements.
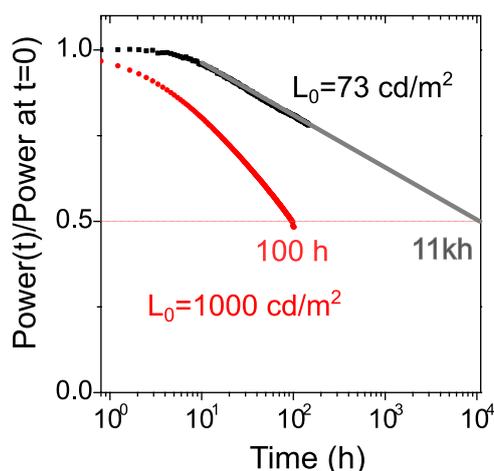
Figure III.13 The luminance variation with time at the intial luminance of 73 cd/m² (black curve) and 1000 cd/m²(red curve).

Device performance under high current flow

The LED based on CdSe/Cd$_{0.05}$Zn$_{0.95}$S NPLs shows interesting performance such as a narrow EL spectrum, low turn-on operation and long lifetime, and when we expand the bias range up to 7 V which corresponds to ≈1000 mA.cm⁻², a high luminance of 35100 cd/m² can be observed. However, a efficiency droop appears (see Figure III.14 a and b) under a bias above 7 V. Efficiency droop, also called roll-off, is a general problem faced by nanocrystal-LEDs. It is a phenomenon that the EQE decreases under higher current density and lead to an irreverable damage to the LED device due to heat generation.[161] Next, I will focus on the mechanism of droop and propose alternative strategies to this issue.
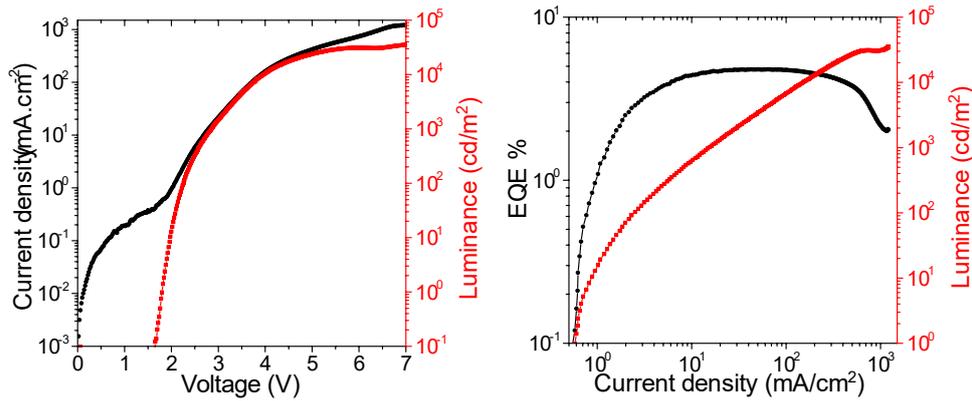
Figure III.14 (a) Current density and luminance as a function of bias. (b) EQE and luminance as a function of current density for the LED with CdSe/Cd$_{0.05}$Zn$_{0.95}$S NPLs as emitting layer.

III.2.4 The origin of efficiency droop: beyond Auger recombination in emitting layer

Up to now, the strategies to mitigate the efficiency droop has been focused on suppressing nonradiative Auger recombinations[161,215]. The most common method is to engineer the band profiles of the emitting materials, for example, to build graded core/shell heterostructures, to control the balance of charge injection.[24] All these methods have been proved effective, confirming that Auger recombination is indeed one of the factors that limits the performance of nanocrystal-LEDs. However, there are limited investigation in decreasing the droop from the perspective of the LED device.

III.2.4.1 Current-voltage-luminance characteristics of LED under low temperature

The I-V-Power of the LED are collected at different temperatures from 300 K to 25 K in a cryostat. Upon cooling, the temperature dependence of transport reveals two regimes of bias in the I-V curve, see Figure III.15 a. At low bias, typically below the turn-on voltage of the LED, the transport barely change with tempreature, while in the high bias range the temperature influence is more significant. We define the bias from which the device enters the strong conduction regime as threshold voltage (V_t). From Figure III.15 a, we particularly observe a temperature-induced shift of V_t. This shift is also responsible for a similar shift of the luminance threshold voltage (where the photons started to be detected) as shown in Figure III.15 b, which presents the EQE as a function of bias at different temperatures. Interestingly, we find that the EQE droop is strongly delayed to higher current density by decreasing the temperature, see Figure III.15 c. At room temperature (300 K), the EQE of the device start to decrese at a current density of around 50 mA/cm², whereas this droop is not observed within 300 mA/cm².under a temperature below 200 K. A higher EQE at higher current density at lower temperatures suggests a high brightness.
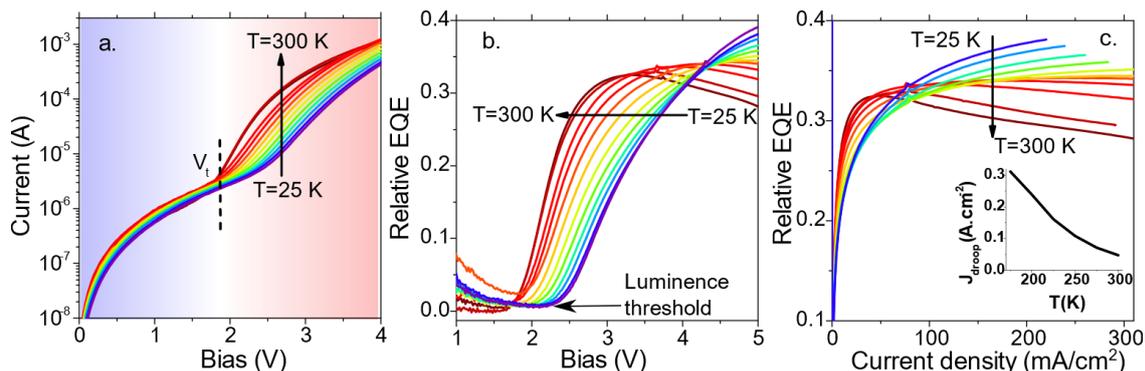
Figure III.15 (a) Current as a function of bias under various temperatures for an LED device based on CdSe/Cd$_{0.05}$Zn$_{0.95}$S core/shell NPLs (b) Uncalibrated EQE as a function of the applied bias under various temperatures. (c) Uncalibrated EQE as a function of the driving current density under different temperatures. The curves are collected every 25 K from 300 K to 25K.

III.2.4.2 The emission properties of LED device under low temperature

We may have naively attributed the above-mentioned shift of transport threshold (V_t) (Figure III.15 a) and luminance threshold (Figure III.15 b) to the change of band gap with temperature. However, the shift of EL (Figure III.16 a) and PL (Figure III.16 b) with temperature are much smaller than the one observed in luminance threshold, as compared in Figure III.16 c. However, a similar shift of V_t with temperature is also observed in the control group diode of the same stack but without NPLs, see Figure III.16 d. As a result, we believe that the NPLs are not related to the shift. This suggests that, in our LED with only several monolayers of nanocrystal emitters, the nanocrystals act as recombination center while the transport is entirely driven by transport layers of the LED stack.

The strong temperature dependence of droop suggests two possible origins. The first is the temperature-dependent Auger recombination within the NPL[191,216]. The research on the temperature dependence of the Auger process in NPLs remains so far limited[217]. However, NPLs thanks to their large volume and anisotropic geometry, are expected to present a reduced auger recombination with respect to other types of nanocrystals[191,218]. In addition, NPL with thin shell, as it is here, are supposed to be the one with the lowest Auger rate[219]. Thus, the delay of droop under lower temperature is determined by the transport layers, that is, the Auger recombination of the transport layers are suppressed with the decrease of temperature.

As a result, to suppress the droop to achieve high-brightness and long-lifetime nanocrystal-based LEDs, future efforts should also be taken on the structure stack rather than only focused on the emitting layers. Thermal management, such as pulse mode operation and Peltier cooling, can be a promising strategies to address the droop of the device.
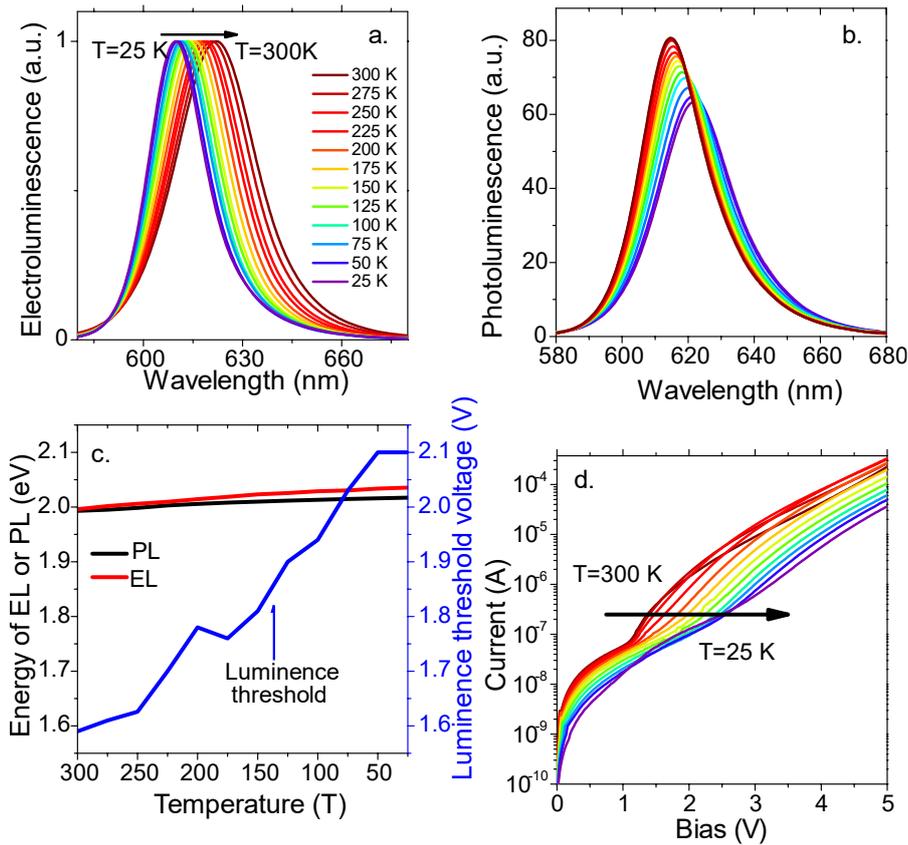
Figure III.16 (a) Electroluminescence spectra obtained at different temperatures under 5V bias. (b) Photoluminescence spectra of $Cd_{0.05}Zn_{0.95}S$ core/shell NPLs at different temperatures. (c). Energy which maximize the photoluminescence and electroluminescene signal from the $CdSe/Cd_{0.05}Zn_{0.95}S$ core/shell NPLs as a function of temperature. The shift of the luminance threshold as a function of temperature is also plotted. (d) I-V curves obtained at various temperatures of the same diode structure as before but without NPL emitting layer.

III.2.5 Toward all-nanocrystal-based LiFi-like communication

Nanocrystals-based LEDs and detectors have been investigated independently. In the present stage, both devices have reached a high level of maturity, which motivate us to integrate them into more complex systems. In this part, an all-nanocrystal-based communication setup which operates in LiFi-like operation will be explored. A schematic graph is given in Figure III.17, in which a light source, here the NPL-based LED, is used not only for lighting but also to send information.

For this application, I have updated the LED device and expanded it to a larger active area up to 50 mm² to generate more photons. Then we use a PbS nanocrystal-based solar cell, which have been proved to be an efficient broadband absorber over the visible range, to detect the modulated photons from the light source.
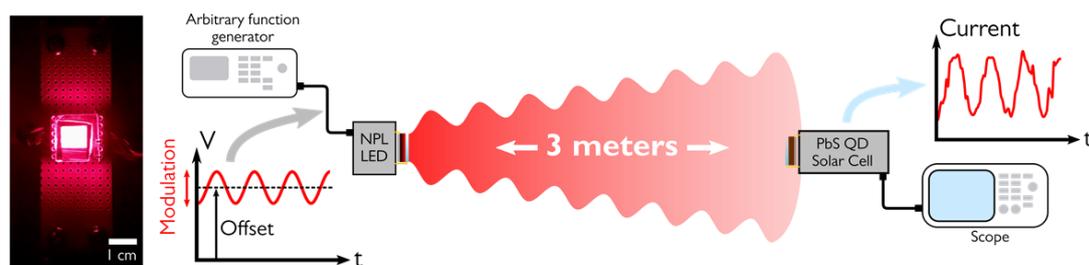
Figure III.17 Schematic graph of a LiFi-like communication setup. In the setup, the large LED is driven under a constant bias, on top of which a modulated signal is added. The signal is then collected by a PbS nanocrystal based solar cell used as a broad band detector from a distance.

III.2.5.1 The development of NPL- LED with large pixels

The fabrication of NPL-LED followed the method described previously in chapter III.2.2, except that the thicknesses of ZnO, NPLs and PEDOT: PSS layers are increased to 150 nm, 28 nm and 50 nm, respectively, to prevent electrical shorts in the device which are more likely to occur as the device size is increased.

At the same time, I investigate how the EQE will be influenced by the area of the pixels Figure III.18 presents the current-voltage-luminance characteristics for the pixel with an area of 1 mm², 18 mm² and 50 mm². The measured EQE of the three shows a high uniformity and all present an average EQE around 3.5%, demonstrating the good homogeneity and reproducibility of the all-solution layer-by-layer fabrication. It is interesting to note that, even with thicker layers, the pixels all show extremely low turn-on voltage around 1.6 V, indicating that the low turn-on voltage is rather decided by a proper band alignment than an optimized thickness.
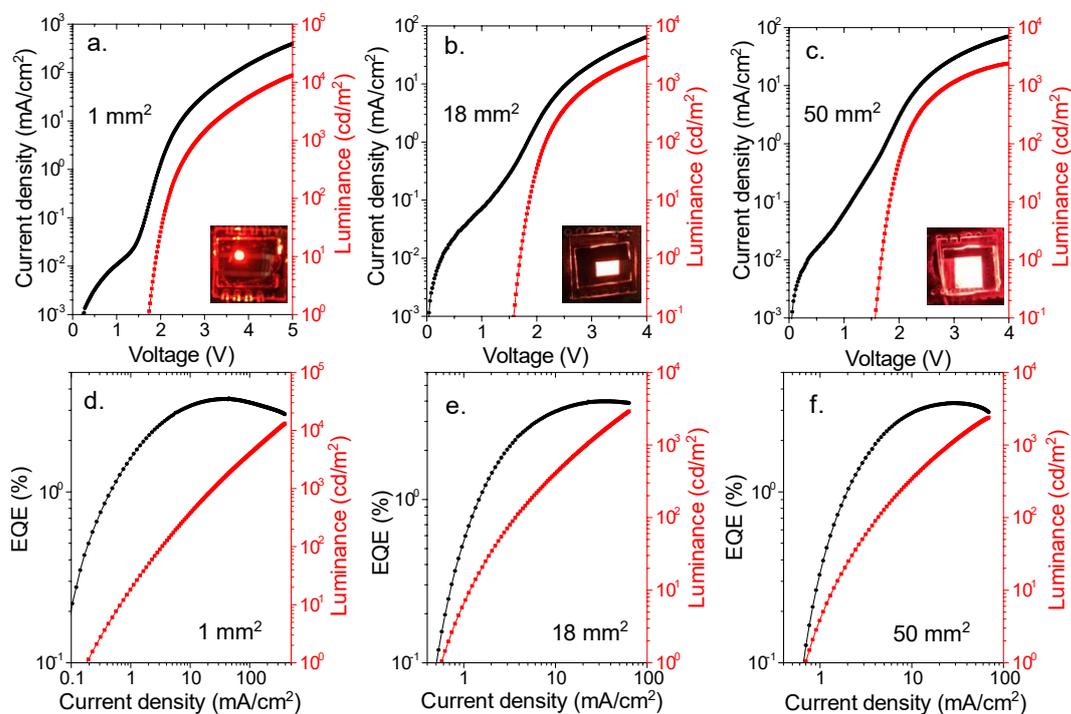
Figure III.18 Current density and luminance as a function of bias for the pixels of 1 mm² (a), 18 mm² (b) and 50 mm² (c). EQE and luminance as a function of current density for the pixels of 1 mm² (d), 18 mm² (e) and 50 mm² (f). In the inset are the working devices of different size corresponding to the curves.

III.2.5.2 Solar cell fabrication and characterization

The structure of the solar cell is proposed by Chuang et al[220]. Briefly, the vertical structure (see the inset of Figure III.19 a) relies on PbS nanocrystals with a band gap at 920 nm. The p-n junction is made of a thick layer of iodide-capped PbS and a p-type layer of EDT-capped PbS nanocrystals. The dark current of such diode operated at 0 V can be as low as 10 nA.cm^{-2},[221] and the diode present a strong current modulation under illumination (see Figure III.19 b). Interestingly, the time response of the diode has been found to be 10 ns for the rise time and 1 µs for the decay time, as shown in Figure III.19 c. This is too slow to establish a high speed (GHz or THz) telecommunication channel but enough to transfer information.
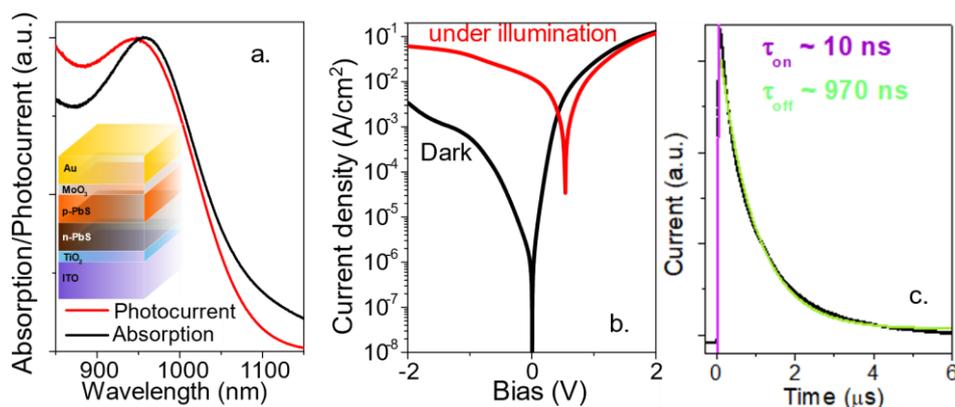
Figure III.19 (a) Absorption spectrum of the PbS nanocrystals and photocurrent spectrum of the solar cell based on the PbS nanocrystals. In the inset is a scheme of the solar cell structure. (b) I-V curves in the dark and under illumination (940 nm laser source with 56 mW.cm^{-2}) at room temperature. (c) Time response of the PbS nanocrystal based solar cell to a 1 ns pulse of laser at 355 nm. Turn-on time is around 10 ns while turn-off is around 1 µs.

The fabrication of the solar cell follows the method in ref.[221], as described below.

PbS nanocrystal synthesis The procedure is taken from Hines *et al.*[222] 0.9 g of PbO is introduced in a 100 mL three neck flask with 3 g of OA and 47 g of ODE. The flask is degassed under vacuum at 120 °C for 2 hours. Meanwhile, in an air free glove box, a mixture of 420 µL of TMS$_2$S and 10 mL of ODE is prepared in a 20 mL vial, then introduced into a 20 mL syringe. The atmosphere of the flask is switched to Ar and the temperature is set equal to 90 °C. The TMS$_2$S solution is quickly injected and the solution turns dark while the temperature drops to 80 °C. After 8 min at 80 °C, the reaction is stopped by removing the heating mantle and prompt cooling of the flask by addition of a mixture of heptane and OA. The nanoparticles are then precipitated by addition of ethanol. The formed pellet is redispersed in toluene. A second step of cleaning is repeated. Finally, the pellet is redispersed in toluene with a 50 mg/mL concentration. The solution is centrifuged to remove any colloidally unstable material. Finally, the solution is filtered on a 0.22 µm PTFE filter.

PbS Ink: A solution of NH$_4$I at 60 mg/mL in DMF (w/v) is prepared. 1 mL of this solution is added in 1 mL of PbS nanocrystal solution of concentration 50 mg.mL^{-1}. The two phases are then mixed, and we observe a phase transfer. The clear non-polar phase is discarded and the DMF solution is cleaned three times using hexane. Finally, the particles are precipitated by adding ethanol. After centrifugation the formed pellet is redispersed in fresh DMF with a concentration of 350 mg.mL^{-1}. The solution is finally centrifuged to discard any unstable material.

TiO$_2$ film deposition: TiO$_2$ films are prepared from a commercial solution (SOLARONIX Ti-Nanoxide HT-L/SC) by spin-coating on clean patterned ITO at 5000 rpm during 45 s. Prior to the spin-coating the ITO substrate heated at 110 °C in order to improve the solution wetting. Resulting ITO/TiO$_2$ sample is then annealed at 450 °C during 30 min.

PbS ink deposition: A 350 mg/mL solution of PbS ink is used for the active material layer. 50 µL of this solution is deposited on the ITO/TiO$_2$ substrate and spin-coated at 500 rpm during 300 s followed by 4000 rpm during 30 s.

p-doped PbS: 50 µL of a 30 mg/mL of OA capped PbS in toluene is deposited on the ITO/TiO$_2$/n-doped PbS substrate and spin-coated at 2000 rpm during 60 s. A solid-state ligand exchange is then performed by dipping the substrate in 1% EDT (v/v) solution in ethanol for 30 s. After that the substrate is rinsed in ethanol. This procedure is repeated twice.

MoO$_3$/Au deposition: After the deposition of PbS layers, the device is transferred from a glovebox to an evaporator. Hole transport layers MoO$_3$ 10 nm followed by 80 nm of gold are evaporated.

III.2.5.3 The LiFi-like communication

To operate the system shown in Figure III.17, we used a MFLI lock-in amplifier to drive the LED and measure the detected signal from the PbS solar cell. The signal output of the MFLI is used to send a periodic signal composed of an offset voltage (V_{offset}) over which a sinusoidal signal at 10 kHz with an amplitude (zero-to-peak) of V_{pk} is added. On the detection side, the solar cell is operated at 0 V bias and current is amplified through a Femto DLPCA-100 transimpedance amplifier (TIA). The output voltage of the TIA is then sent to the signal input of the lock-in. After demodulation, the photocurrent at the reference frequency is measured. The amplitude of the modulation is defined as the ratio of the luminance at peak voltage and the offset voltage L_{pk}/L_{offset}.

We first investigate how the distance between the source and the detector affects the signal acquisition. In this configuration, where signal collection is not optimized and conservative bias are applied on the LED, photocurrent to dark current ratio above 1 can be preserved up to 1.5 m, see Figure III.20. The drop of the signal with distance follows a decay slower than $1/R^2$ (*ie* the optical power decay), with R the source to detector distance. We attribute this behavior to the improvement in the quantum efficiency of the solar cell when the incident power flux is reduced.
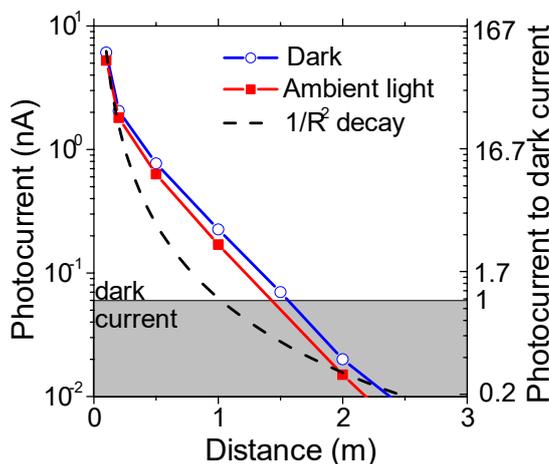
Figure III.20 Photocurrent and photocurrent to dark current ratio as a function of the LED to detector distance. $1/R^2$ decay law is also plotted. Signal here is modulated at 10 kHz.

We also consider the impact of the luminance and the signal amplitude modulation of the LED to the photo/dark current ratio, see Figure III.21 a. The latter increase with the increase of modulation and the luminance under the offset bias. For luminance compatible with lightning (5000 cd/m^2), we can conserve photocurrent to dark current ratio above 1 for signal modulation

as low as 25%, which is not eye detectable. However, the high modulation can be detrimental to the device and has to be kept under low offset bias. Transmission of binary signal of "OCN" (01001111 01000011 01001110) coupled to LED, beyond a simple plane wave, has also been detected at a 1 m distance and the output signal obtained by solar cell matches the LED input, see Figure III.21 b. Although 1 m is not an impressive distance, there has not been any effort taken to effectively collect the photons, and it is worth noting that a signal/noise ratio above 1 is not a mandatory for such a communication system.
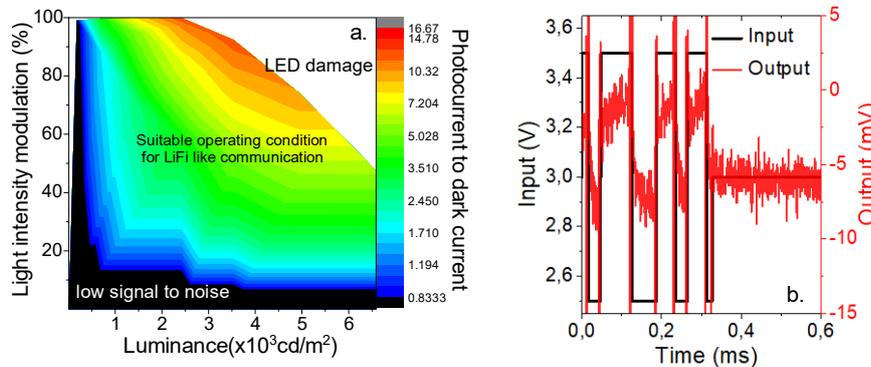
Figure III.21 (a) Photocurrent to dark current ratio as a function of the luminance of the LED and as a function of the signal modulation. 100% modulation means that the LED is turned on and off, while for lower modulation the LED is always emitting some light at certain magntude. (b) Input of the signal to the LED to transmit binarized "OCN" message and the output measured on the solar cell at a distance of 1 m.

III.2.6 Conclusions and perspectives

In this chapter, I start with optimizing the LED device charge balance by tailoring the band structure of high temperature CdSe/CdZnS core/shell NPLs. The tuning of the band gap of the core/shell NPLs is achieved by changing the CdS content in the shell. Finally, the CdSe/Cd$_{0.05}$Zn$_{0.95}$S core/shell NPLs lead to the best LED performance with a maximal EQE of 5.15%, a record-low turn-on voltage of 1.63 V and a record-long lifetime (1100h at 73 cd/m²) for NPL based LEDs.

We also investigate the efficiency droop of NPL-LED beyond focusing on the emitting layer. By characterizing the LED device under low temperatures, we found that the current where droop appears is strongly temperature dependent. At lower temperature, the droop is delayed toward larger current density. Such temperature dependence of the droop is determined by the transport layers instead of the emitting NPL layer, suggesting that more efforts need to be focused on the device stack. Thermal management is essential to mitigate the EQE droop.

We have also demonstrated the potential of all-nanocrystal LiFi-like communication by coupling a nanocrystal based LED and photodetector. This paves the way for future developments of all nanocrystal-based communication setup.

With the development of NPL-based LED with EQE close to the outcoupling efficiency (≈20%), more efforts need to be taken to improve the light extraction. On the one hand, we can rely on the directional emission from the well-aligned anisotropic nanocrystals such as NPLs and nano rods. The assembly of these materials is indeed a heat research topic nowadays. On the other hand, outcoupling of light can be improved by distorting the waveguide mode of the light trapped in the planetary device. Toolboxes of OLEDs are ready to be transferred regarding the similar structure of the two. Strategies such as building micro-lens on the back of the device[223,224] and creating corrugates inside the device[100] are promising to obtain higher efficiency.

III.3 HgTe nanocrystals for infrared electroluminescence and active imaging

As introduced in the previous part of LED, in the visible range, electrically driven quantum dot light emitting diodes (QLEDs) emitting has been tremendously advanced for the next generation cost-effective, large-area, energy-saving, wide-color-gamut, ultra-thin and flexible displays.[20,45,100] When it comes to infrared (IR) nanocrystals,[225] although considerably high photoluminescence quantum yield (PLQY) above 50% [176] has been obtained in the near infrared (NIR) and short wave infrared (SWIR), most of the work has been focused on their absorption to build optoelectronic devices such as solar cells[226-228] and IR sensors[229,230], rather than harnessing their emission properties. However, there is a demand for electrically driven, wavelength tunable infrared light sources which can also be compatible with versatile substrates for optical communications[231], bioimaging[232] and spectroscopy[233].

Current NIR and SWIR light emitting diodes are dominated by epitaxially-grown quantum well structures made of III-V semiconductors. Such sources have been highly desirable for telecommunications where high emitted power and fast modulation are mandatory. Epitaxial structures suffer though, from restricted spectral tunability and difficulties in integration with other materials.[171] Organic LEDs, like QLEDs, enable room-temperature non-epitaxial fabrication, are however limited below 1 μm.[234] As a result, nanocrystals stand out as the best candidate for bright, spectrally tunable and versatile substrate compatible IR light emitting diodes.

For nanocrystal based NIR and SWIR LEDs, lead sulfide (PbS)[222] is the most investigated material, as summarized in Table III-5. However, PbS suffers from a long PL lifetime[235] (μs and more), which prevents high brightness. In addition, in lead chalcogenides, the states in the vicinity of the Fermi level are highly degenerated (8 times), which makes it more challenging to achieve population inversion for stimulated emission. Because of these limitations, other NIR materials including InAs[236], silver chalcogenides,[99,237-239] CIGS[240,241] and derivatives, as well as mercury chalcogenides have been recently investigated for their electroluminescence.[242] Particularly, II-VI semiconductors benefit from a higher growth maturity [63,243] including the growth of 2D emitters (nanoplatelets) with extremely narrow emission linewidth.[244] Among the II-VI nanocrystals, HgTe nanocrystals are the most mature candidates with a tunable absorption from visible to THz[65] . Its vicinity with the bulk HgCdTe alloy has attracted years of efforts to grow confined forms of HgTe for light emission,[68,245-250] including stimulated emission.[251] Paradoxically, in spite of their high PLQY and ability toward longer wavelengths compared to other chalcogenides, researches on electrical pumping of HgTe nanocrystals are still at an early stage[174,175].
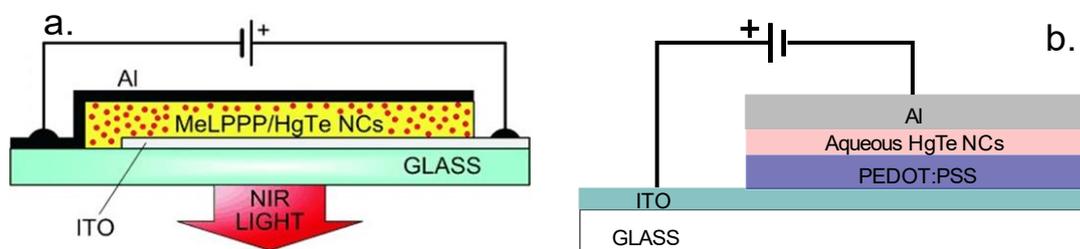
Figure III.22 (a) An infrared LED structure based on a blend of conjugated polymer (MeLPPP) and HgTe nanocrystals. The figure is adapted from [174]. (b) An infrared LED structure with HgTe nanocrystals as emitting layer and PEDOT:PSS transport layer.[252]

Before our study, the HgTe nanocrystal-based LEDs has been based on outdated and suboptimal structures, as presented in

Figure III.22. Those devices show poor performances such as low EQE in the magnitude of 0.01%, turn-on voltage much higher than the infrared bandgap, and parasite emission from the polymers[174].

Table III-5 State-of-the-art for nanocrystal-based infrared LEDs

Device structure	Active material	EL (nm)	V_{on} (V)	Radiance (W/sr.m²)	EQE (%)	Ref
ITO/ZnO/PbS:ZnO/PbS/Au	PbS+ZnO	1400	0.6	9.0	7.9	[177]
ITO/ZnO/PbS:ZnO/PbS/Au	PbS+ZnO	1380	0.7	35	8	[178]
TO/ZnO/Al₂O₃/PbS-halide/CPB/ MoO₃/Au	PbS halide	1280	3.5	7.42	0.1	[253]
ITO/ZnO/QDs/NPB/MoO₃/Al	PbS/CdS Core/shell	1500		6.04	4.12	[254]
ITO/TiO₂/QDs/F8/MoO₃/Al	PbS+ perovskite	1160-1390	<1	2.6	5.2	[255]
ITO/PbS/Ag	PbS	1350	1.2	0.29	1.6	[46]
ITO/ZnO/QDs/CPB/MoO₃/Au	PbS/CdS	1200	0.6	0.75	4.3	[176]
ITO/PEDOT:PSS/QDs/ZnO/Al	PbS	1054	0.7	6.4	2	[171]
TO/PEDOT:PSS/QDs/BCP/LiF/Al	PbSe: MEH-PVV	1280	3	-	0.83	[256]
ITO/Pentacene/QDs/BCP/Al	PbS	1200	1	-	1.15	[257]
ITO/PVV/QDs/Mg/Ag	PbS:MEH-PVV	1160	-	-	0.27	[232]
ITO/TPD or NPD/QDs/Alq₃ or BCP/Mg:Ag	PbSe	1330-1560	-	-	0.0001	[258]
TO/TiO₂/perovskite+Ag₂S@SiO₂ /porphyrin/MoO₃/Ag	Perovskite +Ag₂S@SiO₂	1397	2	83.93	16.98	[237]
ITO/PEDOT:PSS/QDs/Ca/Al	InAs/ZnSe Core/shell	1000-1300	2	-	0.5	[259]
ITO/PEDOT/HgTe/Al	HgTe	1600	1	-	0.02	[175]
ITO/QDs/Al	HgTe:MeLPP	1300	10	-	-	[260]
ITO/ZnO/HgTe:ZnO/PbS/Au Generation 1	HgTe/ZnO	250-1600	0.6	9	0.7	[261]
ITO/ZnO/HgTe:ZnO/PbS/Au Generation 2	HgTe Seeds/ZnO	1400	0.6	19	0.25	

Here in this part of infrared light emitting diodes, I revisit HgTe nanocrystals for bright infrared electroluminescence (EL) by applying a solar-cell-inspired all-inorganic structure, see Figure III.23. The structure is based on a stack of indium tin oxide (ITO)/zinc oxide (ZnO)/ZnO:HgTe/PbS/gold stack, where the emitting layer consists of a ZnO/HgTe nanosized

bulk heterojunction, which drives the doping and charge balance in the system. The resultant LED shows sub-band gap turn-on voltage (0.6 V), long operational lifetime (several hundreds of hours at high radiance), and high radiance up to 19 WSr^{-1}m^{-2}. Finally, we conduct short wavelength infrared (SWIR) active imaging, where illumination is obtained from our bright HgTe nanocrystal-based LED and demonstrate moisture detection.

This work is a result of multiple efforts. I synthesize the nanocrystals with support from Yoann Prado and I fabricate and characterize the LEDs. The photoemission measurement is a teamwork at synchrotron Soleil, with the assistance of Mathieu Silly, the beamline scientist of Tempo. The TEM imgaes are mainly provided by Xiang Zhen Xu from ESPCI, and some are from Gilles Patriarche from C2N. The time-resolved photoluminescence measurements and analysis are conducted by Delphine Lagarde, Cédric Robert, and Xavier Marie from INSA Toulouse. The SWIR imaging and active imaging was conducted in collaboration with Simon Ferré from the New Imaging Technologies (NIT).

III.3.1 The design of the new-generation HgTe nanocrystal-based LED

In a typical nanocrystal-based LED structure, the emissive nanocrystal layer is sandwiched by charge transport layers (CTLs), whose roles are to promote the electrons, or the holes injected from contact electrodes to nanocrystal conduction or valence bands respectively, to radiatively recombine with each other. As a result, the design of a LED depends on the identification of CTLs with appropriate energy levels and conduction properties. For a LED working in IR range, the increase of the energy barrier between the electron and hole transport layers is far less an issue due to the reduced energy spacing between conduction and valence bands of the emitters.
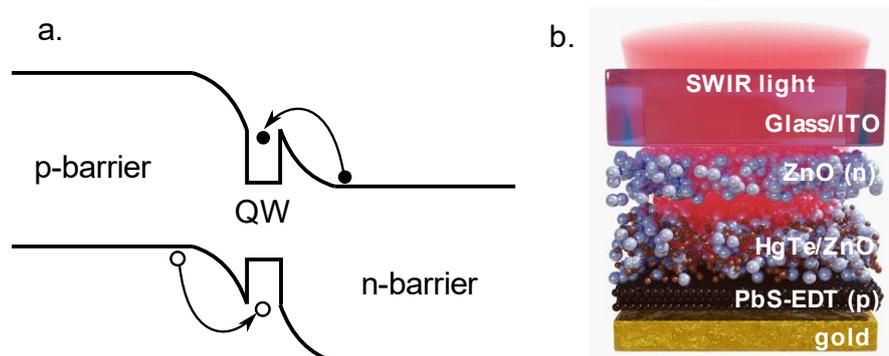
Figure III.23 (a) Schematic of band diagram of a typical III-V LED based on a heterojunction with a quantum well at the interface. (b) A colloidal equivalent of (a), with ZnO nanocrystals as n-barrier and EDT capped PbS nanocrystals as p-barrier. An emitting layer made of a HgTe/ZnO blend is sandwiched between the two barriers. Au and ITO are chosen as anode and cathode, respectively.

In the IR range, LEDs and laser diodes based on III-V epitaxially-grown semiconductors are made of a p-n junction, at the interface of which a quantum well is introduced to confine the carriers and thus facilitates the exciton recombination, as shown in the scheme of Figure III.23 a. A colloidal equivalent of this design for LED has been recently proposed by Pradhan et al.[177] In their device, the n- and p-side of the junction rely respectively on the well-established ZnO and EDT-capped PbS nanocrystals, which are widely utilized for solar cells.[262,263] The emitting layer is constituted of a blend of ZnO and PbS nanocrystals, in which the wide-band-gap ZnO nanocrystals is expected to remotely passivate the mid-gap traps of PbS emitters by forming a type I heterostructure. Here, we apply this concept to the electroluminescence of HgTe nanocrystals. The proposed design of the HgTe based LED is depicted in Figure III.23 b, where the ZnO is used as an electron transport/hole blocking layer, the PbS with EDT as capping

ligands is used as a hole transport/electron blocking layer, and a layer of mixed HgTe/ZnO nanocrystals is designed as emitting layer.

III.3.2 Synthesis and characterization of the building-block nanocrystals

According to the proposed all-nanocrystal-based LED device in Figure III.23 b, I start with the synthesis and characterization of the nanocrystals, including ZnO, HgTe and PbS nanocrystals, which will be integrated to the device structure. Their optical, morphological, and crystalline properties are analyzed with spectrometer, transmission electron microscopy (TEM) and X-ray diffraction. To determine their doping and energy levels at the absolute energy scale, we conducted X-ray photoemission at the Tempo beamline of synchrotron SOLEIL.

III.3.2.1 The synthesis and characterization of ZnO as n-type layer

Synthesis of ZnO nanoparticles dispersed in chloroform: The procedure is adapted from Pradhan et al.[264] with minor modifications. In a 100 mL three-neck flask, Zinc acetate dihydrate (0.98 g) is dissolved in 42 mL of methanol under vigorous stirring and the temperature of the solution is set as 60 °C. In another vial, 0.49 g of KOH is dissolved in 22 mL of methanol. The KOH solution is added dropwise to the zinc acetate solution during 4 min at constant temperature of 60 °C. The reaction mixture is kept under the same conditions for the next 2.5 h. In the end of the reaction, the heating mantle is removed, and the solution cooled down to room temperature naturally. The reaction mixture is separated in two falcons and centrifuged at 6000 rpm for 2 min. After discarding the supernatant, equal amount of methanol is added to mix with the pellet, and another centrifugation is conducted. After three rounds of purification, the ZnO nanoparticles are dispersed in a mixed solvent with 2% butylamine in chloroform. The concentration of ZnO nanocrystals is set at 30 mg/mL, and they are filtered through 0.22 μm PTFE filter before use.

The absorption spectrum of ZnO nanoparticles shows a band edge at around 340 nm or 3.65 eV (Figure III.24 a). TEM image of the ZnO nanocrystals shows a quasi-spherical shape, see the inset of Figure III.24 a. The X-ray diffraction reveals a wurtzite phase of ZnO nanocrystals, see Figure III.24 c. Fitting diffraction peak with the Scherrer's law ($d = \frac{0.93\lambda}{FWHM*cos\theta}$, with d the size of the nanoparticles, λ the wavelength of Cu K$_\alpha$ used, FWHM the linewidth of diffraction peak and θ the diffraction peak) leads to an estimated size of 8.3 nm, which is in consistent with the size observed from the TEM image.
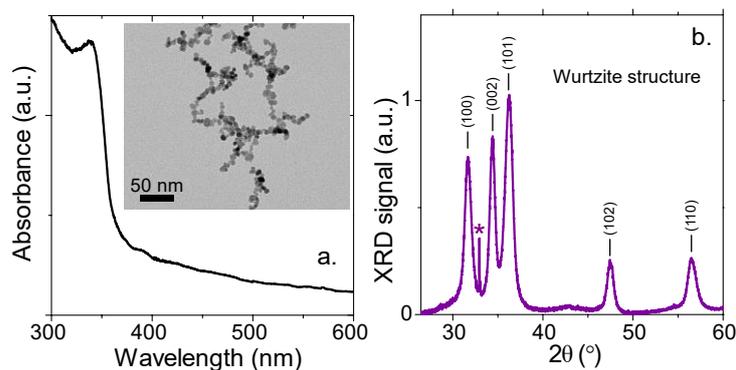
Figure III.24 (a) Absorption spectrum of ZnO nanocrystals. In the inset is a corresponding TEM image. (b) X-ray diffraction pattern of ZnO nanocrystals which shows a wurtzite structure. The peak marked with * corresponds to Si substrate uner the sample.

From X-ray photoemission spectrum related to the cut-off of the secondary electrons, we can determine the work function of the ZnO nanocrystals to be 3.64 eV (Figure III.25 a), while from

the low binding energy part of the photoemission spectrum, the valence band of ZnO nanocrystals is located 3.3 eV below the Fermi level (Figure III.25 b), suggesting a Fermi level close to the conduction band (Figure III.25 c), confirming the n-type doping of ZnO nanocrystals.
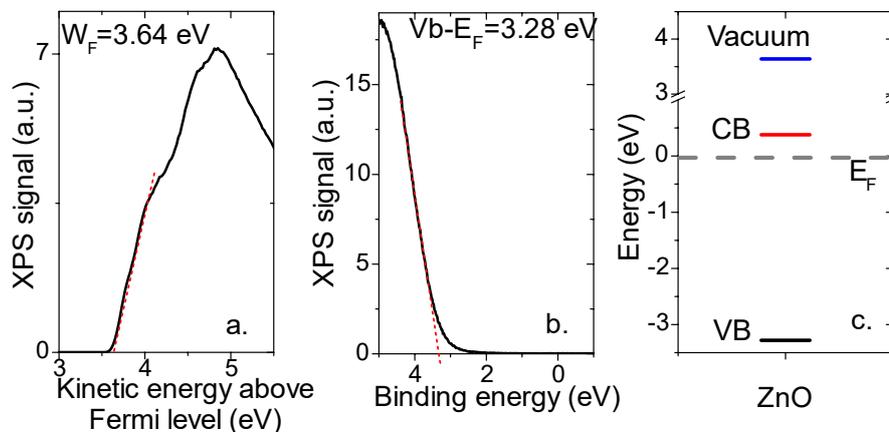
Figure III.25 (a) Photoemission spectrum relative to the secondary electron kinetic energy cut-off for ZnO nanocrystal arrays. (b) Photoemission spectrum relative to the valence band for ZnO nanocrystal arrays. (c) Reconstruction of electronic spectrum for ZnO nanocrystals with respect to vacuum level.

III.3.2.2 The synthesis and characterization of HgTe nanocrystals

The HgTe nanocrystals that will be used as SWIR emitter are synthesized through the reaction of mercury salts with Te precursors in the presence of thiols and a coordinating solvent (oleylamine) at low temperature ($\approx$60 °C). The procedures for the TOP:Te preparation and nanocrystal synthesis are descriebd below.

1 M TOP:Te precursor: 2.54 g of Te powder is mixed in 20 mL of TOP in a three-neck flask. The flask is first degassed at room temperature for 5 min and then degassed for another 20 min after heated up to 100 °C. Next, the atmosphere is switched to N_2 and the temperature is raised to 275 °C. The solution is stirred until a clear orange color is obtained. The flask is cooled down to room temperature and the color switches to yellow. Finally, this solution is transferred to a nitrogen-filled glove box for storage.

HgTe nanocrystal synthesis : The synthesis procedure is taken from Geiregat et al.[265] In a 25 mL three-neck flask, 270 mg of $HgCl_2$ (1 mmol), 1.6 mL (6 mmol) of dodecanethiol and 8 mL of oleylamine are degassed under vacuum at 110 °C for 1 h. The atmosphere is switched to N_2 and the temperature is set to 60 °C. When the temperature stabilizes at 60 °C, 1 mL of TOP:Te solution is quickly injected, and the growth is allowed for 1 min. The reaction is quenched by injecting 10 mL of toluene, and a water bath is used to further cool down the mixture. The reaction mixture is precipitated by methanol and redispersed in toluene twice. Then a centrifugation is conducted while the mixture is dispersed in 7.5 mL of toluene to remove the colloidally unstable parts. The nanocrystals are precipitated and redispersed with methanol/toluene for another three to four times and finally stored at a concentration of 30 mg/mLin toluene. The solution is filtered with a 0.22 μm PTFE filter before use.

The optical feature of the as-synthesized HgTe nanocrystals appears in the SWIR with an absorption edge at 1100 nm (1.12 eV) and a Stokes shifted PL peaking at 1300 nm (0.95 eV), see Figure III.26 a. The photoluminescence quantum yield (PLQY) of the synthesized HgTe nanocrystals is measured to be 45%, which is comparable with visible nanocrystals.The obtained nanocrystals are small with a size around 4 nm, according to TEM image (Figure III.26 b) and Scherrer's law from X-ray diffraction pattern (Figure III.26 c).
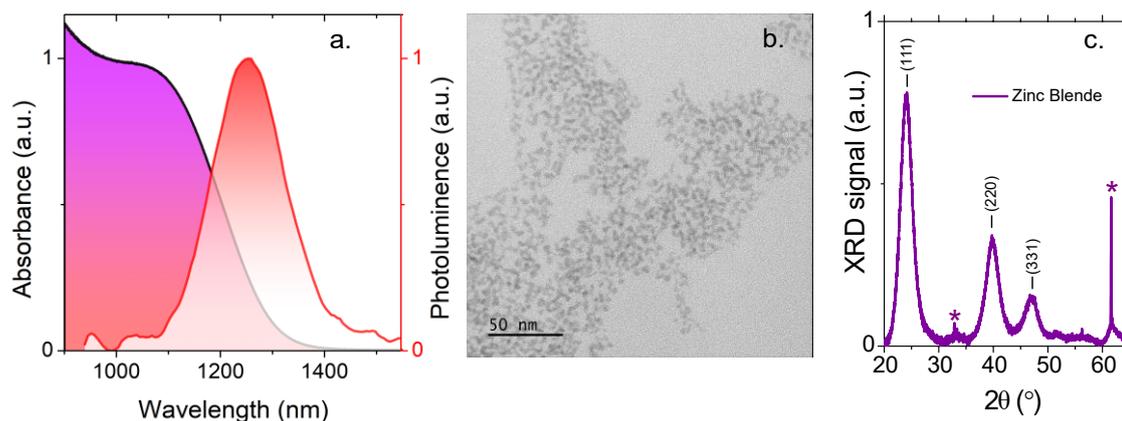
Figure III.26 Absorption and photoluminescence spectra (a), TEM image (b) and X-ray diffraction pattern (c) of HgTe nanocrystals with a PL peak at 1300 nm.

From photoemission, we can determine the work function of the 4 nm HgTe nanocrystals to be around 4.5 eV (Figure III.27 a), consistent with the previously reported value for HgTe nanocrystals.[170,266] The valence band is located ≈0.24 eV below the Fermi level (Figure III.27 b), suggesting a Fermi level in the bottom half of the band gap (Figure III.27 c) and a *p*-nature doping for this HgTe material, which is common for small sized HgTe nanocrystals.[243,267]
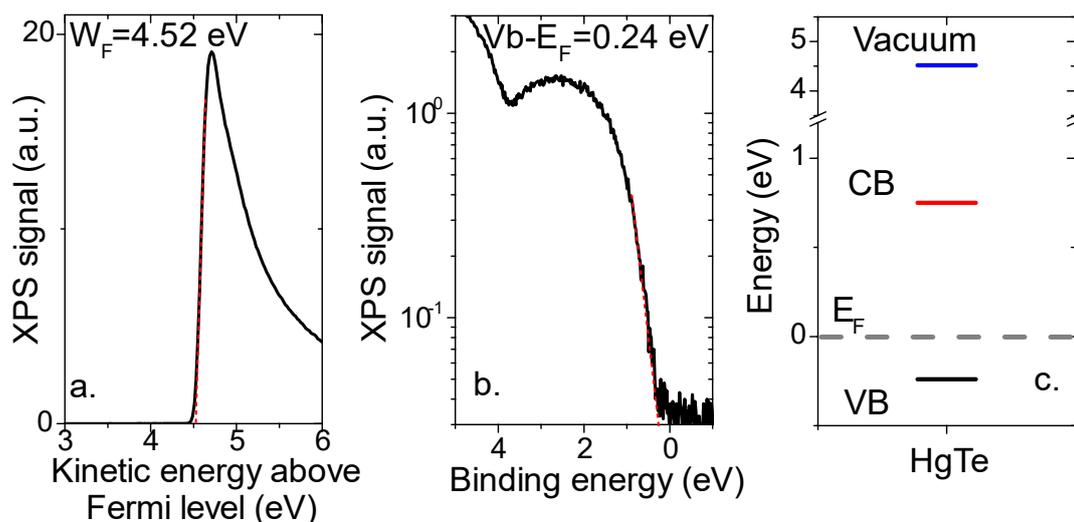
Figure III.27 (a) Photoemission spectrum relative to the secondary electron cut-off of HgTe nanocrystal arrays capped with MPA ligands. (b) Photoemission spectrum relative to the valence band of HgTe nanocrystal arrays. (c) Electronic spectrum of HgTe nanocrystals with respect to vacuum level.

We have also analyzed the temperature dependence of the HgTe band gap through the photoluminescence (PL) spectrum variation as a function of temperature. Two clear trends can be observed: (i) the higher the temperature, the bluer the PL signal (Figure III.28 a). This inverted temperature dependence compared to conventional semiconductors is resulted from the specific band structure of HgTe. We determine a value of 68 $\mu eV.K^{-1}$ for dE_G/dT. The second trend relates to an increase of the PL signal while the temperature is reduced (Figure III.28 b).
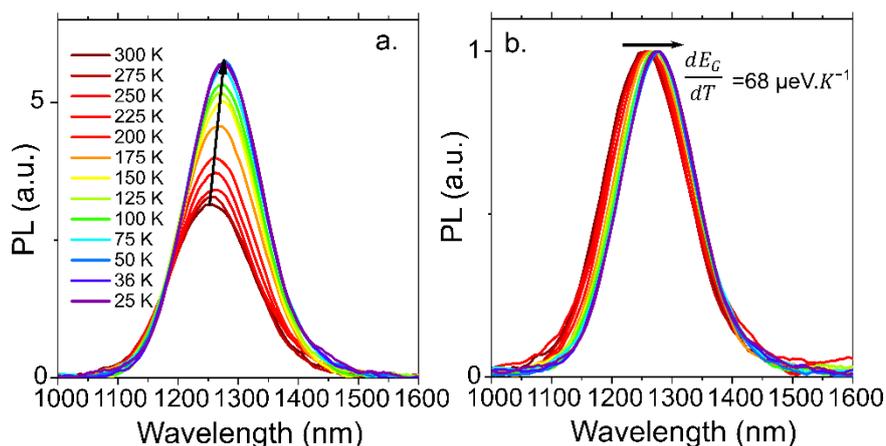
Figure III.28 PL (a) and normalized PL (b) spectra for a film made of HgTe nanocrystals at different temperatures.

III.3.2.3 The synthesis and characterization of PbS nanocrystals

PbS nanocrystal synthesis: The procedure is inspired by Hines *et al.*[268] 0.9 g of PbO powder is introduced in a 100 mL three neck flask with 3 g of OA and 47 g of ODE. The flask is degassed under vacuum at 120 °C for 2 hours. Meanwhile, in an air-free glove box, a mixture of 420 µL of TMS$_2$S and 10 mL of ODE is prepared in a 20 mL vial, then introduced into a 20 mL syringe. The atmosphere of the flask is switched to Ar and the temperature is set as 90 °C. The TMS$_2$S solution is quickly injected and the solution turned dark while the temperature drops to 80 °C. After 8 min at 80 °C, the reaction is stopped by removing the heating mantle and promptly cooling of the flask by the addition of a mixture of heptane and oleic acid. The nanoparticles are then precipitated by the addition of ethanol. The formed pellet is redispersed in toluene. A second step of cleaning is conducted. Finally, the pellet is redispersed in toluene with a 50 mg/mL concentration. The solution is centrifuged to remove colloidally unstable material. Finally, the solution is filtered on a 0.22 µm PTFE filter.

The absorption edge appears around 960 nm (1.3 eV), see Figure III.29 a. The material is also photoluminescent and the maximum of the emission peak is around 1100 nm. According to the TEM image (Figure III.29 b), the PbS nanoparticles are sphere with a diameter around 4 nm.
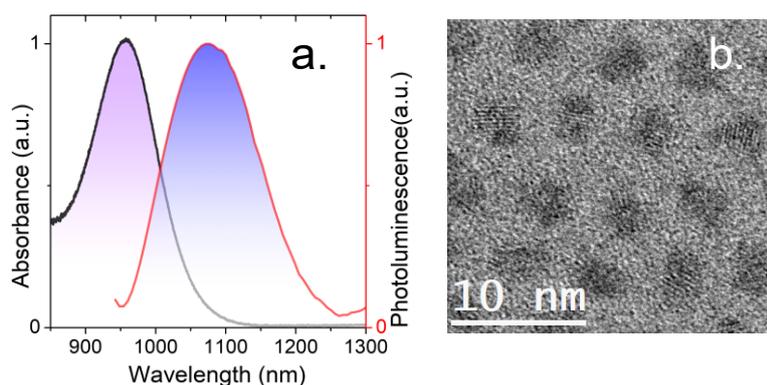
Figure III.29 (a) Absorption and photoluminescence spectra of PbS nanocrystals with a absorption edge at 960 nm. (b) TEM image of the above PbS nanocrystals.

From photoemission spectra, we can determine the work function of the obtained PbS nanocrystals to be 4.3 eV (Figure III.30 a), while the E_F-V_b value is estimated to be ≈0.5 eV (Figure III.30 b), which indicates a Fermi level in the bottom half of the band gap (Figure III.30 c) and a p-type nature of PbS capped with EDT.
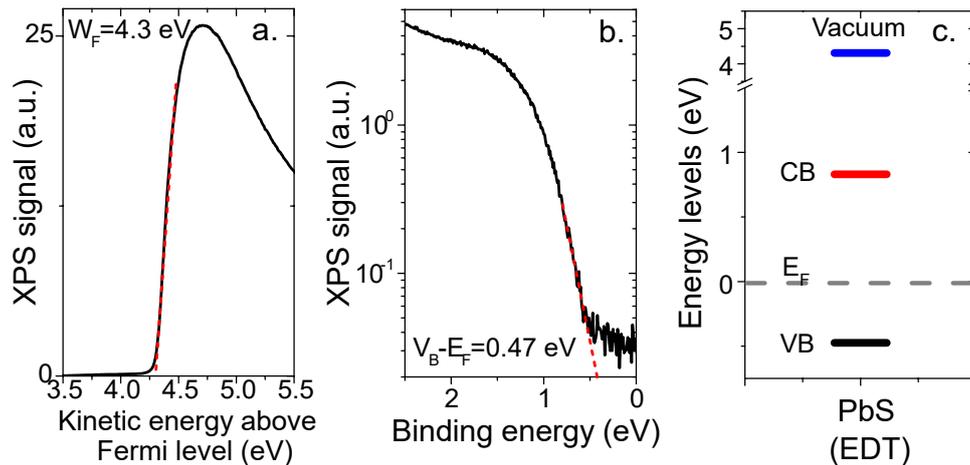
Figure III.30 Photoemission spectra relative to the secondary electron cut-off (a) and relative to the valence band (b) of PbS nanocrystal film with an excitonic peak at 960 nm and capped with EDT. (c) Proposed electronic spectrum of the EDT-capped PbS nanocrystal array with respect to vacuum level.

III.3.2.4 Photoemission spectrum of ITO substrates

To finish the characterization of all the layers of the LED, we conduct X-ray photoemission on the ITO substrates and determine the work function to be 3.92 eV, smaller than commonly cited values, which is around 4.8 eV.[100,173]
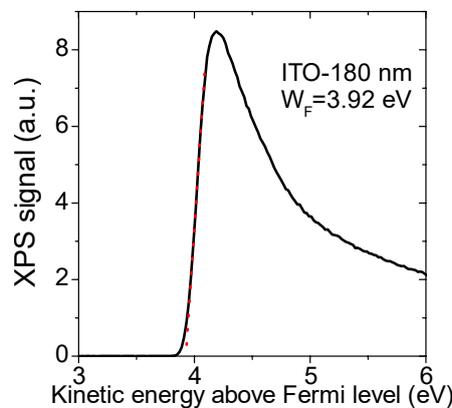
Figure III.31 Photoemission spectrum related to the cut-off of the secondary electrons for ITO substrate with a thickness of 180 nm. The work function is determined to be 3.92 eV.

III.3.2.5 Band alignment and band bending of the LED structure

With the energy levels of components contained in the LED structure, a band alignment of the whole LED stack (ITO/ZnO/HgTe/PbS/Au) can be constructed (Figure III.32 a). Furthermore, the band bending of the device system under equilibrium conditions is also proposed, see Figure III.32b, from which we can see that the electrons injected from ITO cathode can flow to the conduction band of ZnO nanocrystals with ease, and then transferred to HgTe emitting layer for radiative recombination of SWIR photons. The PbS-EDT layer is expected to act as an electron blocking layer with a higher conduction band than that of HgTe nanocrystals. On the other hand, the holes injected from Au can flow to HgTe layer for recombination, while being blocked by ZnO nanocrystals with a deep valence band.
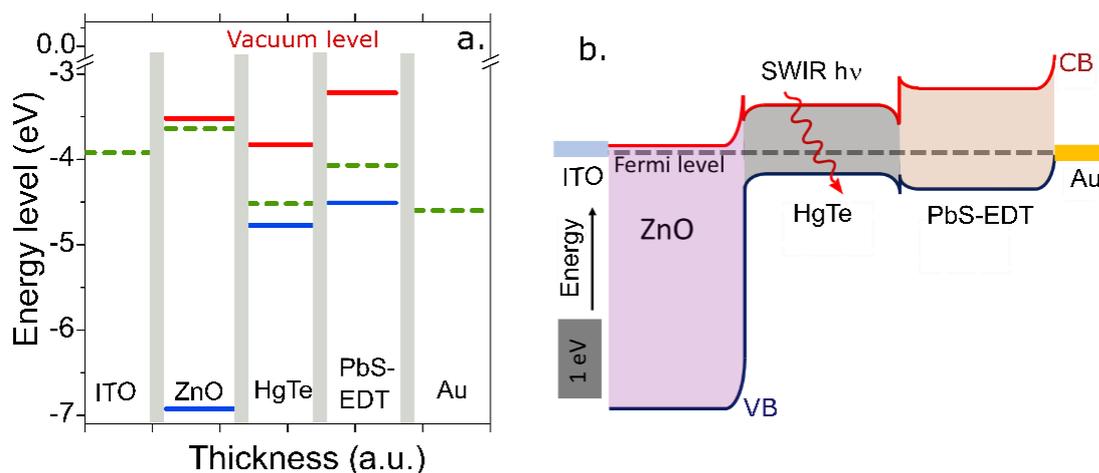
Figure III.32 (a) Band alignment of the different layers involved in the ITO/ZnO/HgTe/PbS/Au diode, with 0 eV corresponding to the vacuum level, the red line to the conduction band, the blue line to the valence band, and the green dashed line representing the Fermi level. (b) Schematic illustration of band bending in the LED device without applying a bias.

III.3.3 The investigation of HgTe/ZnO heterojunction as light emitter

As introduced in III.3.1, the design of emitting layer with mixed HgTe/ZnO nanocrystals is inspired by the LED structure from the group of Konstantatos[177], in which a large-band-gap ZnO competent is expected to remotely passivate the traps of infrared emitters, and in turn improve the electroluminescence properties. We thus transfer this concept to our HgTe-based LED, and before integrating the HgTe/ZnO layer into device, I investigate the composition, optical properties, doping as well as the conduction properties of the ZnO/HgTe mixture nanocrystals with different ratio.

III.3.3.1 The composition of the HgTe/ZnO mixture

In this HgTe/ZnO mixture, the integrity of each particle is preserved, as can be seen from the TEM image (Figure III.33 a) of a HgTe (25%)/ZnO mixture. It is worth noting that, for the sake of convenience, throughout the this part, the HgTe/ZnO mixture ratio is defined by the volume percentage of HgTe solution in the mixture solution. Here, HgTe (25%)/ZnO means the volume of HgTe solution take up 25% of the mixture volume. Before mixing, both the HgTe and ZnO are of the same concentration of 30 mg/mL.

The absorption spectra of different HgTe/ZnO ratio are displayed in Figure III.33 b. From the spectra of HgTe/ZnO mixture film, we can observe a band-edge of HgTe nanocrystals at 1200 nm in the NIR, while the band-edge of ZnO appears as a discontinuity in the curve at 340 nm. The absorption spectra of the mixture are the weighted sum of their two components, which suggests the absence of alloying between the two materials.
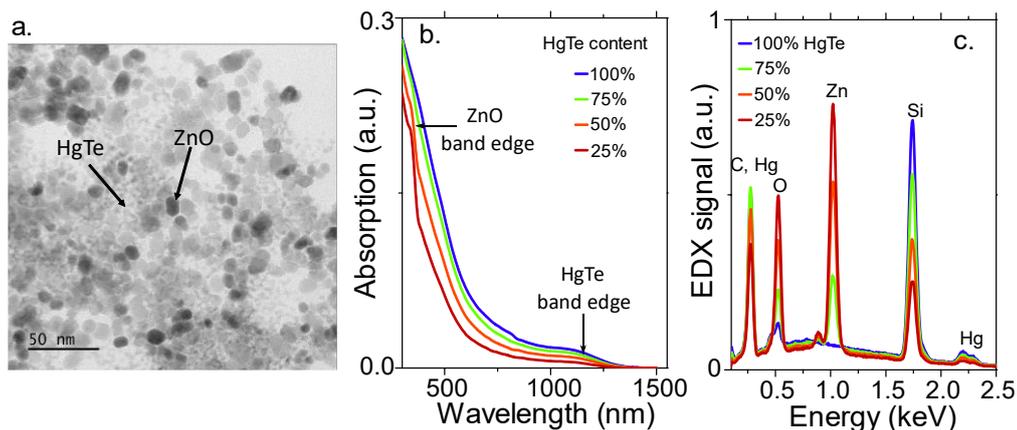
Figure III.33 (a) TEM image of HgTe(25%)/ZnO mixture. (b) Absorption spectra of mixture made of HgTe/ZnO nanocrystals with various HgTe content. (c) Energy dispersive X-ray spectroscopy spectrum relative to mixture made of HgTe/ZnO nanocrystals with various HgTe content.

Figure III.33 c and Table III-6 provide the result of the Energy dispersive X-ray spectroscopy (EDX) for films made of HgTe/ZnO nanocrystals with various HgTe content. From X-ray diffraction, we have extracted the size of the ZnO (8.3 nm) and HgTe (4 nm) nanocrystals. This means a HgTe nanocrystal contains 510 Hg atoms, while each ZnO nanocrystal has around 4180 Zn atoms. In combination with the atomic ratio of Hg/Zn ratio reveled from EDX, we can thus convert the volume ratio into particle number ratio, see Table III-6. The 25-50 % range of HgTe content corresponds to roughly a HgTe:ZnO ratio of 1, which is capable of forming continuous percolation paths with both nanoparticles.

Table III-6 Atomic composition and nanocrystal ratio for the films made of HgTe/ZnO nanocrystals with various HgTe content.

HgTe volume ratio	Hg (%)	Zn (%)	Atom Zn/Hg	HgTe/ZnO NP
100%	2.25			
75%	2.01	4.57	2.27	3.68
50%	1.7	12.62	7.42	1.23
25%	1.52	19.31	12.7	0.66

III.3.3.2 The effect of ZnO addition on the PL of HgTe emitters

The integrity of HgTe nanocrystals upon ZnO addition is further confirmed by the identical PL shape of thin films made of different HgTe/ZnO ratios, see Figure III.34 a. Also, the time-resolved PL on the HgTe/ZnO films are measured and analyzed by our collaborator, Xavier Marie's group from INSA Toulouse. The results show that the PL dynamics of the pristine HgTe are preserved after being mixed with ZnO nanoparticles, see Figure III.34 b. The time-resolved PL intensity of all the thin films with diferrent HgTe/ZnO ratio is characterized by a main decay time of about 20 ns, which is in agreement with recent measurements of the radiative recombination of the HgTe nanocrystals confined states.[245] This PL decay time is two orders of

magnitude shorter than the one measured for PbS nanocrystals.[269] It is also noteworthy that longer decay times (≈400 ns) can be evidenced in at the end of the kinetics. This can be attributed to recombination involving localized states at the surface of the nanocrystals.[251]

This effect of ZnO addition on the PL dynamics of HgTe nanocrystals is however in contrast with the case of PbS nanocrystals when they are blended with ZnO nanocrystals in a solar cell.[270] In this study relating to the PbS nanocrystals[270], the transient PL decay of PbS/ZnO nanocrystal array is fitted with two time constants of 14 ns and 160 ns, while for PbS nanocrystal array, in addiation to these two components, an ultrafast time constant (below 1 ns) is also observed, which signifies the PL quenching process via a nonradiative recombination center.[271] In our case, there is no such untrafast PL decay component observed from HgTe nanocrystal array, in consistent with a high PLQY (above 45%) of this HgTe nanocrystals.
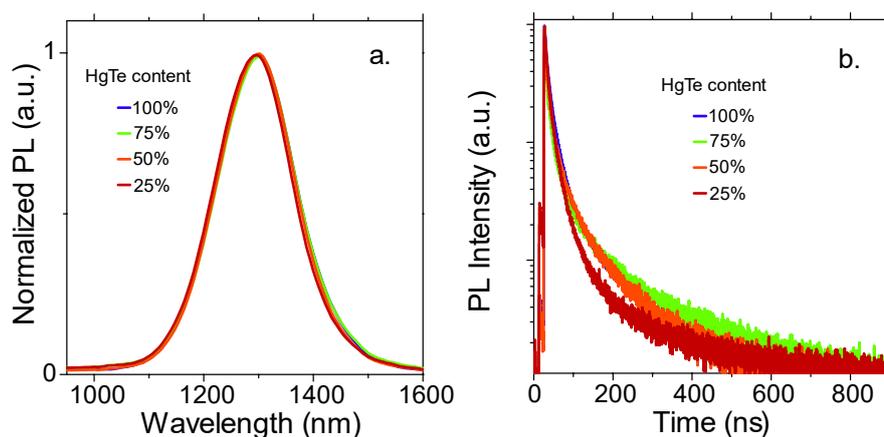
Figure III.34 (a) Normalized photoluminescence of thin films made of various ratio of HgTe/ZnO nanocrystals. (b) Photoluminescence intensity as a function of time after excitation with 1.5 ps laser pulses at 780 nm for a film of HgTe Nanocrystals (100%) and mixtures of HgTe and ZnO nanocrystals (25-75 % HgTe in volume ratio).

Back to the intial motivation of enhancing PLQY of HgTe nanocrystal emitters by remotly passivate their trap states with ZnO nanocrystals, to evaluate this effect of ZnO addition, we compare the PL intensity of HgTe/ZnO nanocrystal arrays normalized the absorbance at the wavelength of excitation (405 nm here). This can be a meaure to compare the relative PLQY of the film. As presented in Table III-7, with 75%, 50% and 25% of HgTe in the mix, the PLQY of the film is increased by a 63%, 69% and 85% compared with the pure HgTe nanocrystal array, respectively. This indeed indicates the benefits of ZnO in improving the PLQY of the film. However, in the follwing we will demonstrate that another more important mechanism is at play related to the addition of ZnO nanocrystals.

Table III-7 The relative PLQY HgTe/ZnO nanocrystal array with various HgTe content.

HgTe volume ratio	Relative PLQY
100%	1
75%	1.63
50%	1.69
25%	1.85

III.3.3.3 The doping of the HgTe/ZnO heterojunction

Photoemission spectroscopy is used to probe the work function and the valence band of the HgTe/ZnO mixture with various HgTe contents. As HgTe nanocrystals are introduced to the ZnO film, we observe that the work function increases with the HgTe content (Figure III.35 a). There also appears new states in the vicinity of the Fermi level coming from the valence band of HgTe nanocrystals (see Figure III.35 b), which gradually shifts the valence band of the HgTe/ZnO toward the Fermi level, making the material more and more p-type, see the inset of Figure III.35 b. This observation is consistent with the p-type nature of pristine HgTe (Figure III.27), whose introduction to the n-type ZnO (Figure III.25) gives rise to an intermediate situation where the valence band states are coming from HgTe nanocrystals.
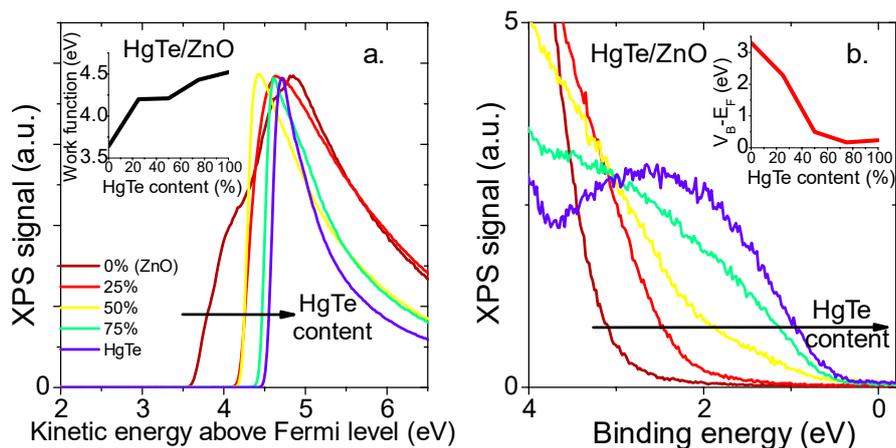
Figure III.35 (a) Photoemission spectra relative to the secondary electron cut-off for ZnO/HgTe thin films with various HgTe content. Inset: the change of work function with the HgTe content in the mix, (b) Low binding energy part of the photoemission spectra, relative to the valence band of ZnO/HgTe with various HgTe content. Inset: the energy difference between valence band and the Fermi level as a function of the HgTe content in a ZnO/HgTe mixture.

This hypothesis is further confirmed by transport measurements conducted in an electrolyte-gated field effect transistor configuration, see Figure III.36 a. A ZnO-based device shows a typical n-type conduction with a rise of conduction under electron injection (i.e. positive gate bias), see Figure III.36 b. Whereas, HgTe-only device presents an opposite behavior with p-type conduction, see Figure III.36 d, consistent with the photoemission data indicating the Fermi level in the vicinity of the valence band (Figure III.35 b and Figure III.27). However, when a mixture of HgTe/ZnO film is prepared, we obtain an ambipolar behavior with both electron and hole conductions, see Figure III.36 c.

Thus, we can conclude that the role of ZnO in the HgTe/ZnO mixture is beyond passivating the trap states of the HgTe nanocrystals, but more evidently electrically tuning the transport of the HgTe/ZnO layer by forming a bulk heterojunction between p-type HgTe and n-type ZnO. The concept of bulk heterojunction has been widely applied in photovoltaics to overcome the trade-off between excitation diffusion length and optical absorption length.[272] The increased interfacial area of the heterojunction allows the depletion region spreading in three dimensions in the photoactive layer. As a result, the photoactive layer can be made thicker to absorb more solar photons yet enabling efficient charge carrier extraction.[273] This heterojunction is promising in the LED as a knob to drive the electron/hole balance of the device.
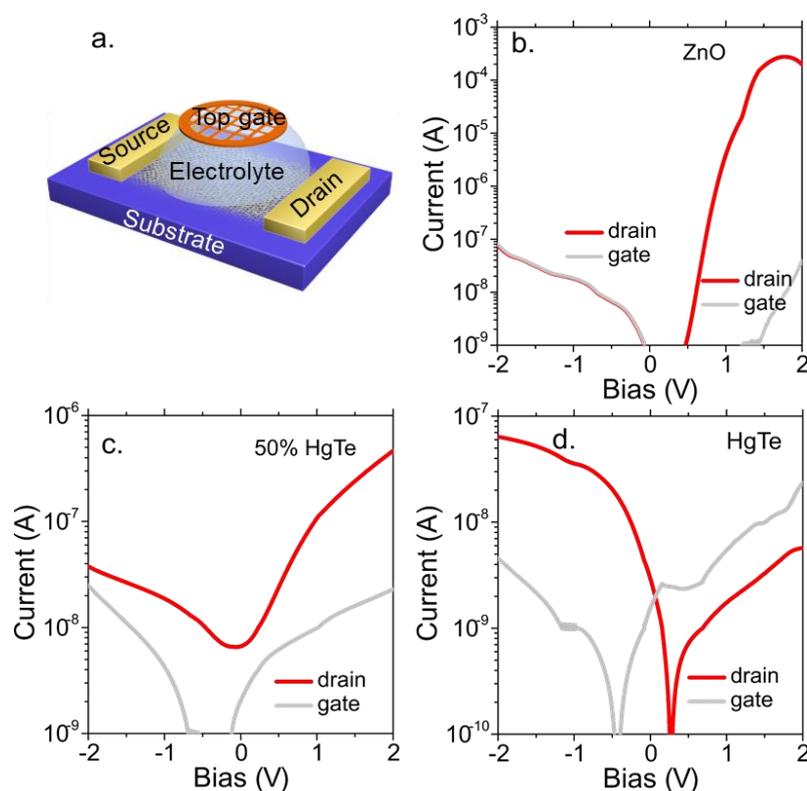
Figure III.36 (a) A scheme of an electrolyte-gated field effect transistor. (b)Transfer curve (i.e. drain and source current as a function of gate bias) of a thin film made of ZnO nanocrystals showing n-type behavior with only electron conduction. (c) Transfer curve of a film made of HgTe (50%)/ZnO mixture presenting an ambipolar behavior with both electron and hole conduction. (d) Transfer curve of a a HgTe nanocrystal film showing a p-type behavior with only hole conduction. The surface chemistry of all the samples are 3-mercaptopropionic acid (MPA). The drain source bias is set as 500 mV except for the case of ZnO nanocrystals, for which the value is set as 1 V.

III.3.4 Fabrication and characterization of the SWIR HgTe based LEDs

In this part, the detailed fabrication method for all-solution nanocrystal-based LED diodes will be presented, which includes the ITO substrate patterning by optical lithography, the layer-by-layer spin coating of n-type ZnO layers, the HgTe/ZnO emitting layers and p-type PbS layers, and a final deposition of Au cathode. The figure of merits for SWIR LEDs and their characterization method will also be introduced.

III.3.4.1 Fabrication of HgTe-based SWIR LEDs

ITO substrate patterning: ITO substrates (10 Ω/sq) with a thickness of 180 nm are cut into 15 mm × 15 mm pieces and cleaned by sonication in acetone for 5 min. After sonication, the substrates are rinsed with acetone and isopropanol before dried completely with N_2 flow. The substrates are further cleaned with O_2 plasma for 5 min to remove organic residuals on the surface. After cleaning, TI-Prime and AZ 5214E photoresist are sequentially spin-coated on the surface of ITO substrates at the rate of 4000 rpm for 30 s and baked at 110 °C for 120 s and 90 s, respectively. In the next stage, a mask aligner is used to expose the substrates to UV light for 20 s through a lithography mask (1 mm width). Photoresist is then developed using AZ 726 developer for 20 s before rinsed with deionized water and dried with N_2 flux. After another 5-

minute plasma cleaning, the substrates are etched in a 25% HCl (in water) bath for 10 min at 40 °C before being dipped in deionized water. Finally, the lift-off is conducted in an acetone bath. Before using, the patterned ITO substrates are cleaned with acetone and isopropanol.

n-type ZnO layer deposition: On a piece of patterned ITO, the ZnO nanoparticles dispersed in chloroform are spin coated at 4000 rpm for 3 min. The ZnO film is then annealed at 250 °C in air. Another layer of ZnO is deposited and annealed, leading to a thickness around 100 nm.

HgTe-ZnO emitting layer deposition: The prepared HgTe solutions in Toluene and ZnO solutions in chloroform are mixed in separated vials according to the desired volume ratio. The mixtures are sonicated for a homogeneous mixing. Since the composition of solvent varies with mix ratio, different spin speed was chosen to make sure that the thickness of 1-layer deposition is around 40 nm. Taking the 50% volume ratio of HgTe and ZnO as an example, 60 mL of mixed solution was used to cover the ZnO-coated substrate and spun at 4000 rpm for 30 s. Several drops of MPA in methanol (0.05% V/V) are casted on the film and allowed to stay for 10 s to conduct ligand exchange. The MPA solution is dried by spinning at 4000 rpm. The excess ligands are rinsed twice with methanol by drop casting and spin. The speed for 100% HgTe, 75% HgTe and 25% HgTe were 2000, 2500 and 6000 rpm, respectively.

p-type PbS layer deposition: The PbS nanocrystals with an excitation peak of 960 nm is used as the hole transport layer. Inside an air-free glovebox, the PbS solution in toluene is diluted to 30 mg/mL and filtered with 0.22 μm PTFE filter before use. Then a layer of PbS nanocrystal is deposited on the top of the HgTe-ZnO emitting layer by spin coating at 2500 rpm for 15 s. The ligand exchange is conducted with EDT in acetonitrile (0.03% V/V). The EDT solution is drop casted to cover the PbS layer and allowed to stay for 45 s before dried with spin coating. Subsequently, the film is rinced twice with acetonitrile and then dried. Three layers of EDT capped PbS nanocrystals are deposited and the thickness is measured to be 50 nm.

Au top contact deposition: Inside a thermal evaporation chamber with a vacuum below 5×10^{-6} mbar, 80 nm of Au is deposited onto the PbS layer though a shadow mask. The pixel size, which is defined as the overlap of the ITO and Au contact, is 1 mm².

III.3.4.2 Characterization of SWIR LEDs

Electroluminescence (EL) and photoluminescence (PL): EL and PL spectra are obtained by a Flame NIR Spectrometer equipped with InGaAs detector from Ocean optics.

Current-Voltage-Radiance characteristics: The current-voltage-power of the LED device is collected with a Keithley K2400 source meter unit and a PM100A power meter coupled with the S122C Ge detector from Thorlabs. The radiance can be calculated from the power of all the photons collected.

EQE and radiance can be extracted according to reference[212], and the method has been introduced in III.2.3.3. Briefly, assuming that the emission of LED is Lambertian, with our setup, the EQE can be calculated as $EQE = \frac{N_p}{N_e} = \frac{\pi P_{det} l^2 \lambda e}{s_1 hcI}$, with P_{det} the power obtained by the detector, l the distance between the pixel and the center of the detector, λ the peak wavelength of the electroluminescence, e the charge of the electron, s_1 the area of the detector, h the planck constant, c the speed of the light and I the current though the pixel. The radiance of the LED can be determined by $R = \frac{F_{ext}}{\pi s_2} = \frac{\pi P_{det} l^2}{\pi s_1 s_2}$, with S_2 the area of the pixel.

Operational lifetime measurement: During the lifetime measurement, the LED is driven at a constant current corresponding to a certain initial radiance. The change of radiance (power) and bias with time were recorded with a source meter and a power meter coupled with the S122C Ge detector.

III.3.4.3 The performance of the HgTe-based SWIR LEDs

Using the fabrication and characterization methods described above, I start with optimizing the LED structure by tuning the ratio of the HgTe/ZnO in the emitting layer and by changing the thickness of the emitting layer.

To determine the optimal ratio of the HgTe/ZnO mixture, a series of devices with identical thickness of emitting layer (80 nm) but different HgTe/ZnO ratio are compared. As shown in Figure III.37, the maximum EQE increases with the addition of ZnO to the HgTe nanocrystals, and the optimal ratio is between 25% and 50% of HgTe, corresponding to a HgTe/ZnO nanocrystal ratio of around 1, in which case a heterojunction with an ambipolar conduction can be achieved. There is indeed EL signal observed for HgTe-only (i.e., ZnO-free) device, but the conductivity and the radiance are very low compared with its ZnO-containing counterparts. The improved performance for HgTe/ZnO-based device can be explained by a more balanced carrier injection in the emitting layer.
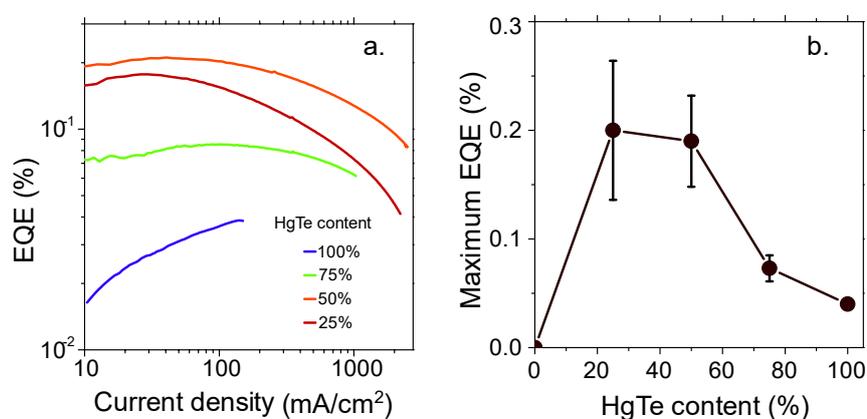
Figure III.37 (a) EQE as a function of current density for LED devices using emitting layers with various HgTe content. (b) The maximum EQE as a function of the HgTe content in the emitting layer.

The thickness dependence of the emitting layer is further tested based on the HgTe (50%)/ZnO heterojunction, and the best performances come from a device with a 120 nm HgTe/ZnO emitting layer, see Figure III.38 a and b. The best device shows a EQE of 0.67% and a turn-on voltage of ≈ 0.6 V (see Figure III.38 b), which reveals a clear sub band gap ($E_G = 0.95$ eV for these HgTe nanocrystals) operation. Interestingly, under a 500 mA.cm^{-2} current density, we obtain a radiance of 9 W.Sr^{-1}m^{-2}, see Figure III.38 b, which is similar to the value reported for PbS LEDs with a 10 times higher EQE.[177] This high brightness is enabled by the fact that the onset of EQE droop ($J_{1/2EQE} \approx 0.75$ A.cm^{-2}, the current density at which EQE drops by half) is much higher than that of PbS-based LEDs, which shows a $J_{1/2EQE} \approx 0.05$ A.cm^{-2}.[177] This higher current roll-off, is likely resulted from a reduced Auger recombination in HgTe nanocrystals and a fairly balanced charge injection in the system due to the bulk heterojunction.[274]

It is also worth pointing that the proposed device significantly enhances the performance (EQE is tens of times higher, turn on voltage is reduced by half) of previously reported LED based on HgTe nanocrystals.[174,252] Last, we have tested the operating lifetime of the diode (see Figure III.38 c) and observe a quasi-constant performance over a 30 h period at a radiance of 0.32 W.Sr^{-1}.m^{-2} in ambient conditions without encapsulation.
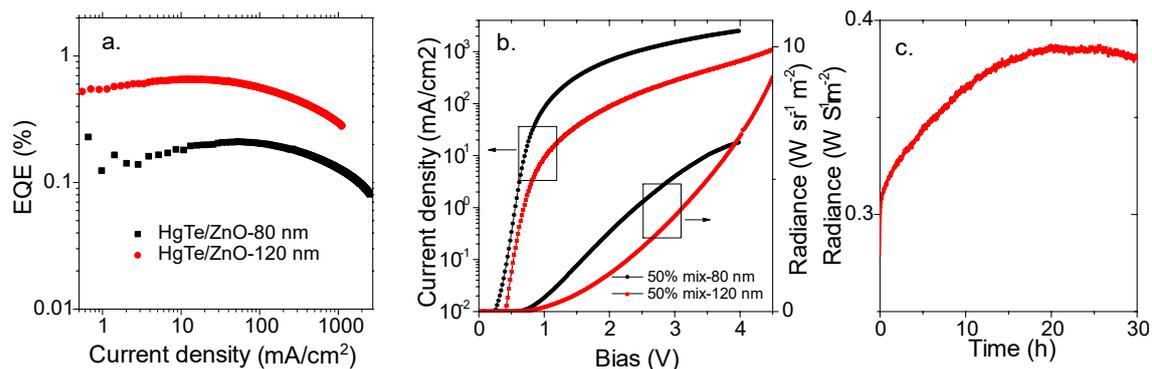
Figure III.38 (a) EQE as a function of applied current density for two thicknesses of the emitting layer made of HgTe(50%)/ZnO. (b) Current density and radiance as a function of applied bias for two thicknesses of the emitting layer made of HgTe (50%)/ZnO. (c) Radiance as a function of time for a diode operated under constant current condition (13 mA.cm^{-2}) corresponding to an initial irradiance of 0.32 W. Sr^{-1}.m^{-2}. The LED are tested and kept in ambient atmosphere without encapsulation.

For all the device fabricated following this structure, there are electroluminescence (EL) observed. Figure III.39 a show the EL spectra of the best performing device under different bias, in the inset we provide a picture of five working SWIR LEDs imaged by an InGaAs camera. The energy of this signal matches well the HgTe PL peak, see Figure III.26 a. Interestingly, there is a small contribution of the PbS NCs layer in the EL spectra around 1050 nm under operating biases just above the turn-on voltage, see Figure III.39 b. The latter disappears under bias above 1 V, because of the less favorable electron injection within the PbS layer when higher bias is applied. It is also worth noticing that the EL wavelength can easily be tuned by changing the size of the HgTe nanocrystals from 1250 to 1600 nm, overlapping with the whole telecom range, see Figure III.39 c.
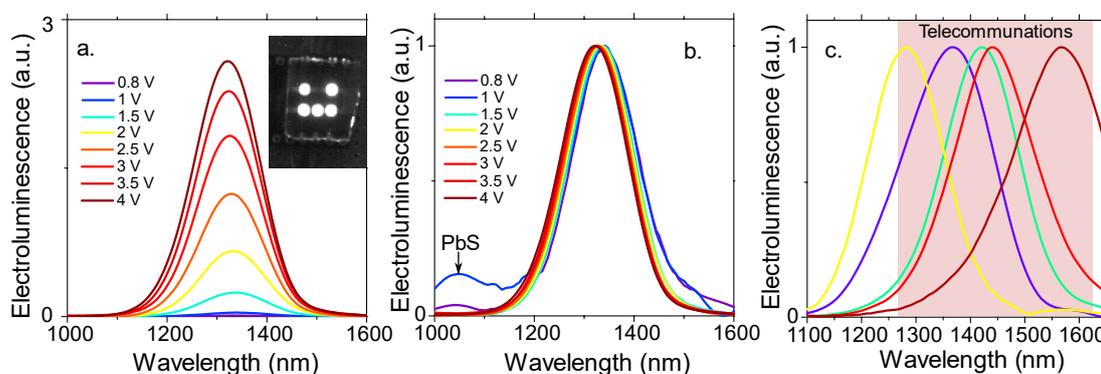
Figure III.39 (a) Electroluminescence (EL) spectra of a diode made of ITO/ZnO/HgTe/PbS/Au emitting at 1320 nm operated under different biases. (b) The normalized EL spectra of (a). (c) Normalized EL spectra obtained from the structure of ITO/ZnO/HgTe/PbS/Au using HgTe nanocrystals with different size, which covers the full telecommunication wavelength.

We also notice a small blue shift of the EL signal as higher bias is applied. There are several possible origins for the shift. Stark effect is expected to reduce the band gap of the material under electric field, which should have red shift the EL spectrum,[275] contrary to our observation. The blue shift of the EL then be due to heating. As current flows, Joule effect leads to a rise of the junction temperature. If the EL blue shift is solely from the heating-induced bandgap widening, a blue shift of 16 mV, between turn-on voltage and 4 V operation, requires a temperature rise by ≈235 °C according to the temperature dependence of the HgTe band gap (dE$_G$/dT =68 µeV.K^{-1}, see Figure III.28 b). The high temperature of ≈235 °C will undoubtedly

107

damage the HgTe nanocrystals that are grown at around 60 °C. Actually, the effect of heating can be better explained by the generalized Kirchoff's law[276,277] in which the emission process is modulated by the blackbody radiation, which generates non-equilibrium carriers and leads to such a blue shift.

III.3.4.4 Active imaging with the bright HgTe based SWIR LEDs

As in the visible, the contrast of active SWIR imaging comes from an external light source scattered differently by the objects/surfaces from the scene. This is different with the mid-IR imaging which relies on thermal contrast (*i.e.* light comes from the blackbody radiation). Briefly, active imaging is a mode of imaging where an eye-safe infrared light source illuminates a scene from which scattered photons get collected by a focal plane array, see a scheme of active imaging in Figure III.40. Beyond obvious defense, surveillance and astronomy applications, such active imaging is widely used for industrial vision such as materials sorting, moisture detection and determination of fill levels inside opaque packings.
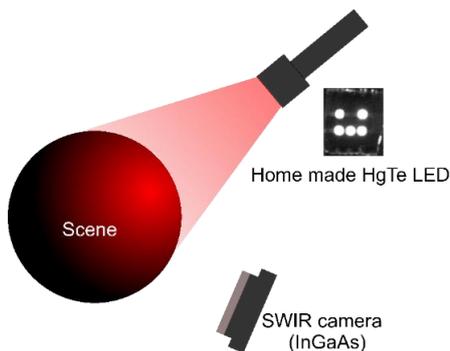
Figure III.40 Scheme of active imaging procedure. Here the home-made LED with 5 pixels working together is used as a SWIR light source.

In this part, we will take advantage of the high brightness of our HgTe based LED and test its potential for SWIR active imaging. The home-made SWIR LED is used as a light source while an InGaAs focal plane array (WiDy SenS camera from NIT) is used to collect the scattered light from the scene, see Figure III.40. The logarithmic operation of the camera enables a large contrast of the image (*i.e.* the direct signal of the LED and the scattered light from the scene) without saturation.
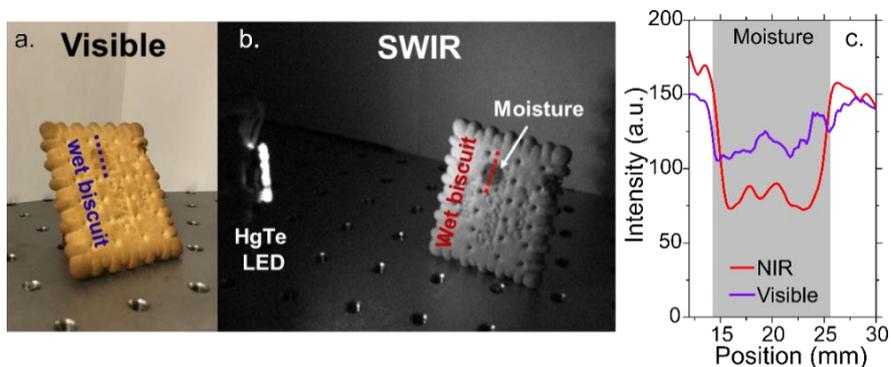
Figure III.41 Visible (a) and SWIR (b) image of a biscuit presenting a moisture stain. (c) Modulation of the intensity of the scattered light from the biscuit around the moisture stain. In the SWIR, the contrast is ≈3 times higher.

A typical application of SWIR imaging relates to water detection. While water is transparent in the visible, it strongly absorbs in the SWIR. This property is usually used to control ripening and detect moisture in food production lines. Here, we show the ability to detect moisture stain on a wet biscuit, see Figure III.41 a and b. In the visible image, the stain is barely seen, while in the SWIR the stain area is more perceivable by eye. As shown in Figure III.41 c, SWIR imaging increases the contrast along the moisture stain by a factor of ≈3 compared to the visible image.

Another important application of SWIR imaging is to see through opaque plastics and coatings. In Figure III.42 a and b, we image in the visible and in the SWIR a PET bottle filled with water. In the visible, the plastic is opaque, and it is impossible to observe the content of the bottle, while in the SWIR image, we clearly observe the presence of absorbing liquid and can thus determine its filling level. SWIR active imaging using HgTe based SWIR LED is also proved effective in segregating water from other chemicals which are also transparent in the visible range, but not absorb as much as water in this range of wavelength, see Figure III.42 c and d.
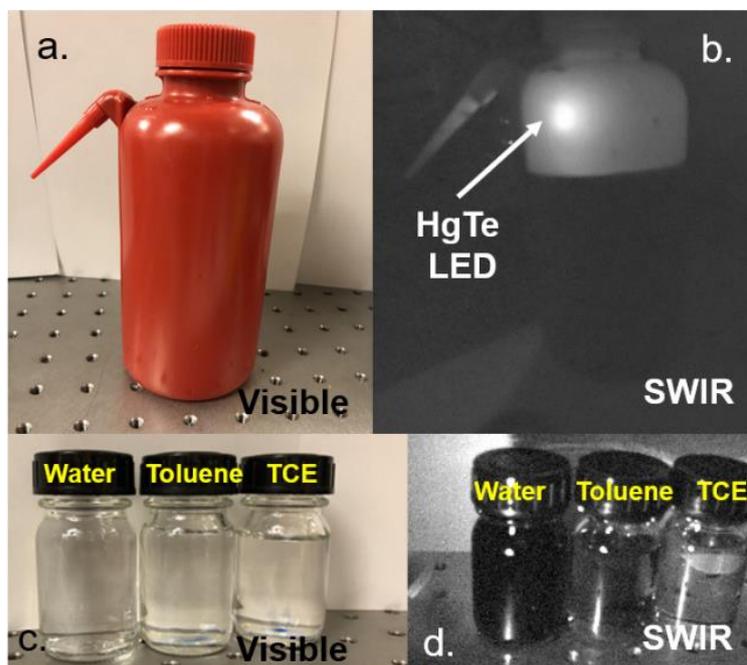
Figure III.42 Visible (a) and SWIR (b) image of a PET washing bottle with water in it. For all SWIR images, only the HgTe LED is used as light source (i.e. no visible light contribution).Visible (c) and SWIR (d) image of vials containing different solvent (water, toluene, tetrachroloethylene: TCE).

III.3.5 Toward narrower and brighter LED using sphere HgTe seeds

So far, we have demonstrated a HgTe based SWIR LED based on the glass/ITO/ZnO/ZnO-HgTe/PbS/Au structure. The LED is featured with a sub-band gap turn-on voltage, a high radiance of around 10 W Sr^{-1}m^{-2}, and a moderately high EQE and operational stability. However, one direction for further development of this LED device is to synthesis HgTe nanocrystals with superior photoluminescence features.

In this part, I will introduce a seed growth approach for highly bright SWIR HgTe nanocrystals with a with a narrower PL linewidth and a higher PLQY (75%) than the HgTe nanocrystals obtained by the procedure of Geiregat et. al. [265]. Moreover, the seed growth of HgTe nanocrystals can be achieved under ambient condition, which makes them even more attractive for low-cost large-scale room-temperature fabrication of the LEDs.

III.3.5.1 The synthesis of HgTe seeds

The seed growth of HgTe nanocrystals was initiated in the group with the support from Yoann Prado, the chemistry engineer of INSP, who has been working on the synthesis of sphere HgTe nanocrystals with a seed growth approach. The concept is inspired by recent works from Zamkov's group on CdSe nanocrystals[278]. They demonstrated the possibility to obtain dissolution recrystallization of small CdSe seeds while heating them in presence of amine and cadmium oleate.
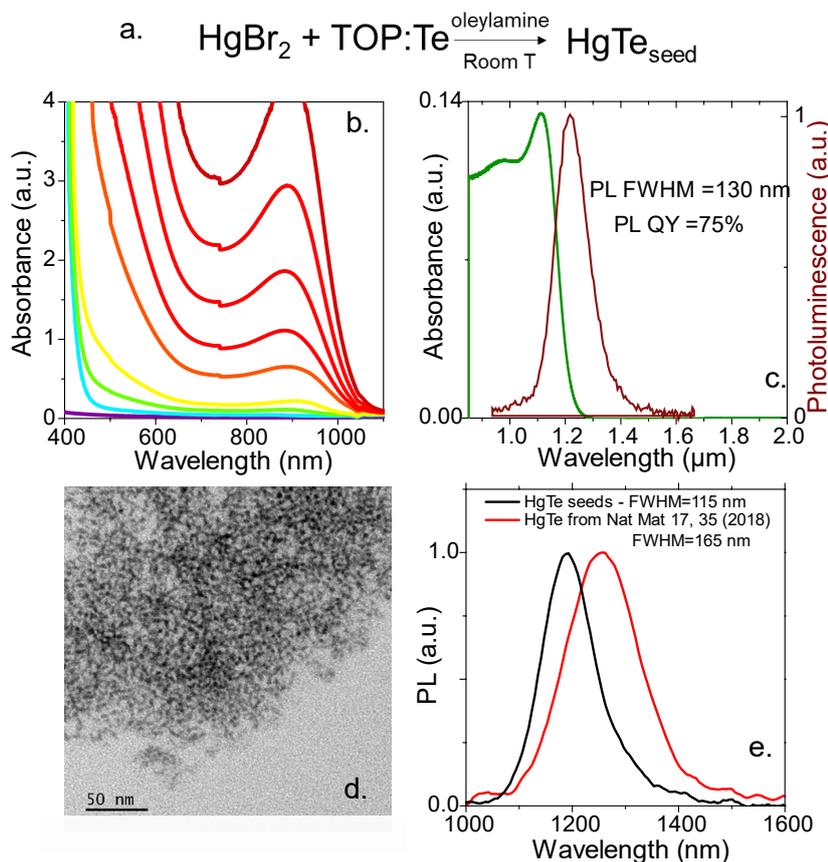
Figure III.43 (a) Chemical reaction conducted to obtain small HgTe seeds. (b) UV-vis absorption spectra for a mixture of HgBr$_2$ and TOP:Te in oleylamine at room temperature, leading to HgTe seeds. (c) Absorption and PL spectra of the quenched HgTe seeds. (d) TEM image of the HgTe seeds. (e) Comparison of PL spectrum between HgTe seeds and the HgTe synthesized using the procedure from Geiregat *et. al.* [265]

Here, we obtain the seed of HgTe by mixing HgBr$_2$ with TOP:Te in oleylamine under ambient conditions, see the reaction procedure in Figure III.43 a. As shown in Figure III.43 b, the seed is characterized by an exciton of around 900 nm, as revealed by UV-vis spectrometry. It is also shown that with time, the exciton increases in the magnitude but its peak energy stays unchanged (Figure III.43 b), indicating that there is only nucleation occurs but no growth. The HgTe seeds are extracted by quenching the reaction with long-chain thiols and the obtained HgTe nanocrystals show a band edge of 1100 nm (Figure III.43 c), suggesting that surface thiols are involved in the charge delocalization. The TEM image shows that the HgTe seeds are extremely small, whose exact size is hard to evaluate due to limited contrast resulting from such small particle and partial material aggregation, see Figure III.43 d. Nevertheless, a band edge of 900 nm is similar to the one observed from 3 monolayers nanoplatelets whose size is around 1.1 nm.[279] Such small size is consistent with the formation of magic size cluster, which will explain why we do not observe a band edge shift during the reaction.

More interestingly, the HgTe seeds show PL, see Figure III.43 c and e. The PL is narrow and presents a quality factor (ratio of the peak emission energy over the full width at half maximum) of 10, higher than the value of HgTe nanocrystals from the synthesis of Geiregat *et. al.*[265], which is 7.5, see Figure III.43 e. In addition, the PLQY reaches 75 %, which is among the highest in the infrared range. This makes that the seeds on their own are of utmost interest for LED application.

III.3.5.2 SWIR LEDs based on HgTe seeds

In this part, I integrate the highly luminescent NIR HgTe seeds to the same stack of glass/ITO/ZnO/ZnO-HgTe/PbS/Au, see Figure III.44 a, where the small HgTe seeds are used as emitting material, the gold/p-type PbS is used as hole injector, while the ITO/ZnO is used as electron injector. The emitting layer is the HgTe/ZnO bulk heterojunction, where electron conduction is ensured by ZnO and hole conduction by HgTe. The fabrication and characterization of the devices follow the procedures described in III.3.4.
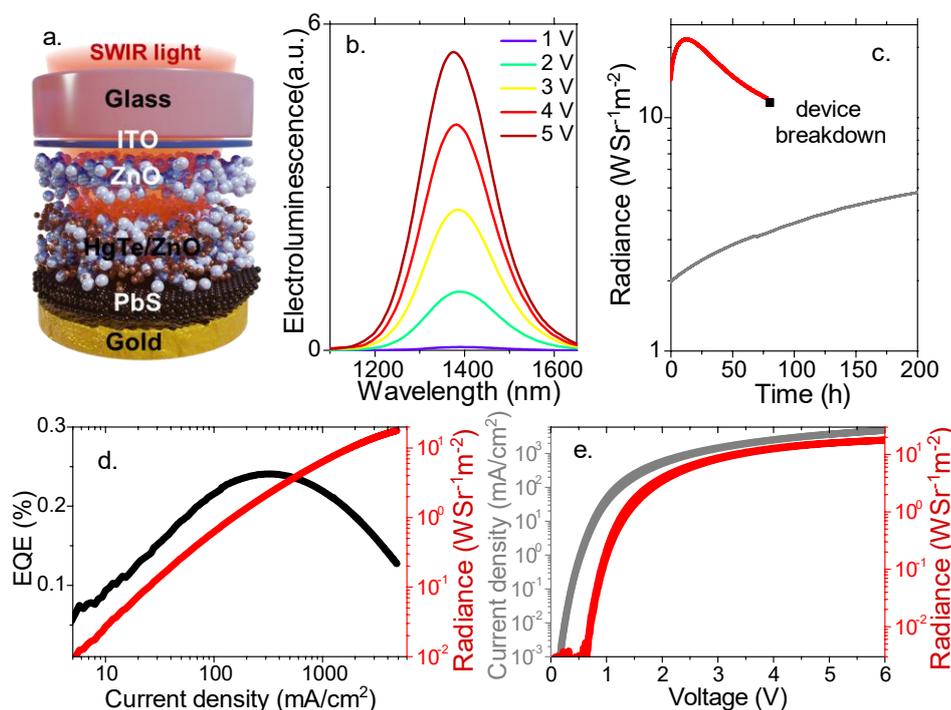
Figure III.44 (a) Scheme of a diode made of ITO/ZnO/ZnO-HgTe/PbS/Au emitting SWIR light. (b) Electroluminescence spectra of the diode as depicted in part (a) operated under different bias. (c) Radiance as a function of time for a diode operated under constant current condition (I= 3 mA for the 2 W. Sr⁻¹.m⁻² initial radiance and I=29 mA for the 15 W. Sr⁻¹.m⁻² initial radiance). (d) External Quantum Efficiency (EQE) and radiance as a function of the driving current. (e) Current density and radiance as a function of applied bias.

This HgTe seeds based LED leads to a bright electroluminescence signal (Figure III.44 b) and a low turn-on voltage of ≈0.6 V (Figure III.44 e), which corresponds to sub-band-gap ($E_G \approx 890$ meV) operation. The maximum external quantum efficiency (EQE) reaches 0.25 %, see Figure III.44 c. This EQE value remains modest compared to that (8%) achieved using PbS nanocrystals,[178] however, this diode is exceptionally bright. 80 h operation has been demonstrated with radiance above 13 W. Sr⁻¹.m⁻², see Figure III.44 c, which matches the brightness of PbS nanocrystals based LED in the SWIR and outperforms the previous HgTe based SWIR LEDs.[174,252,261] Under lower current operation (corresponding to radiance of 2-5 W. Sr⁻¹.m⁻²), we do not even observe a decay of the performance but rather a slow increase of the brightness over a week (>200 h) of continuous operation.

III.3.6 Conclusions and perspectives

To summarize, we have demonstrated LEDs based on SWIR HgTe nanocrystals. The diode structure is based on a vertical stack of ITO/ZnO/HgTe-ZnO/PbS/gold. Specially, the formation of a HgTe/ZnO heterojunction in the emitting layer can effectively tune the doping and carrier injection balance of the system, and its optimal ratio is around ≈1 HgTe per ZnO nanocrystal.

The devices show a sub-band gap operation, suggesting an appropriate band alignment of the structure. While the highest EQE remains modest at around 0.7%, the HgTe based SWIR LEDs are bright thanks to a high droop current. We demonstrate that this high brightness of this LED based LED is capable of moisture detection via active imaging. By switching to a HgTe seed as emitter, a high brightness of 19 W. $Sr^{-1}.m^{-2}$ is achieved, and long operational lifetime is demonstrated. The HgTe seed-based device can work without decay after 200 h at a radiance range of 2-5 W. $Sr^{-1}.m^{-2}$, and has achieved 80 h of operation with a high radiance above 13 W. $Sr^{-1}.m^{-2}$. Our finding paves the way for an all nanocrystal based active imaging setup by combining the proposed LED with the recent demonstration of HgTe nanocrystal based SWIR focal plane array.[266]

To improve the performance of HgTe based LED, it is worth investigating the effects of ligands on the transport and the PL properties of the emitting layer. It is well demonstrated that the surface passivation is essential for optoelectronics such as nanocrystal based solar cell.[280]

Modification of the LED structure is another route for better device performance. The structure of ITO/ZnO/HgTe-ZnO/PbS/gold is commonly adapted and proved effective for PbS based solar cells and LEDs[177,178]. While the ZnO is one of the few versatile electron transport materials, the PbS-EDT is initially designed for PbS-based optoelectronics instead of HgTe nanocrystals. As a result, hole transport layers with better hole transport/electron blocking capacity for HgTe emitters can be explored. The first thing to try is to engineer the hole injection barrier by tuning the band gap of the n-type PbS. Other p-type materials should also be explored, and one of the candidates can be Ag_2Te nanocrystals, which has long been used as hole extraction layer in HgTe nanocrystal based photodiodes.[148]

In terms of emitting layer, a gradient of HgTe/ZnO ratio can be constructed throughout the thickness to electrically engineer the carrier transport by design, and to balance the carrier injection of the system.

Last, being able to cover the telecom range from 1250 to 1600 nm, this HgTe based LED relying solely on inorganic layers rises great promises to address longer wavelengths in the future.

General conclusion and perspectives

In the infrared photodetection part of my thesis, I studied self-doped Ag_2Se nanocrystals and plasmonic ITO nanocrystals to use their mid-infrared absorption for photodetection.

For Ag_2Se nanocrystals, we confirmed their n-type doping and proposed that the doping origin is an excess of cation. We also proposed a electronic band spectrum of Ag_2Se nanocrystals with a bandgap of 260 meV or 4.8 μm, which is essential for further device design. However, the planar photoconductive device sensitized by the Ag_2Se nanocrystal arrays showed a responsivity in the magnitude of several μA/W in the mid-infrared.

For ITO nanocrystals with a straightforward remote doping mechanism and a strong plasmonic absorption, very interestinly, we found that the absorption cross-section (σ) of the doped ITO is two orders of magnitude higher than of the In_2O_3 nanocrystals without Tin doping. Combining the transport of ITO and In_2O_3 nanocrystal arrays, we proposed that the LWIR absorption of In_2O_3 nanocrystals was actually an intraband transition rather than a plasmonic resonance as commonly claimed. However, the infrared photoresponse of ITO is extremely slow with a responsivity in the order of 10 μA/W. We ascribed this responsivity to a bolometric effect and concluded that the strong absorption brought by LSPR was balanced by the extremely short carrier lifetime (several fs), which in turn leads to low photo-generated current.

Since the demonstration of the MWIR photoconduction from Ag2Se nanocrystal arrays, this topic keeps progressing. Ag2Se nanocrystals, as it is doped, suffer from high dark current in a photoconductor geometry. High dark current that generates noise is detrimental for sensitive infrared photodetection. To use the intraband Ag2Se nanocrystals for heavy-metal-free photodetection, there are two approaches that are promising to adress the dark current issue:

The first is to build a vertical device geometry. Until very recently, the group of Ko[94] proposed the first vertically stacked device composed of an Ag2Se/PbS/Ag2Se nanocrystal. This structure is inspired by the nBn (n-type/barrier/n-type) design that is commonly used for InSb[281], MCT[282] and type II superlattice[283] based infrared photodetors. By inserting a barrier layer of PbS nanocrystals between two Ag2Se nanocrystal layers, the electron flow is suppressed in the dark since the conduction band of PbS is higher than that of Ag2Se nanocrystals. The vertical nBn device shows a 8-fold increase of dark resistivity and a 70 times higher responsivity than the device without the PbS barrier.[94] Although introducing a PbS layer is contrary to the goal for heavy-metal-free photodetectors, it opens up new possibilities for device design. Instead of using PbS, we can screen "greener" wide bandgap nanocryatls, such as III-V nanocrystals, as the barrier layer.

The second way to suppress dark current can be uncoupling the absorption and transport by mimicking a quantum well structure. Our group has demonstrated that, using HgSe/HgTe mixed nanocrystals in which the intraband of HgSe nanocrystals governs the absorption while the large-bandgap HgTe barrier drives the transport, the device showed a high intraband responsivity. This concept has generated a substantial amount of opportunities for heterostructure engineering and device design.

The last part of my thesis is dedicated to the nanocrystal-based LEDs in the visible then the infrared. For different wavelengths, we targeted at different potential applications.

In the visible, the nanocrystal-based LED is promising for the next-generation large gamut display. Colloidal type I core/shell CdSe/CdZnS NPLs combines narrow emission linewidth, high PLQY, and potential for direactional emission, had been used as the emitting layer. By engineering the bandgap of the emitting layer, the best device showed a EQE of 5.2%, a record low turn-on voltage of 1.6 V for nanocrystal-based LEDs, and a record long lifetime (11000h at ≈100 cd/m²) for NPL based LEDs.

Specially, we for the first time investigated the efficiency droop of LEDs by low-temperature characterization in the device scale. We found that the efficiency droop is strongly decreased at lower temperatures. By analyzing the temperature dependence of current-voltage-luminance and emission spectra of the LED, we deduce that the delay of droop is determined by the transport layers instead of the emitting NPL layer. This finding suggests that, to mitigate efficiency droop of the device, more efforts need to be focused on the transport layers. We have also for the first time developed an all-nanocrystal LiFi-like communication setup by coupling our LED to a PbS-based broadband photodetector.

During the development of **SWIR LEDs,** I used HgTe nanocrystals, the most versatile material in the infrared, as emitter. Electroluminescence was demonstrated from a solar-cell-inspired stack composed of ITO/ZnO/HgTe-ZnO/PbS/gold. Specially, I confirmed the formation of a HgTe/ZnO heterojunction in the emitting layer, which effectively tune the doping and the charge injection balance of the device. The optimized device shows a sub-bandgap operation, suggesting an appropriate band alignment of the structure. While the highest EQE was modest at around 0.7 %, the HgTe based SWIR LEDs were bright thanks to its high droop current. We also demonstrated that this high brightness of this HgTe-based LED was capable of moisture detection via active imaging.

To further improve performance of nanocrystal-based LEDs, there are several **perspectives**:

Nanocrystal based LEDs in the visible. Since near-unity internal quantum efficiency has been achieved for all three primary colors, further improvements may come from: (1) New synthesis of nanocrystals with higher color purity, below 10 nm.(2) The synthesis of Cd-free emitters such as InP and CuInS2 and CuInSe2 nanocrystals with high emission qualities is highly desirable.[10,284] (3) Optimized LED structure with better band alignment and charge transport and injection balance (4) Thermal management of the LED device to reduce the EQE droop and to improve the long-term stability. (5) Enhanced light extraction One promising way is to use directional emission from well-aligned anisotropic nanocrystals such as NPLs and nano rods. A more versatile way can be distorting the waveguide mode of the light trapped in the planetary device by building nano or microscale lens on the back of the device.

HgTe-based infrared LEDs. (1) The first is to propose an optimized diode structure. As in the case of HgTe-based LED in the SWIR, the EQE is below 1%, despite a high PLQY above 50%. There is huge space for charge injection efficiency improvement. p-type Ag2Te established for HgTe, can be investigated as HTL. (2) The next step is to go toward longer wavelength above SWIR, to harness the widest spectral tunability of HgTe for more applications such as gas sensing. To this end, the PLQY of HgTe will drop rapidly with wavelength, which may be addressed by developing core/shell nanocrystals, or by careful ligand passivation. The low infrared transparency TCO substrate can be a issue at long wavelengths. One possible way is to replace the TCOs with mesh of metals[76]. Graphene and carbon nanotubes[285] that combines high infrared transparency and high conductivity, can also be promising alternative electrodes for infared electroluminescence.

List of References

(1) Reed, M. A.; Randall, J. N.; Aggarwal, R. J.; Matyi, R. J.; Moore, T. M.; Wetsel, A. E. Observation of Discrete Electronic States in a Zero-Dimensional Semiconductor Nanostructure. *Phys. Rev. Lett.* **1988**, *60*, 535–537.

(2) Murray, C. B.; Norris, D. J.; Bawendi, M. G. Synthesis and Characterization of Nearly Monodisperse CdE (E = Sulfur, Selenium, Tellurium) Semiconductor Nanocrystallites. *J. Am. Chem. Soc.* **1993**, *115*, 8706–8715.

(3) Peng, X.; Manna, L.; Yang, W.; Wickham, J.; Scher, E.; Kadavanich, A.; Alivisatos, A. P. Shape Control of CdSe Nanocrystals. *Nature* **2000**, *404*, 59–61.

(4) Ithurria, S.; Tessier, M. D.; Mahler, B.; Lobo, R. P. S. M.; Dubertret, B.; Efros, A. L. Colloidal Nanoplatelets with Two-Dimensional Electronic Structure. *Nature Materials* **2011**, *10*, 936–941.

(5) Hines, M. A.; Guyot-Sionnest, P. Synthesis and Characterization of Strongly Luminescing ZnS-Capped CdSe Nanocrystals. *J. Phys. Chem.* **1996**, *100*, 468–471.

(6) Schneider, H.; Liu, H. C. *Quantum Well Infrared Photodetectors: Physics and Applications*; Springer Series in Optical Sciences; Springer-Verlag: Berlin Heidelberg, 2007.

(7) Ting, D. Z.-Y.; Soibel, A.; Höglund, L.; Nguyen, J.; Hill, C. J.; Khoshakhlagh, A.; Gunapala, S. D. Type-II Superlattice Infrared Detectors. *Semiconductors and Semimetals* **2011**, *84*, 1–57.

(8) Rogalski, A. History of Infrared Detectors. *Opto-Electron. Rev.* **2012**, *20*, 279–308.

(9) CDQ Sensor Technology | Acuros CDQ Sensors | SWIR Vision.

(10) Reiss, P.; Carrière, M.; Lincheneau, C.; Vaure, L.; Tamang, S. Synthesis of Semiconductor Nanocrystals, Focusing on Nontoxic and Earth-Abundant Materials. *Chem. Rev.* **2016**, *116*, 10731–10819.

(11) Pietryga, J. M.; Park, Y.-S.; Lim, J.; Fidler, A. F.; Bae, W. K.; Brovelli, S.; Klimov, V. I. Spectroscopic and Device Aspects of Nanocrystal Quantum Dots. *Chem. Rev.* **2016**, *116*, 10513–10622.

(12) Lhuillier, E. Optoelectronics of Confined Semiconductors : The Case of Colloidal Nanocrystals and Their Application to Photodetection. HDR Thesis, Sorbonne Université, Paris, France, 2017.

(13) Kagan, C. R. Flexible Colloidal Nanocrystal Electronics. *Chem. Soc. Rev.* **2019**, *48*, 1626–1641.

(14) Kagan, C. R.; Lifshitz, E.; Sargent, E. H.; Talapin, D. V. Building Devices from Colloidal Quantum Dots. *Science* **2016**, *353*.

(15) Grim, J. Q.; Manna, L.; Moreels, I. A Sustainable Future for Photonic Colloidal Nanocrystals. *Chem. Soc. Rev.* **2015**, *44*, 5897–5914.

(16) Steigerwald, M. L.; Brus, L. E. Semiconductor Crystallites: A Class of Large Molecules. *Acc. Chem. Res.* **1990**, *23*, 183–188.

(17) Sahu, A.; Qi, L.; Kang, M. S.; Deng, D.; Norris, D. J. Facile Synthesis of Silver Chalcogenide (Ag2E; E = Se, S, Te) Semiconductor Nanocrystals. *J. Am. Chem. Soc.* **2011**, *133*, 6509–6512.

(18) Talapin, D. V.; Lee, J.-S.; Kovalenko, M. V.; Shevchenko, E. V. Prospects of Colloidal Nanocrystals for Electronic and Optoelectronic Applications. *Chem. Rev.* **2010**, *110*, 389–458.

(19) Dabbousi, B. O.; Rodriguez-Viejo, J.; Mikulec, F. V.; Heine, J. R.; Mattoussi, H.; Ober, R.; Jensen, K. F.; Bawendi, M. G. (CdSe)ZnS Core–Shell Quantum Dots: Synthesis and Characterization of a Size Series of Highly Luminescent Nanocrystallites. *J. Phys. Chem. B* **1997**, *101*, 9463–9475.

(20) Dai, X.; Deng, Y.; Peng, X.; Jin, Y. Quantum-Dot Light-Emitting Diodes for Large-Area Displays: Towards the Dawn of Commercialization. *Advanced Materials* **2017**, *29*, 1607022.

List of references

(21) Peng, X.; Schlamp, M. C.; Kadavanich, A. V.; Alivisatos, A. P. Epitaxial Growth of Highly Luminescent CdSe/CdS Core/Shell Nanocrystals with Photostability and Electronic Accessibility. *J. Am. Chem. Soc.* **1997**, *119*, 7019–7029.

(22) Jun, S.; Jang, E. Interfused Semiconductor Nanocrystals: Brilliant Blue Photoluminescence and Electroluminescence. *Chem. Commun.* **2005**, No. 36, 4616–4618.

(23) Caruge, J.-M.; Halpert, J. E.; Bulović, V.; Bawendi, M. G. NiO as an Inorganic Hole-Transporting Layer in Quantum-Dot Light-Emitting Devices. *Nano Lett.* **2006**, *6*, 2991–2994.

(24) Bae, W. K.; Park, Y.-S.; Lim, J.; Lee, D.; Padilha, L. A.; McDaniel, H.; Robel, I.; Lee, C.; Pietryga, J. M.; Klimov, V. I. Controlling the Influence of Auger Recombination on the Performance of Quantum-Dot Light-Emitting Diodes. *Nature Communications* **2013**, *4*, 2661.

(25) Kim, S.; Fisher, B.; Eisler, H.-J.; Bawendi, M. Type-II Quantum Dots: CdTe/CdSe(Core/Shell) and CdSe/ZnTe(Core/Shell) Heterostructures. *J. Am. Chem. Soc.* **2003**, *125*, 11466–11467.

(26) Mahler, B.; Spinicelli, P.; Buil, S.; Quelin, X.; Hermier, J.-P.; Dubertret, B. Towards Non-Blinking Colloidal Quantum Dots. *Nature Materials* **2008**, *7*, 659–664.

(27) Ithurria, S.; Dubertret, B. Quasi 2D Colloidal CdSe Platelets with Thicknesses Controlled at the Atomic Level. *J. Am. Chem. Soc.* **2008**, *130*, 16504–16505.

(28) Tessier, M. D.; Javaux, C.; Maksimovic, I.; Loriette, V.; Dubertret, B. Spectroscopy of Single CdSe Nanoplatelets. *ACS Nano* **2012**, *6*, 6751–6758.

(29) Cunningham, P. D.; Souza, J. B.; Fedin, I.; She, C.; Lee, B.; Talapin, D. V. Assessment of Anisotropic Semiconductor Nanorod and Nanoplatelet Heterostructures with Polarized Emission for Liquid Crystal Display Technology. *ACS Nano* **2016**, *10*, 5769–5781.

(30) Liu, J.; Guillemeney, L.; Choux, A.; Maître, A.; Abécassis, B.; Coolen, L. Fourier-Imaging of Single Self-Assembled CdSe Nanoplatelet Chains and Clusters Reveals out-of-Plane Dipole Contribution. *ACS Photonics* **2020**, *7*, 2825–2833.

(31) Chu, A.; Livache, C.; Ithurria, S.; Lhuillier, E. Electronic Structure Robustness and Design Rules for 2D Colloidal Heterostructures. *Journal of Applied Physics* **2018**, *123*, 035701.

(32) Ithurria, S.; Talapin, D. V. Colloidal Atomic Layer Deposition (c-ALD) Using Self-Limiting Reactions at Nanocrystal Surface Coupled to Phase Transfer between Polar and Nonpolar Media. *J. Am. Chem. Soc.* **2012**, *134*, 18585–18590.

(33) Heuclin, H.; Nadal, B.; grazon, C. Continuously Emissive Core/Shell Nanoplatelets. WO2016156265A1, October 6, 2016.

(34) Altintas, Y.; Quliyeva, U.; Gungor, K.; Erdem, O.; Kelestemur, Y.; Mutlugun, E.; Kovalenko, M. V.; Demir, H. V. Highly Stable, Near-Unity Efficiency Atomically Flat Semiconductor Nanocrystals of CdSe/ZnS Hetero-Nanoplatelets Enabled by ZnS-Shell Hot-Injection Growth. *Small* **2019**, *15*, 1804854.

(35) Liu, B.; Altintas, Y.; Wang, L.; Shendre, S.; Sharma, M.; Sun, H.; Mutlugun, E.; Demir, H. V. Record High External Quantum Efficiency of 19.2% Achieved in Light-Emitting Diodes of Colloidal Quantum Wells Enabled by Hot-Injection Shell Growth. *Advanced Materials* **2020**, *32*, 1905824.

(36) She, C.; Fedin, I.; Dolzhnikov, D. S.; Demortière, A.; Schaller, R. D.; Pelton, M.; Talapin, D. V. Low-Threshold Stimulated Emission Using Colloidal Quantum Wells. *Nano Lett.* **2014**, *14*, 2772–2777.

(37) Jang, J.; Liu, W.; Son, J. S.; Talapin, D. V. Temperature-Dependent Hall and Field-Effect Mobility in Strongly Coupled All-Inorganic Nanocrystal Arrays. *Nano Lett.* **2014**, *14*, 653–662.

(38) Talapin, D. V.; Murray, C. B. PbSe Nanocrystal Solids for N- and p-Channel Thin Film Field-Effect Transistors. *Science* **2005**, *310*, 86–89.

(39) Kang, M. S.; Lee, J.; Norris, D. J.; Frisbie, C. D. High Carrier Densities Achieved at Low Voltages in Ambipolar PbSe Nanocrystal Thin-Film Transistors. *Nano Lett.* **2009**, *9*, 3848–3852.

(40) Liu, Y.; Gibbs, M.; Puthussery, J.; Gaik, S.; Ihly, R.; Hillhouse, H. W.; Law, M. Dependence of Carrier Mobility on Nanocrystal Size and Ligand Length in PbSe Nanocrystal Solids. *Nano Lett.* **2010**, *10*, 1960–1969.

(41) Konstantatos, G.; Howard, I.; Fischer, A.; Hoogland, S.; Clifford, J.; Klem, E.; Levina, L.; Sargent, E. H. Ultrasensitive Solution-Cast Quantum Dot Photodetectors. *Nature* **2006**, *442*, 180–183.

(42) Lhuillier, E.; Keuleyan, S.; Zolotavin, P.; Guyot-Sionnest, P. Mid-Infrared HgTe/As2S3 Field Effect Transistors and Photodetectors. *Advanced Materials* **2013**, *25*, 137–141.

(43) Tang, X.; Ackerman, M. M.; Chen, M.; Guyot-Sionnest, P. Dual-Band Infrared Imaging Using Stacked Colloidal Quantum Dot Photodiodes. *Nature Photonics* **2019**, *13*, 277–282.

(44) Tang, J.; Kemp, K. W.; Hoogland, S.; Jeong, K. S.; Liu, H.; Levina, L.; Furukawa, M.; Wang, X.; Debnath, R.; Cha, D.; et al. Colloidal-Quantum-Dot Photovoltaics Using Atomic-Ligand Passivation. *Nature Materials* **2011**, *10*, 765–771.

(45) Cho, K.-S.; Lee, E. K.; Joo, W.-J.; Jang, E.; Kim, T.-H.; Lee, S. J.; Kwon, S.-J.; Han, J. Y.; Kim, B.-K.; Choi, B. L.; et al. High-Performance Crosslinked Colloidal Quantum-Dot Light-Emitting Diodes. *Nature Photonics* **2009**, *3*, 341–345.

(46) Yang, Z.; Voznyy, O.; Liu, M.; Yuan, M.; Ip, A. H.; Ahmed, O. S.; Levina, L.; Kinge, S.; Hoogland, S.; Sargent, E. H. All-Quantum-Dot Infrared Light-Emitting Diodes. *ACS Nano* **2015**, *9*, 12327–12333.

(47) Kovalenko, M. V.; Scheele, M.; Talapin, D. V. Colloidal Nanocrystals with Molecular Metal Chalcogenide Surface Ligands. *Science* **2009**, *324*, 1417–1420.

(48) Nag, A.; Kovalenko, M. V.; Lee, J.-S.; Liu, W.; Spokoyny, B.; Talapin, D. V. Metal-Free Inorganic Ligands for Colloidal Nanocrystals: S2–, HS–, Se2–, HSe–, Te2–, HTe–, TeS32–, OH–, and NH2– as Surface Ligands. *J. Am. Chem. Soc.* **2011**, *133*, 10612–10620.

(49) Zherebetskyy, D.; Scheele, M.; Zhang, Y.; Bronstein, N.; Thompson, C.; Britt, D.; Salmeron, M.; Alivisatos, P.; Wang, L.-W. Hydroxylation of the Surface of PbS Nanocrystals Passivated with Oleic Acid. *Science* **2014**, *344*, 1380–1384.

(50) Liu, M.; Voznyy, O.; Sabatini, R.; García de Arquer, F. P.; Munir, R.; Balawi, A. H.; Lan, X.; Fan, F.; Walters, G.; Kirmani, A. R.; et al. Hybrid Organic–Inorganic Inks Flatten the Energy Landscape in Colloidal Quantum Dot Solids. *Nature Materials* **2017**, *16*, 258–263.

(51) Chen, M.; Shen, G.; Guyot-Sionnest, P. State-Resolved Mobility of 1 cm²/(Vs) with HgSe Quantum Dot Films. *J. Phys. Chem. Lett.* **2020**, *11*, 2303–2307.

(52) Kagan, C. R.; Murray, C. B. Charge Transport in Strongly Coupled Quantum Dot Solids. *Nature Nanotechnology* **2015**, *10*, 1013–1026.

(53) Wilk, G. D.; Wallace, R. M.; Anthony, J. M. High-κ Gate Dielectrics: Current Status and Materials Properties Considerations. *Journal of Applied Physics* **2001**, *89*, 5243–5275.

(54) Gréboval, C.; Noumbe, U.; Goubet, N.; Livache, C.; Ramade, J.; Qu, J.; Chu, A.; Martinez, B.; Prado, Y.; Ithurria, S.; et al. Field-Effect Transistor and Photo-Transistor of Narrow-Band-Gap Nanocrystal Arrays Using Ionic Glasses. *Nano Lett.* **2019**, *19*, 3981–3986.

(55) Brown, P. R.; Kim, D.; Lunt, R. R.; Zhao, N.; Bawendi, M. G.; Grossman, J. C.; Bulović, V. Energy Level Modification in Lead Sulfide Quantum Dot Thin Films through Ligand Exchange. *ACS Nano* **2014**, *8*, 5863–5872.

(56) Martinez, B.; Livache, C.; Notemgnou Mouafo, L. D.; Goubet, N.; Keuleyan, S.; Cruguel, H.; Ithurria, S.; Aubin, H.; Ouerghi, A.; Doudin, B.; et al. HgSe Self-Doped Nanocrystals as a Platform to Investigate the Effects of Vanishing Confinement. *ACS Appl. Mater. Interfaces* **2017**, *9*, 36173–36180.

(57) Chuang, C.-H. M.; Brown, P. R.; Bulović, V.; Bawendi, M. G. Improved Performance and Stability in Quantum Dot Solar Cells through Band Alignment Engineering. *Nature Materials* **2014**, *13*, 796–801.

(58)   Gréboval, C.; Chu, A.; Magalhaes, D. V.; Ramade, J.; Qu, J.; Rastogi, P.; Khalili, A.; Chee, S.-S.; Aubin, H.; Vincent, G.; et al. Ferroelectric Gating of Narrow Band-Gap Nanocrystal Arrays with Enhanced Light–Matter Coupling. *ACS Photonics* **2021**, *8*, 259–268.

(59)   Liu, H.; Lhuillier, E.; Guyot-Sionnest, P. 1/f Noise in Semiconductor and Metal Nanocrystal Solids. *Journal of Applied Physics* **2014**, *115*, 154309.

(60)   Protesescu, L.; Yakunin, S.; Bodnarchuk, M. I.; Krieg, F.; Caputo, R.; Hendon, C. H.; Yang, R. X.; Walsh, A.; Kovalenko, M. V. Nanocrystals of Cesium Lead Halide Perovskites (CsPbX3, X = Cl, Br, and I): Novel Optoelectronic Materials Showing Bright Emission with Wide Color Gamut. *Nano Lett.* **2015**, *15*, 3692–3696.

(61)   Fu, H.; Tsang, S.-W. Infrared Colloidal Lead Chalcogenide Nanocrystals: Synthesis, Properties, and Photovoltaic Applications. *Nanoscale* **2012**, *4*, 2187–2201.

(62)   Kovalenko, M. V.; Kaufmann, E.; Pachinger, D.; Roither, J.; Huber, M.; Stangl, J.; Hesser, G.; Schäffler, F.; Heiss, W. Colloidal HgTe Nanocrystals with Widely Tunable Narrow Band Gap Energies: From Telecommunications to Molecular Vibrations. *J. Am. Chem. Soc.* **2006**, *128*, 3516–3517.

(63)   Keuleyan, S.; Lhuillier, E.; Guyot-Sionnest, P. Synthesis of Colloidal HgTe Quantum Dots for Narrow Mid-IR Emission and Detection. *J. Am. Chem. Soc.* **2011**, *133*, 16422–16424.

(64)   Keuleyan, S.; Lhuillier, E.; Brajuskovic, V.; Guyot-Sionnest, P. Mid-Infrared HgTe Colloidal Quantum Dot Photodetectors. *Nature Photonics* **2011**, *5*, 489–493.

(65)   Goubet, N.; Jagtap, A.; Livache, C.; Martinez, B.; Portalès, H.; Xu, X. Z.; Lobo, R. P. S. M.; Dubertret, B.; Lhuillier, E. Terahertz HgTe Nanocrystals: Beyond Confinement. *J. Am. Chem. Soc.* **2018**, *140*, 5033–5036.

(66)   Battaglia, D.; Peng, X. Formation of High Quality InP and InAs Nanocrystals in a Noncoordinating Solvent. *Nano Lett.* **2002**, *2*, 1027–1030.

(67)   Liu, W.; Chang, A. Y.; Schaller, R. D.; Talapin, D. V. Colloidal InSb Nanocrystals. *J. Am. Chem. Soc.* **2012**, *134*, 20258–20261.

(68)   Rogach, A.; Kershaw, S. V.; Burt, M.; Harrison, M. T.; Kornowski, A.; Eychmüller, A.; Weller, H. Colloidally Prepared HgTe Nanocrystals with Strong Room-Temperature Infrared Luminescence. *Advanced Materials* **1999**, *11*, 552–555.

(69)   Lhuillier, E.; Scarafagio, M.; Hease, P.; Nadal, B.; Aubin, H.; Xu, X. Z.; Lequeux, N.; Patriarche, G.; Ithurria, S.; Dubertret, B. Infrared Photodetection Based on Colloidal Quantum-Dot Films with High Mobility and Optical Absorption up to THz. *Nano Lett.* **2016**, *16*, 1282–1286.

(70)   Livache, C.; Martinez, B.; Goubet, N.; Ramade, J.; Lhuillier, E. Road Map for Nanocrystal Based Infrared Photodetectors. *Front. Chem.* **2018**, *6*.

(71)   McDonald, S. A.; Cyr, P. W.; Levina, L.; Sargent, E. H. Photoconductivity from PbS-Nanocrystal/semiconducting Polymer Composites for Solution-Processible, Quantum-Size Tunableinfrared Photodetectors. *Appl. Phys. Lett.* **2004**, *85*, 2089–2091.

(72)   Martinez, B.; Ramade, J.; Livache, C.; Goubet, N.; Chu, A.; Gréboval, C.; Qu, J.; Watkins, W. L.; Becerra, L.; Dandeu, E.; et al. HgTe Nanocrystal Inks for Extended Short-Wave Infrared Detection. *Advanced Optical Materials* **2019**, 1900348.

(73)   Chu, A.; Martinez, B.; Ferré, S.; Noguier, V.; Gréboval, C.; Livache, C.; Qu, J.; Prado, Y.; Casaretto, N.; Goubet, N.; et al. HgTe Nanocrystals for SWIR Detection and Their Integration up to the Focal Plane Array. *ACS Appl. Mater. Interfaces* **2019**, *11*, 33116–33123.

(74)   Ciani, A. J.; Pimpinella, R. E.; Grein, C. H.; Guyot-Sionnest, P. Colloidal Quantum Dots for Low-Cost MWIR Imaging. *Infrared Technology and Applications XLII* **2016**, *9819*, 981919.

(75)   Deng, Z.; Jeong, K. S.; Guyot-Sionnest, P. Colloidal Quantum Dots Intraband Photodetectors. *ACS Nano* **2014**, *8*, 11707–11714.

(76) Livache, C.; Martinez, B.; Goubet, N.; Gréboval, C.; Qu, J.; Chu, A.; Royer, S.; Ithurria, S.; Silly, M. G.; Dubertret, B.; et al. A Colloidal Quantum Dot Infrared Photodetector and Its Use for Intraband Detection. *Nature Communications* **2019**, *10*, 2125.

(77) Tang, X.; Ackerman, M. M.; Guyot-Sionnest, P. Thermal Imaging with Plasmon Resonance Enhanced HgTe Colloidal Quantum Dot Photovoltaic Devices. *ACS Nano* **2018**, *12*, 7362–7370.

(78) Chu, A.; Gréboval, C.; Goubet, N.; Martinez, B.; Livache, C.; Qu, J.; Rastogi, P.; Bresciani, F. A.; Prado, Y.; Suffit, S.; et al. Near Unity Absorption in Nanocrystal Based Short Wave Infrared Photodetectors Using Guided Mode Resonators. *ACS Photonics* **2019**, *6*, 2553–2561.

(79) Ramiro, I.; Özdemir, O.; Christodoulou, S.; Gupta, S.; Dalmases, M.; Torre, I.; Konstantatos, G. Mid- and Long-Wave Infrared Optoelectronics via Intraband Transitions in PbS Colloidal Quantum Dots. *Nano Lett.* **2020**, *20*, 1003–1008.

(80) Martinez, B.; Ramade, J.; Livache, C.; Goubet, N.; Chu, A.; Gréboval, C.; Qu, J.; Watkins, W. L.; Becerra, L.; Dandeu, E.; et al. HgTe Nanocrystal Inks for Extended Short-Wave Infrared Detection. *Advanced Optical Materials* **2019**, *7*, 1900348.

(81) Jeong, K. S.; Deng, Z.; Keuleyan, S.; Liu, H.; Guyot-Sionnest, P. Air-Stable n-Doped Colloidal HgS Quantum Dots. *J. Phys. Chem. Lett.* **2014**, *5*, 1139–1143.

(82) Junod, P.; Hediger, H.; Kilchör, B.; Wullschleger, J. Metal-Non-Metal Transition in Silver Chalcogenides. *The Philosophical Magazine: A Journal of Theoretical Experimental and Applied Physics* **1977**, *36*, 941–958.

(83) Sahu, A.; Khare, A.; Deng, D. D.; Norris, D. J. Quantum Confinement in Silver Selenide Semiconductor Nanocrystals. *Chem. Commun.* **2012**, *48*, 5458–5460.

(84) Yang, S.; Cho, K.; Park, Y.; Kim, S. Bendable Thermoelectric Generators Composed of p- and n-Type Silver Chalcogenide Nanoparticle Thin Films. *Nano Energy* **2018**, *49*, 333–337.

(85) Lim, K. H.; Wong, K. W.; Liu, Y.; Zhang, Y.; Cadavid, D.; Cabot, A.; Ng, K. M. Critical Role of Nanoinclusions in Silver Selenide Nanocomposites as a Promising Room Temperature Thermoelectric Material. *J. Mater. Chem. C* **2019**, *7*, 2646–2652.

(86) Gu, Y.-P.; Cui, R.; Zhang, Z.-L.; Xie, Z.-X.; Pang, D.-W. Ultrasmall Near-Infrared Ag2Se Quantum Dots with Tunable Fluorescence for in Vivo Imaging. *J. Am. Chem. Soc.* **2012**, *134*, 79–82.

(87) Langevin, M.-A.; Lachance-Quirion, D.; Ritcey, A. M.; Allen, C. Nì. Size-Dependent Extinction Coefficients and Transition Energies of Near-Infrared β-Ag2Se Colloidal Quantum Dots. *J. Phys. Chem. C* **2013**, *117*, 5424–5428.

(88) Zhu, C.-N.; Jiang, P.; Zhang, Z.-L.; Zhu, D.-L.; Tian, Z.-Q.; Pang, D.-W. Ag2Se Quantum Dots with Tunable Emission in the Second Near-Infrared Window. *ACS Appl. Mater. Interfaces* **2013**, *5*, 1186–1189.

(89) Tan, L.; Wan, A.; Zhao, T.; Huang, R.; Li, H. Aqueous Synthesis of Multidentate-Polymer-Capping Ag2Se Quantum Dots with Bright Photoluminescence Tunable in a Second Near-Infrared Biological Window. *ACS Appl. Mater. Interfaces* **2014**, *6*, 6217–6222.

(90) Dong, B.; Li, C.; Chen, G.; Zhang, Y.; Zhang, Y.; Deng, M.; Wang, Q. Facile Synthesis of Highly Photoluminescent Ag2Se Quantum Dots as a New Fluorescent Probe in the Second Near-Infrared Window for in Vivo Imaging. *Chem. Mater.* **2013**, *25*, 2503–2509.

(91) Hafiz, S. B.; Al Mahfuz, M. M.; Scimeca, M. R.; Lee, S.; Oh, S. J.; Sahu, A.; Ko, D.-K. Ligand Engineering of Mid-Infrared Ag2Se Colloidal Quantum Dots. *Physica E: Low-dimensional Systems and Nanostructures* **2020**, *124*, 114223.

(92) Hafiz, S. B.; Scimeca, M. R.; Zhao, P.; Paredes, I. J.; Sahu, A.; Ko, D.-K. Silver Selenide Colloidal Quantum Dots for Mid-Wavelength Infrared Photodetection. *ACS Appl. Nano Mater.* **2019**, *2*, 1631–1636.

(93) Park, M.; Choi, D.; Choi, Y.; Shin, H.; Jeong, K. S. Mid-Infrared Intraband Transition of Metal Excess Colloidal Ag2Se Nanocrystals. *ACS Photonics* **2018**, *5*, 1907–1911.

(94) Hafiz, S. B.; Al Mahfuz, M. M.; Ko, D.-K. Vertically Stacked Intraband Quantum Dot Devices for Mid-Wavelength Infrared Photodetection. *ACS Appl. Mater. Interfaces* **2021**, *13*, 937–943.

(95) Robin, A.; Livache, C.; Ithurria, S.; Lacaze, E.; Dubertret, B.; Lhuillier, E. Surface Control of Doping in Self-Doped Nanocrystals. *ACS Appl. Mater. Interfaces* **2016**, *8*, 27122–27128.

(96) Goubet, N.; Livache, C.; Martinez, B.; Xu, X. Z.; Ithurria, S.; Royer, S.; Cruguel, H.; Patriarche, G.; Ouerghi, A.; Silly, M.; et al. Wave-Function Engineering in HgSe/HgTe Colloidal Heterostructures To Enhance Mid-Infrared Photoconductive Properties. *Nano Lett.* **2018**, *18*, 4590–4597.

(97) Livache, C.; Goubet, N.; Gréboval, C.; Martinez, B.; Ramade, J.; Qu, J.; Triboulin, A.; Cruguel, H.; Baptiste, B.; Klotz, S.; et al. Effect of Pressure on Interband and Intraband Transition of Mercury Chalcogenide Quantum Dots. *J. Phys. Chem. C* **2019**, *123*, 13122–13130.

(98) Wang, J.; Fan, W.; Yang, J.; Da, Z.; Yang, X.; Chen, K.; Yu, H.; Cheng, X. Tetragonal–Orthorhombic–Cubic Phase Transitions in Ag2Se Nanocrystals. *Chem. Mater.* **2014**, *26*, 5647–5653.

(99) Yarema, M.; Pichler, S.; Sytnyk, M.; Seyrkammer, R.; Lechner, R. T.; Fritz-Popovski, G.; Jarzab, D.; Szendrei, K.; Resel, R.; Korovyanko, O.; et al. Infrared Emitting and Photoconducting Colloidal Silver Chalcogenide Nanocrystal Quantum Dots from a Silylamide-Promoted Synthesis. *ACS Nano* **2011**, *5*, 3758–3765.

(100) Dai, X.; Zhang, Z.; Jin, Y.; Niu, Y.; Cao, H.; Liang, X.; Chen, L.; Wang, J.; Peng, X. Solution-Processed, High-Performance Light-Emitting Diodes Based on Quantum Dots. *Nature* **2014**, *515*, 96–99.

(101) Mir, W. J.; Livache, C.; Goubet, N.; Martinez, B.; Jagtap, A.; Chu, A.; Coutard, N.; Cruguel, H.; Barisien, T.; Ithurria, S.; et al. Strategy to Overcome Recombination Limited Photocurrent Generation in CsPbX3 Nanocrystal Arrays. *Appl. Phys. Lett.* **2018**, *112*, 113503.

(102) Livache, C.; Goubet, N.; Martinez, B.; Jagtap, A.; Qu, J.; Ithurria, S.; Silly, M. G.; Dubertret, B.; Lhuillier, E. Band Edge Dynamics and Multiexciton Generation in Narrow Band Gap HgTe Nanocrystals. *ACS Applied Materials & Interfaces* **2018**, *10*, 11880–11887.

(103) Rastogi, P.; Chu, A.; Gréboval, C.; Qu, J.; Noumbé, U. N.; Chee, S.-S.; Goyal, M.; Khalili, A.; Xu, X. Z.; Cruguel, H.; et al. Pushing Absorption of Perovskite Nanocrystals into the Infrared. *Nano Lett.* **2020**, *20*, 3999–4006.

(104) Jansons, A. W.; Hutchison, J. E. Continuous Growth of Metal Oxide Nanocrystals: Enhanced Control of Nanocrystal Size and Radial Dopant Distribution. *ACS Nano* **2016**, *10*, 6942–6951.

(105) Luther, J. M.; Jain, P. K.; Ewers, T.; Alivisatos, A. P. Localized Surface Plasmon Resonances Arising from Free Carriers in Doped Quantum Dots. *Nature Materials* **2011**, *10*, 361–366.

(106) Rowe, D. J.; Jeong, J. S.; Mkhoyan, K. A.; Kortshagen, U. R. Phosphorus-Doped Silicon Nanocrystals Exhibiting Mid-Infrared Localized Surface Plasmon Resonance. *Nano Lett.* **2013**, *13*, 1317–1322.

(107) Williams, C. R.; Andrews, S. R.; Maier, S. A.; Fernández-Domínguez, A. I.; Martín-Moreno, L.; García-Vidal, F. J. Highly Confined Guiding of Terahertz Surface Plasmon Polaritons on Structured Metal Surfaces. *Nature Photonics* **2008**, *2*, 175–179.

(108) Runnerstrom, E. L.; Bergerud, A.; Agrawal, A.; Johns, R. W.; Dahlman, C. J.; Singh, A.; Selbach, S. M.; Milliron, D. J. Defect Engineering in Plasmonic Metal Oxide Nanocrystals. *Nano Lett.* **2016**, *16*, 3390–3398.

(109) Fang, H.; Hegde, M.; Yin, P.; Radovanovic, P. V. Tuning Plasmon Resonance of In2O3 Nanocrystals throughout the Mid-Infrared Region by Competition between Electron Activation and Trapping. *Chem. Mater.* **2017**, *29*, 4970–4979.

(110) Agrawal, A.; Singh, A.; Yazdi, S.; Singh, A.; Ong, G. K.; Bustillo, K.; Johns, R. W.; Ringe, E.; Milliron, D. J. Resonant Coupling between Molecular Vibrations and Localized Surface Plasmon Resonance of Faceted Metal Oxide Nanocrystals. *Nano Lett.* **2017**, *17*, 2611–2620.

(111) Tandon, B.; Yadav, A.; Nag, A. Delocalized Electrons Mediated Magnetic Coupling in Mn–Sn Codoped In2O3 Nanocrystals: Plasmonics Shows the Way. *Chemistry of Materials* **2016**, *28*, 3620–3624.

(112)   Buonsanti, R.; Llordes, A.; Aloni, S.; Helms, B. A.; Milliron, D. J. Tunable Infrared Absorption and Visible Transparency of Colloidal Aluminum-Doped Zinc Oxide Nanocrystals. *Nano Lett.* **2011**, *11*, 4706–4710.

(113)   De Trizio, L.; Buonsanti, R.; Schimpf, A. M.; Llordes, A.; Gamelin, D. R.; Simonutti, R.; Milliron, D. J. Nb-Doped Colloidal TiO2 Nanocrystals with Tunable Infrared Absorption. *Chem. Mater.* **2013**, *25*, 3383–3390.

(114)   Llordés, A.; Garcia, G.; Gazquez, J.; Milliron, D. J. Tunable Near-Infrared and Visible-Light Transmittance in Nanocrystal-in-Glass Composites. *Nature* **2013**, *500*, 323–326.

(115)   Kim, J.; Ong, G. K.; Wang, Y.; LeBlanc, G.; Williams, T. E.; Mattox, T. M.; Helms, B. A.; Milliron, D. J. Nanocomposite Architecture for Rapid, Spectrally-Selective Electrochromic Modulation of Solar Transmittance. *Nano Lett.* **2015**, *15*, 5574–5579.

(116)   Song, G.; Shen, J.; Jiang, F.; Hu, R.; Li, W.; An, L.; Zou, R.; Chen, Z.; Qin, Z.; Hu, J. Hydrophilic Molybdenum Oxide Nanomaterials with Controlled Morphology and Strong Plasmonic Absorption for Photothermal Ablation of Cancer Cells. *ACS Appl. Mater. Interfaces* **2014**, *6*, 3915–3922.

(117)   Deng, K.; Hou, Z.; Deng, X.; Yang, P.; Li, C.; Lin, J. Enhanced Antitumor Efficacy by 808 Nm Laser-Induced Synergistic Photothermal and Photodynamic Therapy Based on a Indocyanine-Green-Attached $W_{18}O_{49}$ Nanostructure. *Advanced Functional Materials* **2015**, *25*, 7280–7290.

(118)   Nie, L.; Chen, X. Structural and Functional Photoacoustic Molecular Tomography Aided by Emerging Contrast Agents. *Chem. Soc. Rev.* **2014**, *43*, 7132–7170.

(119)   Yang, W.; Guo, W.; Le, W.; Lv, G.; Zhang, F.; Shi, L.; Wang, X.; Wang, J.; Wang, S.; Chang, J.; et al. Albumin-Bioinspired Gd:CuS Nanotheranostic Agent for In Vivo Photoacoustic/Magnetic Resonance Imaging-Guided Tumor-Targeted Photothermal Therapy. *ACS Nano* **2016**, *10*, 10245–10257.

(120)   Agrawal, A.; Cho, S. H.; Zandi, O.; Ghosh, S.; Johns, R. W.; Milliron, D. J. Localized Surface Plasmon Resonance in Semiconductor Nanocrystals. *Chem. Rev.* **2018**, *118*, 3121–3207.

(121)   Lhuillier, E.; Keuleyan, S.; Guyot-Sionnest, P. Optical Properties of HgTe Colloidal Quantum Dots. *Nanotechnology* **2012**, *23*, 175705.

(122)   Anderson, L. J. E.; Mayer, K. M.; Fraleigh, R. D.; Yang, Y.; Lee, S.; Hafner, J. H. Quantitative Measurements of Individual Gold Nanoparticle Scattering Cross Sections. *J. Phys. Chem. C* **2010**, *114*, 11127–11132.

(123)   Qu, J.; Goubet, N.; Livache, C.; Martinez, B.; Amelot, D.; Gréboval, C.; Chu, A.; Ramade, J.; Cruguel, H.; Ithurria, S.; et al. Intraband Mid-Infrared Transitions in Ag2Se Nanocrystals: Potential and Limitations for Hg-Free Low-Cost Photodetection. *The Journal of Physical Chemistry C* **2018**, *122*, 18161–18167.

(124)   Burstein, E. Anomalous Optical Absorption Limit in InSb. *Phys. Rev.* **1954**, *93*, 632–633.

(125)   Moss, T. S. The Interpretation of the Properties of Indium Antimonide. *Proc. Phys. Soc. B* **1954**, *67*, 775–782.

(126)   Hamberg, I.; Granqvist, C. G.; Berggren, K.-F.; Sernelius, B. E.; Engström, L. Band-Gap Widening in Heavily Sn-Doped In_2O_3. *Phys. Rev. B* **1984**, *30*, 3240–3249.

(127)   Delerue, C. Minimum Line Width of Surface Plasmon Resonance in Doped ZnO Nanocrystals. *Nano Lett.* **2017**, *17*, 7599–7605.

(128)   Tandon, B.; Yadav, A.; Khurana, D.; Reddy, P.; Santra, P. K.; Nag, A. Size-Induced Enhancement of Carrier Density, LSPR Quality Factor, and Carrier Mobility in Cr–Sn Doped In_2O_3 Nanocrystals. *Chemistry of Materials* **2017**, *29*, 9360–9368.

(129)   Robinson, J. T.; Welsher, K.; Tabakman, S. M.; Sherlock, S. P.; Wang, H.; Luong, R.; Dai, H. High Performance in Vivo Near-IR (>1 µm) Imaging and Photothermal Cancer Therapy with Carbon Nanotubes. *Nano Res.* **2010**, *3*, 779–793.

(130)   Zhang, Y.; Wei, T.; Dong, W.; Huang, C.; Zhang, K.; Sun, Y.; Chen, X.; Dai, N. Near-Perfect Infrared Absorption from Dielectric Multilayer of Plasmonic Aluminum-Doped Zinc Oxide. *Applied Physics Letters* **2013**, *102*, 213117.

(131)   Ito, D.; Yokoyama, S.; Zaikova, T.; Masuko, K.; Hutchison, J. E. Synthesis of Ligand-Stabilized Metal Oxide Nanocrystals and Epitaxial Core/Shell Nanocrystals via a Lower-Temperature Esterification Process. *ACS Nano* **2014**, *8*, 64–75.

(132)   Lee, J.; Lee, S.; Li, G.; Petruska, M. A.; Paine, D. C.; Sun, S. A Facile Solution-Phase Approach to Transparent and Conducting ITO Nanocrystal Assemblies. *J. Am. Chem. Soc.* **2012**, *134*, 13410–13414.

(133)   Diroll, B. T.; Gordon, T. R.; Gaulding, E. A.; Klein, D. R.; Paik, T.; Yun, H. J.; Goodwin, E. D.; Damodhar, D.; Kagan, C. R.; Murray, C. B. Synthesis of n-Type Plasmonic Oxide Nanocrystals and the Optical and Electrical Characterization of Their Transparent Conducting Films. *Chem. Mater.* **2014**, *26*, 4579–4588.

(134)   Khoshkhoo, M. S.; Joseph, Y.; Maiti, S.; Schreiber, F.; Chassé, T.; Scheele, M. Tunable Charge Transport in Hybrid Superlattices of Indium Tin Oxide Nanocrystals and Metal Phthalocyanines— Toward Sensing Applications. *Advanced Materials Interfaces* **2018**, *5*, 1701623.

(135)   Samadi Khoshkhoo, M.; Maiti, S.; Schreiber, F.; Chassé, T.; Scheele, M. Surface Functionalization with Copper Tetraaminophthalocyanine Enables Efficient Charge Transport in Indium Tin Oxide Nanocrystal Thin Films. *ACS Appl. Mater. Interfaces* **2017**, *9*, 14197–14206.

(136)   Guyot-Sionnest, P. Electrical Transport in Colloidal Quantum Dot Films. *J. Phys. Chem. Lett.* **2012**, *3*, 1169–1175.

(137)   Efros, A. L.; Shklovskii, B. I. Coulomb Gap and Low Temperature Conductivity of Disordered Systems. *J. Phys. C: Solid State Phys.* **1975**, *8*, 49–51.

(138)   Mott, N. F. Conduction in Non-Crystalline Materials. *The Philosophical Magazine: A Journal of Theoretical Experimental and Applied Physics* **1969**, *19*, 835–852.

(139)   Liu, H.; Pourret, A.; Guyot-Sionnest, P. Mott and Efros-Shklovskii Variable Range Hopping in CdSe Quantum Dots Films. *ACS Nano* **2010**, *4*, 5211–5216.

(140)   Moreira, H.; Yu, Q.; Nadal, B.; Bresson, B.; Rosticher, M.; Lequeux, N.; Zimmers, A.; Aubin, H. Electron Cotunneling Transport in Gold Nanocrystal Arrays. *Phys. Rev. Lett.* **2011**, *107*, 176803.

(141)   Zandi, O.; Agrawal, A.; Shearer, A. B.; Reimnitz, L. C.; Dahlman, C. J.; Staller, C. M.; Milliron, D. J. Impacts of Surface Depletion on the Plasmonic Properties of Doped Semiconductor Nanocrystals. *Nature Materials* **2018**, *17*, 710.

(142)   Swisher, S. L.; Volkman, S. K.; Subramanian, V. Tailoring Indium Oxide Nanocrystal Synthesis Conditions for Air-Stable High-Performance Solution-Processed Thin-Film Transistors. *ACS Appl. Mater. Interfaces* **2015**, *7*, 10069–10075.

(143)   Jin, Y.; Wang, J.; Sun, B.; Blakesley, J. C.; Greenham, N. C. Solution-Processed Ultraviolet Photodetectors Based on Colloidal ZnO Nanoparticles. *Nano Lett.* **2008**, *8*, 1649–1653.

(144)   Hasan Farooqi, M. M.; Srivastava, R. K. Structural, Optical and Photoconductivity Study of ZnO Nanoparticles Synthesized by Annealing of ZnS Nanoparticles. *Journal of Alloys and Compounds* **2017**, *691*, 275–286.

(145)   Choi, J.; Jo, J. W.; Arquer, F. P. G. de; Zhao, Y.-B.; Sun, B.; Kim, J.; Choi, M.-J.; Baek, S.-W.; Proppe, A. H.; Seifitokaldani, A.; et al. Activated Electron-Transport Layers for Infrared Quantum Dot Optoelectronics. *Advanced Materials* **2018**, *30*, 1801720.

(146)   Shen, G.; Guyot-Sionnest, P. HgS and HgS/CdS Colloidal Quantum Dots with Infrared Intraband Transitions and Emergence of a Surface Plasmon. *J. Phys. Chem. C* **2016**, *120*, 11744–11753.

(147)   Schimpf, A. M.; Thakkar, N.; Gunthardt, C. E.; Masiello, D. J.; Gamelin, D. R. Charge-Tunable Quantum Plasmons in Colloidal Semiconductor Nanocrystals. *ACS Nano* **2014**, *8*, 1065–1072.

(148)   Ackerman, M. M.; Chen, M.; Guyot-Sionnest, P. HgTe Colloidal Quantum Dot Photodiodes for Extended Short-Wave Infrared Detection. *Appl. Phys. Lett.* **2020**, *116*, 083502.

(149) Martinez, B.; Livache, C.; Goubet, N.; Jagtap, A.; Cruguel, H.; Ouerghi, A.; Lacaze, E.; Silly, M. G.; Lhuillier, E. Probing Charge Carrier Dynamics to Unveil the Role of Surface Ligands in HgTe Narrow Band Gap Nanocrystals. *J. Phys. Chem. C* **2018**, *122*, 859–865.

(150) Livache, C.; Goubet, N.; Martinez, B.; Jagtap, A.; Qu, J.; Ithurria, S.; Silly, M. G.; Dubertret, B.; Lhuillier, E. Band Edge Dynamics and Multiexciton Generation in Narrow Band Gap HgTe Nanocrystals. *ACS Appl. Mater. Interfaces* **2018**, *10*, 11880–11887.

(151) Lhuillier, E.; Keuleyan, S.; Zolotavin, P.; Guyot-Sionnest, P. Mid-Infrared HgTe/As2S3 Field Effect Transistors and Photodetectors. *Advanced Materials* **2013**, *25*, 137–141.

(152) Livache, C.; Martinez, B.; Goubet, N.; Gréboval, C.; Qu, J.; Chu, A.; Royer, S.; Ithurria, S.; Silly, M. G.; Dubertret, B.; et al. A Colloidal Quantum Dot Infrared Photodetector and Its Use for Intraband Detection. *Nature Communications* **2019**, *10*, 1–10.

(153) Lhuillier, E.; Robin, A.; Ithurria, S.; Aubin, H.; Dubertret, B. Electrolyte-Gated Colloidal Nanoplatelets-Based Phototransistor and Its Use for Bicolor Detection. *Nano Lett.* **2014**, *14*, 2715–2719.

(154) Colvin, V. L.; Schlamp, M. C.; Alivisatos, A. P. Light-Emitting Diodes Made from Cadmium Selenide Nanocrystals and a Semiconducting Polymer. *Nature* **1994**, *370*, 354.

(155) Kim, T.-H.; Cho, K.-S.; Lee, E. K.; Lee, S. J.; Chae, J.; Kim, J. W.; Kim, D. H.; Kwon, J.-Y.; Amaratunga, G.; Lee, S. Y.; et al. Full-Colour Quantum Dot Displays Fabricated by Transfer Printing. *Nature Photonics* **2011**, *5*, 176–182.

(156) Shu, Y.; Lin, X.; Qin, H.; Hu, Z.; Jin, Y.; Peng, X. Quantum Dots for Display Applications. *Angewandte Chemie International Edition* **2020**, *59*, 22312–22323.

(157) Li, X.; Lin, Q.; Song, J.; Shen, H.; Zhang, H.; Li, L. S.; Li, X.; Du, Z. Quantum-Dot Light-Emitting Diodes for Outdoor Displays with High Stability at High Brightness. *Advanced Optical Materials* **2020**, *8*, 1901145.

(158) Kim, T.; Kim, K.-H.; Kim, S.; Choi, S.-M.; Jang, H.; Seo, H.-K.; Lee, H.; Chung, D.-Y.; Jang, E. Efficient and Stable Blue Quantum Dot Light-Emitting Diode. *Nature* **2020**, *586*, 385–389.

(159) Cao, Y.; Wang, N.; Tian, H.; Guo, J.; Wei, Y.; Chen, H.; Miao, Y.; Zou, W.; Pan, K.; He, Y.; et al. Perovskite Light-Emitting Diodes Based on Spontaneously Formed Submicrometre-Scale Structures. *Nature* **2018**, *562*, 249–253.

(160) Dain, S. J.; Kwan, B.; Wong, L. Consistency of Color Representation in Smart Phones. *J. Opt. Soc. Am. A* **2016**, *33*, 300–305.

(161) Lim, J.; Park, Y.-S.; Wu, K.; Yun, H. J.; Klimov, V. I. Droop-Free Colloidal Quantum Dot Light-Emitting Diodes. *Nano Lett.* **2018**, *18*, 6645–6653.

(162) Shirasaki, Y.; Supran, G. J.; Tisdale, W. A.; Bulović, V. Origin of Efficiency Roll-Off in Colloidal Quantum-Dot Light-Emitting Diodes. *Phys. Rev. Lett.* **2013**, *110*, 217403.

(163) Jha, P. P.; Guyot-Sionnest, P. Trion Decay in Colloidal Quantum Dots. *ACS Nano* **2009**, *3*, 1011–1015.

(164) Sun, Q.; Wang, Y. A.; Li, L. S.; Wang, D.; Zhu, T.; Xu, J.; Yang, C.; Li, Y. Bright, Multicoloured Light-Emitting Diodes Based on Quantum Dots. *Nature Photonics* **2007**, *1*, 717–722.

(165) Lee, D.-H.; Liu, Y.-P.; Lee, K.-H.; Chae, H.; Cho, S. M. Effect of Hole Transporting Materials in Phosphorescent White Polymer Light-Emitting Diodes. *Organic Electronics* **2010**, *11*, 427–433.

(166) Hoping, M.; Schildknecht, C.; Gargouri, H.; Riedl, T.; Tilgner, M.; Johannes, H.-H.; Kowalsky, W. Transition Metal Oxides as Charge Injecting Layer for Admittance Spectroscopy. *Appl. Phys. Lett.* **2008**, *92*, 213306.

(167) Yamashita, M.; Otani, C.; Okuzaki, H.; Shimizu, M. Nondestructive Measurement of Carrier Mobility in Conductive Polymer PEDOT:PSS Using Terahertz and Infrared Spectroscopy. *2011 URSI General Assembly and Scientific Symposium* **2011**, 1–4.

(168) Redecker, M.; Bradley, D. D. C.; Inbasekaran, M.; Wu, W. W.; Woo, E. P. High Mobility Hole Transport Fluorene-Triarylamine Copolymers. *Advanced Materials* **1999**, *11*, 241–246.

(169) Jiang, F.; Choy, W. C. H.; Li, X.; Zhang, D.; Cheng, J. Post-Treatment-Free Solution-Processed Non-Stoichiometric NiOx Nanoparticles for Efficient Hole-Transport Layers of Organic Optoelectronic Devices. *Advanced Materials* **2015**, *27*, 2930–2937.

(170) Jagtap, A.; Martinez, B.; Goubet, N.; Chu, A.; Livache, C.; Gréboval, C.; Ramade, J.; Amelot, D.; Trousset, P.; Triboulin, A.; et al. Design of a Unipolar Barrier for a Nanocrystal-Based Short-Wave Infrared Photodiode. *ACS Photonics* **2018**, *5*, 4569–4576.

(171) Sun, L.; Choi, J. J.; Stachnik, D.; Bartnik, A. C.; Hyun, B.-R.; Malliaras, G. G.; Hanrath, T.; Wise, F. W. Bright Infrared Quantum-Dot Light-Emitting Diodes through Inter-Dot Spacing Control. *Nature Nanotechnology* **2012**, *7*, 369–373.

(172) Park, Y.-S.; Lim, J.; Klimov, V. I. Asymmetrically Strained Quantum Dots with Non-Fluctuating Single-Dot Emission Spectra and Subthermal Room-Temperature Linewidths. *Nature Materials* **2019**, *18*, 249–255.

(173) Chen, Z.; Nadal, B.; Mahler, B.; Aubin, H.; Dubertret, B. Quasi-2D Colloidal Semiconductor Nanoplatelets for Narrow Electroluminescence. *Advanced Functional Materials* **2014**, *24*, 295–302.

(174) Koktysh, D. S.; Gaponik, N.; Reufer, M.; Crewett, J.; Scherf, U.; Eychmüller, A.; Lupton, J. M.; Rogach, A. L.; Feldmann, J. Near-Infrared Electroluminescence from HgTe Nanocrystals. *ChemPhysChem* **2004**, *5*, 1435–1438.

(175) O'Connor, É.; O'Riordan, A.; Doyle, H.; Moynihan, S.; Cuddihy, A.; Redmond, G. Near-Infrared Electroluminescent Devices Based on Colloidal HgTe Quantum Dot Arrays. *Appl. Phys. Lett.* **2005**, *86*, 201114.

(176) Supran, G. J.; Song, K. W.; Hwang, G. W.; Correa, R. E.; Scherer, J.; Dauler, E. A.; Shirasaki, Y.; Bawendi, M. G.; Bulović, V. High-Performance Shortwave-Infrared Light-Emitting Devices Using Core–Shell (PbS–CdS) Colloidal Quantum Dots. *Advanced Materials* **2015**, *27*, 1437–1442.

(177) Pradhan, S.; Di Stasio, F.; Bi, Y.; Gupta, S.; Christodoulou, S.; Stavrinadis, A.; Konstantatos, G. High-Efficiency Colloidal Quantum Dot Infrared Light-Emitting Diodes via Engineering at the Supra-Nanocrystalline Level. *Nature Nanotechnology* **2019**, *14*, 72–79.

(178) Pradhan, S.; Dalmases, M.; Baspinar, A.-B.; Konstantatos, G. Highly Efficient, Bright, and Stable Colloidal Quantum Dot Short-Wave Infrared Light-Emitting Diodes. *Advanced Functional Materials* **2020**, *30*, 2004445.

(179) Lhuillier, E.; Pedetti, S.; Ithurria, S.; Nadal, B.; Heuclin, H.; Dubertret, B. Two-Dimensional Colloidal Metal Chalcogenides Semiconductors: Synthesis, Spectroscopy, and Applications. *Acc. Chem. Res.* **2015**, *48*, 22–30.

(180) Christodoulou, S.; Climente, J. I.; Planelles, J.; Brescia, R.; Prato, M.; Martín-García, B.; Khan, A. H.; Moreels, I. Chloride-Induced Thickness Control in CdSe Nanoplatelets. *Nano Lett.* **2018**, *18*, 6248–6254.

(181) Diroll, B. T.; Schaller, R. D. Shape-Selective Optical Transformations of CdSe Nanoplatelets Driven by Halide Ion Ligand Exchange. *Chem. Mater.* **2019**, *31*, 3556–3563.

(182) Dufour, M.; Qu, J.; Greboval, C.; Méthivier, C.; Lhuillier, E.; Ithurria, S. Halide Ligands To Release Strain in Cadmium Chalcogenide Nanoplatelets and Achieve High Brightness. *ACS Nano* **2019**, *13*, 5326–5334.

(183) Cho, W.; Kim, S.; Coropceanu, I.; Srivastava, V.; Diroll, B. T.; Hazarika, A.; Fedin, I.; Galli, G.; Schaller, R. D.; Talapin, D. V. Direct Synthesis of Six-Monolayer (1.9 nm) Thick Zinc-Blende CdSe Nanoplatelets Emitting at 585 nm. *Chem. Mater.* **2018**, *30*, 6957–6960.

(184) Khan, A. H.; Pinchetti, V.; Tanghe, I.; Dang, Z.; Martín-García, B.; Hens, Z.; Van Thourhout, D.; Geiregat, P.; Brovelli, S.; Moreels, I. Tunable and Efficient Red to Near-Infrared Photoluminescence by Synergistic Exploitation of Core and Surface Silver Doping of CdSe Nanoplatelets. *Chem. Mater.* **2019**, *31*, 1450–1459.

(185) Sharma, M.; Olutas, M.; Yeltik, A.; Kelestemur, Y.; Sharma, A.; Delikanli, S.; Guzelturk, B.; Gungor, K.; McBride, J. R.; Demir, H. V. Understanding the Journey of Dopant Copper Ions in Atomically Flat Colloidal Nanocrystals of CdSe Nanoplatelets Using Partial Cation Exchange Reactions. *Chem. Mater.* **2018**, *30*, 3265–3275.

(186) Dufour, M.; Izquierdo, E.; Livache, C.; Martinez, B.; Silly, M. G.; Pons, T.; Lhuillier, E.; Delerue, C.; Ithurria, S. Doping as a Strategy to Tune Color of 2D Colloidal Nanoplatelets. *ACS Appl. Mater. Interfaces* **2019**, *11*, 10128–10134.

(187) Liu, B.; Sharma, M.; Yu, J.; Shendre, S.; Hettiarachchi, C.; Sharma, A.; Yeltik, A.; Wang, L.; Sun, H.; Dang, C.; et al. Light-Emitting Diodes with Cu-Doped Colloidal Quantum Wells: From Ultrapure Green, Tunable Dual-Emission to White Light. *Small* **2019**, *15*, 1901983.

(188) Feng, F.; Nguyen, L. T.; Nasilowski, M.; Nadal, B.; Dubertret, B.; Coolen, L.; Maître, A. Consequence of Shape Elongation on Emission Asymmetry for Colloidal CdSe/CdS Nanoplatelets. *Nano Res.* **2018**, *11*, 3593–3602.

(189) Jana, S.; Phan, T. N. T.; Bouet, C.; Tessier, M. D.; Davidson, P.; Dubertret, B.; Abécassis, B. Stacking and Colloidal Stability of CdSe Nanoplatelets. *Langmuir* **2015**, *31*, 10532–10539.

(190) Yoon, D.-E.; Kim, W. D.; Kim, D.; Lee, D.; Koh, S.; Bae, W. K.; Lee, D. C. Origin of Shape-Dependent Fluorescence Polarization from CdSe Nanoplatelets. *J. Phys. Chem. C* **2017**, *121*, 24837–24844.

(191) Li, Q.; Lian, T. Area- and Thickness-Dependent Biexciton Auger Recombination in Colloidal CdSe Nanoplatelets: Breaking the "Universal Volume Scaling Law." *Nano Lett.* **2017**, *17*, 3152–3158.

(192) Lhuillier, E.; Ithurria, S.; Descamps-Mandine, A.; Douillard, T.; Castaing, R.; Xu, X. Z.; Taberna, P.-L.; Simon, P.; Aubin, H.; Dubertret, B. Investigating the n- and p-Type Electrolytic Charging of Colloidal Nanoplatelets. *J. Phys. Chem. C* **2015**, *119*, 21795–21799.

(193) She, C.; Fedin, I.; Dolzhnikov, D. S.; Dahlberg, P. D.; Engel, G. S.; Schaller, R. D.; Talapin, D. V. Red, Yellow, Green, and Blue Amplified Spontaneous Emission and Lasing Using Colloidal CdSe Nanoplatelets. *ACS Nano* **2015**, *9*, 9475–9485.

(194) Grim, J. Q.; Christodoulou, S.; Di Stasio, F.; Krahne, R.; Cingolani, R.; Manna, L.; Moreels, I. Continuous-Wave Biexciton Lasing at Room Temperature Using Solution-Processed Quantum Wells. *Nature Nanotechnology* **2014**, *9*, 891–895.

(195) Rossinelli, A. A.; Rojo, H.; Mule, A. S.; Aellen, M.; Cocina, A.; De Leo, E.; Schäublin, R.; Norris, D. J. Compositional Grading for Efficient and Narrowband Emission in CdSe-Based Core/Shell Nanoplatelets. *Chem. Mater.* **2019**, *31*, 9567–9578.

(196) Olutas, M.; Guzelturk, B.; Kelestemur, Y.; Yeltik, A.; Delikanli, S.; Demir, H. V. Lateral Size-Dependent Spontaneous and Stimulated Emission Properties in Colloidal CdSe Nanoplatelets. *ACS Nano* **2015**, *9*, 5041–5050.

(197) Fan, F.; Kanjanaboos, P.; Saravanapavanantham, M.; Beauregard, E.; Ingram, G.; Yassitepe, E.; Adachi, M. M.; Voznyy, O.; Johnston, A. K.; Walters, G.; et al. Colloidal CdSe1−XSx Nanoplatelets with Narrow and Continuously-Tunable Electroluminescence. *Nano Lett.* **2015**, *15*, 4611–4615.

(198) Liu, B.; Delikanli, S.; Gao, Y.; Dede, D.; Gungor, K.; Demir, H. V. Nanocrystal Light-Emitting Diodes Based on Type II Nanoplatelets. *Nano Energy* **2018**, *47*, 115–122.

(199) Mahler, B.; Nadal, B.; Bouet, C.; Patriarche, G.; Dubertret, B. Core/Shell Colloidal Semiconductor Nanoplatelets. *J. Am. Chem. Soc.* **2012**, *134*, 18591–18598.

(200) Xiao, P.; Huang, J.; Yan, D.; Luo, D.; Yuan, J.; Liu, B.; Liang, D. Emergence of Nanoplatelet Light-Emitting Diodes. *Materials* **2018**, *11*, 1376.

(201) Vitukhnovsky, A. G.; Lebedev, V. S.; Selyukov, A. S.; Vashchenko, A. A.; Vasiliev, R. B.; Sokolikova, M. S. Electroluminescence from Colloidal Semiconductor CdSe Nanoplatelets in Hybrid Organic–Inorganic Light Emitting Diode. *Chemical Physics Letters* **2015**, *619*, 185–188.

(202) Giovanella, U.; Pasini, M.; Lorenzon, M.; Galeotti, F.; Lucchi, C.; Meinardi, F.; Luzzati, S.; Dubertret, B.; Brovelli, S. Efficient Solution-Processed Nanoplatelet-Based Light-Emitting Diodes with High Operational Stability in Air. *Nano Lett.* **2018**, *18*, 3441–3448.

(203) Cruguel, H.; Livache, C.; Martinez, B.; Pedetti, S.; Pierucci, D.; Izquierdo, E.; Dufour, M.; Ithurria, S.; Aubin, H.; Ouerghi, A.; et al. Electronic Structure of CdSe-ZnS 2D Nanoplatelets. *Appl. Phys. Lett.* **2017**, *110*, 152103.

(204) Feng, F.; NGuyen, L. T.; Nasilowski, M.; Nadal, B.; Dubertret, B.; Maître, A.; Coolen, L. Probing the Fluorescence Dipoles of Single Cubic CdSe/CdS Nanoplatelets with Vertical or Horizontal Orientations. *ACS Photonics* **2018**, *5*, 1994–1999.

(205) Polovitsyn, A.; Dang, Z.; Movilla, J. L.; Martín-García, B.; Khan, A. H.; Bertrand, G. H. V.; Brescia, R.; Moreels, I. Synthesis of Air-Stable CdSe/ZnS Core–Shell Nanoplatelets with Tunable Emission Wavelength. *Chem. Mater.* **2017**, *29*, 5671–5680.

(206) Altintas, Y.; Gungor, K.; Gao, Y.; Sak, M.; Quliyeva, U.; Bappi, G.; Mutlugun, E.; Sargent, E. H.; Demir, H. V. Giant Alloyed Hot Injection Shells Enable Ultralow Optical Gain Threshold in Colloidal Quantum Wells. *ACS Nano* **2019**, *13*, 10662–10670.

(207) Rossinelli, A. A.; Riedinger, A.; Marqués-Gallego, P.; Knüsel, P. N.; Antolinez, F. V.; Norris, D. J. High-Temperature Growth of Thick-Shell CdSe/CdS Core/Shell Nanoplatelets. *Chem. Commun.* **2017**, *53*, 9938–9941.

(208) Kelestemur, Y.; Shynkarenko, Y.; Anni, M.; Yakunin, S.; De Giorgi, M. L.; Kovalenko, M. V. Colloidal CdSe Quantum Wells with Graded Shell Composition for Low-Threshold Amplified Spontaneous Emission and Highly Efficient Electroluminescence. *ACS Nano* **2019**, *13*, 13899–13909.

(209) Kwak, J.; Bae, W. K.; Lee, D.; Park, I.; Lim, J.; Park, M.; Cho, H.; Woo, H.; Yoon, D. Y.; Char, K.; et al. Bright and Efficient Full-Color Colloidal Quantum Dot Light-Emitting Diodes Using an Inverted Device Structure. *Nano Letters* **2012**, *12*, 2362–2366.

(210) Zhang, F.; Wang, S.; Wang, L.; Lin, Q.; Shen, H.; Cao, W.; Yang, C.; Wang, H.; Yu, L.; Du, Z.; et al. Super Color Purity Green Quantum Dot Light-Emitting Diodes Fabricated by Using CdSe/CdS Nanoplatelets. *Nanoscale* **2016**, *8*, 12182–12188.

(211) Kim, W. D.; Kim, D.; Yoon, D.-E.; Lee, H.; Lim, J.; Bae, W. K.; Lee, D. C. Pushing the Efficiency Envelope for Semiconductor Nanocrystal-Based Electroluminescence Devices Using Anisotropic Nanocrystals. *Chem. Mater.* **2019**, *31*, 3066–3082.

(212) Chen, Z.-Q.; Ding, F.; Bian, Z.-Q.; Huang, C.-H. Efficient Near-Infrared Organic Light-Emitting Diodes Based on Multimetallic Assemblies of Lanthanides and Iridium Complexes. *Organic Electronics* **2010**, *11*, 369–376.

(213) Luo, H.; Zhang, W.; Li, M.; Yang, Y.; Guo, M.; Tsang, S.-W.; Chen, S. Origin of Subthreshold Turn-On in Quantum-Dot Light-Emitting Diodes. *ACS Nano* **2019**, *13*, 8229–8236.

(214) Shen, H.; Gao, Q.; Zhang, Y.; Lin, Y.; Lin, Q.; Li, Z.; Chen, L.; Zeng, Z.; Li, X.; Jia, Y.; et al. Visible Quantum Dot Light-Emitting Diodes with Simultaneous High Brightness and Efficiency. *Nature Photonics* **2019**, *13*, 192.

(215) Cragg, G. E.; Efros, A. L. Suppression of Auger Processes in Confined Structures. *Nano Lett.* **2010**, *10*, 313–317.

(216) Pelton, M.; Wang, Y.; Fedin, I.; Talapin, D. V.; O'Leary, S. K. Hot-Carrier Relaxation in CdSe/CdS Core/Shell Nanoplatelets. *J. Phys. Chem. C* **2020**, *124*, 1020–1026.

(217) Philbin, J. P.; Brumberg, A.; Diroll, B. T.; Cho, W.; Talapin, D. V.; Schaller, R. D.; Rabani, E. Area and Thickness Dependence of Auger Recombination in Nanoplatelets. *J. Chem. Phys.* **2020**, *153*, 054104.

(218) Klimov, V. I.; Mikhailovsky, A. A.; McBranch, D. W.; Leatherdale, C. A.; Bawendi, M. G. Quantization of Multiparticle Auger Rates in Semiconductor Quantum Dots. *Science* **2000**, *287*, 1011–1013.

(219) Pelton, M.; Andrews, J. J.; Fedin, I.; Talapin, D. V.; Leng, H.; O'Leary, S. K. Nonmonotonic Dependence of Auger Recombination Rate on Shell Thickness for CdSe/CdS Core/Shell Nanoplatelets. *Nano Lett.* **2017**, *17*, 6900–6906.

(220) Chuang, C.-H. M.; Brown, P. R.; Bulović, V.; Bawendi, M. G. Improved Performance and Stability in Quantum Dot Solar Cells through Band Alignment Engineering. *Nature Materials* **2014**, *13*, 796–801.

(221) Ramade, J.; Qu, J.; Chu, A.; Gréboval, C.; Livache, C.; Goubet, N.; Martinez, B.; Vincent, G.; Lhuillier, E. Potential of Colloidal Quantum Dot Based Solar Cells for Near-Infrared Active Detection. *ACS Photonics* **2020**, *7*, 272–278.

(222) Hines, M. A.; Scholes, G. D. Colloidal PbS Nanocrystals with Size-Tunable near-Infrared Emission: Observation of Post-Synthesis Self-Narrowing of the Particle Size Distribution. *Adv. Mater.* **2003**, *15*, 1844–1849.

(223) Zhou, L.; Ou, Q.-D.; Li, Y.-Q.; Xiang, H.-Y.; Xu, L.-H.; Chen, J.-D.; Li, C.; Shen, S.; Lee, S.-T.; Tang, J.-X. Efficiently Releasing the Trapped Energy Flow in White Organic Light-Emitting Diodes with Multifunctional Nanofunnel Arrays. *Advanced Functional Materials* **2015**, *25*, 2660–2668.

(224) Kwon, J.; Kim, J.; Park, Y.-S.; Cho, D.-H.; Kwon, O. E.; Lee, K. M.; Lee, H. C.; Cho, N. S.; Yu, B. Fab-Compatible Nano-Lens Array Integration for Optically Efficient Flexible Top-Emitting Organic Light-Emitting Diodes. *Jpn. J. Appl. Phys.* **2019**, *58*, SDDH01.

(225) Lu, H.; Carroll, G. M.; Neale, N. R.; Beard, M. C. Infrared Quantum Dots: Progress, Challenges, and Opportunities. *ACS Nano* **2019**, *13*, 939–953.

(226) Semonin, O. E.; Luther, J. M.; Choi, S.; Chen, H.-Y.; Gao, J.; Nozik, A. J.; Beard, M. C. Peak External Photocurrent Quantum Efficiency Exceeding 100% via MEG in a Quantum Dot Solar Cell. *Science* **2011**, *334*, 1530–1533.

(227) Luther, J. M.; Law, M.; Beard, M. C.; Song, Q.; Reese, M. O.; Ellingson, R. J.; Nozik, A. J. Schottky Solar Cells Based on Colloidal Nanocrystal Films. *Nano Lett.* **2008**, *8*, 3488–3492.

(228) McDonald, S. A.; Konstantatos, G.; Zhang, S.; Cyr, P. W.; Klem, E. J. D.; Levina, L.; Sargent, E. H. Solution-Processed PbS Quantum Dot Infrared Photodetectors and Photovoltaics. *Nature Materials* **2005**, *4*, 138–142.

(229) Hafiz, S. B.; Scimeca, M.; Sahu, A.; Ko, D.-K. Colloidal Quantum Dots for Thermal Infrared Sensing and Imaging. *Nano Convergence* **2019**, *6*, 7.

(230) Lhuillier, E.; Guyot-Sionnest, P. Recent Progresses in Mid Infrared Nanocrystal Optoelectronics. *IEEE Journal of Selected Topics in Quantum Electronics* **2017**, *23*, 1–8.

(231) Klem, E. J. D.; Levina, L.; Sargent, E. H. PbS Quantum Dot Electroabsorption Modulation across the Extended Communications Band 1200–1700nm. *Appl. Phys. Lett.* **2005**, *87*, 053101.

(232) Konstantatos, G.; Huang, C.; Levina, L.; Lu, Z.; Sargent, E. H. Efficient Infrared Electroluminescent Devices Using Solution-Processed Colloidal Quantum Dots. *Advanced Functional Materials* **2005**, *15*, 1865–1869.

(233) Medintz, I. L.; Uyeda, H. T.; Goldman, E. R.; Mattoussi, H. Quantum Dot Bioconjugates for Imaging, Labelling and Sensing. *Nature Materials* **2005**, *4*, 435–446.

(234) Qian, G.; Zhong, Z.; Luo, M.; Yu, D.; Zhang, Z.; Wang, Z. Y.; Ma, D. Simple and Efficient Near-Infrared Organic Chromophores for Light-Emitting Diodes with Single Electroluminescent Emission above 1000 nm. *Advanced Materials* **2009**, *21*, 111–116.

(235) Liu, H.; Guyot-Sionnest, P. Photoluminescence Lifetime of Lead Selenide Colloidal Quantum Dots. *J. Phys. Chem. C* **2010**, *114*, 14860–14863.

(236) Tessler, N.; Medvedev, V.; Kazes, M.; Kan, S.; Banin, U. Efficient Near-Infrared Polymer Nanocrystal Light-Emitting Diodes. *Science* **2002**, *295*, 1506–1508.

(237) Vasilopoulou, M.; Kim, H. P.; Kim, B. S.; Papadakis, M.; Ximim Gavim, A. E.; Macedo, A. G.; Jose da Silva, W.; Schneider, F. K.; Mat Teridi, M. A.; Coutsolelos, A. G.; et al. Efficient Colloidal

Quantum Dot Light-Emitting Diodes Operating in the Second near-Infrared Biological Window. *Nature Photonics* **2020**, *14*, 50–56.

(238) Qu, J.; Goubet, N.; Livache, C.; Martinez, B.; Amelot, D.; Gréboval, C.; Chu, A.; Ramade, J.; Cruguel, H.; Ithurria, S.; et al. Intraband Mid-Infrared Transitions in Ag2Se Nanocrystals: Potential and Limitations for Hg-Free Low-Cost Photodetection. *J. Phys. Chem. C* **2018**, *122*, 18161–18167.

(239) Sahu, A.; Qi, L.; Kang, M. S.; Deng, D.; Norris, D. J. Facile Synthesis of Silver Chalcogenide (Ag2E; E = Se, S, Te) Semiconductor Nanocrystals. *J. Am. Chem. Soc.* **2011**, *133*, 6509–6512.

(240) Cassette, E.; Pons, T.; Bouet, C.; Helle, M.; Bezdetnaya, L.; Marchal, F.; Dubertret, B. Synthesis and Characterization of Near-Infrared Cu–In–Se/ZnS Core/Shell Quantum Dots for In Vivo Imaging. *Chem. Mater.* **2010**, *22*, 6117–6124.

(241) Panthani, M. G.; Akhavan, V.; Goodfellow, B.; Schmidtke, J. P.; Dunn, L.; Dodabalapur, A.; Barbara, P. F.; Korgel, B. A. Synthesis of CuInS2, CuInSe2, and Cu(InxGa1-x)Se2 (CIGS) Nanocrystal "Inks" for Printable Photovoltaics. *J. Am. Chem. Soc.* **2008**, *130*, 16770–16777.

(242) Green, M.; Mirzai, H. Synthetic Routes to Mercury Chalcogenide Quantum Dots. *J. Mater. Chem. C* **2018**, *6*, 5097–5112.

(243) Goubet, N.; Thomas, M.; Gréboval, C.; Chu, A.; Qu, J.; Rastogi, P.; Chee, S.-S.; Goyal, M.; Zhang, Y.; Xu, X. Z.; et al. Near- to Long-Wave-Infrared Mercury Chalcogenide Nanocrystals from Liquid Mercury. *J. Phys. Chem. C* **2020**, *124*, 8423–8430.

(244) Izquierdo, E.; Robin, A.; Keuleyan, S.; Lequeux, N.; Lhuillier, E.; Ithurria, S. Strongly Confined HgTe 2D Nanoplatelets as Narrow Near-Infrared Emitters. *J. Am. Chem. Soc.* **2016**, *138*, 10496–10501.

(245) Sergeev, A. A.; Pavlov, D. V.; Kuchmizhak, A. A.; Lapine, M. V.; Yiu, W. K.; Dong, Y.; Ke, N.; Juodkazis, S.; Zhao, N.; Kershaw, S. V.; et al. Tailoring Spontaneous Infrared Emission of HgTe Quantum Dots with Laser-Printed Plasmonic Arrays. *Light: Science & Applications* **2020**, *9*, 16.

(246) Keuleyan, S.; Kohler, J.; Guyot-Sionnest, P. Photoluminescence of Mid-Infrared HgTe Colloidal Quantum Dots. *J. Phys. Chem. C* **2014**, *118*, 2749–2753.

(247) Harrison, M. T.; Kershaw, S. V.; Burt, M. G.; Eychmüller, A.; Weller, H.; Rogach, A. L. Wet Chemical Synthesis and Spectroscopic Study of CdHgTe Nanocrystals with Strong Near-Infrared Luminescence. *Materials Science and Engineering: B* **2000**, *69–70*, 355–360.

(248) Rogach, A. L.; Koktysh, D. S.; Harrison, M.; Kotov, N. A. Layer-by-Layer Assembled Films of HgTe Nanocrystals with Strong Infrared Emission. *Chem. Mater.* **2000**, *12*, 1526–1528.

(249) Harrison, M. T.; Kershaw, S. V.; Rogach, A. L.; Kornowski, A.; Eychmüller, A.; Weller, H. Wet Chemical Synthesis of Highly Luminescent HgTe/CdS Core/Shell Nanocrystals. *Advanced Materials* **2000**, *12*, 123–125.

(250) Kalytchuk, S.; Adam, M.; Tomanec, O.; Zbořil, R.; Gaponik, N.; Rogach, A. L. Sodium Chloride Protected CdHgTe Quantum Dot Based Solid-State Near-Infrared Luminophore for Light-Emitting Devices and Luminescence Thermometry. *ACS Photonics* **2017**, *4*, 1459–1465.

(251) Geiregat, P.; Houtepen, A. J.; Sagar, L. K.; Infante, I.; Zapata, F.; Grigel, V.; Allan, G.; Delerue, C.; Van Thourhout, D.; Hens, Z. Continuous-Wave Infrared Optical Gain and Amplified Spontaneous Emission at Ultralow Threshold by Colloidal HgTe Quantum Dots. *Nature Materials* **2018**, *17*, 35–42.

(252) O'Connor, É.; O'Riordan, A.; Doyle, H.; Moynihan, S.; Cuddihy, A.; Redmond, G. Near-Infrared Electroluminescent Devices Based on Colloidal HgTe Quantum Dot Arrays. *Applied Physics Letters* **2005**, *86*, 1–3.

(253) Marus, M.; Xia, Y.; Zhong, H.; Li, D.; Ding, S.; Turavets, U.; Xu, B.; Wang, K.; Zhang, J.; Sun, X. W. Bright Infra-Red Quantum Dot Light-Emitting Diodes through Efficient Suppressing of Electrons. *Appl. Phys. Lett.* **2020**, *116*, 191103.

(254) Yang, X.; Ren, F.; Wang, Y.; Ding, T.; Sun, H.; Ma, D.; Sun, X. W. Iodide Capped PbS/CdS Core-Shell Quantum Dots for Efficient Long-Wavelength near-Infrared Light-Emitting Diodes. *Scientific Reports* **2017**, *7*, 14741.

(255) Gong, X.; Yang, Z.; Walters, G.; Comin, R.; Ning, Z.; Beauregard, E.; Adinolfi, V.; Voznyy, O.; Sargent, E. H. Highly Efficient Quantum Dot Near-Infrared Light-Emitting Diodes. *Nature Photonics* **2016**, *10*, 253–257.

(256) Choudhury, K. R.; Song, D. W.; So, F. Efficient Solution-Processed Hybrid Polymer–Nanocrystal near Infrared Light-Emitting Devices. *Organic Electronics* **2010**, *11*, 23–28.

(257) Bourdakos, K. N.; Dissanayake, D. M. N. M.; Lutz, T.; Silva, S. R. P.; Curry, R. J. Highly Efficient Near-Infrared Hybrid Organic-Inorganic Nanocrystal Electroluminescence Device. *Appl. Phys. Lett.* **2008**, *92*, 153311.

(258) Steckel, J. S.; Coe-Sullivan, S.; Bulović, V.; Bawendi, M. G. 1.3 μm to 1.55 μm Tunable Electroluminescence from PbSe Quantum Dots Embedded within an Organic Device. *Advanced Materials* **2003**, *15*, 1862–1866.

(259) Tessler, N.; Medvedev, V.; Kazes, M.; Kan, S.; Banin, U. Efficient Near-Infrared Polymer Nanocrystal Light-Emitting Diodes. *Science* **2002**, *295*, 1506–1508.

(260) Koktysh, D. S.; Gaponik, N.; Reufer, M.; Crewett, J.; Scherf, U.; Eychmüller, A.; Lupton, J. M.; Rogach, A. L.; Feldmann, J. Near-Infrared Electroluminescence from HgTe Nanocrystals. *ChemPhysChem* **2004**, *5*, 1435–1438.

(261) Qu, J.; Rastogi, P.; Gréboval, C.; Lagarde, D.; Chu, A.; Dabard, C.; Khalili, A.; Cruguel, H.; Robert, C.; Xu, X. Z.; et al. Electroluminescence from HgTe Nanocrystals and Its Use for Active Imaging. *Nano Lett.* **2020**, *20*, 6185–6190.

(262) Chuang, C.-H. M.; Brown, P. R.; Bulović, V.; Bawendi, M. G. Improved Performance and Stability in Quantum Dot Solar Cells through Band Alignment Engineering. *Nature Materials* **2014**, *13*, 796–801.

(263) Lu, K.; Wang, Y.; Liu, Z.; Han, L.; Shi, G.; Fang, H.; Chen, J.; Ye, X.; Chen, S.; Yang, F.; et al. High-Efficiency PbS Quantum-Dot Solar Cells with Greatly Simplified Fabrication Processing via "Solvent-Curing." *Advanced Materials* **2018**, *30*, 1707572.

(264) Pradhan, S.; Stasio, F. D.; Bi, Y.; Gupta, S.; Christodoulou, S.; Stavrinadis, A.; Konstantatos, G. High-Efficiency Colloidal Quantum Dot Infrared Light-Emitting Diodes via Engineering at the Supra-Nanocrystalline Level. *Nature Nanotechnology* **2019**, *14*, 72.

(265) Geiregat, P.; Houtepen, A. J.; Sagar, L. K.; Infante, I.; Zapata, F.; Grigel, V.; Allan, G.; Delerue, C.; Van Thourhout, D.; Hens, Z. Continuous-Wave Infrared Optical Gain and Amplified Spontaneous Emission at Ultralow Threshold by Colloidal HgTe Quantum Dots. *Nature Materials* **2018**, *17*, 35–42.

(266) Chu, A.; Martinez, B.; Ferré, S.; Noguier, V.; Gréboval, C.; Livache, C.; Qu, J.; Prado, Y.; Casaretto, N.; Goubet, N.; et al. HgTe Nanocrystals for SWIR Detection and Their Integration up to the Focal Plane Array. *ACS Appl. Mater. Interfaces* **2019**, *11*, 33116–33123.

(267) Goubet, N.; Jagtap, A.; Livache, C.; Martinez, B.; Portalès, H.; Xu, X. Z.; Lobo, R. P. S. M.; Dubertret, B.; Lhuillier, E. Terahertz HgTe Nanocrystals: Beyond Confinement. *J. Am. Chem. Soc.* **2018**, *140*, 5033–5036.

(268) Hines, M. A.; Scholes, G. D. Colloidal PbS Nanocrystals with Size-Tunable Near-Infrared Emission: Observation of Post-Synthesis Self-Narrowing of the Particle Size Distribution. *Advanced Materials* **2003**, *15*, 1844–1849.

(269) Clark, S. W.; Harbold, J. M.; Wise, F. W. Resonant Energy Transfer in PbS Quantum Dots. *J. Phys. Chem. C* **2007**, *111*, 7302–7305.

(270) Rath, A. K.; Arquer, F. P. G. de; Stavrinadis, A.; Lasanta, T.; Bernechea, M.; Diedenhofen, S. L.; Konstantatos, G. Remote Trap Passivation in Colloidal Quantum Dot Bulk Nano-Heterojunctions and Its Effect in Solution-Processed Solar Cells. *Advanced Materials* **2014**, *26*, 4741–4747.

(271) Bozyigit, D.; Yarema, O.; Wood, V. Origins of Low Quantum Efficiencies in Quantum Dot LEDs. *Advanced Functional Materials* **2013**, *23*, 3024–3029.

(272) Barkhouse, D. A. R.; Debnath, R.; Kramer, I. J.; Zhitomirsky, D.; Pattantyus-Abraham, A. G.; Levina, L.; Etgar, L.; Grätzel, M.; Sargent, E. H. Depleted Bulk Heterojunction Colloidal Quantum Dot Photovoltaics. *Advanced Materials* **2011**, *23*, 3134–3138.

(273) Atomsa Gonfa, B.; Zhao, H.; Li, J.; Qiu, J.; Saidani, M.; Zhang, S.; Izquierdo, R.; Wu, N.; El Khakani, M. A.; Ma, D. Air-Processed Depleted Bulk Heterojunction Solar Cells Based on PbS/CdS Core–Shell Quantum Dots and TiO2 Nanorod Arrays. *Solar Energy Materials and Solar Cells* **2014**, *124*, 67–74.

(274) Melnychuk, C.; Guyot-Sionnest, P. Slow Auger Relaxation in HgTe Colloidal Quantum Dots. *J. Phys. Chem. Lett.* **2018**, *9*, 2208–2211.

(275) Rosencher, E.; Vinter, B. *Optoélectronique: cours et exercices corrigés*; Dunod: Paris, 2002.

(276) Wang, H.; Aassime, A.; Le Roux, X.; Schilder, N. J.; Greffet, J.-J.; Degiron, A. Revisiting the Role of Metallic Antennas to Control Light Emission by Lead Salt Nanocrystal Assemblies. *Phys. Rev. Applied* **2018**, *10*, 034042.

(277) Greffet, J.-J.; Bouchon, P.; Brucoli, G.; Marquier, F. Light Emission by Nonequilibrium Bodies: Local Kirchhoff Law. *Phys. Rev. X* **2018**, *8*, 021008.

(278) Cassidy, J.; Ellison, C.; Bettinger, J.; Yang, M.; Moroz, P.; Zamkov, M. Enabling Narrow Emission Line Widths in Colloidal Nanocrystals through Coalescence Growth. *Chemistry of Materials* **2020**, *32*, 7524–7534.

(279) Izquierdo, E.; Robin, A.; Keuleyan, S.; Lequeux, N.; Lhuillier, E.; Ithurria, S. Strongly Confined HgTe 2D Nanoplatelets as Narrow Near-Infrared Emitters. *J. Am. Chem. Soc.* **2016**, *138*, 10496–10501.

(280) Pradhan, S.; Stavrinadis, A.; Gupta, S.; Bi, Y.; Stasio, F. D.; Konstantatos, G. Trap-State Suppression and Improved Charge Transport in PbS Quantum Dot Solar Cells with Synergistic Mixed-Ligand Treatments. *Small* **2017**, *13*, 1700598.

(281) Evirgen, A.; Abautret, J.; Perez, J. P.; Cordat, A.; Nedelcu, A.; Christol, P. Midwave Infrared InSb NBn Photodetector. *Electronics Letters* **2014**, *50*, 1472–1473.

(282) Kopytko, M.; Kębłowski, A.; Gawron, W.; Madejczyk, P.; Kowalewski, A.; Jóźwikowski, K. High-Operating Temperature MWIR NBn HgCdTe Detector Grown by MOCVD. *Opto-Electronics Review* **2013**, *21*, 402–405.

(283) Rodriguez, J. B.; Plis, E.; Bishop, G.; Sharma, Y. D.; Kim, H.; Dawson, L. R.; Krishna, S. NBn Structure Based on InAs/GaSb Type-II Strained Layer Superlattices. *Appl. Phys. Lett.* **2007**, *91*, 043514.

(284) Aldakov, D.; Lefrançois, A.; Reiss, P. Ternary and Quaternary Metal Chalcogenide Nanocrystals: Synthesis, Properties and Applications. *J. Mater. Chem. C* **2013**, *1*, 3756–3776.

(285) Zhao, Y.; Wang, V.; Lien, D.-H.; Javey, A. A Generic Electroluminescent Device for Emission from Infrared to Ultraviolet Wavelengths. *Nature Electronics* **2020**, *3*, 612–621.

Applications en optoélectronique des Nanocristaux colloïdaux, le cas des photodétecteurs et des diodes électroluminescentes

Resumé : Les nanocristaux dont la dimension est inférieure à leur rayon de Bohr excitonique peuvent fournir des propriétés optoélectroniques accordable avec la taille. Cela permet d'obtenir des propriétés éléctroniques à façon. En particulier, le développement de la synthèse par voie colloidale des nanocristaux en fait des briques élémentaires prometteuses pour des applications optoélectroniques à bas cout. Ma thèse cible deux aspects des dispositifs à base de nanocristaux: les photodétecteurs infrarouges et les diodes électroluminescentes (LED).

Ma thèse est d'abord centrée sur la photodétection infrarouge sans métaux lourds utilisant soit la transition intrabande d'Ag2Se, soit des nanocristaux plasmoniques ITO. J'ai étudié leurs propriétés optiques et de transport ainsi que leur spectre électronique. J'ai ensuite testé leurs performances pour la photodétection infrarouge. Les performances obtenus sont mis en perspective par rapport à leurs homologues contenant des métaux lourds.

Dans une second partie de ma thèse, je me focalise sur les LEDs à base de nanocristaux avec des longueurs d'onde visées à la fois dans le visible te le proche infrarouge. La LED visible conçue à l'aide de nanoplaquettes CdSe/CdZnS montre une faible tension de fonctionnement et la durée de vie la plus longue obtenue pour les LED à base de nanoplaquettes. Ensuite, cette LED est couplée à un photodétecteur PbS maison pour réaliser pour la première fois une communication de type LiFi tout nanocristal. Pour les LED proche infrarouge, j'ai utilisé HgTe comme matériau optiquement actif. En formant une hétérojonction à partir de HgTe / ZnO, une LED infrarouge lumineuse capable d'imagerie active est obtenue.

Mots clés : nanocristaux; infrarouge; photodétecteur; diodes électroluminescentes

Colloidal semiconductor nanocrystals for optoelectronic applications: photodetectors and light emitting diodes

Abstract: Nanocrystals with a dimension below their excitonic Bohr radius can provide size-tunable optoelectronic properties, enabling on-demand tailoring of properties for specific applications. Especially, the advance of wet chemistry synthesis of colloidal nanocrystals makes them promising building blocks for the next-generation solution-processible low-cost optoelectronics such as light emitting, sensing, and harvesting. My thesis targets two aspects of the nanocrystal-based devices: infrared (IR) photodetector and light emitting diode (LED).

My thesis is first focused on the heavy-metal-free IR photodetection using the intraband transition of self-doped Ag2Se or the plasmonic resonance of remotely doped ITO (tin doped indium oxide) nanocrystals. Before integrating them to photoconductive devices, I study their optical and transport properties as well as their energy spectra. I then test their IR photodetection performance and rationalize their weak performance compared with their heavy metal counterparts.

In the second part of my thesis, I advance to the all-solution nanocrystal-based LEDs in the visible and SWIR, with an emphasis on their practical applications. The designed visible LED using CdSe/CdZnS nanoplatelets (NPLs) shows the lowest turn-on voltage and the longest lifetime for NPL-based LED. I also provide insights on the origin of efficiency droop. Then, this LED is coupled with a homemade PbS broadband photodetector to achieve, for the first time, an all-nanocrystal based LiFi-like communication setup. For SWIR LEDs, HgTe is used as IR emitter. By forming a HgTe/ZnO bulk heterojunction in the emitting layer, a bright SWIR LED capable of active imaging is obtained.

Key words: Nanocrystals; infrared; photodetectors; light emitting deiodes